LUMINESCENT HARNESSING OF 2D TRANSITION METAL DICHALCOGENIDE EXCITONS

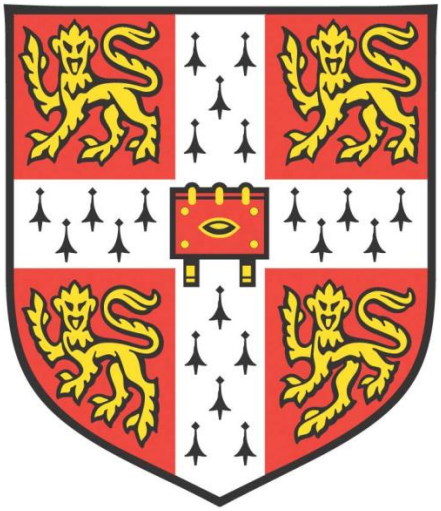

Arelo Obuadum Abiola Tanoh

Clare Hall

Department of Physics

University of Cambridge

This dissertation is submitted for the degree of

Doctor of Philosophy

June 2021

DECLARATION

This thesis is the result of my own work and includes nothing which is the outcome of work done in collaboration except where specifically indicated in the text. It is not substantially the same as any that I have submitted for a degree or diploma or other qualification at the University of Cambridge or any other University or similar institution. I further state that no substantial part of my thesis has already been submitted, or is being concurrently submitted for any such degree, diploma or other qualification at the University of Cambridge or any other University. In accordance with the Department of Physics guidelines, this thesis does not exceed 60,000 words, and it contains less than 150 figures.

Arelo Obuadum Abiola Tanoh

June 2021

ABSTRACT

Two-dimensional (2D) semiconducting transition metal dichalcogenides (TMDs) are regarded as viable candidates for future high-performance optoelectronic and electronic devices due to their chemical stability, low dimensionality, direct bandgap and favourable electronic mobilities. Their direct bandgap facilitates strong light coupling, yielding photoluminescence (PL). Their quantum confined nature produces tightly bound excitons that exhibit intriguing many-body phenomena. 2D excitons may be transferred to other emissive materials in a heterostructure system. This has applications in *e.g.*, photon harvesting with luminescent solar concentrators (LSCs). Newly prepared monolayers are however susceptible to chalcogen atom vacancies, which quench bright excitons and trap mobile charges, amounting to material with poor PL yields and low mobilities, which is of little practical use. Post-fabrication defect passivation schemes offer a means to recover and enhance optical and electronic properties of newly fabricated monolayers. This thesis presents a novel surface treatment based on oleic acid (OA) ligands, which unlike previously reported schemes, is applicable to both sulphide and selenide TMDs. As separate studies, we investigate the effects of OA on monolayer tungsten disulphide (WS_2) and molybdenum diselenide ($MoSe_2$). Steady state and time resolved PL (TRPL) microscopy uncover the photophysics of PL enhancement by OA treatment, and provides insights into the surface passivation mechanism. Electronic measurements of 2D TMD field effect transistors support the conclusions drawn from optical measurements. The following study reports exciton transfer from a 2D TMD absorber to a quantum dot (QD) emitter in a 2D-QD heterostructure. WS_2 is harnessed as an optical antenna, from which excitons are funnelled to near infrared (NIR) lead sulphide-cadmium sulphide QDs. This describes the opposite process to what has been reported for similar hybrid systems, where 2D TMDs quench excitons. Steady state PL techniques confirm excitation energy transfer (ET), and the ET mechanism. TRPL studies reveal ET dynamics and confirm ET efficiency. Combining steady state PL and TRPL elucidates the ET pathway and competing loss channels. Finally, the concept of an LSC based on 2D-QD heterostructure luminophores is developed with the aid of Monte Carlo light transport simulations. Using an idealised luminophore model, Heterostructure LSC performance is compared to other LSCs based on typical luminophore materials namely, Lumogen Red 305 dye and NIR QDs.

ACKNOWLEDGEMENTS

Not so long ago, the idea of pursuing a PhD seemed far-fetched. It all started with a mere suggestion from my thesis supervisor in Edinburgh, Prof. Alistair Borthwick, to whom I owe my gratitude for seeing my potential. Cambridge offered a change of scenery, which I was not quite prepared for following the Edinburgh years. Nonetheless it has been memorable, and I would like to acknowledge the people who were part of this experience: Dr. Akshay Rao for his contagious enthusiasm for science and guidance throughout the PhD. Rao group members Raj, Jesse, Nicolas, Tomi, Hope, all of whom offered their expertise in spectroscopy and general assistance with experimental work. I also thank post-doctoral researchers, Jooyoung Sung, James Xiao, Ye Fan, Zhaojun Li, Simon Dowland and Jack Alexander Webber, whose combined patience and input enabled me to produce high quality experimental results worthy of publication. To my MRes Graphene CDT colleagues, Ollie, Cyan, Tahmida, Alex, Mustafa, and Vito-the camaraderie and Dar bar drinks between RSS deadlines smoothed out the rough edges. I thank you all for your friendship throughout the years. I thank my family for their unwavering support. My mother Karen for being a guiding light in my life, who offered nothing but encouragement every step of the way. My brother Christopher, for reminding me that there is a life to be lived beyond the confines of a laboratory and my father Augustus for urging me to persevere. Finally, to Alessia, for making wonderful memories with me in Paris, Paphos and beyond!

CONTENTS

LIST OF PUBLICATIONS

1) **Tanoh, A. O. A**.; Alexander-Webber, J.; Xiao, J.; Delport, G.; Williams, C. A.; Bretscher, H.; Gauriot, N.; Allardice, J.; Pandya, R.; Fan, Y.; Li, Z.; Vignolini, S.; Stranks, S.D.; Rao, A. Enhancing Photoluminescence and Mobilities in WS_2 Monolayers with Oleic Acid Ligands. *Nano Lett*. **2019**, 19 (9), 6299–6307. https://doi.org/10.1021/acs.nanolett.9b02431.

2) **Tanoh, A. O. A**.; Alexander-Webber, J.; Fan, Y.; Gauriot, N.; Xiao, J.; Pandya, R.; Li, Z.; Hofmann, S.; Rao, A. Giant Photoluminescence Enhancement in $MoSe_2$ Monolayers treated with Oleic Acid. *Nanoscale Adv.* **2021**, Advance Article. https://doi.org/10.1039/D0NA01014F

3) **Tanoh, A. O. A**.; Gauriot, N.; Delport, G.; Xiao, J.; Pandya, R.; Sung, J.; Allardice, J.; Li, Z.; Williams, C. A.; Baldwin, A.; Stranks, S. D.; Rao, A. Directed Energy Transfer from Monolayer WS_2 to Near-Infrared Emitting PbS-CdS Quantum Dots. *ACS Nano*. **2020**, 14 (11), 15374–15384. https://doi.org/10.1021/acsnano.0c05818.

LIST OF TABLES

LIST OF FIGURES

LIST OF ABBREVIATIONS AND ACRONYMS

0D	Zero Dimensional
2D	Two Dimensional
A.M 1.5 G	Air Mass coefficient at 1.5 atmospheres thickness
AFM	Atomic Force Microscopy
ADF	Atomic Resolution Dark Field Microscopy
BZ	Brillouin Zone
CB	Conduction Band
CBM	Conduction Band Minimum
CCD	Charged Couple Device
CDF	Cumulative Distribution Function
CT	Charge Transfer
CVD	Chemical Vapour Deposition
DET	Dexter Energy Transfer
EC	Escape cone
EL	Electroluminescence
EQE	External Quantum Efficiency
ET	Energy Transfer
FET	Field Effect Transistor
FRET	Förster Resonance Energy Transfer
FWHM	Full Width Half Maximum
hBN	Hexagonal Boronitride
IGS	Inter-gap States
IPA	Iso Propyl Alcohol
IRF	Instrument Response Function

LED	Light Emitting Diode
LPE	Liquid Phase Exfoliation
LSC	Luminescent Solar Concentrator
MC	Monte Carlo
NA	Numerical Aperture
ND	Neutral Density
NIR	Near Infrared
NREL	National Renewable Energy Lab
NRD	Non-Radiative
OA	Oleic Acid
PDF	Probability Density Function
PL	Photoluminescence
PLE	Photoluminescence Excitation
PLQE	Photoluminescence Quantum Efficiency
PLQY	Photoluminescence Quantum Yield
PMT	Photomultiplier Tube
PV	Photovoltaics
QD	Quantum Dot
QY	Quantum Yield
FTIR-SNOM	Fourier transform infrared scanning near near-field optical microscopy
SPAD	Single Photon Avalanche Diode
STEM	Scanning Tunnelling Electron Microscopy
STM	Scanning Tunnelling Microscopy
STS	Scanning Tunnelling Spectroscopy
TA	Transient Absorption
TCSPC	Time Correlated Single Photon Counting

TEM	Transmission Electron Microscopy
TFSI	Bis(trifluoromethane)sulfonimide `super acid’
TIR	Total Internal Reflection
TRPL	Time Resolved Photoluminescence
UV-Vis	Ultraviolet-Visible
VBM	Valence Band Maximum
Vis-SPAD	Visible range Single Photon Avalanche Diode
XPS	X-ray photoelectron spectroscopy

LIST OF APPENDICES

1 Introduction

The isolation of single layer graphene from bulk graphite *via* `scotch tape' exfoliation, and subsequent characterisation has ushered in a new era of research into atomically thin layered nanomaterials, otherwise referred to as 2D materials.[1] Over recent years, the area of 2D materials has rapidly developed into one of the most active fields in condensed matter physics, chemistry, electronics and materials science.[2] The reasons for the field's rapid ascension lie in the remarkable mechanical, optical and electronic properties, as well as chemical stability displayed by a number of these materials. In particular, their strong light coupling yields a wealth of interesting fundamental physical processes. From a device perspective, this highly efficient light-matter interaction compounded with low dimensionality firmly places 2D materials as potential candidates for applications in future optoelectronic technologies.[2–5]

Graphene, the most prolific of this class of materials, is known to have extraordinary electronic transport properties and wide-band absorption of electromagnetic radiation on account of its linear `zero gap' band structure. Graphene's lack of a band gap however means that it can neither be switched off or re-emit absorbed light (*i.e.*, photoluminesce). The application of graphene to optoelectronic and electronic devices is thus restricted where semiconductors are essential.[3,5]

Transition metal dichalcogenides (TMDs) are an alternative class of layered materials that can be processed into 2D monolayers in the same manner as graphene. A number of TMDs are semiconducting, transitioning from indirect bandgap to direct bandgap semiconductors in the monolayer limit. Consequently, these monolayer TMDs possess photoluminescence (PL) with strong wide-band absorption from the visible to

near infrared (NIR) spectral region.[3,5,6] These properties compounded with their potentially high charge carrier mobilities[7] are essential for high performance electronics and optoelectronic applications, which include: light emission; light detection; light harvesting; photovoltaics (PV) and; single photon emission and detection for quantum information processing.[3,5,8–12]

Realising the full potential of TMDs for a number of optoelectronic technologies requires monolayers of high optical quality as given by bright, uniform, efficient PL. In spite of this, newly fabricated monolayer TMDs exhibit extremely low PL yields.[3–5] A leading explanation for this outcome is the prevalence of point defects,[13] namely, chalcogen vacancies[14–16] and oxygen substitutions[17,18] within the monolayer's crystal lattice. The loss of optical energy (*i.e.* PL) in the form of *excitons* is known to occur *via* inter-bandgap defect or `*trap'* states associated with chalcogen vacancies.[19–21] Although the mechanism for defect-assisted PL quenching is yet to be fully understood,[19] defect `repair' or `passivation' offers a means to avert optical losses and thereby fully harness the luminescent properties of monolayer TMDs. Towards this end, a number of passivation schemes have been developed to improve PL yields in monolayer TMDs. These methods include solution-based or `*wet*' chemical treatments, which have been successful in enhancing monolayer PL, but are however limited to sulphur based TMDs.[20–24] The leading example of this is treatment with bis(trifluoromethane)sulfonimide (TFSI) `super-acid', which greatly improves PL emission in sulphur based TMDs *i.e.* molybdenum disulphide (MoS_2) and tungsten disulphide (WS_2) monolayers,[20] but quenches PL in their selenium based counterparts, molybdenum diselenide ($MoSe_2$) and tungsten diselenide (WSe_2).[25]

Monolayer TMDs may also be combined with other nanomaterials with strong light-matter interaction such as quantum dots (QDs) to realise heterostructures with improved light detection and light harvesting capabilities enabled by interfacial charge or energy transfer at the heterostructure interface.[26]

In this thesis, we present a novel `wet' chemical passivation scheme based oleic acid (OA), a long chain organic acid commonly used to terminate surface defects in colloidal nanocrystal QDs. We find that OA treatment drastically enhances PL yields and improves electrical transport characteristics in both sulphur and selenium based group VI TMDs, WS_2[27] and $MoSe_2$.[28] To demonstrate how the luminescent properties of monolayer TMDs may be utilised, we developed and characterised a photon energy down-conversion 2D TMD-quantum dot (2D-QD) heterostructure, in which a monolayer TMD absorber

directly funnels optically generated excitons to near infrared (NIR) QD emitters.[29] This novel system is unlike other 2D-QD heterostructures studied in the wider literature, where QD excitons are quenched by a 2D TMD exciton sink.[30–36] As well as lighting and other optoelectronic device applications, the heterostructure system developed herein could be applied to photon management technologies for light harvesting, particularly luminescent solar concentrators (LSCs). We go on to simulate light transport in 2D-QD based LSC using Monte Carlo (MC) raytracing. The details and structure of this thesis are outlined as follows:

Chapter 2 covers the scientific foundation and background knowledge pertaining to the experimental work presented in the later chapters. The chapter begins with basic band theory, inorganic semiconductor physics, the exciton and quantum confinement in nanocrystals. We move onto the optoelectronic properties of 2D TMDs, which includes: their structural and electronic properties; 2D confined excitons; PL; defects and their impact on optoelectronic quality and; existing defect passivation techniques for improving optoelectronic performance. Next, we introduce 2D field effect transistors and other 2D TMD based (optoelectronic) devices. This follows with a brief review on 2D TMD-quantum dot (2D-QD) energy transfer heterostructures and the underlying energy transfer mechanisms. We then introduce the concept of a luminescent solar concentrator (LSC) based on the 2D TMD absorber and QD emitter heterostructure system. Finally, TMD monolayer preparation techniques are summarised.

Chapter 3 introduces the main experimental techniques used in this thesis. First, a detailed description of the TMD monolayer preparation method is provided. This is followed with an overview of the steady state and time resolved optical spectroscopy techniques employed in this work. The last section describes the Monte Carlo raytracing method for simulating light transport in LSCs.

Chapter 4 provides the first demonstration of OA treatment for enhancing PL and electronic transport properties in a sulphur based TMD monolayer, WS_2. Steady state PL microscopy reveals that OA treatment produces monolayers with bright PL comparable to TFSI treatment. High laser excitation intensities give rise to bright charged exciton (trion) emission in OA treated monolayers, which is otherwise undetected with TFSI treatment. Probing the PL dynamics of OA treated monolayers reveals non-trap limited exciton dynamics, unlike those treated with TFSI. Electronic measurements of OA treated WS_2 field effect transistors (FETs) show an improvement in carrier mobilities and reduced charge trap density. These results point to defect passivation, where OA

ligands terminate chalcogen vacancies as seen in colloidal lead sulphide (PbS) QDs, for example.

Chapter 5 extends OA treatment to a selenide based TMD, $MoSe_2$. Steady state PL measurements show that OA treatment greatly enhances PL, improving spatial uniformity in brightness and reducing emission linewidth. A combination of steady state excitation intensity dependent PL and time resolved PL measurements reveal trap free exciton dynamics dominated by neutral exciton recombination in OA treated monolayers. $MoSe_2$ FETs show reduced charge trap density and increased on-off ratios when treated. The combination of enhanced optical and electronic properties due to OA treatment serve as strong evidence for defect passivation by OA ligands. The possibility of defect passivation *via* oleate group coordination to molybdenum dangling bonds at chalcogen (Se) vacancies is discussed. Importantly however, this study establishes OA treatment as the first solution based chemical passivation scheme applicable to both group VI TMD selenide and sulphide monolayers.

Chapter 6 explores energy transfer (ET) from monolayer WS_2 to NIR emitting lead sulphide-cadmium sulphide (PbS-CdS) QDs in a luminescent 2D-QD heterostructure. Due to its high absorption cross-section in the visible region, monolayer WS_2 serves as an optical antenna from which high energy excitons are generated and funnelled to high PL yield NIR QD emitters, where exciton emission energy is downshifted over hundreds of milli electron volts (meV). The ET process was characterised using a combination of steady state and time resolved PL microscopy. Time resolved PL measurements reveal a 2D to QD ET rate that outcompetes intrinsic PL quenching by defect states in the TMD monolayer, thus allowing for efficient energy transfer (58%). We find that the WS_2 band-edge to trap state exciton transfer channel acts as a parasitic energy pathway that requires passivation to further enhance ET efficiency. The results demonstrate, for the first time, the use of QDs as tuneable high PL emitters to modify TMD monolayer emission properties. This has applications in *e.g.*, lighting, and artificial light harvesting.

Chapter 7 investigates the potential application of the 2D-QD ET system as a luminophore material for artificial light harvesting with LSCs *via* Monte Carlo light transport simulations. The validity of the simulations is discussed in detail. Further recommendations for refining the simulations are made towards the development of a predictive tool to for 2D-QD heterostructure LSC design.

Chapter 8 Summarises the key findings of the work presented in this thesis and provides recommendations for future work.

2 Background

This chapter provides the essential background knowledge and terminology required to navigate the research presented in this thesis. In section 2.1, we briefly recap the origin of band structure in solids along with some basic principles and concepts in semiconductor physics, namely doping and importantly, the exciton.

In section 2.2., we go on to introduce quantum confinement, which is extremely relevant towards understanding the origins of the electronic structure and optoelectronic properties of semiconducting nanomaterials such as monolayer transition metal dichalcogenides. Nanocrystal quantum dots (QDs) are used as a model system to explain quantum confinement effects. Section 2.3 covers the optoelectronic properties of 2D TMDs in considerable depth. The section begins with the structural and electronic properties of the 2D TMDs of interest, followed with a detailed overview of excitons in 2D TMDs, photoluminescence, defects, and their effects on optical and electronic performance of 2D TMDs. We briefly review recent work on defect passivation techniques for improving the optoelectronic quality of these materials as a prelude to chapters 4 and 5.

Section 2.4 introduces 2D TMD-based field effect transistors (2D-FETs) and their performance characteristics. This is deemed necessary as 2D-FET characteristics are used as a measure of electronic performance of surface treated monolayers in chapters 4-5. Section 2.5 summarises optoelectronic device applications of 2D TMDs for light emission, photovoltaics (PV) and photodetection.

Section 2.6. provides a brief review of notable studies on 2D TMD-Quantum dot (2D-QD) energy transfer (ET) heterostructures. The main energy transfer mechanisms in these systems are outlined. Section 2.7 introduces the concept of a luminescent solar concentrator (LSC) based on a heterostructure luminophore comprising of a 2D TMD absorber and a near infrared (NIR) nanocrystal QD emitter. The section first details the working principle and performance parameters of LSCs prior to detailing the added advantage of the novel luminophore system. Finally, in section 2.8, various TMD monolayer preparation techniques are summarised.

2.1 Introduction to Inorganic Semiconductor Physics

Electrons in an individual atom have well-defined discrete energy-levels within orbitals. In accordance with the Pauli exclusion principle, each energy level can be occupied by two electrons provided that they have opposite spin. We consider two separate atoms that have electrons occupying the same energy level. Bringing them together subdivides this energy level, so that no more than two electrons occupy the same level. In the same way, tightly packing many atoms in a solid splits the atomic orbitals into numerous closely spaced energy levels, effectively forming a continuum or band of allowed states that electrons can occupy as shown in Figure 2.1 below. Between these allowed states are forbidden states.[37]

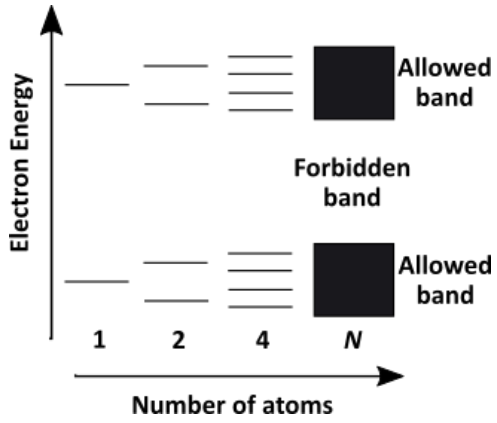

Figure 2.1: Energy band formation in a solid. Closely packing individual atoms leads to subdivision of electronic states amounting to continuous bands in a solid. Adapted from G. Parker.[37]

The highest occupied band is known as the valence band (VB) which contains valence electrons, whereas the lowest unoccupied band is the conduction band (CB). The energy difference between the band edges, that is the bandgap (E_g), defines a solid as a metal, semiconductor or insulator. Semiconductors have a small non-zero bandgap, (E_g ~0.5-3 eV). The relative position of the CB minimum and VB maximum in momentum space characterises a semiconductor as direct or indirect. This has profound implications for a semiconductor's optoelectronic properties, which we uncover subsequently on the topic of semiconducting 2D TMDs. At absolute zero temperature, T = 0 K, semiconductors become insulators, with a filled VB and empty CB.[37] At room temperature, few valence electrons are thermally excited across the bandgap to the CB, leaving positively charged *`holes'* in the VB. These free charges are able to partake in electrical or thermal conduction. In pure *or* intrinsic semiconductors however, the number

of charge carriers is small in comparison to metals. For example, silicon (Si) has 1.4×10^{10} electrons cm^{-3} in the conduction band at 300 K, whereas a typical metal has $\sim10^{34}$ electrons cm^{-3}. The conductivity of intrinsic semiconductors can be modified by doping, which involves introducing of a small number of impurity atoms. Taking the example of Si, which has four valence electrons, a small number of group V atoms (*e.g.*, phosphorus, P) can be introduced into the lattice. Each phosphorus atom has five valence electrons, four of which are covalently bound in the Si lattice, leaving one weakly bound electron. This excess electron sits in a `*donor*' level just below the conduction band edge, requiring little energy to promote it. Such a semiconductor is known as *n*-type. On the other hand, a group III element such as boron (B) can be introduced into the Si lattice. Each boron atom has three valence electrons, leaving an absent bonding electron in the lattice. This introduces an electron acceptor level just above the valence band, where valence electrons can be easily promoted, leaving holes in the valence band as dominant charge carriers. These are known as *p*-type semiconductors.[37]

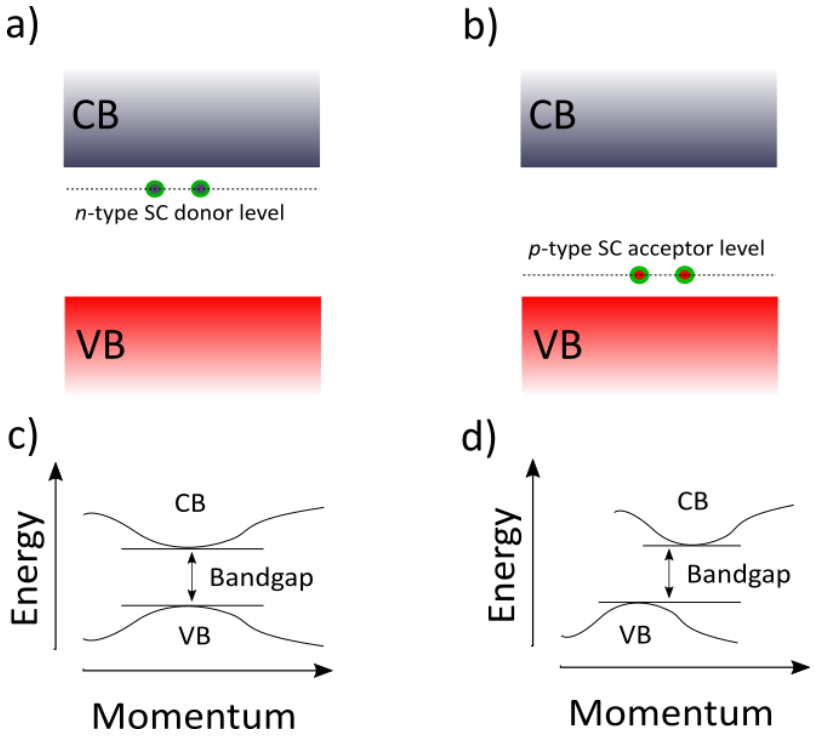

Figure 2.2: Inorganic semiconductor band structure schematic. a) and b) show band diagram of *n* and *p* type semiconductors (SC) with respective positions of electron donor and acceptor levels relative to conduction and valence bands; c) and d) show energy-momentum diagrams of direct and indirect bandgap semiconductors. In a direct bandgap SC, conduction band minima and valence band maxima share the same momentum value, while in an indirect semiconductor, these values differ. Adapted with permission from Dr. Raj Pandya.

2.1.1 Excitons

Excitation of a negatively charged electron from a semiconductor's valence band to conduction band, by *e.g.*, photon absorption, leaves a hole in the valence band. The electron-hole pair are bound by Coulombic interaction. This excited state can be described as a quasi-particle bound state between electron and hole, also referred to as the exciton. In a direct bandgap semiconductor, excitons directly recombine, re-emitting a photon at a wavelength corresponding to the semiconductor bandgap in a process known as photoluminescence (PL), which is illustrated in Figure 2.3 below.

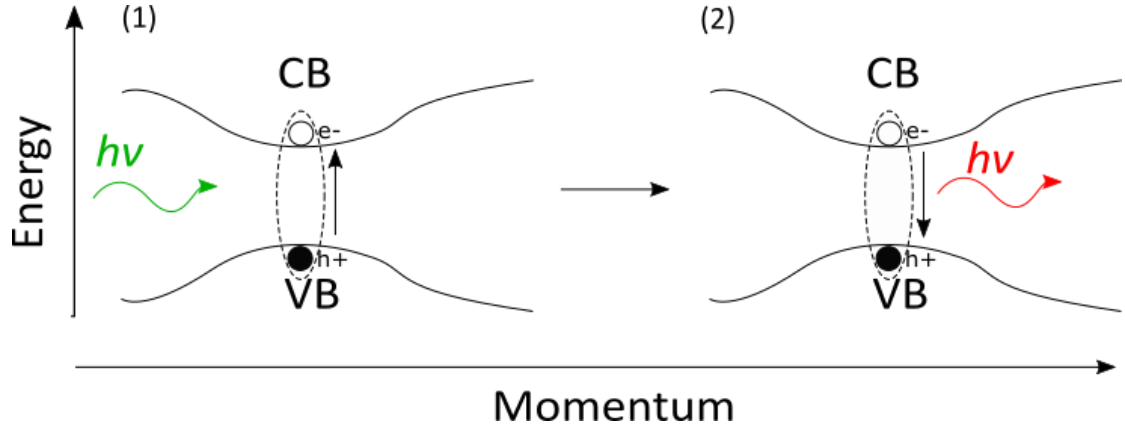

Figure 2.3: Exciton generation and recombination in a direct bandgap semiconductor. (1) exciton generation from photon absorption, and (2) subsequent exciton recombination resulting in PL.

The strong dielectric screening in bulk semiconductors results in reduced binding energy between electron and hole, down to the order of ~10 meV, that is, low enough to be thermally dissociated into individual charges at room temperature. Excitons in such systems are hence indistinguishable from charge carriers at room temperature. These excitons are classified as `Mott-Wannier excitons'.[38] In materials with significantly lower dielectric constants *e.g.* organic semiconductors, exciton binding energies range within 100s of meV. These excitons are termed `Frenkel excitons'.[39]

2.2 Quantum Confinement in Semiconducting Nanocrystals

Quantum confinement defines the changes in a bulk semiconductor's optoelectronic properties when its size is reduced below the characteristic electron-hole separation distance, *i.e.*, the exciton Bohr radius- a property unique to the bulk material.

Confining the exciton's spatial extent restricts the bulk semiconductor's continuous energy bands to discrete energy levels as per a semiconducting nanocrystal, *or* quantum dot (QD). Figure 2.4. illustrates the phenomenon. The quantization of energy states in QDs is reminiscent of the discrete electronic energy levels in individual atoms. Due to confinement in all directions, the excited state energy levels in a QD are well approximated by the *`particle in a box'* infinite potential well model. Following this model, the excited state energy levels of a QD, E, are directly related to its diameter, L, such that $E \propto 1/L^2$. As a consequence, the QD bandgap, E_g, and thus PL emission wavelength, can be tuned by controlling nanocrystal size.[40,41]

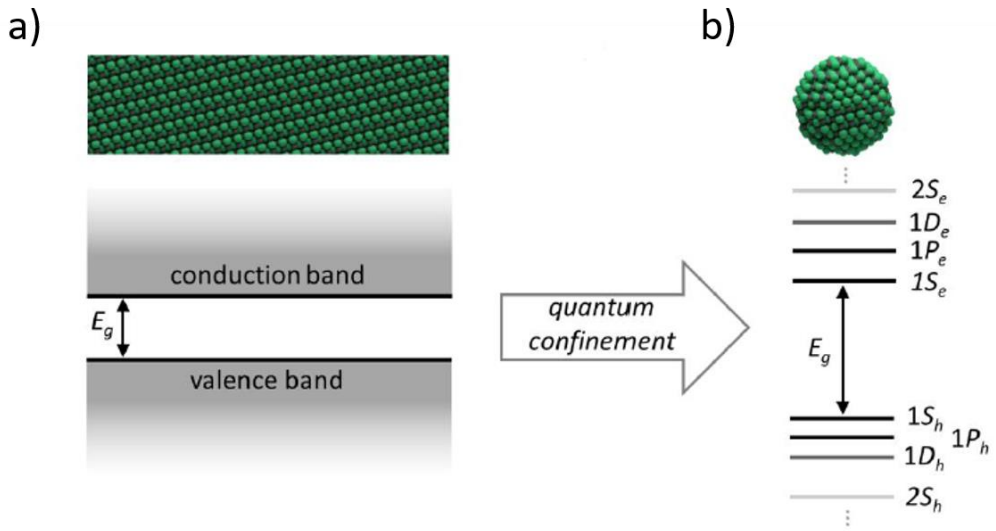

Figure 2.4: Effects of quantum confinement on electronic structure in nanocrystals. a) Bulk semiconductor with continuous conduction and valence band structure; b) Discretised energy states of electrons (*e*) and holes (*h*) in nanocrystal due to quantum confinement. Reproduced with permission form Dr. Jesse Allardice.

In essence, the electronic structure and resulting optoelectronic properties of zero (0D) dimensional QDs arise from confinement of exciton movement in all three (*x*, *y*, z) directions. In the next section, we find that exciton confinement in the out-of-plane direction (*z*) plays a critical role in defining the unique optoelectronic properties of two dimensional (2D) semiconducting transition metal dichalcogenides (TMDs).

2.3 Optoelectronic Properties of 2D TMDs

2.3.1 Structural and Electronic Properties

Transition metal dichalcogenides (TMDs) are a class of materials generalised by the chemical formula MX_2, where M is the transition metal (*e.g.*, Molybdenum (Mo)) and X is the chalcogen (*e.g.* Sulphur (S)).[5] TMDs vary from metallic to semiconducting.[5,6] This thesis is concerned with semiconducting TMDs, particularly, group-VI TMDs (M = Mo, W; X = S, Se), which are known to transition from indirect bandgap semiconductors as bulk crystals to direct bandgap semiconductors as monolayers.[3,5,6]

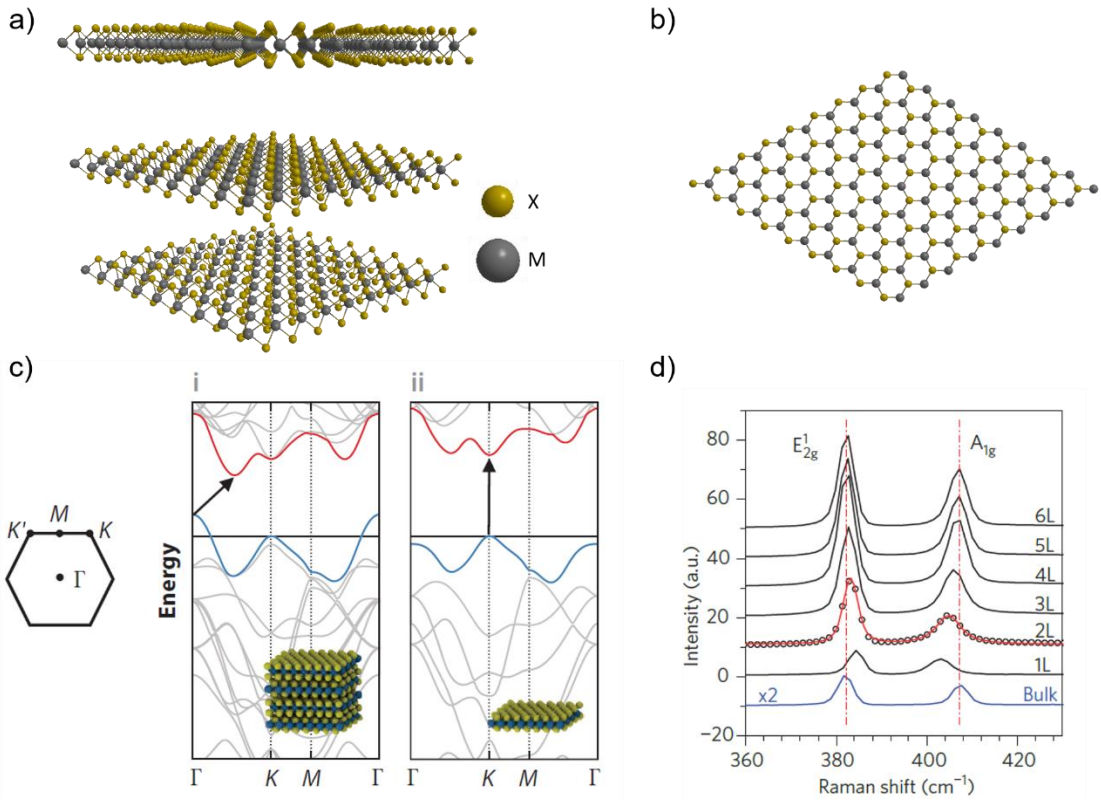

Figure 2.5: Structural and electronic properties of 2D TMDs. a) 3D representation of typical MX_2 layered structure with chalcogen atoms in yellow and metal atoms in grey; b) Hexagonal structure of a single layer; c) (LHS) Hexagonal Brillouin Zone with high symmetry points labelled. (RHS) theoretical band structure of (i) bulk and (ii) monolayer TMD crystals. Taken from Berkelbach *et al.*[2];d) Raman spectra of bulk and 1-6 layer MoS_2. Taken from Wang *et al.*[5]

Figure 2.5.*a* shows the layered TMD structure in the form X-M-X, where the chalcogen atoms lie in two hexagonal planes separated by a plane of metal atoms. Adjacent layers of thickness ~ 0.6-0.7 nm are held together by weak out-of-plane

interlayer van der Waals interactions to form the bulk crystal. [3,5,6] Figure 2.5.*b*, shows the hexagonal lattice structure from above. The hexagonal lattice structure translates, *via* Fourier transform, into a hexagonal Brillouin zone (BZ) in reciprocal space, shown in Figure 2.5.*c*, left-hand side (LHS). The high symmetry points are labelled *Γ, K* and *K'* at the corners of the hexagonal BZ. Theoretical studies[6,42] show that the indirect to direct semiconductor transition occurs at *K* and *K'* points (*i.e. K* points) due to quantum confinement in the out-of-plane (*z*) direction and the resulting changes to the atomic orbitals in the valence and conduction bands. The right-hand side (RHS) of Figure 2.5.*c* shows the theoretical band structures of (i) bulk and (ii) monolayer TMD crystals transitioning from an indirect to direct semiconductor. The valence states at the *K* points are dominated by transition metal *d* orbitals, which have weak interlayer coupling, and are therefore unaffected by the number of layers present. In contrast, the valence states about the *Γ* point possess a large proportion of antibonding chalcogen p_z orbitals hybridized with transition metal *d* orbitals and exhibit strong interlayer coupling. In a bulk crystal, multiple layers in close proximity cause strong interlayer interaction between chalcogen p_z orbitals, raising the energy of the valence band at the *Γ* point, while the direct transitions at the *K* points remain relatively unchanged. In similar fashion, the conduction band is lowered within in the path between the *Γ* and *K* points, resulting in an indirect band gap away from the *K* points. As the layers are separated, the interlayer coupling between chalcogen orbitals is reduced, lowering the energy of the valence band at the *Γ* point, leaving the direct gap at the *K* points unaffected as the monolayer limit is approached.[2,5,6,42] In essence, a reduction in the number of layers causes a movement in the conduction band minimum (CBM) from the point between the *K* and *Γ* point to the *K* points in the Brillouin zone, shifting the lowest energy transition from an indirect to a direct one in the monolayer limit.[4]

Raman spectroscopy has been shown to be a powerful non-destructive tool for distinguishing TMD monolayers from multilayers.[43] Inelastic scattering of incoming photons (from *e.g.* laser excitation) by the TMD lattice gives rise to distinct Raman modes, E^1_{2g} and A_{1g}, representing in-plane and out-of-plane vibrational modes respectively. As shown in Figure 2.5.*d*, the spectral difference between these modes reduces monotonically with fewer layers. The E^1_{2g} mode blue-shifts, due to reduced di-electric screening, whereas the A_{1g} mode red-shifts due to the reduced stiffening effect by van-der Waals forces on atomic vibrations. The general underlying principles of Raman spectroscopy are provided in Chapter 3, section 3.2.2.

2.3.2 Excitons in 2D TMDs

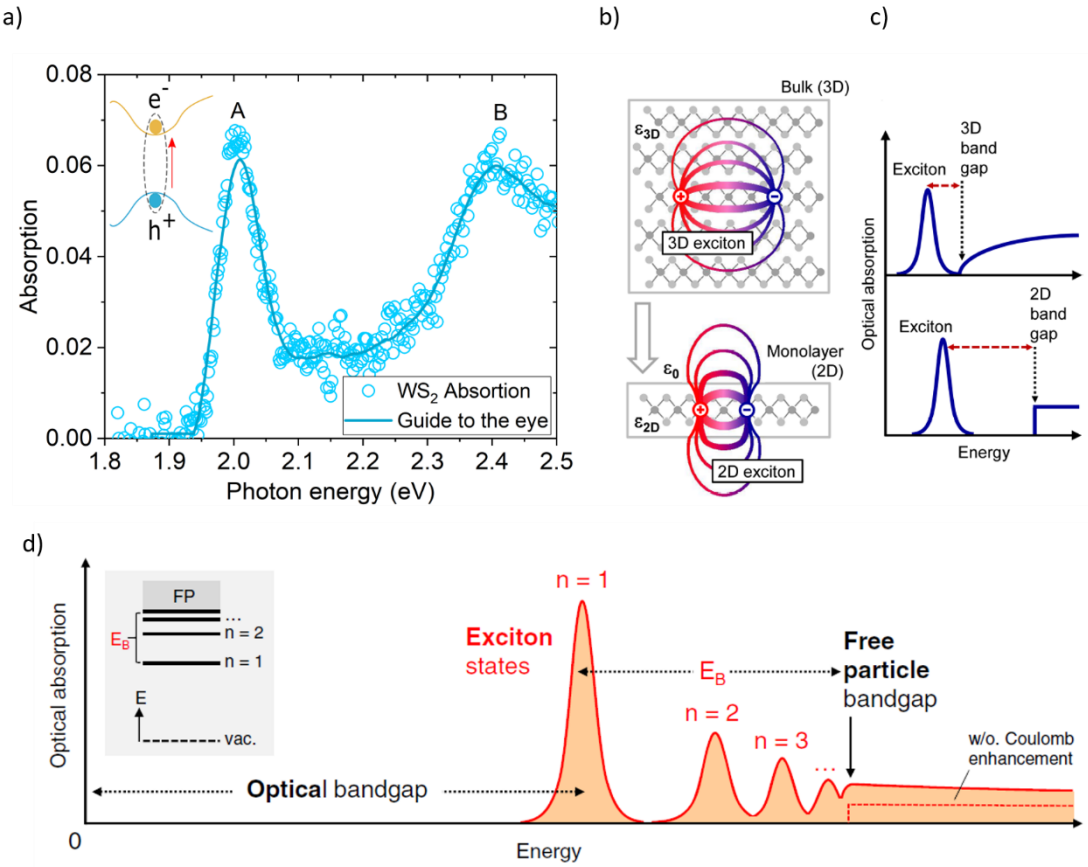

Figure 2.6: Excitons in 2D TMDs. a) Measured room temperature absorption spectrum of monolayer WS_2 showing `A' and `B' resonance peaks. b) Illustration of electric field lines between electron and hole in a 3D bulk material versus a 2D monolayer; c) Minimised screening and confinement in the 2D-plane increases exciton binding energy and bandgap energy. Reproduced from Chernikov *et al.*[44] d) Optical absorption spectrum of a generalised 2D material with excited states (n = 1,2 etc.) given by sharp resonance features. The lowest transition (n = 1) corresponds to the optical bandgap energy E_g, which combined with the exciton binding energy E_B, yields the free particle bandgap energy, E. Inset figure shows the excited state energy levels. Reproduced from Wang *et al.* [45]

Optical absorption in monolayer TMDs is dominated by direct transitions between valence and conduction band states, forming excitons that are strongly localised about the *K* points in the Brillouin zone.[3,45] The sharp `A' and `B' resonance features (*i.e.* excitonic peaks) in the exemplary WS_2 monolayer absorption spectrum, shown in Figure 2.6.*a*, characterises the highly excitonic nature of these materials.[3] The inset of Figure 2.6.*a* depicts the direct exciton transition upon optical absorption. We delve into the origins of this behaviour with the aid of Dr. Palacios-Berraqero's introductory thesis chapter on *2-d Based Quantum Technologies*,[46] which provides an excellent overview on

excitons in 2D TMDs. Further insights are gleaned from a study by Chernikov *et al.*[44] and a review by Wang *et al.*[45] on *Excitons in atomically thin transition metal dichalcogenides.* Other recent articles are also referenced.

In the monolayer limit, excitons are strongly confined to the monolayer's 2D plane, minimizing the effective separation between electron and hole, specifically in the out-of-plane (*z*) direction. Excitons also experience massively reduced dielectric screening of the electric field between electron-hole pairs compared to excitons within a 3D bulk crystal, where the electron-hole pair's electric field is screened by the combined dielectric properties of multiple layers. In the monolayer limit however, the electron-hole electric field only extends into air and the underlying substrate, which have low dielectric constants in comparison to the TMD bulk crystal. The combination of spatial and dielectric confinement greatly enhances coulomb interaction between electron and hole, resulting in large exciton binding energies of the order of 0.5 eV, and an increase in quasiparticle band gap energy as illustrated in Figure 2.6.*b-c.* These tightly bound `Frenkel-like' excitons dominate the optical properties of atomically thin TMDs, presenting strong excitonic features that are detectable even in room temperature spectral measurements. Figure 2.6.*d* shows the optical absorption spectrum of a generalised 2D material with strong resonance features typical of monolayer TMDs. The inset figure shows an energy band diagram with excited states labelled n = 1,2, *etc*. The resonance features represent the excitonic transitions in the material. The strong excitonic effects in monolayer TMDs causes significant intraband transfer of oscillator strength from higher states (n >1) to the fundamental exciton state (n =1). This results in strong absorption at the lowest exciton state, as exemplified by the sharp `A' excitonic peak of $WS_2$ in Figure 2.6.*a*. The lowest `A' exciton transition (Figure 2.6.*a*) or intergap transition (Figure 2.6.*d*), defines the monolayer TMD optical bandgap energy, which is (*e.g.*) E_g ~ 2.0 eV for WS_2. For materials that generate excitons with the large binding energies, it is important to differentiate optical bandgap energy E_g from the free particle *or* electronic bandgap energy E. The free particle band gap, E, is defined as the energy required to generate a free unbound electron and hole in the continuum of states. E_g is related to E *via* the exciton binding energy E_B such that $E_g = E - E_B$.[45] E_g for monolayer TMDs can be easily obtained by measuring optical absorption spectra, or radiative recombination energy *via* photoluminescence spectroscopy. Monolayer TMD electronic gaps have also been determined theoretically[47–50] and experimentally *via* scanning tunnelling

microscopy (STM).[17,18,51] We note that the terms `*optical bandgap energy'* is used interchangeably with `*bandgap'* or `*optical gap'* in this thesis.

While neutral excitons (*i.e.*, single electron-hole pairs) dominate the optical properties of monolayer TMDs, the strong confinement in these materials enables the formation of higher order multi-exciton and charged exciton complexes, making them a useful medium for studying fundamental many-body exciton-exciton or exciton charge interactions. These complexes include biexcitons,[52–54] consisting of two electrons and two holes, and trions,[55–57] consisting of (*e.g.)* two electrons and one hole or *vice-versa*. Trions are particularly prevalent in monolayer TMDs, showing signatures in room temperature PL spectra.[58,59] Trions form as a result of binding between excess charges from uncontrolled *n*-type (electron) or *p*-type (hole) doping, and (neutral) excitons,[55] producing negatively or positively charged excited states. Doping may be induced by the monolayer's substrate material (e.g. Si-SiO_2) or adsorbant molecules such as oxygen (O_2) and ambient water (H_2O).[18,60] Formation of trions and other complexes can however be manipulated by tuning charge density *via* electrostatic gating[61–63] or controlled chemical doping.[64–66] A notable study by Barbone *et al*.[62] recently reported on neutral and charged biexciton formation in a gated charge tuneable tungsten diselenide (WSe_2) based device. Figure 2.7. below illustrates the exciton complexes observed in monolayer TMDs.

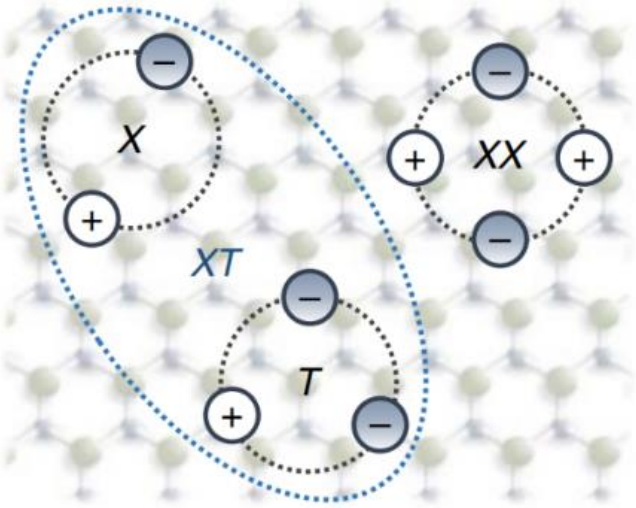

Figure 2.7: Excitonic species in 2D TMDs. Illustration of exciton (X), trion (T), neutral biexciton (XX) and charged biexciton (XT). Taken from Hao *et al*.[54]

2.3.3 Photoluminescence in 2D TMDs

Photoluminescence (PL) is defined as re-emission of absorbed photons by a material. In a semiconductor, recombination of electrically or optically generated electron-hole pairs produces photons. This occurs more efficiently in direct bandgap semiconductors compared with indirect bandgap semiconductors. The efficiency of radiative electron-hole recombination is given by the ratio of absorbed photons to emitted photons *i.e.* PL quantum efficiency (PLQE) *or* PL quantum yield (PLQY).[20] In semiconducting TMDs, the transition from indirect bandgap bulk crystal to direct bandgap monolayer is accompanied with orders of magnitude increase in PLQE.[3,6,45]

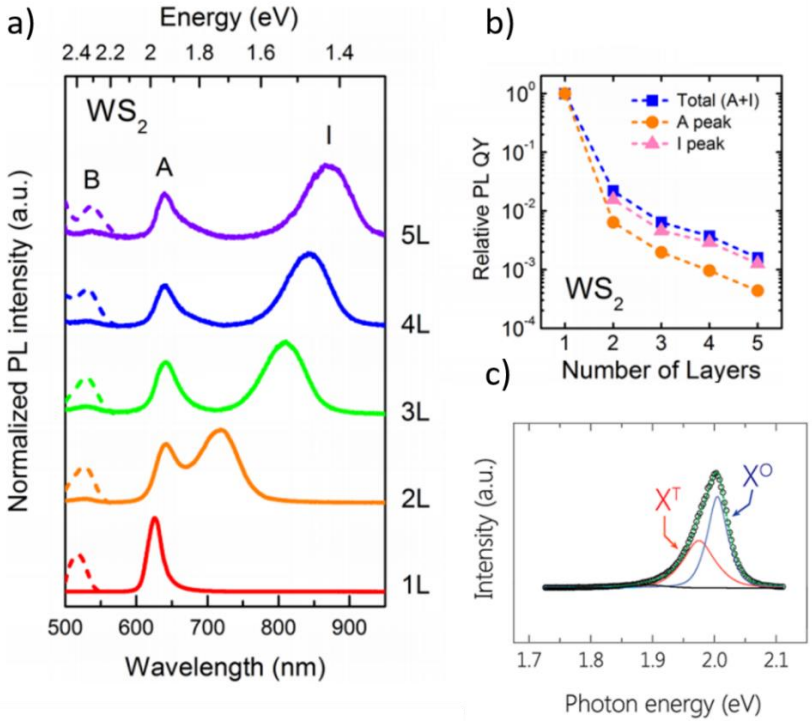

Figure 2.8: Emergence of PL in WS2. a) Normalized PL spectra of 1–5-layer WS_2 showing evolution of peaks from direct `A', `B' exciton transitions and indirect `I' exciton transitions; b) PLQY of `A' and `I' transitions as a function of number of layers. Figures *a-b* adapted from Zhao *et al.*[67]; c) Typical PL spectrum of WS_2 showing neutral exciton (X^O) and trion (X^T) contributions represented by single Gaussian fits. Figure *c* adapted from Chow *et al.*[68]

Figure 2.8.*a* shows the evolution of WS_2 PL with reducing number of layers. We observe the increasing prominence of the PL peak associated with the `A' excitonic transition, and a simultaneous reduction of the indirect `I' peak as the monolayer limit is approached. Figure 2.8.*b* shows that WS_2 undergoes an increase in `A' peak PLQE in excess of 100-fold when transitioning from bi-layer to monolayer, in accordance with the

indirect-direct bandgap shift. The large oscillator strengths of the lowest `A' excitonic transitions leads to high neutral exciton radiative recombination rates and hence short radiative lifetimes[3] ranging within few picoseconds as demonstrated *via* low temperature PL lifetime measurements[69,70] and theoretical calculations.[71] Room temperature PL in monolayer TMDs is dominated by direct radiative recombination of neutral `A' excitons with significant contributions from trions and other bound states (*e.g.* biexcitons) at lower energies.[67] Figure 2.8.*c* shows an exemplary monolayer WS_2 PL spectrum with neutral exciton (X^O) and trion (X^T) components represented by single Gaussian peak fits. Additional low energy signatures in monolayer TMD PL spectra may also arise as a result of radiative exciton recombination from sub-gap states. Sub-gap states, also referred to as *inter-gap states* (IGS) or *trap states* are associated with atomic vacancies within the monolayer crystal lattice.[17,72] Atomic vacancies are subsequently discussed further due to their profound influence on the optical and electronic performance of monolayer TMDs.[15]

2.3.4 Defects in 2D TMDs

In spite of the dramatic increase in PLQE observed when transitioning from multi-layer to monolayer TMDs, newly prepared or *pristine* monolayers have low PLQEs, often below ~1%.[73,74] Low PLQEs in pristine monolayers are often accompanied with low electronic mobilities, thus limiting their practical applications in optoelectronic devices. The poor optical and electronic performance of pristine monolayer TMDs are attributed to externally induced disorder and intrinsic structural defects.[13,15,18]

External sources of disorder, shown in Figure 2.9.*a*, originate from the underlying substrate and ambient adsorbates. Substrate induced disorder includes surface strain, and unintentional doping. Ambient adsorbates such as water molecules and charged impurities also contribute to unintentional doping. These external perturbations cause charge scattering and trapping, and local band structure modifications, which hamper electronic mobilities and quench monolayer PL respectively.[13] Charged impurities and substrate doping introduce free charge carriers, converting bright neutral excitons to trions, which have lower radiative efficiency, resulting in an overall reduction in PLQE.[19,75]

Intrinsic structural defects, shown in Figure 2.9.*b*, include grain boundaries, edge terminations and point defects *i.e.,* atomic vacancies, anti-sites and substitutions.[13,76] Grain boundaries induce local strain, altering local electronic structure in chemical vapour

deposition (CVD) grown large area polycrystalline monolayers.[43] In the absence of grain boundaries, as per the single crystal monolayers studied in this thesis, point defects persist. Chalcogen vacancies are predicted to be the prevalent form of point defects in monolayer TMDs.[13,15,76,77] The low formation energy of chalcogen vacancies is often cited as the reason for their abundance.[13,15,72,76,77] Transmission electron microscopy (TEM) and scanning tunnelling microscopy (STM) studies have been used to experimentally identify chalcogen vacancies in monolayer TMDs.[14,78–81] Sulphur vacancy densities of the order of ~10^{13} cm^{-2} have been reported in mechanically exfoliated MoS_2 and CVD prepared WS_2 respectively.[79,80] A number of these studies incorporate theoretical computations to confirm sub-gap states associated with chalcogen vacancies.[14,78–80] An important study by Zhou *et al.*[14] characterises intrinsic defects in monolayer MoS_2[14] *via* scanning tunnelling electron microscopy (STEM). Figure 2.9.*c* shows the resulting atomic resolution dark field (ADF) images of common point defects identified,[14] namely: sulphur vacancies (V_S); vacancy complexes of single Mo and three S (V_{MoS3}); anti-sites of Mo replacing S_2 (Mo_{S2}) and; S_2 replacing Mo ($S2_{Mo}$). STM studies by Schuler *et al.*[81,82] probe the local electronic structure in the vicinity of chalcogen vacancies (V_S) in monolayer WS_2 *via* scanning tunnelling spectroscopy (STS), revealing defect associated inter-gap states, as shown in Figure 2.9.*d* (red peaks at ~0.35-0.75 V). PL studies[68,80] also detect low energy emission from chalcogen vacancy induced sub-optical gap states in WS_2. Figure 2.9.*e* shows low temperature PL emission from defect states located in CVD WS_2 monolayer edges.[80] Figure 2.9.*f* shows room temperature emission from chalcogen vacancy induced defect states (X^D) in mechanically exfoliated WS_2, where defects were created *via* argon plasma treatment over the periods t_{plasma}.[68] Chalcogen vacancies in pristine monolayers are predicted to trap free charge carriers, reducing electronic mobilities, and act as PL quenching sites where neutral excitons are more likely to non-radiatively recombine.[16,19,83] Recently however, a study combining STS, atomic force microscopy (AFM) and theoretical calculations argues in favour of oxygen substitutions at chalcogen sites as dominant point defects in monolayer TMDs.[17] Interestingly, unlike chalcogen vacancies, oxygen substitutions are shown to have no associated sub-gap state. The nature of point defects and their charge carrier trapping and PL quenching mechanisms are yet to be fully understood.[16,19] To this end, a first-principles study by Li *et al.*[16] sought to identify possible mechanisms for defect-assisted charge carrier trapping and non-radiative exciton recombination in WSe_2 monolayers. In spite of the challenges posed by extrinsic disorder and intrinsic defects, significant

advances have been made in improving the optoelectronic properties of monolayer TMDs, which we go on to review briefly.

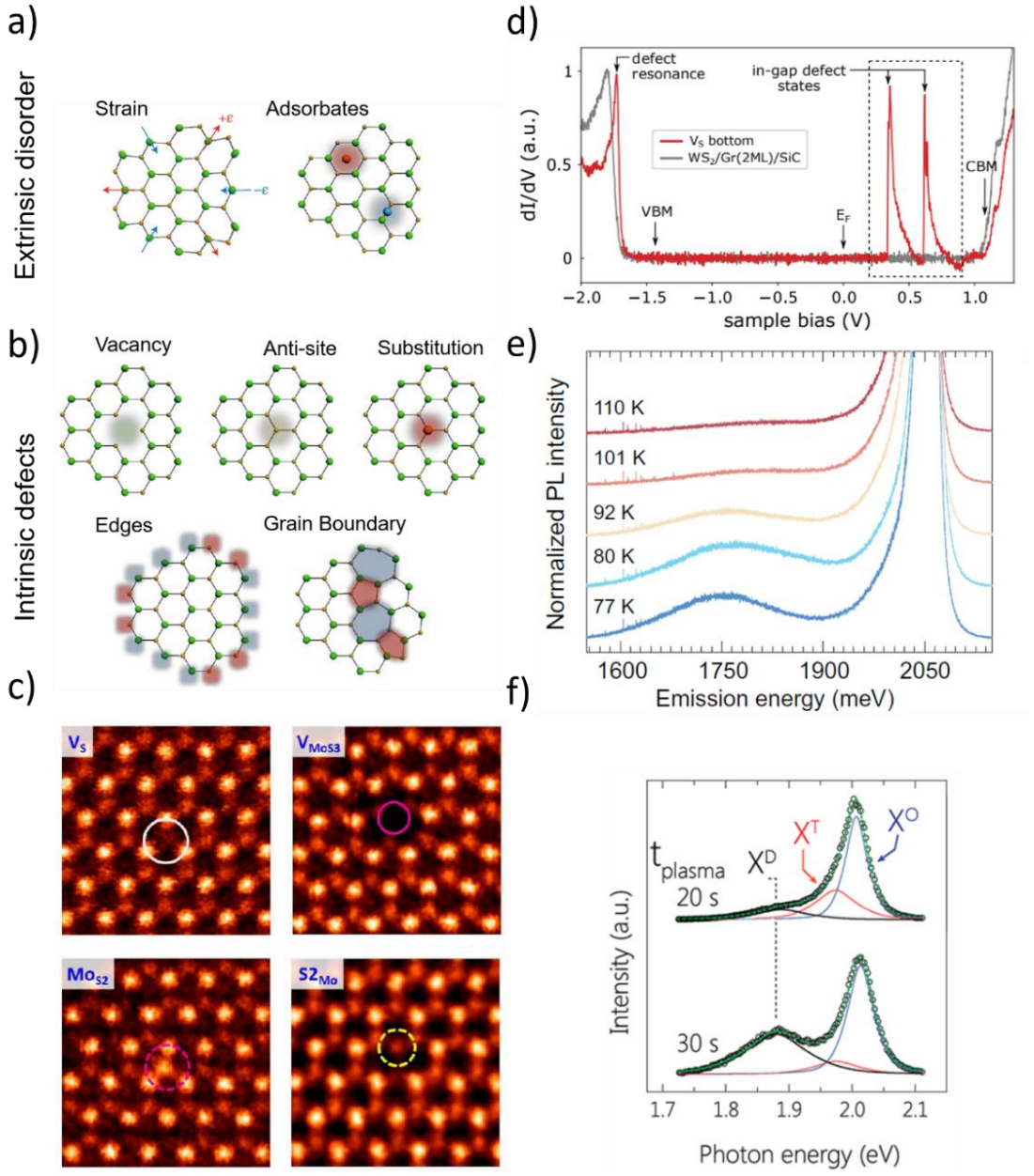

Figure 2.9: Defects TMD monolayers. a) Extrinsic disorder and; b) Intrinsic defects in 2D TMDs. Adapted from Rhodes *et al.*[13]; c) ADF images of common point defects in monolayer MoS_2, clockwise: V_S, V_{MoS3}, Mo_{S2} and $S2_{Mo}$. Adapted from Zhou *et al.*[14] d) STS spectra on sulphur vacancy (red) and pristine WS_2 (grey). In-gap vacancy states (~0.35-0.75 V) indicated. Reproduced from Schuler *et al.*[81] e) Defect emission in WS_2 at low temperatures. Reproduced from Carozo *et al.*[80] f) Normalized room temperature PL of Ar plasma monolayer WS_2 treated over period t_{plasma} with defect-related exciton transition (X^D). Image adapted from Chow *et al.*[68]

2.3.5 Improving optoelectronic performance of 2D TMDs

Eliminating the detrimental effects of intrinsic defects and extrinsic disorder on the optical (and electronic) performance of TMD monolayers holds the key to fully harnessing their luminescent properties for practical applications in optoelectronic devices.[4] As previously highlighted, non-radiative exciton recombination in pristine monolayers has been attributed to substrate induced strain, unintentional doping, chalcogen (*i.e.* S and Se) vacancies,[20,84] atomic substitutions[17,18] and trion formation.[20,75] Methods to improve material performance broadly take two routes; encapsulation with hexagonal boron nitride (hBN) and chemical treatments.[28]

Encapsulation exploits the atomically flat dielectric properties of hBN, using it as an encapsulation medium[85,86] or sub-layer[87] that isolates TMD monolayers from sources of extrinsic disorder *i.e.*, substrate induced strain, and unintentional doping. This preserves monolayer intrinsic properties, improving optical quality as given by reduced spectral linewidths,[86] as shown in Figure 2.10.*a*, and increased spatial homogeneity in PL intensity.[85] HBN encapsulated WS_2 shows slightly improved PL, although at high optical excitation intensities, indicating little effect on PLQE.[88] Importantly however, hBN encapsulation has been shown to markedly improve electronic mobilities in MoS_2.[13]

A number of chemical treatments have been proposed to improve PLQEs in newly prepared monolayer TMDs. The vast majority of these treatments enhance PLQEs in sulphur based TMDs, MoS_2 and WS_2. Such methods include the use of *p*-doping agents such as 2,3,5,6-tetrafluoro 7,7,8,8-tetracyanoquinodimethane (F4TCNQ),[66,23] hydrogen peroxide,[24] or deposition of a defect passivating titanyl phthalocyanine (TiOPc) monolayer charge transfer interface.[89] These electron withdrawing species supress trion formation between electrons and neutral excitons, improving neutral exciton recombination. The most prominent treatment to date utilizes `super acid' bis(trifluoromethane)sulfonimide (TFSI)[20,21,25] to drastically increase PLQEs in MoS_2 and WS_2 monolayers. Figure 2.10.*b* shows an exemplary increase in PL intensity observed in MoS_2 treated with TFSI under low power optical excitation.[20] The authors of the initial study[20] cited chalcogen vacancy passivation by TFSI as the reason for the observed improvements. Recently however, the same authors concluded that TFSI rather behaves as a strong *p*-doping agent.[75] Separate studies also show that TFSI withdraws electrons occupying sub-gap sulphur vacancy (trap) states, leaving them unoccupied as opposed to passivating them.[90,91] Under room temperature excitation, trapped excitons

acquire sufficient thermal energy to `de-trap' to the band-edge, where they radiatively recombine as illustrated in Figure 2.10.*c*.[91] The photodynamic process of PL enhancement due to TFSI treatment is detailed further in Chapter 4 (Section 4.3-4.4). An in-depth discussion on the surface chemistry of TFSI is given in section 4.5. Consistent with its strong electron withdrawing nature, TFSI has been shown to reduce electronic mobilities in *n*-type MoS_2 and WS_2.[90] TFSI is also known to quench PLQEs in selenide TMDs, $MoSe_2$ and WSe_2.[25] Unlike for sulphide TMDs, treatments for as-prepared selenide TMDs are lacking thus far, with a single study that reports on structural repair of defect-rich CVD grown $MoSe_2$ *via* exposure to hydrobromic acid (HBr) vapour, yielding enhanced PL as shown in Figure 2.10.*d*.[92] Chapter 5, section 5.1. provides further details on this study.

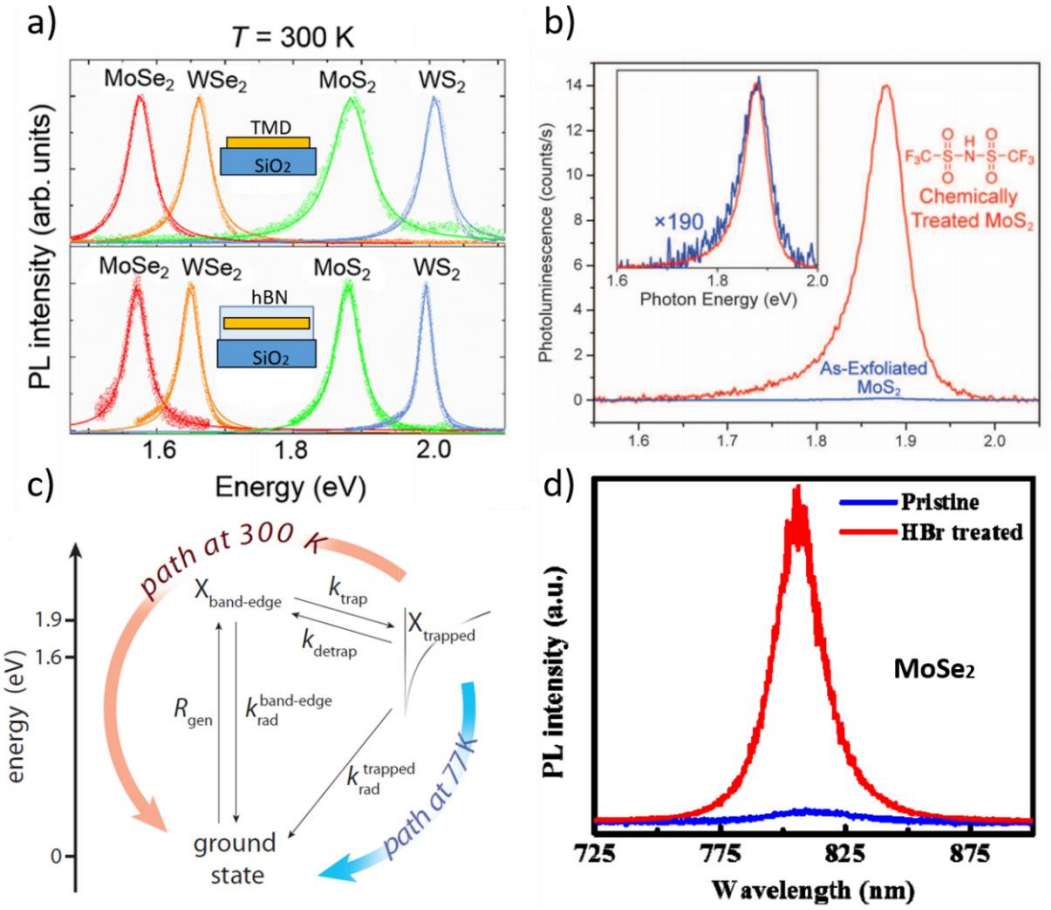

Figure 2.10: Enhancing PL in 2D TMDs. a) 2D TMD PL linewidth narrowing *via* hBN encapsulation. Adapted from Cadiz *et al.*[86]; b) Room temperature PL spectra of as-exfoliated and TFSI treated MoS_2. Taken from Amani *et al.*[20] c) Proposed exciton dynamics in TFSI treated MoS_2. Taken from Goodman *et al.*[91]; d) Room temperature PL spectra of as-grown and HBr treated $MoSe_2$. Taken from Han *et al.*[92]

2.4 Electronic Device Applications of 2D TMDs: 2D FETs

A Field Effect Transistor (FET) is a three terminal system consisting of a semiconducting channel between source and drain electrodes. Current between source and drain (I_{DS}) is controlled electrostatically *via* a gate electrode, which is isolated from the channel semiconductor by an insulating dielectric material.[93] I_{DS} is adjusted by modulation of electric resistance of the semiconductor channel between drain and source electrodes by an applied gate voltage (V_G) *via* the dielectric interface. The applied V_G generates an electric field, attracting minority charge carriers in the semiconductor, forming a conductive channel between source and drain. This describes the *on* state of the transistor. The *off* state corresponds to $V_G = 0$.[93] FETs are integral to modern electronic devices where efficient, rapid switching between *on* (1) and *off* (0) states is required for digital information processing and data storage.[7]

There are ongoing efforts to integrate 2D TMDs as channel materials in future high performance FETs.[7] Figure 2.11.*a* shows a typical back gated FET architecture with a 2D TMD channel (2D FET). In this arrangement, the gate electrode addresses the source and drain *via* an insulating substrate *e.g.* Si-SiO_2.[93]

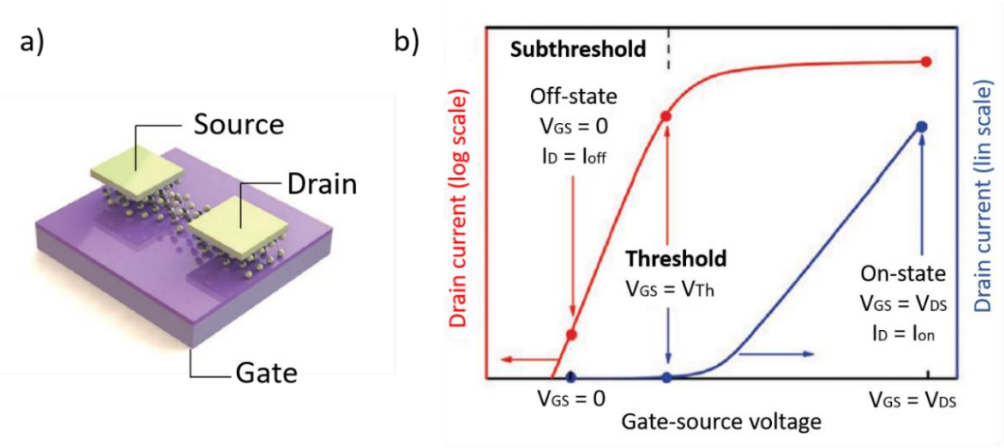

Figure 2.11: 2D FET device architecture and transfer characteristics. a) Structure for back-gated 2D FET with Si gate; b) Typical transfer characteristic for *n*-type 2D TMD channel FET. Adapted from Jing *et al.*[93]

FET performance is assessed using the transfer characteristic and output characteristic. For the transfer characteristic, the current flowing between drain and source (I_{DS}) is monitored against applied gate voltage (V_G) for a specific voltage between drain and source (V_{DS}). Figure 2.11.*b* shows a typical transfer characteristic for an *n*-type

2D TMD channel FET. For the output characteristic, I_{DS} is monitored against V_{DS} for different V_G.[93]

In chapters 4 and 5 of this thesis, 2D FETs were fabricated and measured to evaluate the impact of chemical treatments on monolayer electronic transport properties and overall device performance. In this work, we focus on the operational parameters obtainable from 2D FET transfer characteristics only. This includes *off* and *on* state currents, I_{off} and I_{on}; on-off current ratio, I_{on}/I_{off}; threshold voltage, V_{th}; subthreshold swing, *SS* and; field effect mobility, μ. We refer to Figure 2.11.*b* for clarity. I_{off} should be minimal to abate parasitic standby power losses and I_{on} should be high enough to power the transistor output circuitry. I_{on}/I_{off} quantifies the magnitude of the difference between on and off states, which should exceed 10^5 for digital logic applications. V_{th} is equal to V_G at the transition from off to on state. Subthreshold swing, *SS* is the inverse of the subthreshold slope, *S*, which is the gradient of the log-linear regime within the subthreshold region. *SS* simply quantifies the V_G required to increase drain current (I_D) by a decade. As such, *S* and *SS* indicate FET switching efficacy and switching speed. Field effect mobility, μ estimates the average charge carrier velocity across the channel at a given electric field, and is estimated *via* the transconductance equation below:[93]

$$\mu = \left[\frac{dI_{DS}}{dV_G}\right] \times \left[\frac{L}{WC_G V_{DS}}\right] \tag{2.1}$$

where *L* and *W* are the channel length and width, respectively. C_G is the capacitance per unit area between gate electrode and semiconducting channel.

2.5 Optoelectronic Device Applications of 2D TMDs

Here, we summarise some applications of 2D TMDs in optoelectronic devices for light emission, photovoltaics (PV) and, photodetection.

Whereas photoluminescence is defined as photon re-emission due to optical excitation, electroluminescence (EL) describes photon emission induced by electrical stimulation. Electroluminescence is central to light emitting applications, namely, light emitting diodes (LEDs) and laser diodes.[94] A key figure of merit for LEDs is the external quantum efficiency (EQE), which is defined as the ratio of emitted photons to injected electrons. Monolayer TMDs are considered as attractive for light emission applications due to their direct band gap. Consequently, a number of 2D TMD based LED device

concepts have been reported. EL from monolayer MoS_2 was initially demonstrated by direct injection of hot electrons *via* metal/TMD Schottky junction.[95] EL derived from electrostatically driven exciton formation and radiative recombination was also achieved *via* simultaneous bi-polar carrier injection into monolayer WSe_2 in a lateral *p-n* junction device configuration (Figure 2.12.*a*).[9,96,97] Vertical van der Waals heterostructure based excitonic LEDs, consisting of graphene electrodes and hBN tunnel barriers encapsulating monolayer MoS_2 or WS_2 have also been demonstrated.[8] A slightly modified vertical heterostructure device arrangement, as shown in Figure 2.12.*c*, has enabled electrically driven quantum light emission from monolayer WSe_2.[12] Due to non-radiative recombination however, room temperature EQEs of TMD monolayer based LEDs typically lie within ~0.1-1%,[8,9,12,94] which is essentially the same order of magnitude as their PLQEs, thereby emphasising the need for improvements in optical quality of starting material.

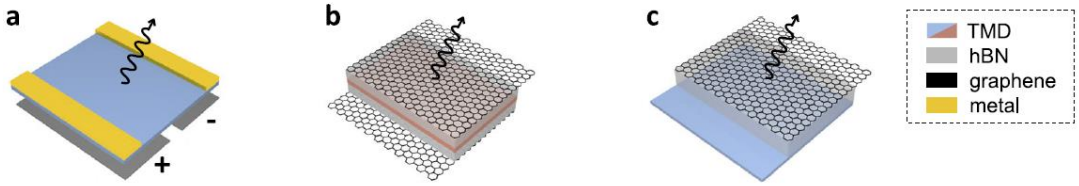

Figure 2.12: 2D TMD based LED device architectures. a) Lateral *p-n* junction LED with metal contacts; b) Graphene/hBN/TMD/hBN/graphene vertical van der Waals heterostructure LED; c) Graphene/hBN/TMD quantum LED. Adapted from Mueller *et al*.[94]

Photovoltaic (PV) cells convert solar light into electricity *via* the photovoltaic effect. The photovoltaic effect is based on the separation of photogenerated electron-hole pairs, or exciton dissociation by the electric field of electrostatically defined lateral or vertical *p-n* junctions.[94] Ultimately, the key parameter for PV converters is the power conversion efficiency η, and is defined as the ratio of output electrical power P_{el} to incident optical power, P_{Opt}, that is $\eta = P_{el}/P_{Opt}$. TMD monolayers are regarded as promising candidates for single-junction and heterojunction tandem cells for thin-film PV energy conversion devices due to their strong, broad band absorbance, which overlap well with the solar spectrum (Figure 2.13.*a*),[11] and potentially high PLQEs.[20,94] Theoretical calculations predict power conversion efficiencies of over 25% using these materials,[98] thus exceeding the performance of conventional Silicon based PV technologies. Recently however, studies on lateral *p-n* junction diodes based on monolayer WSe_2 showed photovoltaic response with power conversion efficiencies ranging within 0.1 – 1% under

white light illumination.[9,96] Vertical *p-n* junction PV devices based on van der Waals TMD heterostructures have also been demonsrated,[99–101] notably using an optimised MoS_2/WSe_2 heterojunction (Figure 2.13.*b*), yielding 3.4% power conversion efficiency under monochromatic light.[102] Evidently, power conversion efficiencies of TMD monolayer and heterostructure based PV devices have so far remained below the predicted value. This has been attributed to: energy losses associated with charge separation of tightly bound excitons; poor carrier transport due to charge trapping and; inefficient carrier extraction at metal contacts.[94,103] While this presents a clear case for further improvements in device engineering and material quality, the energy penalty inflicted by exciton dissociation is however unavoidable.[94] Alternatively, 2D TMD excitons may be harnessed differently in light management applications for traditional silicon PV technology, which we propose in section 2.7.

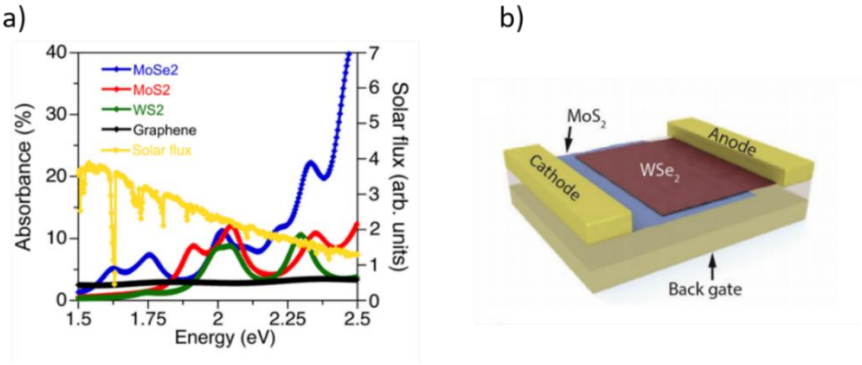

Figure 2.13: 2D TMDs for Photovoltaics. a) Absorbance spectra of 2D TMDs and graphene overlapped with AM1.5G solar flux. Taken from Bernardi *et al.*[11]; b) Schematic layout of vertical heterojunction PV device with lateral contacts. Taken from Popischil *et al.*[103]

Photodetectors convert light into electrical signals and are central to the operation of optical communications, imaging, and sensing devices. The sensitivity of a photodetector is given by the photoresponsivity, $R = I_{ph}/P_{opt}$, *i.e.* the ratio of output electrical current I_{ph}, to input optical power P_{opt}.[103] Monolayer TMD based photodetectors can operate on the basis of the photovoltaic effect, however, with low photoresponsivities (~10^{-1} A/W). [9,94] The application of an external bias, as per a 2D TMD phototransistor, can be used to detect changes in conductance due to photogenerated carriers with substantially improved photoresponsivities (>10^3 A/W).[104] Photoresponsivities can be enhanced further by incorporating other TMD materials[105] or quantum dots[106–115] as charge transfer (CT) interfaces in hybrid photodetection devices. A review by Popischil *et al.*[103] provides further reading on the operating principles of TMD-based photodetectors.

2.6 2D-QD Energy Transfer Heterostructures

2D TMDs can be combined with other nanomaterials such as quantum dots (QDs) to tune their optoelectronic properties. Combining these materials in heterostructures gives rise to useful interfacial phenomena, namely charge transfer (CT) and exciton transfer, *i.e.* energy transfer (ET) under optical or electrical stimulation.[26] CT simply refers to charge tunnelling from one species to another. As mentioned previously, CT between 2D TMDs and QDs has applications in photodetection.[106–115]

Nonradiative ET between QDs and 2D TMDs in heterostructures has also been studied for applications in light intensity modulation, colour modulation, light harvesting, and light detection. To date, these studies have been limited to exciton transfer from 0D QD donor to 2D TMD acceptor.[30–36] ET may occur *via* a donor-acceptor dipole-dipole coupling mechanism as per Förster resonance energy transfer (FRET), or direct simultaneous electron-hole tunnelling *i.e.* Dexter energy transfer (DET).[116] Before delving into the mechanisms of ET, we first outline a selection of notable studies on QD→ 2D ET heterostructures.

Prins *et al.*[30] first reported on nonradiative ET from cadmium selenide/ cadmium zinc sulphide (CdSe/CdZnS) QDs to few layer and monolayer MoS_2, revealing increased transfer efficiency as a function of reduced number of layers. This outcome was attributed to reduced dielectric screening approaching the monolayer limit. Raja *et al.*[31] later investigated the role of absorption and screening in ET from QDs to MoS_2 using experiment and theoretical predictions. This work provided further physical explanations for the observations previously made by Prins *et al.* Prasai *et al.*[32] demonstrated electronic modulation of nonradiative ET from core-shell Cadmium Sulphide Selenide ($CdS_{1-x}Se_x$) QDs to MoS_2 *via* electrostatically gating the TMD, thereby selectively tuning the QD PL intensity with an externally applied gate voltage. Using transient absorption (TA) spectroscopy, Li *et al.*[33] probed ET from caesium lead bromide ($CsPbBr_3$) QDs to monolayer WS_2, revealing an efficient, `ultrafast' ET process occurring within ~100 ps of excitation. Supporting PL spectra showed emission quenching in donor $CsPbBr_3$ PL and a concomitant enhancement in acceptor WS_2 PL, consistent with non-radiative ET. Liu *et al.*[36] probed nonradiative ET between cadmium selenide/ zinc sulphide QDs and monolayer TMDs (MoS_2, WS_2 and WSe_2) using time resolved PL spectroscopy.

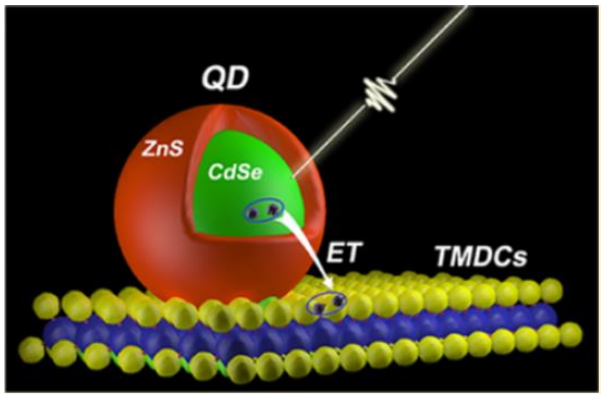

Figure 2.14: Nonradiative ET from QD to TMD upon optical excitation. Taken from Liu *et al.* [36]

The majority of the previously cited studies explicitly attribute ET to FRET-like dipole-dipole coupling processes,[30–32,36] which are inherently long-range *i.e.* > 1 nm between donor and acceptor. Close proximity between species (≤ 1 nm) however presents the required conditions for DET.[116] We outline the distinctive features of FRET and DET in the next subsection.

2.6.1 Förster Resonance Energy Transfer (FRET)

FRET is defined as nonradiative transfer of excitation energy from a donor molecule to an acceptor molecule *via* coulombic dipole-dipole interaction, resulting in a quenched donor excited state lifetime.[117] FRET involves the transfer of a `virtual' photon, and can be envisioned as photon emission by the donor and subsequent absorption by the acceptor.[118] Assuming the point dipole approximation, where the spatial extent of donor and acceptor are neglected, the FRET rate, k_{FRET}, follows the relationship:

$$k_{FRET} \propto \frac{f_D f_A}{d^6 \nu^2} J \tag{2.2}$$

where f_D and f_A are the donor and acceptor species oscillator strengths respectively; d is their physical separation; ν is the photon frequency and J is the overlap integral between area normalized donor emission and acceptor absorption, which indicates the presence of acceptor states that are energetically resonant to donor excited states. In the case of FRET, J is related to the acceptor extinction coefficient, and is therefore a function of acceptor oscillator strength.[116] Strictly speaking, the length-scale for FRET rate is inherently dependent on acceptor molecule geometry. For further reading, Martinez *et al.*[119] provide a generalised theory for Förster-like nonradiative ET between nanostructures of differing

dimensions. Importantly however, the critical distance between donor and acceptor is defined by the Förster radius, R_0, that is the separation distance at which there is a 50% probability of ET. For the point dipole approximation, R_0 is expressed as:

$$R_0^6 = \frac{9ln10}{128\pi^5 N_A}\frac{\kappa^2 PLQE_D}{n^4}J \tag{2.3}$$

where N_A is Avogadro's number, n is the refractive index, $PLQE_D$ is the donor photoluminescence quantum efficiency and κ^2 is the dipole orientation factor.[117] Typically, Förster radii range within few nm, however R_0 > 10 nm have been demonstrated with acceptor materials that have strong light coupling.[116] For example, Prins *et al.*[30] estimated a R_0 value of 19 nm for a single layer MoS_2 acceptor and CdSe/CdZnS QD donor.

2.6.2 Dexter Energy Transfer (DET)

Dexter energy transfer (DET) describes an electron exchange interaction between donor and acceptor. This exchange can be regarded as simultaneous electron-hole tunnelling from donor to acceptor species.[120] The DET rate, k_{DET}, follows the relationship:

$$k_{DET} \propto e^{\frac{-2d}{L}}J \tag{2.4}$$

where d is the separation distance between donor and acceptor molecules, L is the characteristic wave function decay length (*e.g.*, van der Waals radius). As with FRET, there is dependence on spectral overlap, J to satisfy the resonance condition, however the associated oscillator strengths are not important for DET.[116] Considering the exponential dependence on separation distance, d, DET can only be effective at close proximities, where there is sufficient donor-acceptor charge orbital (*i.e.* wave function) overlap. Typically, DET occurs within ≤ 1nm.

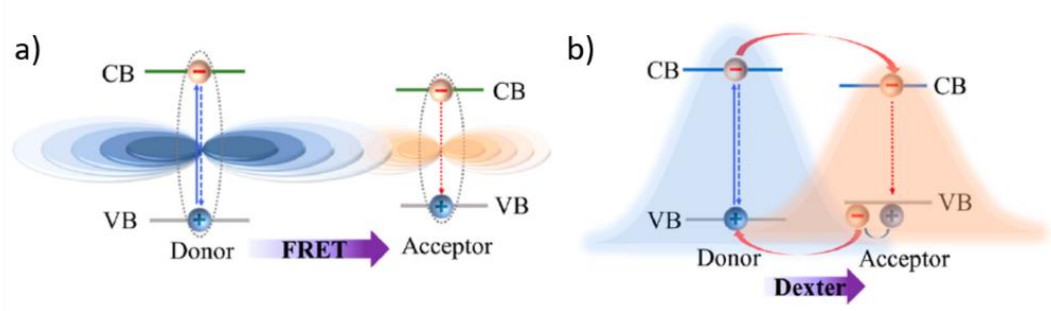

Figure 2.15: Nonradiative energy transfer mechanisms. Schematic illustration of a) Donor-acceptor dipole-dipole interaction in FRET and; b) Dexter ET showing donor-acceptor wave function overlap. Adapted from Li *et al.* [26]

2.7 Concept: 2D-QD heterostructure based LSCs

As previously highlighted, integrating monolayer semiconducting TMDs into solar PV cells poses formidable engineering challenges. Importantly, the energy penalty incurred by the necessary separation of tightly bound excitons into individual charges presents a major practical limitation. Considering this, we propose an alternative means to harness the excitonic properties of monolayer TMDs for light harvesting by integrating them into luminescent solar concentrators (LSCs). We first introduce LSCs and their underlying concepts.

Rather than replace the well-established Si based PV technology altogether, complementary photon management strategies can be employed to enhance performance of traditional PV energy conversion systems. A notable example of such strategies involves photon multiplication with singlet fission materials, which could break the efficiency limit *i.e.* the Shockley-Queissier limit of a single junction PV cell.[121] For our interests however, we look at light concentration with LSCs. LSCs can improve photon capture and reduce PV device area leading to reduced material and transport costs associated with PV module production.

LSCs consist of luminophores embedded in a transparent polymer waveguide. The luminophores absorb incident high energy light and re-emit it at an energy matching the optical gap of silicon PV (~ 1.1 eV). The down-shifted light is internally reflected by the waveguide and concentrated at the edges where Si-PV cells are located.[122] Figure 2.16 shows a concept application of LSCs as façade integrated photovoltaic windows. LSCs can concentrate diffuse light which is entropically forbidden in geometric light

concentration schemes based on mirrors and lenses. Also, unlike geometric concentrators, LSCs are not sensitive to the directionality of incoming light, which negates the need for solar tracking devices and therefore could provide further PV system cost reductions.[123]

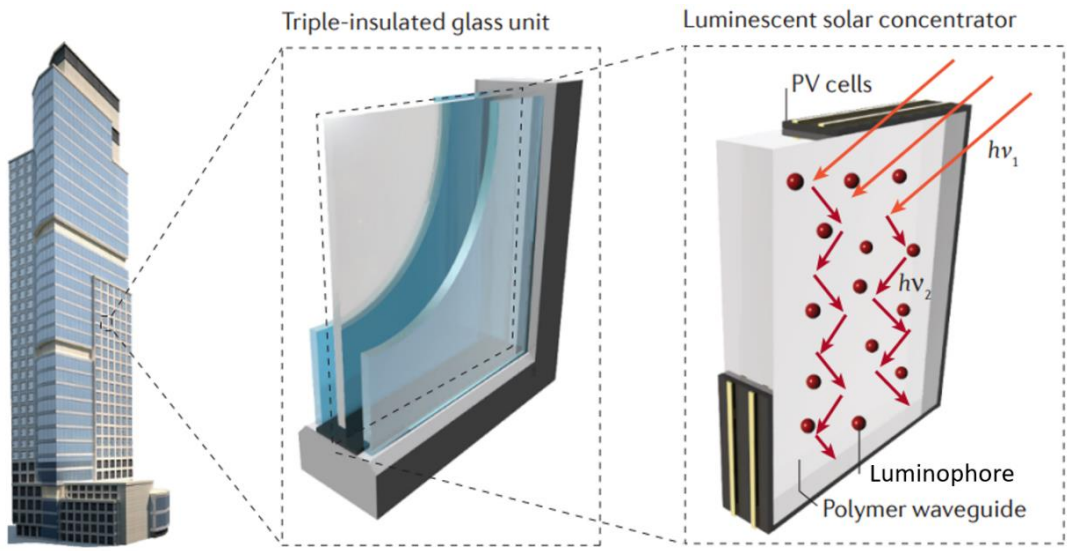

Figure 2.16: LSC as façade embedded photovoltaic window. Solar light ($h\nu_1$) absorbed by luminophores, re-emitted ($h\nu_2$) and internally reflected to edge PV. Adapted from Meinardi *et al.*[122]

The theoretical limit of light concentration by an LSC is directly related to the energy loss that occurs between photon absorption and re-emission by a luminophore, *i.e.*, the Stokes shift. From thermodynamic considerations, the limit of concentration C_{th} is given in terms of photon wavelength λ as: [124]

$$C_{th} = \frac{\lambda_1^2}{\lambda_2^2} exp\left[\frac{hc}{k_B T}\left(\frac{1}{\lambda_1} - \frac{1}{\lambda_2}\right)\right] \quad (2.5)$$

where h, k_B, T and c are the Planck's constant, Boltzmann's constant, absolute temperature and the speed of light. Subscripts 1 and 2 represent incident and re-emitted light respectively. In theory, an LSC based on luminophores with 80 nm Stokes shift has a maximum concentration factor of ~ 3400 at room temperature. In reality LSC concentration factors remain orders of magnitude below the theoretical limit due to inherent optical losses associated with typical luminophore materials and the optical cavity. In practice the concentration factor, C, is computed as: [123]

$$C = G\eta_{opt} \quad (2.6)$$

where G is the geometric gain factor, which is the ratio of the LSC frontal area incident to incoming irradiation, A_1 and the combined area of its edges, A_2. The optical efficiency,

η_{opt} is given by the ratio of photon fluxes at the LSC edges Φ_2 to the incoming incident photon flux Φ_1, that is

$$\eta_{opt} = \frac{\Phi_2}{\Phi_1} \tag{2.7}$$

The optical efficiency represents a combination of efficiency terms as shown in equation 2.7 below. This gives a clear picture of the exact optical loss mechanisms at play in LSCs:[125]

$$\eta_{opt} = (1 - R)\eta_{trap}\eta_{host}\eta_{TIR}\eta_{abs}\eta_{PLQE}\eta_{reabsorption} \tag{2.8}$$

where R is the Fresnel reflection coefficient of light incident to the LSC surface; η_{trap} is the waveguide light trapping efficiency; η_{host} is the transport efficiency of waveguided photons; η_{TIR} is the internal reflection efficiency of the waveguide surface; η_{abs} is the fraction of incoming light absorbed by the luminophores; η_{PLQE} is the luminophore PLQE and $\eta_{reabsorption}$ accounts for photon losses due to reabsorption by neighbouring luminophores. The first four terms of equation 2.8 can be represented by a single term for waveguide efficiency *i.e.*, $\eta_{waveguide}$. Improving $\eta_{waveguide}$ is a matter of optical cavity engineering. We concern ourselves with optical losses due to the luminophore, particularly reabsorption $\eta_{reabsorption}$. Reabsorption accounts for significant optical losses in LSCs and occurs because of overlapping emission and absorption spectra in typical luminophores as shown in Figure 2.17.*a*. Reabsorption increases the likelihood of non-radiative and `escape cone' losses. Escape cone losses occur when light is emitted at an angle below the critical angle of the waveguide.[125]

Eliminating reabsorption altogether requires luminophores with a sizeable Stokes shift (ΔE) between absorption and emission as illustrated in Figure 2.17.*b*. Various studies have demonstrated LSCs based on Stokes shift engineered materials, namely core-shell QDs.[126–130] We consider an alternative luminophore system based on monolayer TMDs hybridized with NIR emitting QDs. In this instance, we combine the large absorption cross section of 2D TMDs with high PLQE of nanocrystal QDs. Unlike other 2D-QD heterostructures discussed in the wider literature,[30–36] the monolayer TMD absorbs high energy visible photons, generating excitons, which are funnelled to the NIR QD emitter *via* a nonradiative ET process. This induces a large Stokes shift of hundreds of meV (*i.e.*, hundreds of nm) between absorption and emission events, eliminating reabsorption. Chapter 6 reports on the development and optical characterisation of this type of 2D-QD ET heterostructure consisting of a monolayer WS_2 absorber and lead

sulphide-cadmium sulphide (PbS-CdS) QD emitters. Due to time constraints, full development of a 2D-QD LSC remains a task for future research endeavours. Towards the realisation of this technology, the concept is developed further in Chapter 7 using light transport simulations to predict LSC performance under solar irradiation. LSC simulations were performed using a Monte Carlo ray tracing algorithm as commonly practiced.[131] The ray tracing algorithm is detailed in the chapter 3, section 3.4.

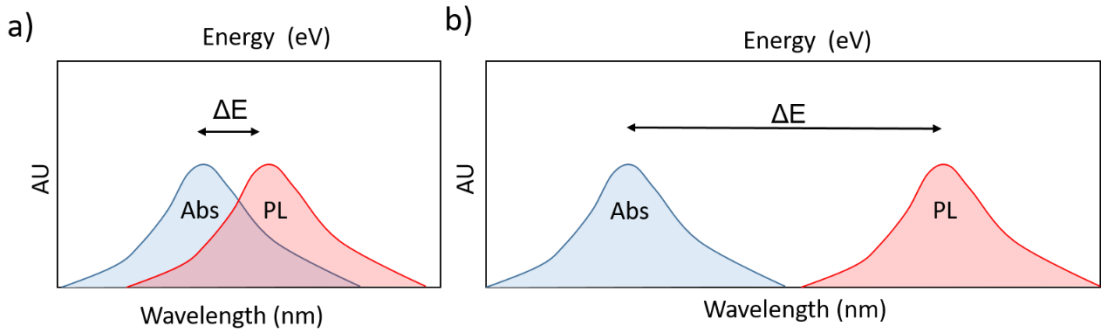

Figure 2.17: Eliminating reabsorption in LSC luminophores *via* Stokes shift engineering. Illustration of luminophores with a) high reabsorption due to overlapping absorption and PL spectra i.e., low Stokes shift, ΔE and b) zero reabsorption due to well separated absorption and PL spectra i.e. large ΔE.

2.8 TMD Monolayer Preparation Methods

Single layer TMDs can be isolated from their bulk counterparts by overcoming the weak interlayer forces. This is the basis of `*top down*' monolayer synthesis, which start with the bulk material and end with the monolayer.[5] As with graphene,[1] the renowned `scotch tape' method otherwise known as micromechanical cleavage, can be used to produce single layer TMDs. The method involves repeatedly exfoliating bulk material and depositing the exfoliate onto a desired substrate, whereupon microscopic monolayer flakes are identified by optical contrast using a microscope.[132,133] While this method produces high quality single crystals suitable for fundamental studies[2,134] and single device fabrication and characterisation,[135] it is highly unscalable. Moreover, monolayer yields are often low and flake lateral dimensions range only within a few microns (< 10 μm). As an alternative to scotch tape, gel-assisted exfoliation (with *e.g.* PF-X4 film) has been shown to produce larger sized monolayers (> 20 μm) free of tape

residue.[136] This technique has however been shown to produce fewer flakes compared with the scotch tape method.

Mechanical cleavage can be enhanced using a gold intermediary to produce large monolayers with lateral sizes in the 100s μm – 100s mm range at high yields.[137–140] Gold mediated exfoliation utilises gold's affinity to chalcogen atoms in the TMD lattice.[141] Magda *et al.*[137] demonstrated a method in which thermal release tape was used to directly deposit mechanically cleaved TMD bulk crystal onto an atomically flat gold coated substrate. The gold coated substrate was heated, removing the thermal tape prior to ultrasonication in acetone to remove excess bulk TMD crystal. Optical contrast microscopy[133] revealed monolayers with lateral sizes of few hundred microns. To transfer monolayers, thermal tape was attached to the TMD/gold sample and immersed in potassium iodide (KI) to etch the underlying gold layer. The TMD supported on thermal tape was then deposited onto the target substrate and heated, peeling the thermal tape. Alternatively, a spin-coated layer of poly(methyl methacrylate) (PMMA) on the gold coated substrate has been shown to be an effective monolayer transfer medium.[138] Following gold etch and target substrate deposition, the PMMA layer was removed by soaking in acetone. Liu *et al.*[139] presented a modified gold mediated exfoliation technique for production of centimetre scale TMD monolayers. An atomically smooth thin gold film was evaporated onto a polished silicon wafer and stripped away with thermal release tape and a polyvinylpyrrolidone (PVP) interfacial layer. The gold-coated layer was used to exfoliate TMD material from a low defect density flux grown bulk crystal. The exfoliate was deposited onto a target substrate and heated, removing the thermal release tape. The substrate was then immersed in deionised water to dissolve the PVP. Finally, the gold was etched by immersion in KI solution, leaving large macroscopic monolayer(s). Liu *et al.*'s method is shown in Figure 2.18 for its noteworthy result. Desai *et al.*[140] provided a simplified gold mediated exfoliation technique, where TMD bulk crystal cleavaged onto cleanroom tape was coated with a thin gold layer (~50 -100 nm) *via* thermal evaporation. The TMD/gold coated tape was exfoliated with thermal release tape, which was placed onto the target substrate. Heating the substrate peeled off the thermal release tape leaving the TMD monolayers between the substrate and gold. The gold was then etched away by immersing in KI and subsequently cleaned with solvent, leaving multiple monolayers with lateral dimensions of few hundred microns. Desai *et al.*'s method is used in this thesis for its simplicity, high throughput capability, high yield and adequately sized monolayers. Specific details of the methodology are given in chapter 3, section 3.1.

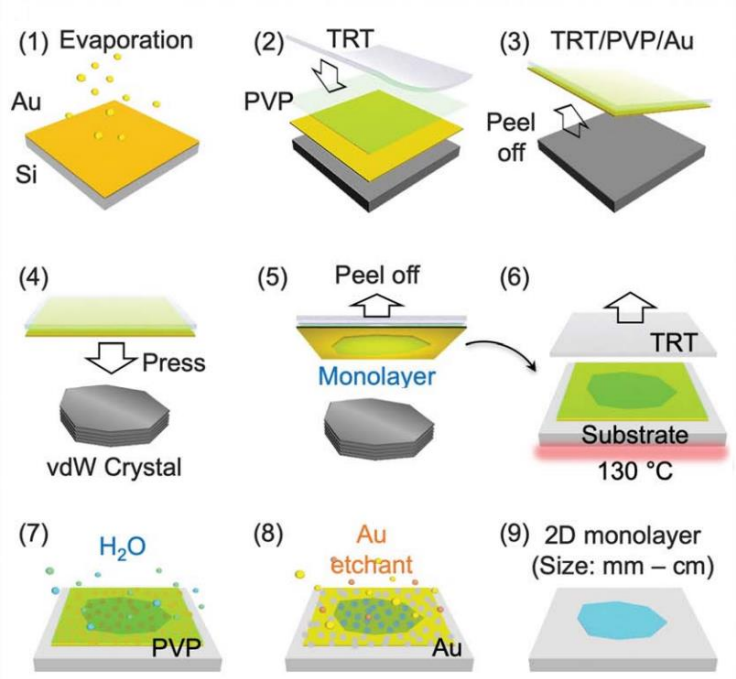

Figure 2.18: Modified gold exfoliation technique for production of centimetre scale TMD monolayers. Image reproduced from article by Liu *et al.*[139]

Liquid phase exfoliation (LPE) enables scalable production of single to few layer TMD nanosheet colloidal suspensions. Well stabilized TMD nanosheet suspensions have been investigated in various studies for their potential use as semiconducting inks for flexible, printable optoelectronic devices.[10,142] The main methods for LPE of bulk TMDs are ion intercalation and ultrasonication.[143] Ion intercalation typically involves mixing bulk TMD powder in a solution containing ionic compounds.[5] The ions intercalate between the TMD layers, weakening the interlayer attraction. Agitation from *e.g.* heat, separates the layers to form an exfoliated dispersion.[143] Ultrasonication of bulk TMD powder in a solvent or aqueous surfactant mechanically exfoliates layered crystals by hydrodynamic shear forces induced by cavitation, which form due to rapid pressure fluctuations.[144,145] Solvents with the appropriate surface energy prevent nanosheet re-aggregation.[143] On the other hand, surfactants stabilize the nanosheet dispersions by electrostatic repulsion of adsorbed surfactant molecules encapsulating the nanosheets.[144] Figure 2.19 overleaf illustrates the LPE methods described.

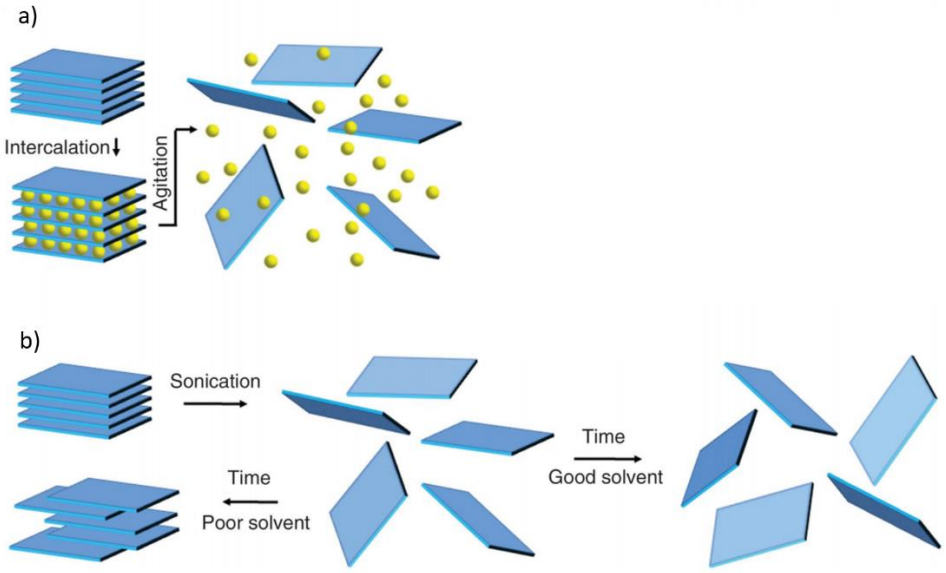

Figure 2.19: Liquid phase exfoliation of 2D materials. a) Illustration of TMD LPE *via* ion intercalation and agitation; b) Sonication assisted LPE for TMD nanosheet production. Good solvents with correct surface energy prevent re-agglomeration of nanosheets over long periods. Bad solvents result in nanosheet precipitation. Image reproduced from review article by Nicolisi *et al.*[143]

Wafer-scale fabrication of high-performance flexible electronics and optoelectronics requires continuous large-area uniform monolayers, which cannot be achieved using the `top down' methods previously described. Epitaxial growth *via* chemical vapour deposition (CVD) is poised to enable controlled `*bottom up'* synthesis of wafer-scale TMD monolayers from precursor materials.[5] The CVD monolayer TMD growth methods reported in the wider literature are variations of powder-based CVD and metal-organic CVD.[77] For the sake of brevity, we provide a short general overview of the two principal techniques. Powder-based CVD involves positioning precursor powders upstream of substrates in a quartz tube furnace as shown in Figure 2.20.*a*. A carrier gas transports the vaporized precursor material under steady flow conditions to the nearby substrates where they nucleate, forming crystalline films. In metal-organic CVD, volatile metal-organic precursors are introduced into a stream of carrier gases flowing into a reactor where they react with inflowing gaseous hydrogen chalcogenides (H_2S, H_2Se), forming crystalline films on a target surface (Figure 2.20.*b*).[77] Detailed insights into recent advances in CVD growth of TMDs can be found in a review article by Zhang *et al.*[146]

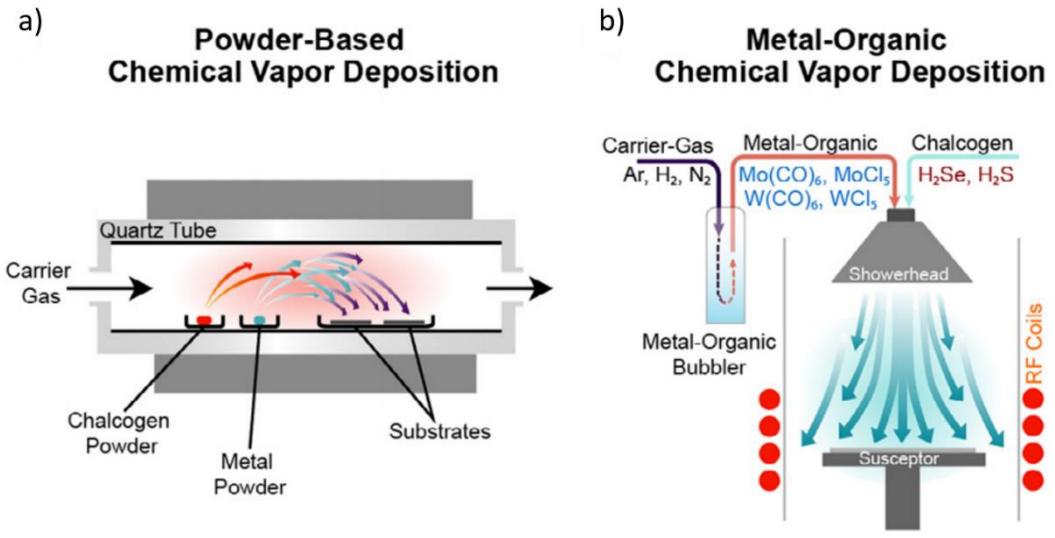

Figure 2.20: CVD techniques for wafer scale monolayer TMD production. a) Powder-based CVD; b) Metal-Organic CVD. Image reproduced from Briggs *et al.*[77]

3 Experimental Methods

In this chapter, we introduce the key sample preparation methods and optical characterisation techniques used in the series of work presented in this thesis. We first describe TMD monolayer preparation. This is followed with a general overview of photoluminescence (PL) microscopy; Raman microscopy; absorption microscopy; UV-Vis absorption spectroscopy; photoluminescence excitation (PLE) microscopy and; time correlated single photon counting (TCSPC) microscopy. We note the extensive use of microscopy techniques, which is owed to the micron-scale TMD monolayer samples studied. Microscopy techniques enable accurate spatial resolution of the sample's spectral properties. PL microscopy is described in particular detail because of its central role in the development of the experimental work detailed in this thesis. A Monte Carlo (MC) raytracing algorithm for simulating and visualising photon transport in luminescent solar concentrators (LSCs) in Chapter 7 is also described. Sample preparation procedures specific to each chapter, namely: chemical treatments with TFSI `super acid' (Chapter 4) and oleic acid (Chapter 4 and 5) and; 2D-QD heterostructure preparation (Chapter 6) are given in a sample preparation section within the main body of the respective chapters. Ancillary sample preparation procedures, namely: TFSI preparation (Chapter 4); field effect transistor (FET) fabrication (Chapter 4 and 5); quantum dot (QD) synthesis (Chapter 6) are given in a methods section at the end of each of the respective chapters. Descriptions of optical and electronic characterisation setups, including measurement parameters used are provided in the dedicated methods sections.

Monolayer exfoliation was carried out between the Cambridge Graphene Centre (CGC) cleanrooms and Cavendish labs by the author. PL microscopy was performed in the CGC by the author. Raman microscopy in Chapters 4 and 5 was performed in the CGC and Nano Doctoral Training Centre (DTC) Raman suites respectively by the author. Confocal absorption microscopy in Chapters 4 and 6 was performed by Cyan Williams (Vignolini group, Department of Chemistry). TCSPC microscopy in Chapters 4 and 6 were performed chiefly by Dr. Geraud Delport (Stranks lab, Optoelectronics). The PLE setup used in Chapter 6 was built by Nicolas Gauriot (Rao group, Optoelectronics). PLE measurements were performed by the author in the Rao group's Uberfast lab. The TCSPC

microscope setup used in Chapter 5 was built by Nicolas Gauriot and measurements were performed by the author in the Uberfast lab. FETs in Chapters 4 and 5 were fabricated and characterised by Dr. Alexander Webber (Electrical Engineering (EE) Department) and Dr. Ye Fan (Hofmann group, EE department) in EE cleanrooms. QDs used in chapter 6 were synthesised by Dr. James Xiao and characterised for UV-Vis absorption and PL by the author in Cavendish labs. 2D-QD heterostructures in Chapter 6 were fabricated by the author in Cavendish labs. The MC raytracing algorithm used in Chapter 7 was developed by the author. Tomi Baikie provided a more physically accurate LSC simulation for comparison.

3.1 TMD Monolayer Preparation

3.1.1 Gold Mediated TMD Monolayer Exfoliation

Prior to TMD monolayer exfoliation, all substrates were cleaned using a standard glass cleaning method described as follows: sonication in acetone for ~15 minutes; sonication in isopropyl alcohol (IPA) for 15 minutes and; surface treatment in oxygen (O_2) plasma etcher to enhance monolayer adhesion to the substrate surface.

We employed a gold mediated exfoliation technique by Desai *et al.*,[140] for the production of large area (~100 μm lateral dimensions) TMD monolayers. TMD bulk crystals were purchased from 2D semiconductors. Other materials and chemicals pertaining to monolayer exfoliation were purchased from Sigma-Aldrich. Figure 3.1, taken from Desai *et al.*,[140] illustrates the process. Figure 3.2 shows exemplary WS_2 monolayers on silicon-silicon dioxide (90 nm oxide layer).

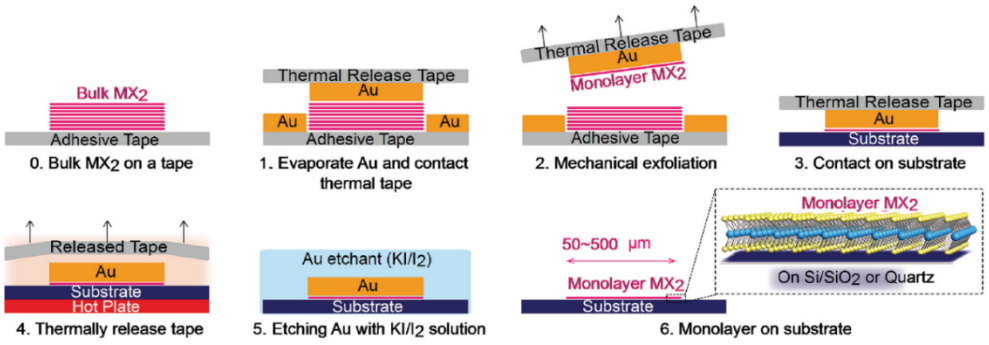

Figure 3.1: Gold mediated exfoliation technique for production large area TMD monolayers. Taken from Desai *et al.*[140]

A thick TMD layer was first pealed from its crystal using low density clean-room tape. The thick layer was then sandwiched with another piece of tape and pealed apart. This exfoliation process was repeated until the crystal was visibly thin. We now describe the remainder of the process with the aid of Figure 3.1:

0. The tape with a thin layer of bulk material was secured onto an evaporation mask with the exfoliated bulk material exposed.

1. The evaporation mask was placed in a thermal evaporator where a thin gold layer (~100 – 150 nm) was deposited onto the bulk material on tape under vacuum conditions.

2. Following gold evaporation, thermal release tape was adhered onto the gold coated TMD exfoliate and pealed, leaving the top-most layer of TMD attached to the gold on thermal release tape.

3. The thermal release tape was secured onto the newly cleaned plasma etched target substrate, sandwiching the gold and underlying monolayers between the substrate and thermal release tape.

4. The substrate was placed on a hot plate and heated to 125 °C, pealing the thermal release tape, leaving the TMD monolayers in-between a top gold layer and bottom substrate.

5. The excess gold was removed by immersing the substrate in potassium iodide (KI) and Iodine (I_2) standard gold etch (Sigma Aldrich) and gently swirled for ~5 minutes. The sample was then rinsed in deionised water and sonicated for 10 minutes in acetone and left to rinse in IPA for 5 minutes. Samples were then dried with a nitrogen (N_2) gun.

6. Monolayers were identified using optical contrast.[133] Figure 3.2 shows an exemplary WS_2 monolayer on silicon-silicon dioxide (90 nm oxide layer) substrate obtained *via* the gold mediated exfoliation method described.

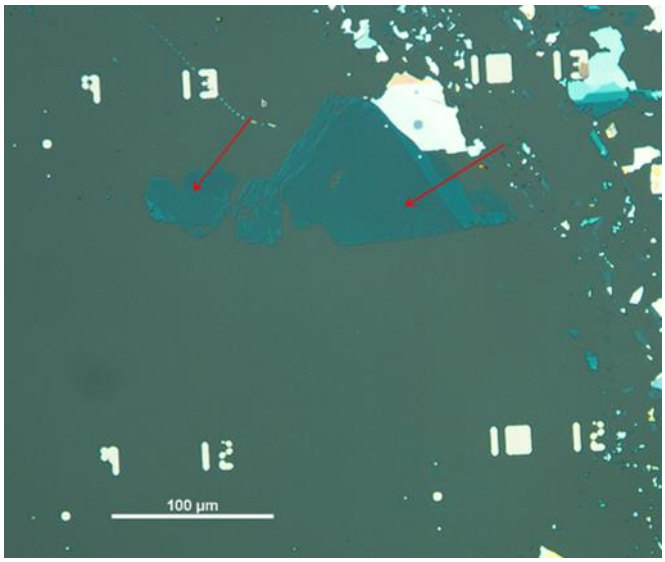

Figure 3.2: Exemplary gold exfoliated WS2 monolayer on Si-SiO2 (90 nm) substrate. Red arrows indicate monolayer regions. Scale bar represents 100 μm.

3.2 Steady State Optical Characterisation Techniques

3.2.1 Photoluminescence Microscopy

Photon absorption by a direct bandgap semiconductor generates excitons. Excitons eventually recombine, emitting PL as they transition from excited state to ground state. In general, PL spectroscopy enables characterisation of emissive excited states in luminescent materials.

In this work we employ PL microscopy to provide steady state emission properties of TMD monolayers. PL microscopy can be used to identify TMD monolayers on account of their direct optical gap. PL mapping provides spatial information on a material's optical quality in terms of spatial homogeneity in brightness and spectral linewidth. While PL microscopy is inherently steady state, it can provide initial insights into exciton recombination dynamics *via* excitation intensity dependent PL studies. PL microscopy was performed using an industry standard Renishaw Invia confocal setup shown in Figure 3.3. An air-cooled Argon (Ar) ion source provided a continuous wave (CW) 514.5 nm laser beam. A motorized piezo sample stage enabled PL mapping.

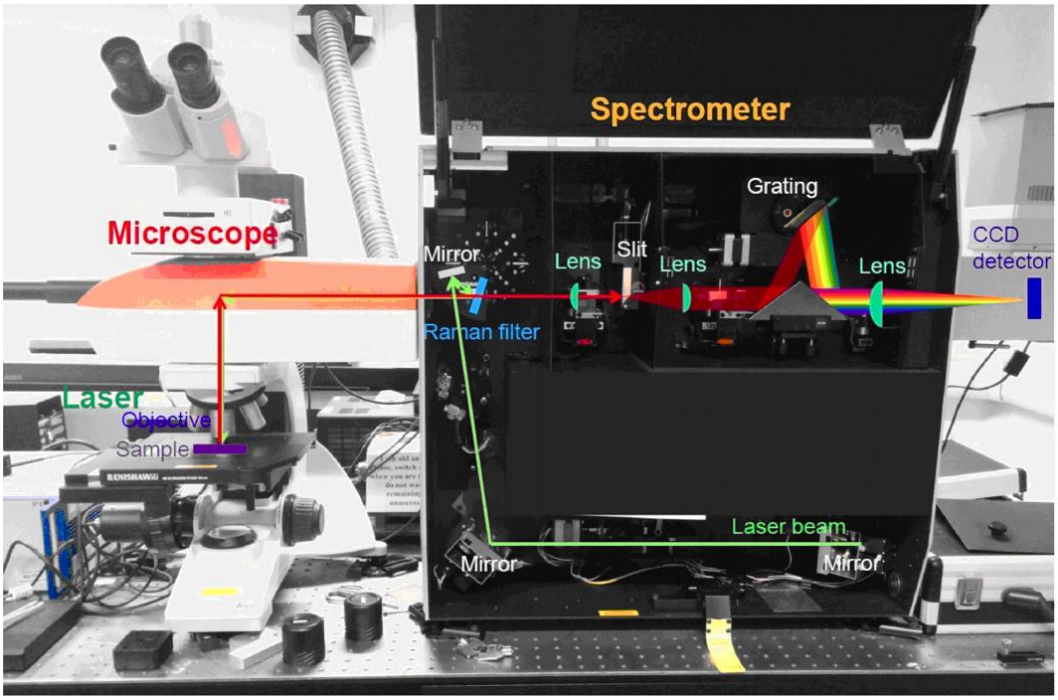

Figure 3.3: Renishaw Invia PL/ Raman microscope. Green and red arrows denote excitation and detection paths respectively. Reproduced with permission from the Cambridge Graphene Centre.

Following Figure 3.3, the laser beam is guided by a series of mirrors and focused onto the sample *via* the microscope objective. The diffraction limited beam spot size on the sample is dependent on the excitation wavelength and the objective's numerical aperture (NA). PL from the sample is reflected back into the objective where a mirror mounted in the microscope reflects the PL into the spectrometer. Within the spectrometer, the PL signal is collimated and reflected by a triangular mirror onto a PL diffraction grating. The diffraction grating disperses the components of the PL signal. The dispersed PL signal is then reflected onto a Peltier cooled charged couple device (CCD) detector. The system is operated *via* a dedicated computer using Renishaw's proprietary data acquisition `Wire' software interface where PL spectra and PL maps are visualised. The software interface allows the user to manipulate measurement parameters. Laser power is adjusted *via* a series of enclosed neutral density (ND) filters in the laser path leading up the laser beam entry point of the spectrometer housing. The ND filters are controlled using the software interface, where the user selects the percentage of laser power directed onto the sample. Laser power can be tuned further by manually adjusting the input electrical power with a dial. Laser power to the sample was accurately measured by placing a photodiode underneath a low objective. Power readings were taken with a dedicated power meter.

PL spectra of bulk colloidal quantum dots in a cuvette were obtained using a fluorimeter, which operates on the same principle as the system previously described. In this case free space excitation was provided by a high voltage lamp *via* a monochromator.

3.2.2 Raman Microscopy

The interaction between a molecule and incoming monochromatic light (*e.g.*, from a laser) results in elastic and inelastic light scattering. In the former case, light is scattered at the frequency of incident radiation, which is known also as Rayleigh scattering. In the latter, scattered light is shifted in frequency by the vibrational energy gained or lost in the molecule. This is called Raman scattering. If the scattered light gains vibrational energy as a result of energy loss in the molecule, this is referred to as anti-Stokes Raman scattering. Conversely, if the scattered light loses vibrational energy owing to an energy gain in the molecule, this is called Stokes Raman scattering. The shift in energy (or frequency) is known as the Raman shift.[147] The Raman shift gives information on the lattice vibrations in a material. As discussed previously in chapter 2, the technique can be used to distinguish monolayer TMDs from their multi-layer or bulk counterparts.[6] In this thesis, Raman microscopy was mainly used to detect changes in TMD monolayer lattice vibrations due to surface chemical treatments (Chapters 4 and 5). Raman spectra were obtained using the same setup described in 3.4.1 (Figure 3.3). A Raman filter was used to filter out Rayleigh scattering components (see Figure 3.3.). Raman gratings were used for signal dispersion.

3.2.3 Absorption Microscopy

Steady state absorption spectra of monolayer TMDs were measured with an inverted microscope. A schematic of the setup is provided in Figure 3.4. Incident white light from a halogen source (blue arrows) is reflected by a mirror onto an objective, which focuses the beam directly onto the sample on a transmissive substrate (*e.g.*, quartz). The transmitted light (red) is divided with a beam splitter, directing one component to a CCD camera to visualize the sample, and the other to an optical fiber connected to a spectrometer, where the components of the transmitted light are dispersed *via* diffraction grating prior to detection. The resulting transmission spectrum is visualized on a dedicated software interface. The proportion of light absorbed by the sample (*Abs*) is

computed from the transmission spectrum (T) using the relationship: $Abs = 1 - T - R$, where reflection is considered negligible i.e. $R \approx 0$. Prior to measuring the sample, a reference or baseline transmission measurement was taken on a blank substrate. The reference was subtracted from the sample transmission spectrum before converting to *Abs*.

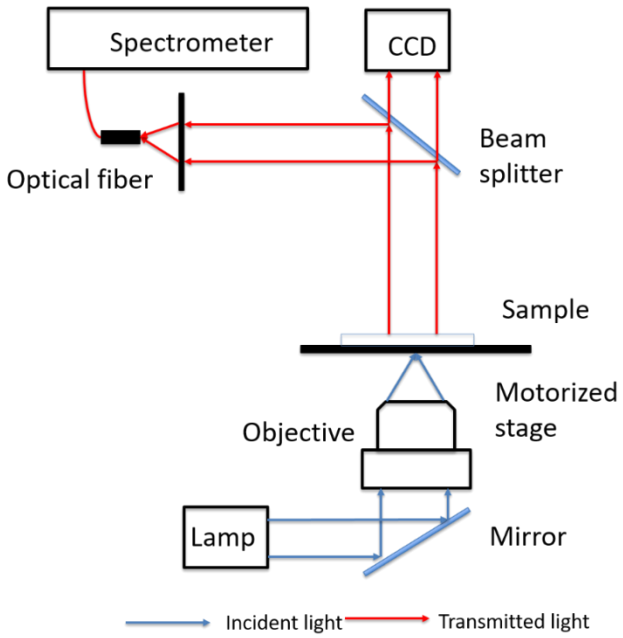

Figure 3.4: Inverted microscope schematic. Blue and red arrows denote incident light and transmitted light respectively.

3.2.4 UV-Vis Absorption Spectroscopy

The absorption spectrum of suspended bulk material can be obtained using UV-Vis absorption spectroscopy. In general, a UV-Vis spectrometer consists of a white light source, monochromator, sample compartment and detectors (e.g., CCD) linked to data logging software. The white light is focused onto the monochromator which may consist of a movable prism or diffraction grating coupled with a movable mirror to select or scan wavelengths. The monochromated light is divided with a beam splitter, directing one component of light to the sample in a transparent cell and the other to a reference cell containing the suspension's solvent. Sample and reference cells are held in separate compartments. For each wavelength, the intensities of light transmitted *via* the reference (I_0) and sample (I) cells are measured by separate detectors. The detectors convert the transmitted light intensities to absorbance signals A, *via* the Beer Lambert law: $A =$

$-log\left(\frac{I}{I_0}\right) = \alpha \times l \times c$. Where α is the extinction or absorption coefficient; l is the cell path length and c is the material concentration.[148]

3.2.5 Photoluminescence Excitation Microscopy

In general, photoluminescence excitation (PLE) spectroscopy operates by detecting emission of a sample at a fixed wavelength with *e.g.*, a CCD camera, and sweeping the excitation wavelength using *e.g.*, white light *via* monochromator or variable laser source. This allows one to ascertain the excitation wavelengths that contribute the sample's emission, thus revealing its emissive excited states, *i.e.*, the material's PL excitation spectrum. For an emissive material, the PLE spectrum overlaps its absorption spectrum. PLE also provides a convenient means to characterise energy transfer in luminescent hybrid systems in which excitonic energy is known to transfer non-radiatively from a donor molecule the to the acceptor molecule's band edge. By detecting the acceptor's PL and scanning the excitation wavelengths resonant to the donor, energy transfer is characterised by the presence of the donor's resonant features, most notably it's excitonic peaks, in the acceptor's PLE spectrum. The steady state nature of this technique makes PLE spectroscopy a simple, yet powerful tool for detecting energy transfer in hybrid systems such as the 2D TMD donor-QD acceptor heterostructure studied in Chapter 6.

3.3 Time Resolved Photoluminescence Spectroscopy

3.3.1 Time Correlated Single Photon Counting Microscopy

Time resolved photoluminescence (TRPL) spectroscopy provides insights into the dynamics of emissive excited states in a material. In this work, the PL dynamics of TMD monolayers were measured with a commonly used TRPL technique known as time correlated single photon counting (TCSPC) microscopy. Following Wahl,[149] the operating principle of TCSPC involves recording a single photon's arrival time with respect to a trigger pulse from the excitation laser. Photon counts are binned according to

their arrival times relative to the trigger pulse and sorted into a histogram. The statistical distribution given by the histogram is interpreted as the material's transient PL profile as illustrated in Figure 3.5.

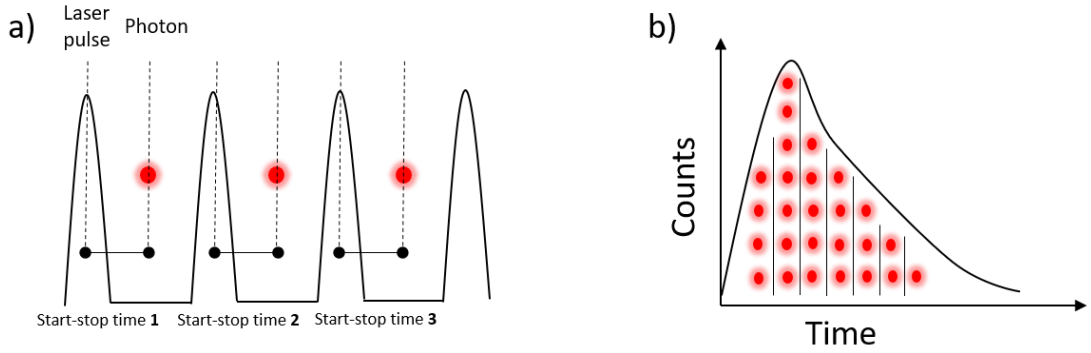

Figure 3.5: Time correlated single photon counting. a) Illustration of photon arrival times relative to trigger pulse shown as `start-stop' times; b) Histogram of arrival times, with photon counts in each time bin given by vertical lines. Adapted from Wahl.[149]

Due to the uncertainty of a single photon event, high repetition pulsed excitation is required for the collection of a sufficient number of photon events over multiple cycles, which in turn enables accurate reconstruction of a material's time dependent PL profile. Photon detection is commonly provided by a single photon avalanche diode (SPAD) or photomultiplier tube (PMT). For accurate TCSPC measurements, the probability of recording more than one photon per excitation cycle must be kept low to prevent photon pile-up, which we go on to explain. For a given excitation cycle, while a photon is being processed by the detector, it experiences a dead-time in which another photon event cannot be detected. Should the number of excited photons per cycle > 1, the resulting histogram will be skewed in favour of earlier arriving photons, amounting to an inaccurate representation of the sample's PL decay profile.[149] Photon pile-up can be avoided by keeping the photon detection rate to ~5% of the excitation pulse rate. This can be achieved by attenuating excitation intensity to the sample using *e.g.*, neutral density filters.

The resolution of any TCSPC measurement is limited to the sensitivity of the detector. Instrument sensitivity is given by the width of the instrument response function (IRF). This can easily be measured by detecting the laser excitation scatter. The narrower the IRF, the more sensitive the detector. In this work, TCSPC enabled time resolved characterisation of PL decay channels present the monolayer TMDs, namely: i) direct optical transitions from the lowest vibrational state to ground state *i.e.*, direct band gap

recombination; ii) emission from intermediate sub-gap or `trap' states to ground state; ii) PL quenching due to native non-radiative trap states or the presence of exciton acceptors.

3.4 Simulating Photon Transport in LSCs: Monte Carlo Method

The Monte Carlo (MC) method is a numerical technique that incorporates random numbers and applicable stochastic data to find approximate solutions to mathematical problems.[150] In principle, the method involves randomly sampling a probability distribution function (PDF). To do this, a random number ξ, drawn from a uniform distribution [0,1] is equated to the cumulative distribution function (CDF) *i.e.*, the integral of the PDF as shown in Equation 3.1. The CDF expression can then be re-arranged for the sought-after random variable. Sampling the variable repeatedly reproduces the original PDF.[151]

$$\xi = \int_a^X P(x)dx \Longrightarrow X \tag{3.1}$$

The inherently random events that take place in LSCs, *e.g.*, absorption and emission are well approximated by MC based algorithms. Raytracing tracks the path of photons, factoring in the random physical interactions with their environment, based on mathematical equations and spectral data governing *e.g.*, light absorption and emission trajectory to name a few. Where wave effects can be ignored, LSC Monte Carlo raytracing simulations provide reasonable predictions whilst avoiding the complexities introduced by radiative transfer equations.[151,152]

The MC algorithm described here was initially intended as an exercise for understanding the basic principles of LSCs. In chapter 7, the algorithm is used to provide approximate visualization of photon transport in various LSCs. The code was written in FORTRAN 90, with post-processing in Matlab. FORTRAN 90 was chosen for computational speed. The algorithm was inspired by existing Matlab-based simulators written by Dr. Maja Gajic[151] and Dr. Rowan MacQueen,[153] respectively. Dr. Gajic's code is available on the Mathsworks website.[154] Dr. MacQueen's code was provided by Dr. Nathaniel Davis.

3.4.1 Monte Carlo LSC Raytracing simulation algorithm

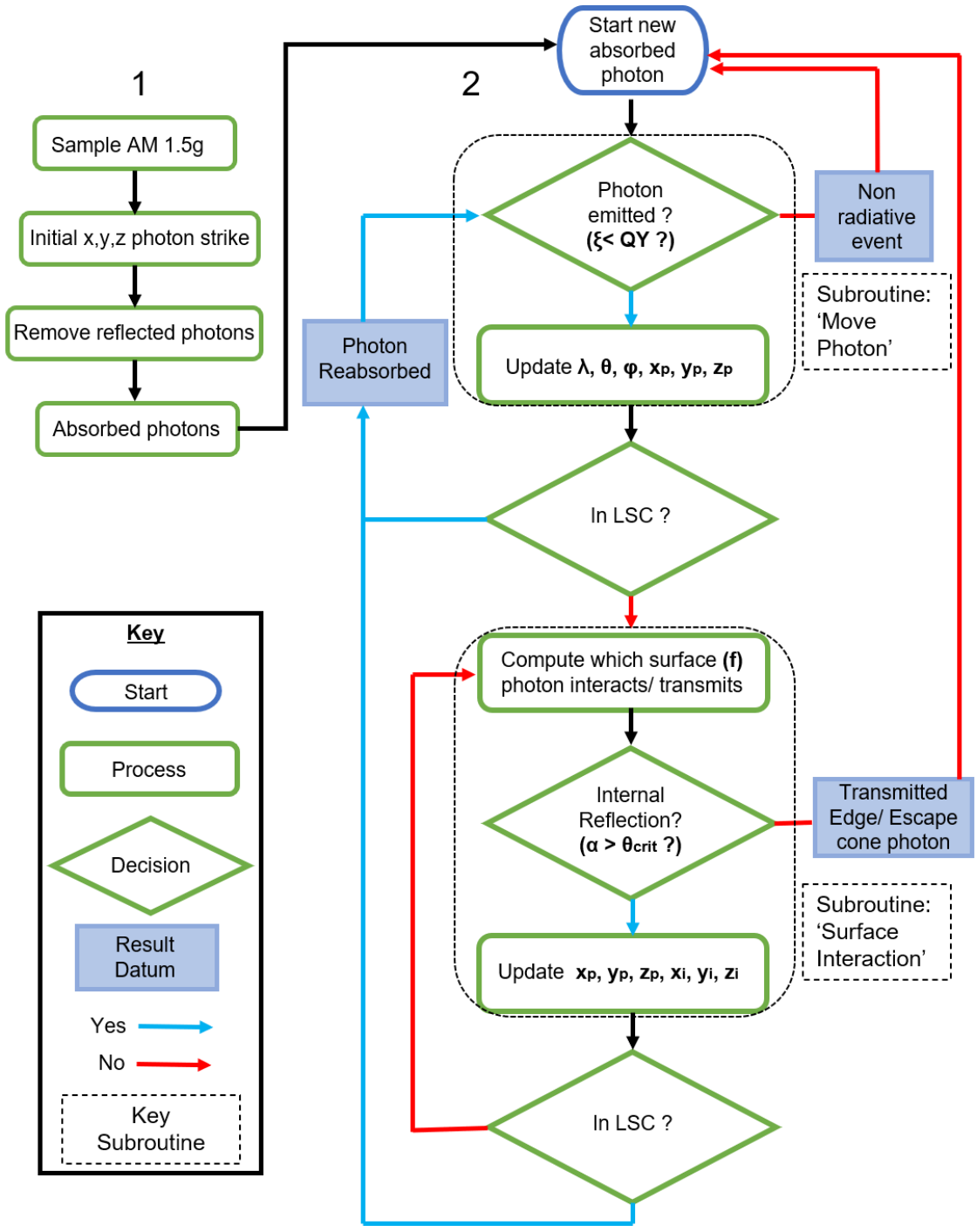

Figure 3.6: Schematic representation of MC LSC raytracing algorithm

3.4.1.1 General Overview

Figure 3.6 shows the flow chart for the MC raytracing algorithm. The code comprises of a module containing various subroutines, and a main script. Subroutines consist of multiple processes and decisions. For clarity and brevity some subroutines are represented as a single process. The key subroutines are enclosed in dotted lines. The main script calls back each subroutine in the order shown in the figure. The algorithm is split into two parts (1) and (2). In (1), randomly sampled solar photons are narrowed down to an array of photons initially absorbed by the luminophores, with externally reflected and transmitted unabsorbed photons removed and accounted for. In (2), each absorbed photon is processed in the `LSC loop', where the algorithm determines the fate of each photon *i.e.*, if it transmits *via* an edge or escape cone, or is lost because of non-radiative reabsorption. Each fate is recorded to compute LSC performance. Prior to providing an overview of the subroutines, the general simulation assumptions are detailed.

3.4.1.2 Assumptions

All incoming solar photons have normal incidence to the top surface of the LSC. Scattering and absorption by the waveguide material is ignored. Wave effects such as interference and diffraction are ignored. The luminophore's refractive index is the same as the host waveguide material. The waveguide refractive index is constant irrespective of photon wavelength. Luminophores are dispersed homogenously throughout the host matrix, hence the absorption spectrum is constant throughout the LSC cross section.[155] Luminophore quantum yields (QY) are constant regardless of concentration and incoming photon energy. LSCs are square slabs of length L and thickness d. Refraction between air and LSC boundary is ignored, which is acceptable for incoming photons at normal incidence and outgoing edge photons. For simplicity, if the incidence angle, α, between an emitted photon and the LSC boundary normal exceeds the critical angle, θ_{crit}, the photon is waveguided to the LSC edge. Otherwise, if $\alpha<\theta_{crit}$, the photon is transmitted *via* an escape cone. A more refined approach considers a photon with α slightly less than θ_{crit}, (*i.e.*, $\alpha\sim\theta_{crit}$) to have a some probability of internal reflection before being refracted *via* an escape cone after a predicted number of waveguide reflections.[155] Such a photon therefore stands a chance of being collected if emission occurs close to an LSC edge. In any case, efficiency gains from these partially reflected photons are minimal due to the likelihood of transmission *via* escape cones, unless they are reabsorbed and emitted at $\alpha>\theta_{crit}$.[155] Consequently, the simplifications made amount to slight underestimates for

edge photons. Finally, edge reflections are switched off to `collect' photons for performance calculations.

3.4.1.3 Subroutines

Photon generation and incident photon striking locations

In the first step, incident photons (λ_i) are randomly sampled from the AM 1.5g spectrum (NREL),[156] shown in Figure 3.7.*a*. In doing so, the solar spectrum *i.e.*, the probability density function (PDF) is converted to a normalized cumulative distribution function (CDF) by numerical integration. Figure 3.7.*b* shows the resulting CDF. By equating the CDF to a random number, ξ, drawn from a uniform distribution ($0<\xi<1$), a photon of wavelength λ_i and flux, $F_i(\lambda_i)$ can be randomly sampled from the PDF. Typically, for LSC simulations N =10,000 random photons are initialized. The randomly selected photons are stored in an array. In the next step, each photon is allocated an initial striking coordinate on the LSC incident surface. This is done by randomly selecting x_o and y_o points from a grid, while z_o is the LSC thickness. The grid is defined by the LSC side lengths (L_x and L_y), each divided into N points, resulting in an $N \times N$ grid.

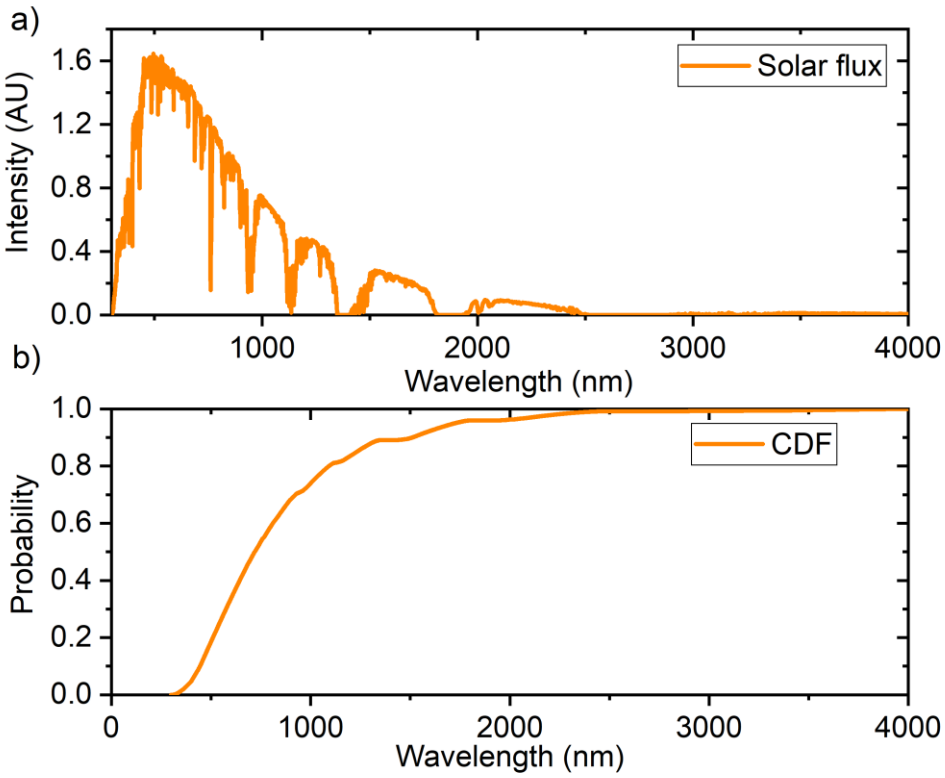

Figure 3.7: AM1.5G Solar spectrum. a) Full solar spectrum PDF of flux against wavelength[156]; b) CDF derived from numerical integration.

Removing external reflections

Once incident striking positions are determined, a weight of the array of incident solar photons is removed by simulating external reflection. This is done by associating each incident photon with a random number, ξ, and comparing it to the probability of reflection. This probability is given by Fresnel reflection coefficient, *R* in equations 3.2.

$$R = \left[\frac{(n-1)}{(n+1)}\right]^2 \tag{3.2}$$

, where *n* is the waveguide refractive index. If $\xi < R$, the photon is rejected and counted. This random rejection process leaves an updated array of non-reflected photons and their initial coordinates to be passed into the initial absorption subroutine. Typically, waveguide materials such as PMMA have a refractive index of 1.5, hence roughly ~4% of incident photons are externally reflected.

Initial absorption

This subroutine removes the portion of incident photons that are not absorbed. Here, the absorption path length, *s*, is computed and compared to the LSC thickness t_{LSC}. The absorption path length, *s*, is the distance a photon of wavelength λ will travel before being absorbed. The decadic Beer Lambert law (Equation 3.3) is used to calculate *s*:

$$A = 1 - 10^{-\varepsilon(\lambda)cz} \tag{3.3}$$

, where *A* is fractional absorbance spectrum, *c* and $\varepsilon(\lambda)$ are the luminophore concentration and molar extinction coefficient, and *z* is the path length. *A* is essentially a CDF which gives the probability of a photon being absorbed before or at a distance *z*. Therefore, the associated PDF is determined by taking the spatial derivative of equation 3.3 to get:

$$\frac{dA}{ds} = \varepsilon(\lambda)c10^{-\varepsilon(\lambda)cz} \tag{3.4}$$

To sample the PDF, its integral (Equation 3.3) is simply set to ξ [0,1]. Then, by rearranging for *z*, the randomized path length for each photon can be determined *via* equation 3.5. Replacing *z* with *s* we obtain

$$s = \frac{-log_{10}(\xi)}{\varepsilon(\lambda)c} \tag{3.5}$$

If $s < t_{LSC}$ the incident photon (λ) is absorbed. The photon's *z* coordinate is updated to $z_o = t_{LSC} - s$. The initial coordinates x_o and y_o are maintained and the absorbed photon counter

is updated. Absorbed photons and their coordinates are stored in an array for passing into the LSC loop (2). If $s > t_{LSC}$ the photon is transmitted and counted.

Moving emitted photons

Each initially absorbed photon (λ) and their spatial information is now processed in the LSC loop (2). The first subroutine in (2), called `Move Photon' is responsible for propagating emitted photons in random directions. The routine first determines if an absorbed photon is emitted by comparing a random number, ξ to the luminophore QY set by the user. If $\xi >$ QY, the photon is lost non-radiatively and counted. However, if $\xi <$ QY, an emission event is counted, and the photon wavelength is updated by random selection from the luminophore's emission spectrum CDF. The extinction coefficient $\varepsilon(\lambda)$ at the new wavelength, λ, is used to compute a new path length, *s*, *via* equation 3.5. This is used in combination with the luminophore emission angles to project the photon. Here we assume the isotropic spherical emission angles, which suits the dye and QD emitters simulated in Chapter 7. The azimuthal angle, ϕ and zenith angle, θ are randomly sampled as: $\phi = 2\pi\xi$, where $0 \leq \phi \leq 2\pi$ and $\theta = \cos^{-1}(2\xi - 1)$, where $0 \leq \theta \leq \pi$. These are used to compute direction cosines *via* equations 3.6-3.8:

$$\mu_x = sin\theta cos\phi \tag{3.6}$$

$$\mu_y = sin\theta sin\phi \tag{3.7}$$

$$\mu_z = cos\theta \tag{3.8}$$

The new *x*, *y* and *z* projected coordinates are then calculated as:

$$x_p = x_o + \mu_x s \tag{3.9}$$

$$y_p = y_o + \mu_y s \tag{3.10}$$

$$z_p = z_o + \mu_z s \tag{3.11}$$

Once the photon's spatial and spectral information is updated, the algorithm determines if the photon's new position lies within the bounds of the LSC. If so, the photon is reabsorbed and reprocessed by the `Move Photon' subroutine. If not, the algorithm checks for an internal reflection at the LSC boundary by calling the `Surface Interaction' subroutine.

Surface interactions

The `Surface Interaction' subroutine plays the critical role of simulating photon waveguiding to the LSC edge by internal reflection. Within the subroutine another subroutine known as `Which Surface' first is called. This returns the face, *f*, which the photon reflects off or transmits through the LSC boundary. As a visual aid, Figure 3.8 shows the LSC in 3D cartesian space with faces and plane normal vectors labeled.

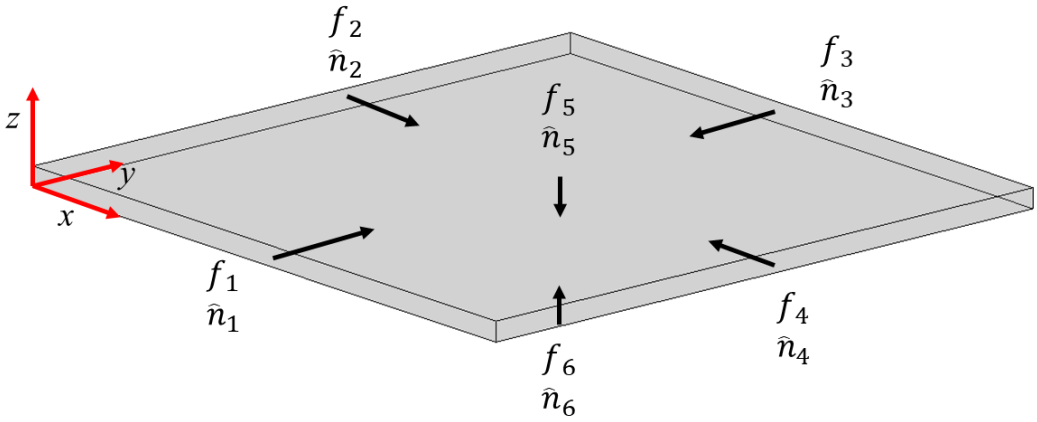

Figure 3.8: Region bound by LSC in 3D space.

Using 3D vector geometry, `Which Surface' first checks for plane intersections by the photon ray. A second check is performed to confirm that the plane intersection point lies on the LSC boundary. Once *f* is known, another embedded subroutine, `IS TIR' is called to determine whether photon is transmitted or internally reflected at the boundary. This is done by comparing the photon's angle of incidence with the plane, α, to the critical angle, $\theta_{crit} = sin^{-1}(1/n)$. The incidence angle, α, is simply derived from the direction cosines. For example, for a photon incident to the *z* plane, $\alpha = \cos^{-1}(|\mu_z|)$. If $\alpha < \theta_{crit}$, it is transmitted through the face and a photon counter for that face is updated accordingly. Transmission through top and bottom surfaces are counted as escape cone losses. If $\alpha > \theta_{crit}$ the photon is internally reflected, and its positional information is updated using 3D vector geometry. The algorithm then determines whether the new coordinates (x_p, y_p, z_p) lie within the bounds of the LSC. If so, the photon is reabsorbed and processed by the `Move Photon' subroutine. If not, then the photon interacts with another surface and the `Surface Interaction' procedure is repeated.

Here, we provide an exemplary procedure of how a photon is waveguided by total internal reflection (TIR). We consider a photon reflected between the *z* plane boundaries, f_6 and f_5, as shown in Figure 3.9 overleaf.

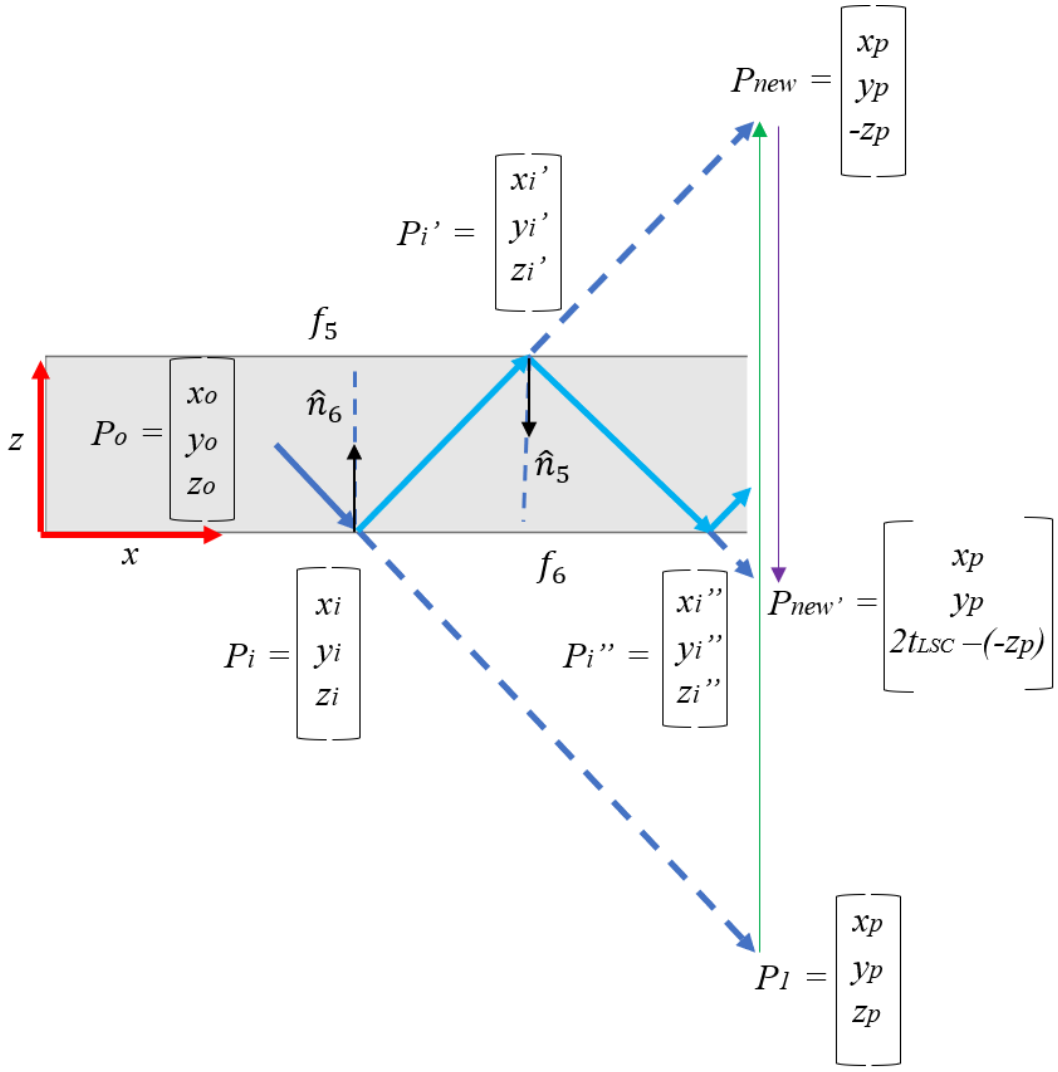

Figure 3.9: Illustration of waveguiding calculations performed by raytracing algorithm

First, the algorithm determines the initial point of intersection P_i between the vector connecting positions P_o and P_1, and the boundary plane f_6. P_o is the origin of the photon from within the LSC and P_1, is the end point of the projected ray. The plane equation for f_6 is simply $z = 0$. The parametric equation of the vector connecting P_o and P_1 is:

$$r(t) = P_o + t\,\overrightarrow{P_oP_1} \tag{3.12}$$

, which is expanded to the equations for the point of intersection on the plane:

$$x_i = x_o + t\,\overrightarrow{P_oP_1}\,(1) \tag{3.13}$$

$$y_i = y_o + t\,\overrightarrow{P_oP_1}\,(2) \tag{3.14}$$

$$z_i = z_o + t\,\overrightarrow{P_oP_1}\,(3) \tag{3.15}$$

Setting equation 3.15 to zero yields the plane equation, $z_i = 0$. The parameter t is then calculated and substituted into the other equations to determine the coordinates of intersection. Now, the position of the photon must be reflected around the intersection point, P_i, about the plane $z = 0$ (green arrow) so that $P_{new} = [x_p, y_p, -z_p]$, with x and y components unchanged as shown in Figure 3.9.

Using the same procedure, the second point of intersection, P_i', between the reflected ray connecting P_i and P_{new}, and the plane boundary f_5 is computed. In this case, the plane equation for f_5 is $z = t_{LSC}$. Equation 3.15 is set to $z_i = t_{LSC}$ and the origin of the reflected ray is updated to the previous intersection point at f_6, so that $P_o = P_i$. The ray's end point is also updated so that $P_1 = P_{new}$. As previous, t is calculated from equation 3.15 and substituted into equations 3.13 and 3.14 to calculate the coordinates of P_i'. The subsequent $P_{new'}$ is obtained *via* reflection around the intersection point, P_i', about the plane $z = t_{LSC}$ (purple arrow) so that $P_{new'} = [x_p, y_p, 2t_{LSC} - (-z_p)]$ as shown in Figure 3.9.

The process repeats in the photon's projected direction until it is reabsorbed (*i.e.*, P_{new} lies within the LSC bounds), or reaches the LSC edge. The path of waveguided photon is tracked by tracing the intersection points. Figure 3.10 below shows the simulated 3D path of a single waveguided photon traversing the LSC.

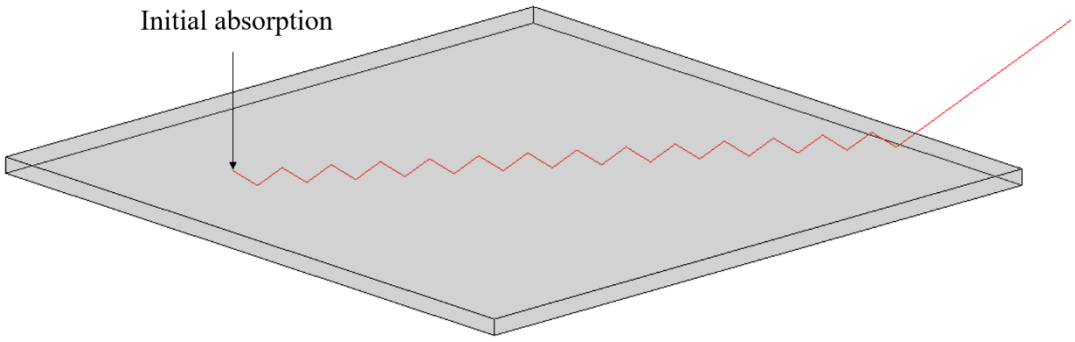

Figure 3.10: Simulated path of single waveguided photon traversing LSC

The fully annotated code can be made available upon reasonable request from the author.

4 Enhancing Photoluminescence and Mobilities in WS_2 Monolayers with Oleic Acid Ligands

Many potential applications of monolayer transition metal dichalcogenides (TMDs) require both high photoluminescence (PL) yield and high electrical mobilities. However, the PL yield of as prepared TMD monolayers is low and believed to be limited by defect sites and uncontrolled doping. This has led to a large effort to develop chemical passivation methods to improve PL and mobilities. The most successful of these treatments is based on the non-oxidizing organic 'super-acid' bis(trifluoromethane)sulfonimide (TFSI) which has been shown to yield bright monolayers of molybdenum disulphide (MoS_2) and tungsten disulphide (WS_2), but with trap limited PL dynamics and no significant improvements in field effect mobilities. Here, using steady-state and time-resolved PL microscopy we demonstrate that treatment of WS_2 monolayers with oleic acid (OA) can greatly enhance the PL yield, resulting in bright neutral exciton emission comparable to TFSI treated monolayers. At high excitation densities the OA treatment allows for bright trion emission, which has not been demonstrated with previous chemical treatments. We show that unlike the TFSI treatment, the OA yields PL dynamics that are largely trap free. In addition, field effect transistors show an increase in mobilities with the OA treatment. These results suggest that OA serves to passivate defect sites in the WS_2 monolayers, in a manner akin to the passivation of colloidal quantum dots with OA ligands. Our results open up a new pathway to passivate and tune defects in monolayer TMDs using simple `wet' chemistry techniques, allowing for trap free electronic properties and bright neutral exciton and trion emission.

The work detailed in this chapter is adapted from an article published in ACS Nano Letters: Tanoh, A. O. A.; Alexander-Webber, J.; Xiao, J.; Delport, G.; Williams, C. A.; Bretscher, H.; Gauriot, N.; Allardice, J.; Pandya, R.; Fan, Y.; Li, Z.; Vignolini, S.; Stranks, S.D.; Rao, A. Enhancing Photoluminescence and Mobilities in WS_2 Monolayers with Oleic Acid Ligands. *Nano Lett.* **2019**, 19 (9), 6299–6307. https://doi.org/10.1021/acs.nanolett.9b02431.**[27]**[27]

All the work in this chapter was performed by the author except where stated. Dr. Alexander Webber and Dr. Ye Fan prepared WS_2 transistors, measured their respective electronic characteristics and provided detailed analysis of the resulting data (Section 4.6, paragraphs 1 and 3); Dr. Delport measured TRPL; Cyan Williams performed absorption microscopy and; Dr. James Xiao contributed to the discussion on the surface chemistry that gives rise to observed improvements in optical and electronic properties in WS_2 monolayers upon OA treatment (Section 4.5, paragraph 2).

4.1 Background and Motivation

TMDs are a class of layered materials which have garnered intense research interest due to their unique optical, electronic and catalytic properties. [6,3,157] TMD bulk crystals consist of monolayers bound by weak Van der Waals interactions, which can be overcome *via* dry mechanical cleavage (e.g. scotch tape method [1]) or *via* liquid phase exfoliation.[158,143] Also, there are numerous ongoing efforts to directly grow highly crystalline few or monolayer TMD films in particular by chemical vapour deposition (CVD).[159,77] Many of these materials show a transition from indirect bandgap in the bulk material to a direct bandgap in the monolayer limit.[6,3] The direct bandgap, high absorption coefficient and potentially high carrier mobilities of TMD monolayers hold great potential for optoelectronic applications such as photodetectors, light emitting diodes (LEDs) and photovoltaics.[3] Reduced dielectric screening in TMD monolayers in contrast to the bulk crystal gives rise to tightly bound excitons at room temperature.[56,160] This provides an interesting arena to study many-body exciton-exciton and exciton-carrier interactions that result in diverse multi-exciton[52,161] and charged exciton species [55,62] respectively. A number of potential applications of TMDs, such as in optoelectronic

devices, quantum light sources[162] or on-chip quantum information processing,[63,163,164] are dependent on having materials of high optical quality. In particular, there is a need for materials with high photoluminescence quantum efficiencies (PLQE) and also tuneable emission properties. This raises a fundamental challenge for TMDs, because as exfoliated or CVD prepared monolayers show extremely low PLQE, typically ~0.001-5%.[73,74] There have been various proposals for the cause of the non-radiative exciton recombination such as trion formation,[66] the presence of chalcogen vacancies, [20] or other atomic substitutions. [15,18] However, the exact nature of the defects and the mechanism by which they quench PLQE is still debated. [20,25,21,91,84,165] This has led to a number of treatments being proposed to enhance the PLQE of monolayer TMDs, most commonly MoS_2 and WS_2. For instance, studies have sought to improve PL *via* surface treatments using electron withdrawing dopants such as 2,3,5,6-tetrafluoro 7,7,8,8-tetracyanoquinodimethane (F4TCNQ)[66,23] and hydrogen peroxide.[24] Monolayer deposition of titanyl phthalocyanine (TiOPc) as a charge transfer interface also increases PL yield in MoS_2.[89] These are proposed to reduce electron density, suppressing low PLQE trion formation therefore promoting neutral exciton recombination. Other studies have sought to preserve the intrinsic optical properties of TMDs *via* exfoliation onto hexagonal boron nitride (hBN)[87] or hBN encapsulation, [85,86] which isolates monolayers from doping and disorder induced by the underlying substrate (e.g. Si-SiO_2). This has been shown to result in more uniformly distributed dominant neutral exciton PL with narrow homogeneous spectral linewidth free of substrate effects, which otherwise manifest as inhomogeneous contributions in monolayer TMD PL spectra[85]. While hBN encapsulation improves overall optical quality, however large increase in PL at low excitation intensities has not been demonstrated. Hoshi *et al*.[88] have demonstrated that hBN encapsulation suppresses exciton-exciton annihilation rates in monolayer WS_2 as indicated by large PL enhancement at high excitation intensities compared with non-encapsulated monolayers. Most notably, surface treatment with non-oxidizing organic `super acid' bis(trifluoromethane)sulfonimide (TFSI) has been shown to yield very bright PL from monolayer MoS_2 and WS_2. While the exact mechanism of the PL enhancement is still debated, it has been shown that the TFSI treatment reduces the extent of *n*-type behaviour in MoS_2,[20] which is consistent with the observed suppression of trion formation [166]. The authors of *ref. 20* [20] have recently demonstrated PL enhancement and exciton dynamics similar to TFSI treated MoS_2 and WS_2 *via* electric gating.[75] The application of a negative bias is said to de-dope the intrinsically *n*-type materials, which suppresses trion formation thus enhancing radiative recombination of

the neutral exciton. By comparing the exciton dynamics of TFSI treated and gated TMDs, the authors conclude that TFSI acts as an electron drawing species which suppresses trion formation. However, it has been shown that the TFSI treatment leads to trap limited PL dynamics [91] and does not give rise to improved mobilities in field-effect transistors.[20] In addition, the harsh nature of TFSI necessitates additional fabrication steps to protect commonly used electrode materials such as nickel.[20] Lastly, while treatments like the TFSI boost neutral exciton PL, they do not lead to bright trion emission, which would be of use in applications such as optical readout of trions for spintronics.[167] Thus, an alternative benign chemical treatment that simultaneously improves PL and mobilities whilst easing device fabrication would provide an attractive means to functionalise and passivate monolayer TMDs.

Here, we demonstrate that a simple long-chain acid, oleic acid (OA) can greatly enhance the PL of monolayer WS_2 yielding bright neutral exciton emission comparable to TFSI treated monolayers. In addition, OA allows for bright trion emission and an increase in field effect mobilities. We also show that in comparison to previous TFSI treatment, where PL is trap limited, the OA treatment yields predominantly trap free PL characteristics. Our demonstration that a weak acid can be used to passivate and tune the properties of monolayers WS_2, draws parallels to the surface treatment of inorganic colloidal quantum dots, such as cadmium sulphide (CdS) and lead sulphide (PbS), where long-chain acids and in particular OA are used to passivate surfaces, and thus opens a range of options for passivating and tuning the properties of monolayer TMDs.

4.2 Sample Preparation

WS_2 Monolayers were exfoliated *via* gold assisted exfoliation technique[140] described in chapter 3 (section 3.1) onto silicon-silicon dioxide (Si-SiO_2) with 90 nm oxide layer and quartz substrates. Monolayers on Si-SiO_2 were used for PL maps, Raman spectroscopy and electronic characterisation. Samples on quartz were used for steady state absorption microscopy, excitation dependent steady state PL, and time-resolved PL measurements. All measurements were performed at room temperature. After initial characterisation of untreated (*i.e.*, `pristine') monolayers, samples were chemically treated. OA treated samples were immersed in degassed OA in a tightly closed vial overnight in a nitrogen (N_2) glovebox on a hot plate set at 25 °C for ~12 hours. After OA treatment, samples were rinsed with anhydrous toluene and dried with a N_2 gun. TFSI in

1,2 dichloroethane (DCE) solution was prepared using a procedure described in section 4.8.1. Following Kim *et al.* [21], in a N_2 glovebox, TFSI treated samples were immersed in a 0.2 mg ml $^{-1}$ TFSI-DCE solution in a tightly closed vial for 40 minutes at room temperature. After treatment, samples were removed and dried with a N_2 gun.

4.3 Steady State Photoluminescence

Figures 4.1.*a* and *c* show the scatter plot for peak PL emission intensities and their corresponding spectral positions extracted from PL maps of multiple WS_2 monolayers on Si-SiO_2 (90 nm) before and after surface treatment with OA and TFSI respectively. Maps were measured at 135 W cm^{-2}. Figure 4.1.*b* and *d* show representative PL spectra, for points, which correspond to the median PL intensity of exemplary monolayers before and after treatment. Median enhancement factors, Δ_{median} of 40× and 9× were calculated for OA and TFSI treatment, respectively. Table 4.1 shows key statistics that accompany PL enhancement, namely: average enhancement across the monolayers (Δ_{ave}) *i.e.,* the ratio of post- and pre-treatment peak PL counts; standard deviation in PL intensity (σ_{counts}); average emission peak wavelength (λ_{ave}); and standard deviation in peak wavelength (σ_{λ}). The untreated case is indicated by (*) where appropriate. The data presented in Figure 4.1 and Table 4.1 were derived from non-fitted raw PL spectra.

Table 4.1: WS_2 monolayer PL enhancement statistics derived from PL maps. Characteristics prior to treatment marked with (*).

Treatment	Δ_{ave}	σ_{counts}	λ_{ave}	σ_{λ}
OA	27	116 %	618.3 nm*→614.2 nm	1.57 nm*→0.57 nm
TFSI	10	87.3 %	618.4 nm*→617 nm	2.16 nm*→1.29 nm

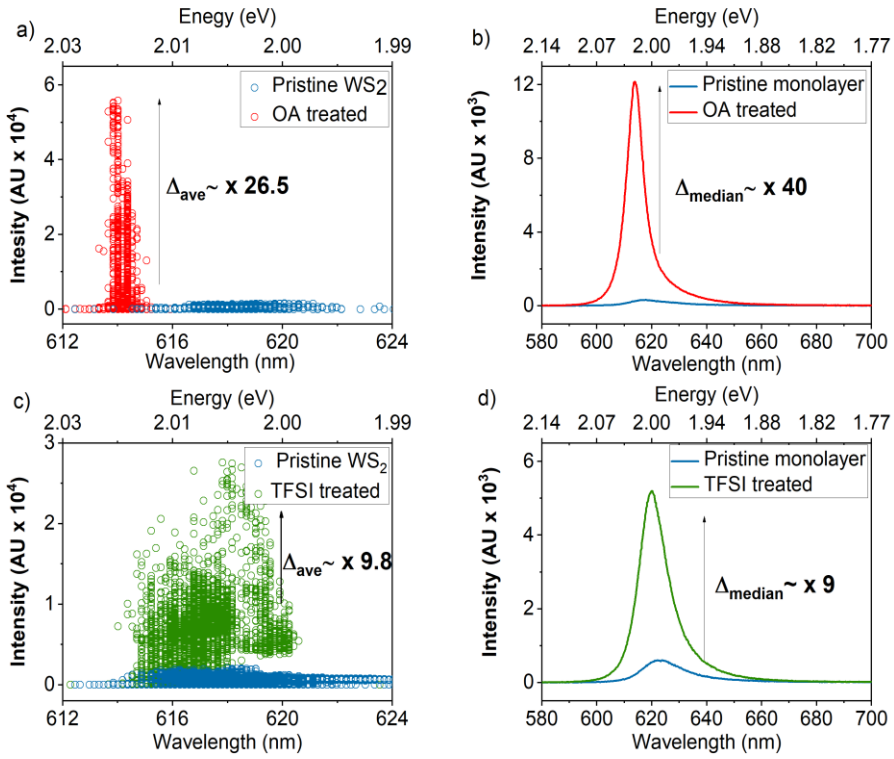

Figure 4.1: WS2 PL enhancement statistics. a) and **c)** PL enhancement scatter plot showing maximum untreated monolayer PL counts (blue) and peak OA (red) and TFSI (green) maximum treated monolayer PL counts measured at 135Wcm^{-2}. Data derived from non-fitted raw spectra from PL maps; **b)** and **d)** Raw PL spectra for points that represent the median peak PL counts before (blue) and after OA (red) and TFSI (green) treatment on exemplary monolayers.

For the data collected the OA treated samples show a higher average enhancement factor compared to TFSI treated samples. The standard deviation in PL intensity, σ_{counts}, reveals that TFSI treatment results in a more spatially homogeneous brightness, as compared to the OA case. Better spectral uniformity is achieved with OA treatment as quantified by ~58% reduction in σ_λ, compared with a ~40% reduction in σ_λ with TFSI. The spectral narrowing in OA treated monolayers is potentially due to changes in strain induced by ligand coordination. The statistical data derived from the PL maps clearly reveals that the OA treatment significantly improves the PL of the WS_2 monolayer.

In order to understand the exciton dynamics that underpin the PL enhancement with the OA treatment, we study the excitation intensity dependent PL of the monolayers. Due to experimental limitations, the excitation power was limited to low (0.018 W cm^{-2}- 0.3 W cm^{-2}) and high (110 W cm^{-2}- 5820 W cm^{-2}) regimes, making sure to remain below

9000 W cm^{-2} to avoid thermal damage.[168,25] We first comment on the spectral changes that occur in the samples in response to increasing excitation intensity as shown in Figure 4.2 *a-c*.

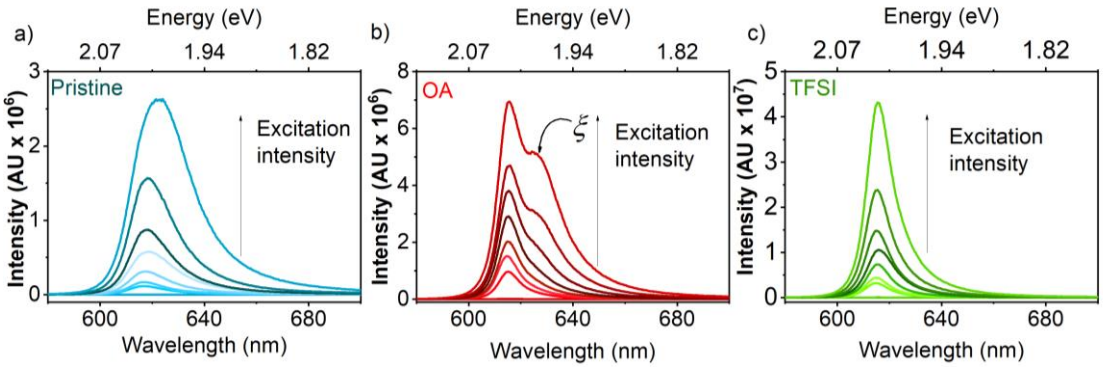

Figure 4.2: PL excitation intensity spectra. a-c) Raw PL spectra of pristine, OA and TFSI treated samples taken with 514nm CW laser.

Figure 4.2.*a* shows noticeable changes in spectral shape with increasing excitation intensity in the pristine monolayer. The spectra appear to broaden and red-shift. This spectral red-shift with increasing excitation intensity in pristine monolayers has been attributed to trion (X^-) formation, which occurs as a result of binding between excess charges in the conduction band from photoionized native *n*-dopants and neutral excitons (X).[59] With large binding energies of the order of 10s meV due to reduced screening in monolayers, these quasi-particles can be observed and studied at ambient conditions.[55] The perceived red-shift and spectral broadening as a function of excitation intensity is caused by the contributions of trions alongside excitons. The close overlap between the excitons and trions makes deconvoluting the pristine WS_2 PL spectra challenging, which prevents resolution of the relative contributions from excitons and trions.

Figure 4.2.*b* shows comparable data for the OA treated monolayer. In the high excitation intensity regime (10^2-10^4 W cm^{-2}), in addition to the neutral exciton peak (which does not shift in energy), a red-shifting peak, ζ, emerges. The well separated ζ feature enables spectral fitting with Gaussians and thus further characterisation of the feature, as shown in Figure 4.5 and subsequently discussed.

Figure 4.2.*c* shows the spectra for the TFSI treated sample, where the single narrow emission peak throughout the series indicates dominant neutral exciton recombination, which is consistent with what has been reported in *ref 20*.[20] We also note the narrower spectral linewidth in OA treated WS_2 on Si-SiO_2 shown in Figure 4.1.*b* compared with that on quartz (Figure 4.2.*b*) at similar excitation intensities. The

differences in spectral linewidth are potentially due to variations in strain and/or dielectric environment between the substrates. These factors may also contribute to spectral broadening,[87] which in this case appears to be more present on quartz. For clarity, the normalized spectra are shown below in Figure 4.3.

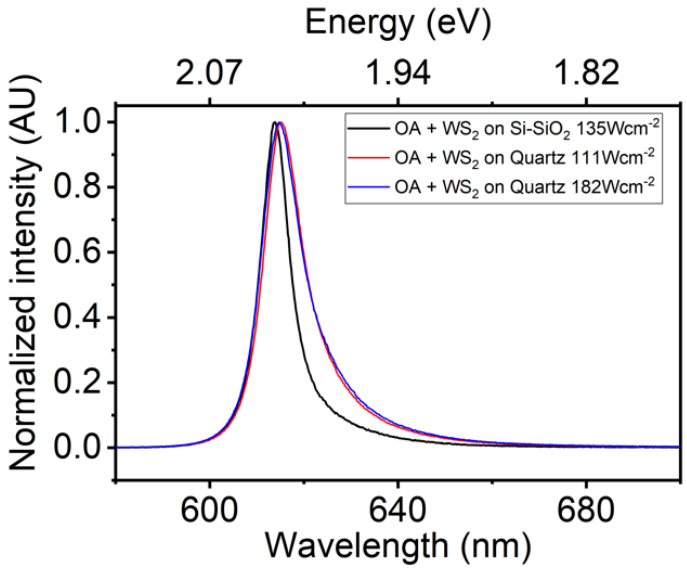

Figure 4.3: PL spectra of OA treated monolayers on Si-SiO2 and quartz. Spectra show broader spectral linewidth on quartz compared with Si-SiO_2 potentially due to differences in strain/ dielectric environments experienced by the monolayers.

Figure 4.4.*a-b* shows the steady state excitation intensity dependence series over four orders of magnitude derived from the spectra shown in Figure 4.2.*a-c*. Figure 4.4.*a* shows a log-log plot of the PL intensity dependence as a function of excitation intensity for each sample. We note that under low power excitation, the brightness of the OA treated sample is comparable to the TFSI treated sample. The gradients of the series in the two regions give insight to the recombination regimes present. The gradient values are the exponent to a power law fit given by $I = P^m$.[25] Figure 4.4.*b* shows the ratio of PL to excitation intensity (γ), which serves as a relative PLQE value.

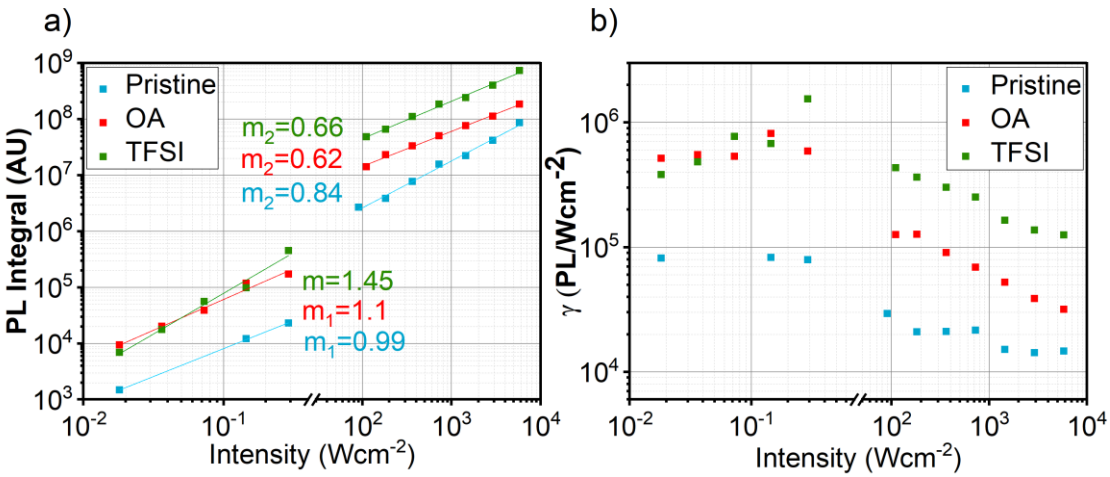

Figure 4.4: WS_2 PL excitation intensity series. **a)** Excitation series derived from PL integrals from *a-c* for pristine (blue), OA (red) and TFSI (green) treated monolayers; **b)** Ratio of PL integral to excitation intensity *i.e.*, relative PLQE (γ) variation with excitation intensity for pristine (blue), OA (red) and TFSI (green) treated monolayers.

At low intensities, the pristine sample shows near-linear behaviour (m_1=0.99) with respect to excitation intensity, as expected of band-edge to ground-state recombination, and little variation in its low γ ratios reflective of inherently low PLQE. At high intensities the trend become sub-linear (m_2 = 0.84). This suggests the presence of non-radiative exciton-exciton annihilation, however, given its low effective PLQE (*i.e.*, low γ), non-radiative defect assisted processes dominate exciton dynamics in both regimes.

When treated with OA, PL enhancement under low excitation intensity is comparable to the TFSI case, but with a power law exponent close to the pristine case (m_1 = 1.1). The γ ratio increases only slightly, indicating predominant radiative neutral exciton recombination directly from the band edge in the low intensity regime. At high laser intensities the power law diminishes more drastically than the pristine case (m_2 = 0.62).

Interestingly, the TFSI treated sample shows super-linear (m_1 = 1.45) behaviour and increasing γ ratio (*i.e.*, relative PLQE) at low intensity. This manifests itself as a dependence of the relative PLQE on excitation intensity, as seen in Figure 4.4.*b*. Goodman *et al.*'s [91] study on long-lived trapped excitons in defect states best explains this observed super-linear behaviour. At the low end of the low intensity regime, a proportion of excitons decay from traps to the ground state over a long period (~μs). These long-lived low energy transitions form part of the tail-end region of the PL spectra.[80] Available ambient thermal energy at room temperature statistically favours de-trapping for a

significant proportion of trapped excitons, which return to the band edge and recombine radiatively to the ground state. With increasing excitation density, traps become saturated causing any further excitations to radiatively recombine directly from the band edge. Hence, the super-linear behaviour and increasing γ ratio in the low intensity regime characterises the process of trap state filling prior to predominant radiative recombination where the effective PLQE (γ) saturates. The diminishing γ ratio in the high intensity regime signifies the onset of exciton-exciton annihilation.[20, 25]

To characterise the excitonic species that give rise to the additional low energy PL peak (ζ) in OA treated WS_2 PL shown in Figure 4.2.*b*, a two Gaussian model was used to fit the low energy species (ζ) and neutral exciton (X). Gaussian fits are shown in Figure 4.5. Figure 4.6.a shows the power laws of the low energy species (ζ) and neutral exciton (X). Both fits follow the same near-linear power laws with $m_{x1} = m_{\zeta 1} = 1.1$ in the low intensity regime. In the high intensity regime, two distinct sub-linear power laws arise with $m_{x2} = 0.36$ and $m_{\zeta 2} = 0.75$.

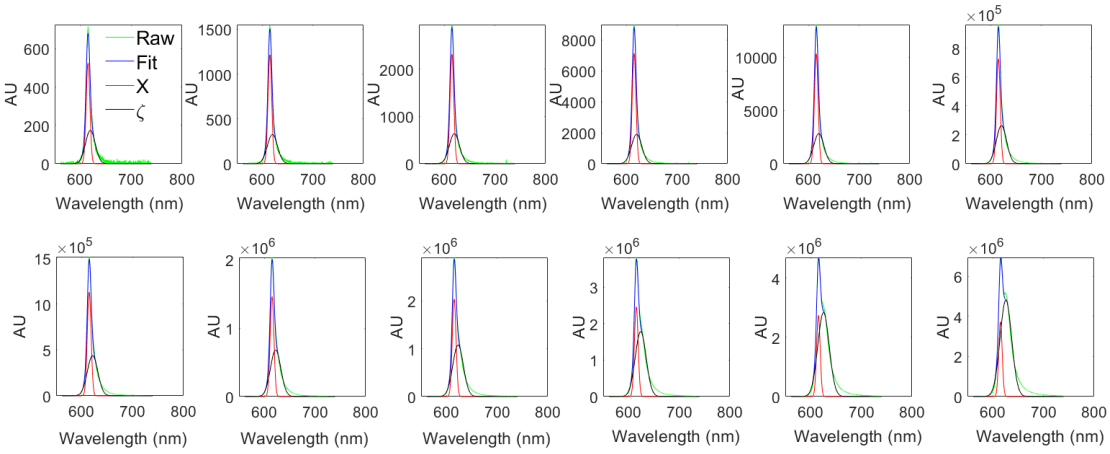

Figure 4.5: Two Gaussian model fits of low energy species (ζ) and neutral exciton (X) PL peaks in OA treated monolayer WS_2 PL spectra

In the low intensity regime, the identical power law indicates that contributions from both species to overall PL are close in magnitude as confirmed in figure 4.6.*d*. Figure 4.6.*b* also shows that their relative PLQE (γ) in this regime are close in magnitude. In addition, Figure 4.6.*c* shows little spectral movement of either contribution which is indicative of strong spectral overlap at low excitation intensities. The identical power laws, similar relative PLQE, spectral overlap and proportional PL contribution of the fits makes it difficult to confirm the presence of trions in the low intensity regime, which is reasonable as photoionization of native *n*-dopants is less likely at low excitation intensity

as shown in previous studies.[59] This implies the dominance of neutral exciton recombination at low excitation intensities.

In the high power regime however, where photoionization is more likely,[59,53] Figure 4.6.d shows an increase in *ζ/X* ratio , which is a notable characteristic of trion emission.[58] The power law and *γ* ratio (Figure 4.6.*a*-*b*) reveal more efficient evolution of *ζ* emission in this regime. A study by Paradisanos *et al.*[53] shows trion emission in monolayer WS_2 at high excitation intensity, with a power law of m=0.9, which is close to the value obtained for the *ζ* feature ($m_{\zeta 2}$ =0.75) in Figure 4.6.*a*.

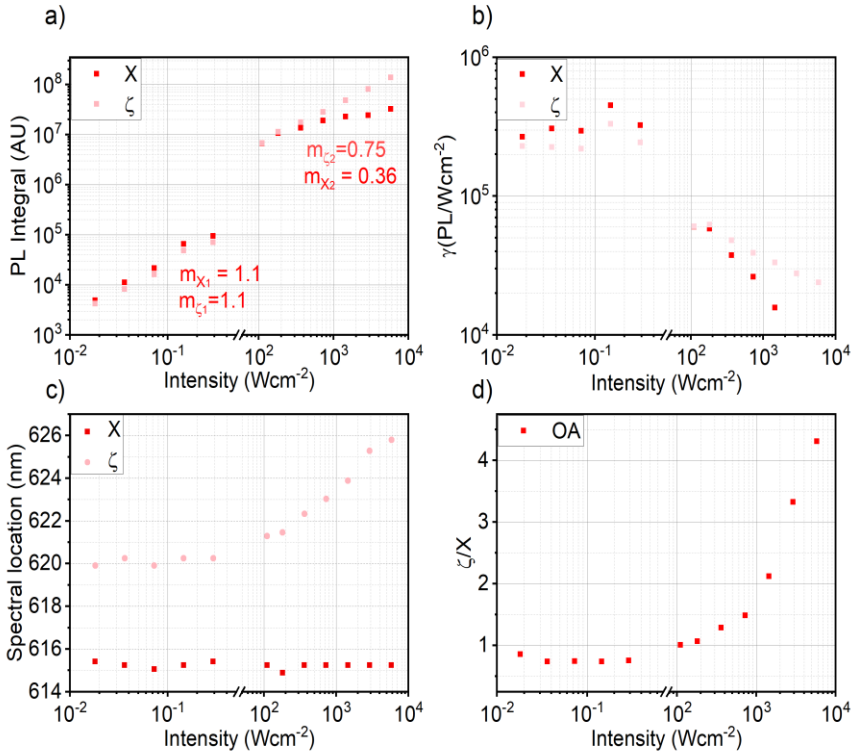

Figure 4.6: Trion emission characterisation. **a)** Excitation series derived from Gaussian fit integrals of neutral exciton (X) and *ζ* peaks from OA treated WS_2 PL spectra shown in Figure 4.5; **b)** Ratio of neutral exciton (X) and *ζ* Gaussian fit integrals to excitation intensity i.e. relative PLQE (*γ*) variation with excitation intensity; **c)** Spectral locations of neutral exciton (X) and *ζ* peaks as a function of excitation intensity; **d)** Ratio of *ζ* and neutral exciton (X) peaks fitted from OA sample PL spectra to show increasing *ζ* PL intensity to neutral exciton PL with increasing laser excitation intensity, indicating the presence of trions at high excitation intensities.

Identifying *ζ* as trion emission partly explains the drastic reduction in overall relative PLQE (*γ*) and neutral exciton relative PLQE seen in Figure 4.4.*b* and Figure 4.6.*b* respectively. Given the inherently lower PLQE of trions compared to neutral excitons,

the reduction in overall radiative recombination rate due in part to trion generation in the high excitation intensity regime is plausible. In effect, a combination of exciton-exciton annihilation, trion generation and any persisting defect related non-radiative decay mechanisms should account for the overall reduction in γ seen in the OA treated sample's PL excitation intensity series. The increased availability of photoionized carriers at high intensities increases the likelihood of a higher proportion of neutral excitons binding to these charges to form trions. The noticeable redshift of the ζ peak at high intensities shown in Figure 4.6.*c* is another characteristic of trion behaviour.[59] The subsequently observed *n*-type behaviour, improved current density and mobilities derived from OA treated FET measurements in section 4.6 indicate an increase in freely moving charges available to form trions. The combination of the factors discussed serve as sufficient evidence to identify the low energy feature ζ as trion emission.

4.4 Time Resolved Photoluminescence

To explore the photophysics of the treatment further we turn to time-resolved PL microscopy, which is described in the experimental methods (Chapter 3, section 3.3). Figure 4.7 shows normalized time resolved PL signals of untreated and treated samples at room temperature under low power excitation (0.67 W cm^{-2}). Bi-exponential decay fits best describe the decay dynamics observed, with a fast component τ_1 and a slow component τ_2. The time resolved data analysed in this section places emphasis on the fast component, τ_1, as this represents the decay time associated with direct radiative transitions from band-edge to ground state, while the slow component τ_2 is associated with the decay of trapped excitons from trap to ground state, which occurs over long periods (~μs).[91]

The fast decay (τ_1~64 ps) of the pristine sample indicates a pronounced onset of non-radiative recombination at early times, consistent with the intrinsically low PLQE. The OA and TFSI treated samples show signal growth beyond the instrument response function (IRF) region. While the exact nature of this growth in the PL signal is unclear, it might be related to trapping and detrapping dynamics at early times. The OA treatment gives rise to a 4× increase in lifetime for the fast decay component (τ_1~248 ps) versus the pristine sample, close to the TFSI-treated sample (τ_1~310 ps), which is expected by nature of the improved PLQE for these samples and suggests a suppression of the early time quenching observed in the pristine sample.

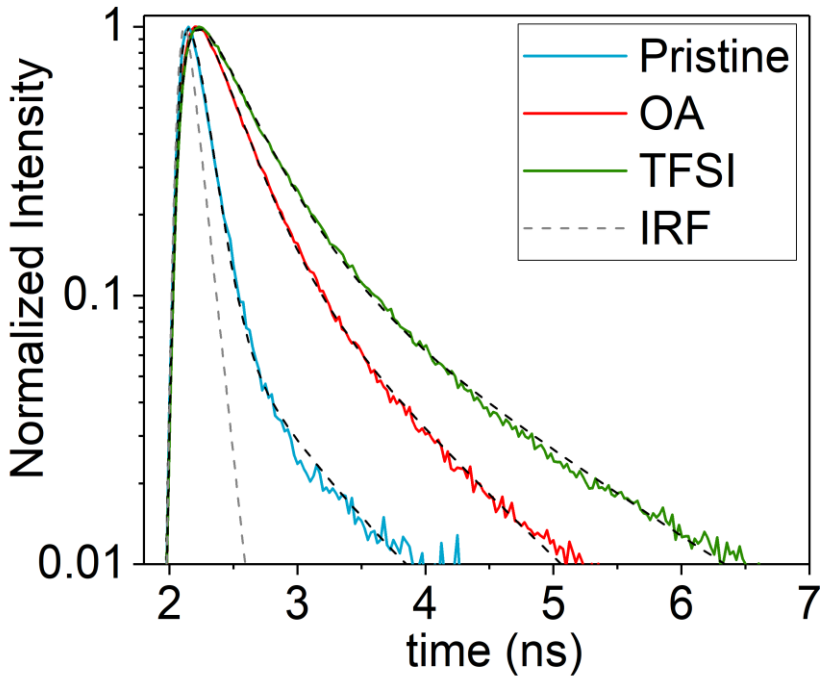

Figure 4.7:Transient PL spectra of chemically treated WS_2. Pristine (blue), OA (red) and TFSI (green) treated WS_2 TRPL signals with bi-exponential decay fits (black dashed lines), measured at 0.67 W cm^{-2} pump intensity with 405 nm excitation.

Figure 4.8.*a-c* overleaf shows time-resolved PL decay spectra at all fluences measured for each sample along with bi-exponential decay fits. Figure 4.8.*d* shows the absorption spectrum of monolayer WS_2 on quartz, which was used in combination with excitation intensities to compute initial carrier concentrations (n_0) for Figure 4.9.*a-b*.

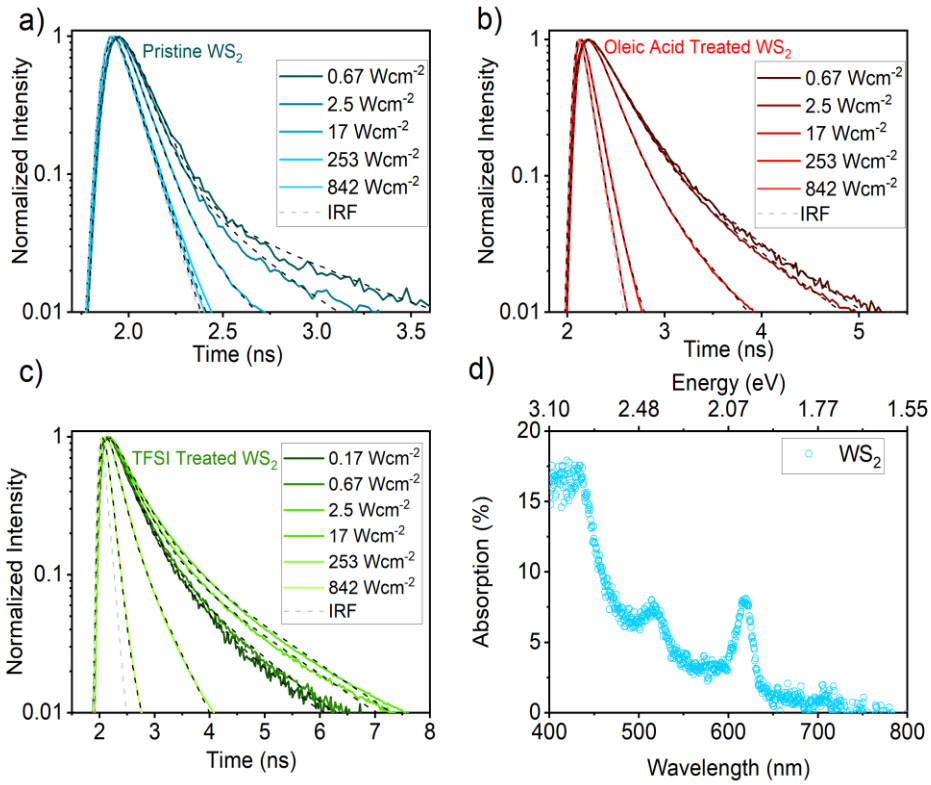

Figure 4.8:Transient PL series spectra of chemically treated WS_2 and WS_2 absorption spectrum. (a-c) Time resolved photoluminescence signals for pristine (blue), OA treated (red) and TFSI (green) treated samples with bi-exponential decay fits (black dashed lines); **d)** Absorption spectrum of pristine WS_2 as a function of wavelength (bottom axis) and photon energy (top axis).

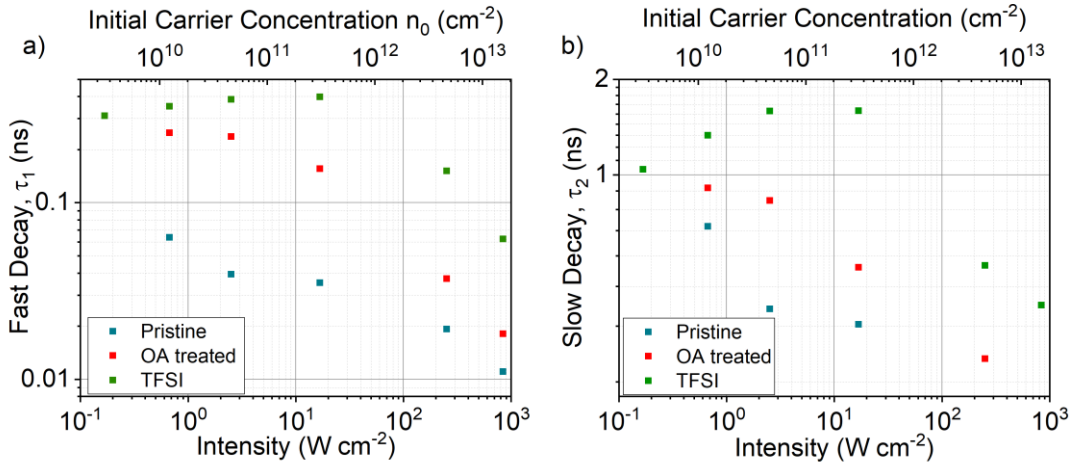

Figure 4.9:Transient PL series of chemically treated WS_2. Variation of fast decay component, τ_1 **(a)** and τ_2 **(b)**, with initial carrier concentration derived from absorption data in figure 4.8.*d* at pump wavelength (405nm) and pump intensities (Wcm^{-2}).

Figure 4.9.*a*-*b* shows the variation in the fast (τ_1) and slow (τ_2) decay component as a function of initial carrier concentration (n_0). Time constants were taken from decay fits shown in Figure 4.8.*a*-*c*. As shown in Figure 4.8.*a*-*b*, at the maximum intensity (842 W cm^{-2}), the OA treated and pristine decay signal fit a single exponential decay, while the TFSI signals follow the bi-exponential model throughout the series. The extremely fast initial decay times (~10s of picoseconds) in the pristine samples even at the low end of the initial carrier concentration range implies the presence of a strong quenching channel. Further reduction in τ_1 as a function of n_0 confirms the presence of exciton-exciton annihilation.

The continuous reduction in τ_1 as a function of n_0 in the OA treated sample implies non-trap limited movement of excitons that are able to annihilate even at low carrier concentrations. At higher excitation intensities the formation of low PLQE trions, as seen in Figure 4.2.*b*, will contribute to the sharp reduction in τ_1. The TFSI treated sample's gradual increase in τ_1 at lower initial carrier concentrations agrees with the increase in relative PLQE (γ) in the low intensity (steady state) excitation regime shown in Figure 4.4.*a*. At low excitation densities a proportion of trap states are filled, and any further transition from the band edge to those states is forbidden, which promotes direct recombination from the band edge with τ_1. As carrier concentrations increase, trap states are filled giving rise to dominant radiative recombination from the band edge as indicated by the saturated τ_1 value. The reduction in τ_1 at high carrier concentrations signals the onset of exciton-exciton annihilation.[25] The trapped exciton decay, τ_2, shown in Figure 4.9.*b* shows a similar trend.

To summarise the photophysical measurements presented so far, the OA treatment is found to greatly increase the PL of monolayer WS_2, with average increases higher than TSFI treatment. At higher excitation intensities a pronounced trion peak emerges, which is not found in TFSI treated samples. Both steady-state and time-resolved measurements indicate that the OA treatment leads to trap-free excitonic behaviour in contrast to TFSI treatment where trap limited behaviour is observed, consistent with previous reports. This suggests that the mechanism of PL enhancement for the OA and TFSI are quite different.

4.5 Discussion on Surface Chemistry

Various studies identify chalcogen point defects, which manifest themselves as sub-gap states through which non-radiative emission occurs, as the prime cause of poor quantum yields in pristine TMD monolayers.[72,169] Chalcogen point defect passivation *via* surface treatment is often used as the basis to explain the observed PL improvements with TFSI treatment. While the exact mechanism of such treatment is unclear,[20,165,84] it has been suggested that TFSI being a `super acid' (pKa = -12.3) protonates the native *n*-doped monolayer surface, removing excess dopants or charges occupying existing trap/defect states.[20] The freeing up of defect sites gives rise to the trap limited exciton dynamics, as has been discussed by Goodman *et al*.[91] Atallah *et al*.[170] however proposed that electrons in the *n*-type TMD material reduce protons (H^+) to hydrogen (H_2), leaving the TFSI counter-ion ($[(CF_3SO_2)_2N]^-$) to passivate the positively charged defect sites. The observation of excitons decaying to the trap states by Goodman *et al.*,[91] is however, at odds with the notion of passivation of point defects by the TFSI counter-ion, as true passivation would block the movement of excitons to trap states and thus promote direct band-edge recombination. In contrast, as we have shown in Figures 4.4 and 4.9, the OA treatment leads to non-trap limited exciton dynamics, while also giving high PL yield. This suggests that the OA is passivating defect sites.

OA is a weak acid, and unlike TFSI, cannot effectively protonate the monolayer TMD surface and reduce *n*-doping (this is confirmed by the transistor measurements described in Section 4.6). The electron-rich carboxylic acid moiety is a good coordinating group and OA is commonly used as ligands in stabilizing colloidal quantum dots, providing steric and electronic passivation of surface defects *e.g.* dangling bonds caused by sulphur vacancies on lead sulphide (PbS) quantum dots.[171,172,173] It is therefore reasonable to speculate that the observed improvements in emission could be due to similar passivation, where the carboxylate group behaves as a Lewis base, coordinating to the electrophilic metal (W) atom at the S vacancy forming a dative covalent bond as illustrated in Figure 4.10. The W atoms in WS_2 possess an unfilled *d*-orbital, due to the energetic gap between the 6*s* and 5*d* orbitals. The empty *d* orbital does not contribute to covalent bonding and the band structure within monolayer WS_2. The empty orbital provides a binding site for OA as a ligand. At vacancy sites, the ligand attachment increases localised electron density and provides mitigation for the non-radiative loss channels at defect sites which are normally electron deficient. This increased electron

density at these sites may contribute towards the observed additional trion formation at higher excitation intensities. In addition, binding of oleic acid to the monolayer surface provides a hydrophobic long alkyl chain providing a steric and dielectric barrier towards other mechanisms of non-radiative loss mechanisms such as interactions with adsorbates including oxygen and water.

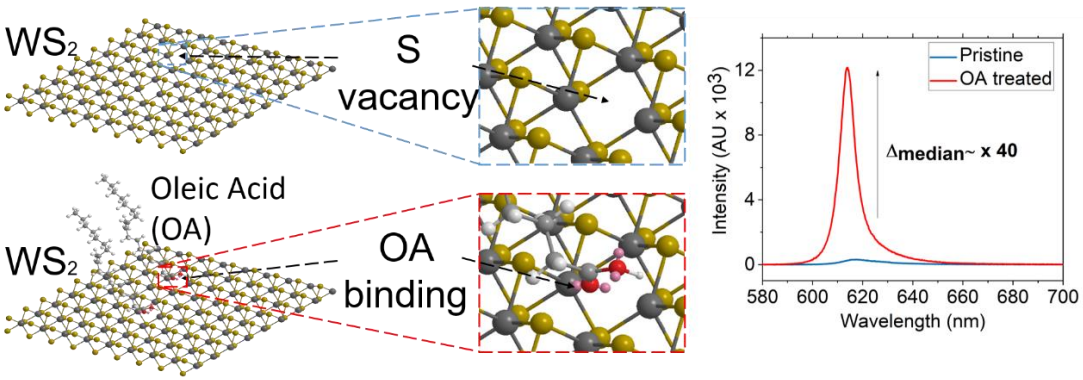

Figure 4.10: Illustration of S vacancy passivation by OA coordination. OA ligand coordinating to tungsten (W) atom at chalcogen vacancy in WS_2 monolayer (LHS) and resulting PL enhancement (RHS).

4.6 Structural and Electronic Characterisation

Lastly, we explore what impact the OA treatment has on charge transport and structural characteristics in WS_2. Figure 4.11.*a* shows the Raman spectra of a WS_2 monolayer channel in an exemplary transistor before and after OA treatment. The conservation of characteristic E^1_{2g} (355 cm^{-1}) and A_{1g} (417 cm^{-1}) vibrational peak positions confirms no discernible structural changes due to treatment. Figure 4.11.*b*-*c* show the transfer characteristics of the same monolayer WS_2 field effect transistor (FET) before and after OA treatment.

After OA treatment the *on*-state current, measured at back gate voltage V_G = 25 V, consistently improves for all of the devices studied (6 devices in total) from an average of 11 nA before to 290 nA after (Figure 4.11.*b*, inset). The device maintains *n*-type behaviour. This confirms that the OA does not significantly dope the monolayer, as is the case for TFSI [75]. The field effect mobility improves from $5x10^{-4}$ cm^2/Vs to $1x10^{-2}$ cm^2/Vs, a factor of 20, after OA treatment. The absolute values of field effect mobility

are likely limited by contact resistance and could be further improved using recent developments in contact engineering such as van der Waals contacts.[174]

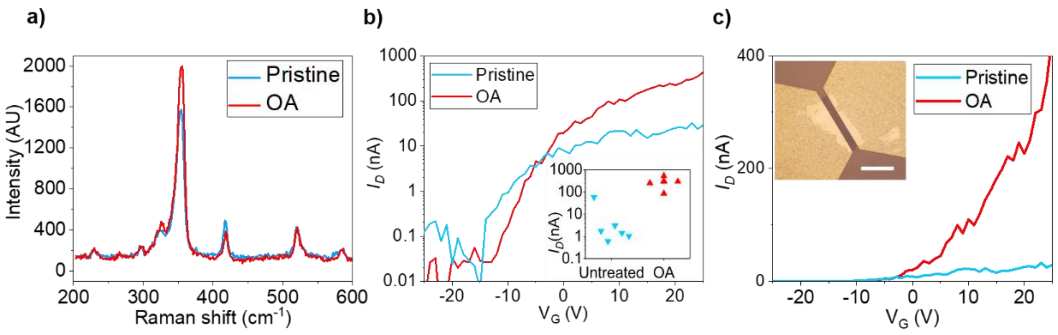

Figure 4.11: Structural and electronic characterisation of OA treated WS_2 FETs. a) Raman spectra of a WS_2 transistor before and after OA treatment; **b-c)** Transfer characteristics of a WS_2 transistor measured on the same flake before and after OA treatment at V_{DS}=10V. The arrows indicate the gate voltage sweep direction. Inset (b): On state current I_D at back gate voltage V_G=25V for 6 devices before (red) and after (blue) OA treatment. Inset (c) Image of transistor structure with scale bar measuring 20 μm.

The subthreshold swing decreases from 16 V/dec to 8 V/dec (Figure 4.11.b), indicating a reduction in the interface charge trap density in the presence of ligands, which supports the notion of ligands passivating traps. The increase in drain current may also be due to an injection of charges from the electron rich coordinating ligand carboxylate group to the conduction band of the electron deficient metal species at a vacancy. The transfer characteristics confirm that at V_G = 0 V there are mobile electrons available in the conduction band to form trions with excitons under high intensity photoexcitation as previously described. It should be noted that the contact regions did not need protection during oleic acid treatment and all of the devices studied showed similar behaviour (Figure 4.11.*b*, inset). By contrast, TFSI is known to etch several common contact metals and protective layers were required to prevent deterioration of the contact region during treatment in previous studies.[20] When using TFSI without a protective layer a very low yield of working devices is obtained. For the single measurable device, a shift from *n*-type to *p*-type field effect behaviour is observed as shown in Figure 4.12, with an initial FET electron mobility of $5x10^{-3}$ cm^2/Vs switching to 2 $x10^{-3}$ cm^2/Vs FET hole mobility once treated. This change in transport behaviour is consistent with Lien *et al.'s* observation of hole-doping by TFSI on TMD FETs with palladium (Pd) contacts.[75] Importantly however, the results show that it is possible to dramatically improve the PL of monolayer WS_2 while improving mobility and reducing charge trapping without additional device fabrication steps using OA.

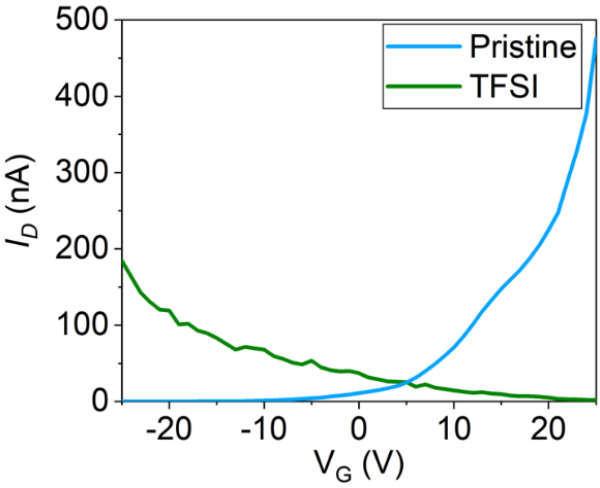

Figure 4.12: Electronic characterisation of TFSI treated WS2 FET. Transfer characteristics of a WS_2 transistor before (blue) and after (green) TFSI treatment, showing a transition from intrinsic *n*-type transport characteristics to *p*-type characteristics.

4.7 Conclusions

In conclusion, we have demonstrated the ability to significantly increase PL in monolayer WS_2 *via* surface treatment with OA ligands. Statistical analysis shows that OA treatment improves spectral uniformity as compared to untreated and TFSI treated samples. Steady state excitation intensity and time resolved pump intensity studies reveal trap free exciton dynamics, unlike the trap limited dynamics observed in TFSI treated samples, [91] which is taken as an indication of defect passivation by the ligands. In support of this hypothesis, electrical transport characteristics of OA treated WS_2 transistors show an increase in field effect mobilities, reduced charge trap density and no detectable additional doping upon treatment with OA. At increased excitation densities we observe bright trion emission, which is not observed with TFSI treatment. These bright trions may be of interest for future spintronics and quantum information applications. Although future experimental and theoretical work are required to elucidate the exact chemical changes that accompany OA treatment, we hypothesise that the carboxylate group forms a dative covalent bond with the electrophilic metal atom (W) at a chalcogen vacancy, similar to the passivation of PbS quantum dots with OA. This trap state passivation by the ligand forbids non-radiative trap-assisted exciton decay, promoting direct radiative band edge recombination. Our results open up a new pathway to passivate and tune

defects in monolayer TMDs using simple `wet' chemistry techniques, allowing for trap free electronic properties and bright neutral exciton and trion emission.

4.8 Methods

4.8.1 'Super-acid' Bis(trifluoromethane)sulfonimide (TFSI) Preparation

Following the method described by Amani *et al*. [20], 2 mg/ml of acid was prepared in a nitrogen glovebox by dissolving 20 mg of TFSI crystals in 10 mL 1,2-dicholoroethane (DCE). Further dilution produced a 0.2 mg/mL solution of acid.

4.8.2 Steady State Photoluminescence Microscopy

All samples were characterised *via* steady state PL to confirm monolayer identity. PL spectroscopy was performed using the Renishaw Invia confocal setup described in chapter 3, section 3.3.1. A 50× objective (NA = 0.75) was used. The diffraction limited beam spot size was estimated as 0.84 μm. PL signals were collected in reflection *via* notch filter and dispersed with a 600 l/mm grating prior to detection. Laser power to the sample was measured directly under a 5× objective with a Thorlabs S130C photodiode connected to a PM100D optical power meter.

PL maps were generated from multiple WS_2 monolayers before and after respective chemical treatments. For the OA treated sample, 5 monolayers on a single substrate were mapped prior to treatment. Following treatment two out of five were delaminated, most likely due to surface tension effects exerted by OA. The remaining 3 treated monolayers were measured for PL and compared to their untreated cases. For TFSI, 5 untreated monolayers on a single substrate were mapped and remained intact following treatment. Maps were generated with 0.5 μm resolution and 0.5 s integration time at 0.75 μW with cosmic ray correction engaged *via* the microscope's WIRE software.

Excitation intensity dependent PL measurements were performed on the WS_2 monolayers deposited on quartz. Care was taken to measure PL in the same locations prior to and following treatment. The spatial *x*, *y* and *z* position of the measurement site and photodiode were recorded to accurately switch between photodiode and monolayer location for each measurement using the WIRE software piezo stage control interface. PL

signals were scaled up to 500 s integration time, which was used on the lowest excitation intensity measurement. Dark counts were measured for each integration time and subtracted from raw PL data.

Trion and neutral exciton emission were deconvoluted from OA treated WS_2 PL signals with dark counts subtracted using a procedure written in Matlab, which incorporates the `gauss2' two Gaussian model fit. Further information on the Gaussian model is available on the mathsworks website.

4.8.3 Steady State Confocal Absorption Microscopy

The absorption spectra of monolayer WS_2 on quartz were measured with a Zeiss axiovert inverted microscope described in chapter 3, section 3.3.3. Measurements were made in transmission mode using a halogen white light source *via* a Zeiss EC Epiplan Apochromat 50x objective (numerical aperture (*NA*) = 0.95) forming a collection area diameter measured at 10μm, with the field of view and aperture fully opened. Light transmitted *via* the sample was split *via* beam splitter, with one component directed to a CCD camera (DCC3240C, Thorlabs) and the other coupled to a UV600 nm optical fibre (200-800 nm spectral range) connected to a spectrometer (Avaspec-HS2048, Avantes).

4.8.4 Time Resolved Photoluminescence Microscopy

Time resolved PL measurements were performed on the samples on quartz before and after treatment. A PicoQuant Microtime 200 confocal time correlated single photon counting (TCSPC) microscope setup was used. Excitation was provided from a 405 nm pulsed laser *via* 20× objective (NA = 0.4), with estimated diffraction limited spot size of ~1.23 μm. All TRPL data was obtained with 20 MHz repetition rate and 25 ps resolution. PL signals were integrated for 300 s and collected in transmission. PL was detected with a photomultiplier tube (PMT). The instrument response function (IRF) was measured with a blank quartz substrate. Power was measured using an inbuilt photodetector at each intensity and read *via* the microscope's software interface. Care was taken to ensure that excitation was performed in the same spot on the monolayers prior to and following treatment. PL decay data were fitted with the aid of an openly available Matlab based deconvolution procedure, *fluofit* devised by Jorg Enderlein.[175]

4.8.5 Transistor Preparation and Characterisation

As-exfoliated isolated WS_2 flakes on doped Si (used as global back gate) covered with 90 nm of thermally grown SiO_2 were identified through optical microscopy and PL spectroscopy. Electrical contacts were defined by electron beam lithography followed by thermal evaporation of indium/gold (In/Au) (10 nm/80 nm). Transfer characteristics were measured with a source drain bias of V_{DS}=10 V using a Keithley 4200-SCS parameter analyser and probe station under dark ambient conditions.

4.8.6 FET Raman Characterisation

Field effect transistors (FETs) were characterised *via* Raman spectroscopy with the Renishaw Invia confocal setup described in section 3.3.1, at 0.7 μW with 50× objective. The Raman signal was collected in reflection *via* notch filter and dispersed *via* 2400 l/mm grating prior to detection.

5 Giant Photoluminescence Enhancement in $MoSe_2$ Monolayers treated with Oleic Acid

The inherently low photoluminescence (PL) yields in as prepared transition metal dichalcogenide (TMD) monolayers are broadly accepted to be the result of atomic vacancies (*i.e.*, defects) and uncontrolled doping, which give rise to non-radiative exciton decay pathways. While a number of chemical passivation schemes have been successfully developed to improve PL in sulphur based TMDs *i.e.*, molybdenum disulphide (MoS_2) and tungsten disulphide (WS_2) monolayers, solution based chemical passivation schemes for improving PL yields in selenium (Se) based TMDs are lacking in comparison, with only one known study that uses hydrobromic acid (HBr) vapour to improve PL yields in chemical vapour deposited (CVD) molybdenum diselenide ($MoSe_2$). In this chapter, we demonstrate that treatment with oleic acid (OA) provides a simple wet chemical passivation method for selenium based TMDs, particularly monolayer $MoSe_2$, enhancing PL yield by an average of 58-fold, while also enhancing spectral uniformity across the material and reducing emission linewidth. Excitation intensity dependent PL reveals trap-free PL dynamics dominated by neutral exciton recombination. Time-resolved PL (TRPL) studies reveal significantly increased PL lifetimes, with pump intensity dependent TRPL measurements also confirming trap free PL dynamics in OA treated $MoSe_2$. Field effect transistors show reduced charge trap density and improved on-off ratios after treatment with OA. These results indicate defect passivation by OA, which we hypothesise act as ligands, passivating chalcogen defects through oleate coordination to molybdenum (Mo) dangling bonds.

The work detailed in this chapter is adapted from an article published in RSC Nanoscale Advances: Tanoh, A. O. A.; Alexander-Webber, J.; Fan, Y.; Gauriot, N.; Xiao, J.; Pandya, R.; Li, Z.; Hofmann, S.; Rao, A. Giant Photoluminescence Enhancement in $MoSe_2$ Monolayers treated with Oleic Acid. *Nanoscale Adv.* **2021**, Advance Article. https://doi.org/10.1039/D0NA01014F.**[28]**[28]

All the work in this chapter was performed by the author except where stated. Dr. Alexander Webber and Dr. Fan prepared $MoSe_2$ transistors, measured their respective electronic characteristics and provided an analysis of the resulting data (Section 5.6); N. Gauriot built the time resolved photoluminescence (TRPL) setup; Dr. James Xiao contributed to the discussion on the surface chemistry that gives rise to observed improvements in optical and electronic properties in $MoSe_2$ monolayers when treated with OA (Section 5.5, paragraph 2).

5.1 Background and Motivation

In spite of the range of chemical treatments for sulphur based TMDs as discussed and demonstrated in the previous chapter, there has been little success in developing treatments for selenium based TMDs *i.e.,* molybdenum diselenide ($MoSe_2$) and tungsten diselenide (WSe_2).[25] For instance, TFSI is also known to quench PL in both these materials instead of enhancing it.[25] Han *et al.*[92] however achieved 30-fold enhancement of defect rich CVD $MoSe_2$ PL at room temperature *via* exposure to hydrobromic acid (HBr) vapour. The authors attributed this outcome to *p*-doping by the HBr combined with structural repair of chalcogen vacancies. Structural repair was reported to occur *via* the replacement of oxygen substitutions by bromine (Br) ions at selenium (Se) vacancies which acts to suppress trapped exciton states, thus eliminating non-radiative pathways. Recently, high PLQE in as-prepared CVD WSe_2 has been demonstrated *via* solvent evaporation-mediated decoupling (SEMD),[176] whereby the solvent evaporation process assists in the separation of as-grown synthetic monolayers from the underlying substrate. This serves as alternative to polymer assisted transfer methods, which involve the use of harsh chemicals *e.g.*, hydrofluoric acid (HF). The drastic improvement in optical quality

compared to standard CVD monolayer transfer techniques is considered to be related to overcoming substrate induced mechanical strain, which can introduce band structure modifications that reduce PL.[176,177] These methods however, do not provide the ease of processing that simple solution based chemical approaches do and rely on specific growth conditions, restricting their general purpose application.

Here, we extend oleic acid (OA) treatment to $MoSe_2$ monolayers. We demonstrate that OA treatment of $MoSe_2$ greatly enhances neutral exciton PL, yielding trap-free PL dynamics. In addition, OA treated $MoSe_2$ monolayer field effect transistors (FETs) exhibit marked improvement in transfer characteristics. The reduced subthreshold swing (SS) indicates reduced charge trap density and hence improved current on/off ratios. These results highlight the versatility of OA treatment and provides a simple solution based chemical passivation protocol for selenide based TMDs.

5.2 Sample Preparation

$MoSe_2$ Monolayers were exfoliated from their bulk crystal *via* the gold assisted exfoliation technique [140] described in chapter 3 (section 3.1) onto silicon-silicon dioxide (Si-SiO_2) with 90 nm oxide layer and thin (170 µm) glass slides. Monolayers on Si-SiO_2 were used for PL maps and electronic characterisation, while those on glass were used for excitation dependent PL studies, time-resolved PL (TRPL) measurements and Raman microscopy. All measurements were performed at room temperature. After initial optical and electronic characterisation of untreated (*i.e.*, `pristine') monolayers, samples were chemically treated. Samples were coated with OA *via* drop-casting in a nitrogen (N_2) glovebox and left for ~12 hours on a hot plate set at 25 °C. After OA treatment, samples were rinsed with anhydrous toluene and dried with a N_2 gun before further optical and electronic characterisation.

5.3 Steady State Photoluminescence

Figure 5.1.*a* shows the scatter plot of spectral peak position and corresponding PL emission integrals extracted from PL maps of multiple $MoSe_2$ monolayers on Si-SiO_2 substrates before and after OA treatment. Maps were measured at 126 W cm^{-2}. Figure 5.1.*b* shows the PL spectra for points on an exemplary monolayer that correspond to the

median PL enhancement, Δ_{median}, where $\Delta = PL_{\ after\ treatment} / PL_{\ before\ treatment}$. Table 5.1 shows statistical information derived from figure 5.1.*a*, namely: average PL enhancement across the monolayers (Δ_{ave}); standard deviation in PL integral (σ_{PL}); average emission peak wavelength (λ_{ave}); and standard deviation in peak wavelength (σ_{λ}). The untreated case is indicated by (*).

Table 5.1: $MoSe_2$ monolayer PL enhancement statistics derived from PL maps. Characteristics prior to treatment marked with (*).

Δ_{ave}	σ_{PL}	λ_{ave}	σ_{λ}
58	56%*→ 29%	794 nm*→787 nm	3.31 nm*→1.02 nm

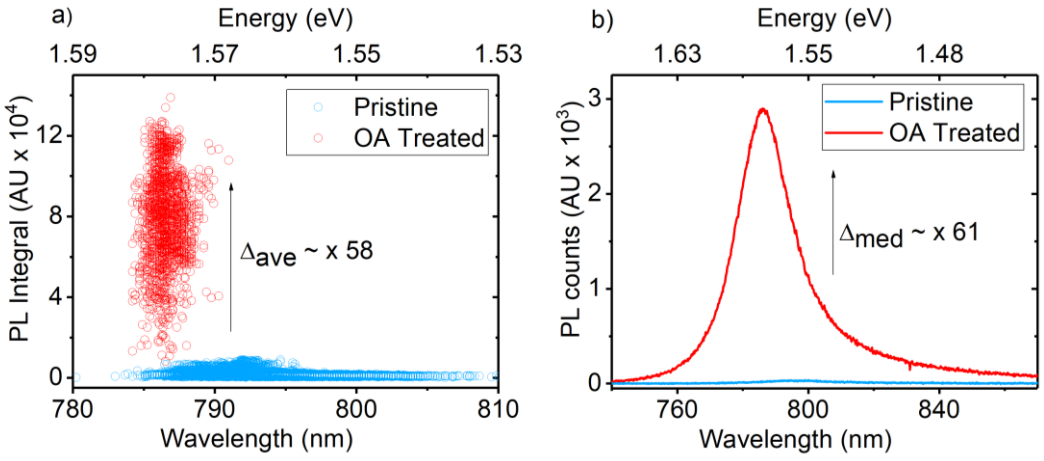

Figure 5.1: $MoSe_2$ PL enhancement statistics. a) PL enhancement scatter plot showing untreated monolayer PL integrals (blue) and OA treated monolayer PL integrals (red); **b)** Raw PL spectra for points that represent the median PL integrals before (blue) and after OA treatment (red) on an exemplary monolayer

An average PL enhancement of 58-fold is observed upon OA treatment. The standard deviation in PL intensity decreases from 56% to 29%. This demonstrates that OA treatment improves overall PL emission and spatial homogeneity in brightness. Spectral linewidth narrowing is also observed with an average blue shift λ_{ave} of 7 nm with improved spectral uniformity given by a 69% reduction in σ_{λ} from the untreated to the treated case. The median PL enhancement was calculated as Δ_{median} ~ 61-fold.

Figure 5.2. shows the normalized median spectra (circles) from Figure 5.1.b, with single Gaussian peaks (solid lines) fitted to estimate the change in spectral linewidth

between untreated (blue) and treated (red) cases. The spectra show a blue shift in spectral peak of 12 nm (798 nm → 786 nm) and reduction in full width half maximum (FWHM) of 5.5 nm (27.2 nm → 21.7 nm) from the untreated to treated case. As previously observed in OA treated WS_2,[27] the spectral blue-shift and line-width narrowing of $MoSe_2$ PL may be attributed to changes in strain induced by ligand coordination. These results however establish of the efficacy of the OA treatment to enhance the PL properties of $MoSe_2$.

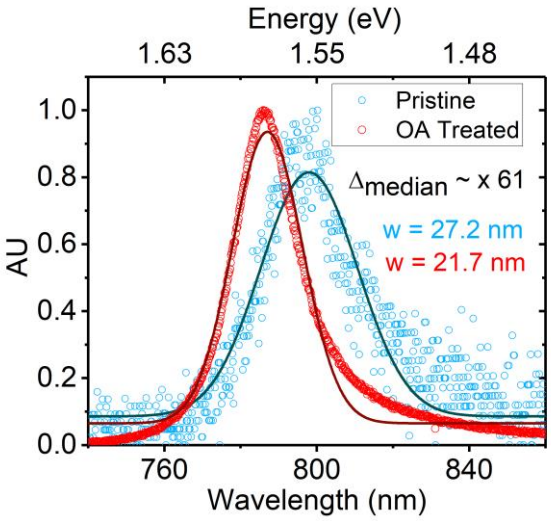

Figure 5.2: Comparing FWHM of pristine OA treated $MoSe_2$ PL spectra. Normalized median spectra (circles) from Figure 5.1.*b*, with single Gaussian peaks (solid lines) fitted to estimate the change in FWHM from untreated (blue) to OA treated (red) case.

To probe the exciton dynamics that accompany the PL enhancement, we first look at the excitation intensity dependent room temperature PL of a monolayer before and after OA treatment. Figures 5.3-5.4 show the results derived from a room temperature steady state excitation intensity dependent PL series over five orders of magnitude. Intensities range between 0.018 W cm^{-2} and 909 W cm^{-2}, staying well below 9000 W cm^{-2} to avoid thermal damage.[20] We first look for any spectral changes that may occur as a result of increasing excitation intensity. Figure 5.3.a shows no noticeable changes in spectral properties in the untreated monolayer under increasing excitation intensity. When treated with OA, Figure 5.3.b shows overall spectral narrowing compared to the untreated case, however no additional spectral components are observed, unlike the case of OA treated WS_2, which shows strong trion contribution at high excitation intensities.[27]

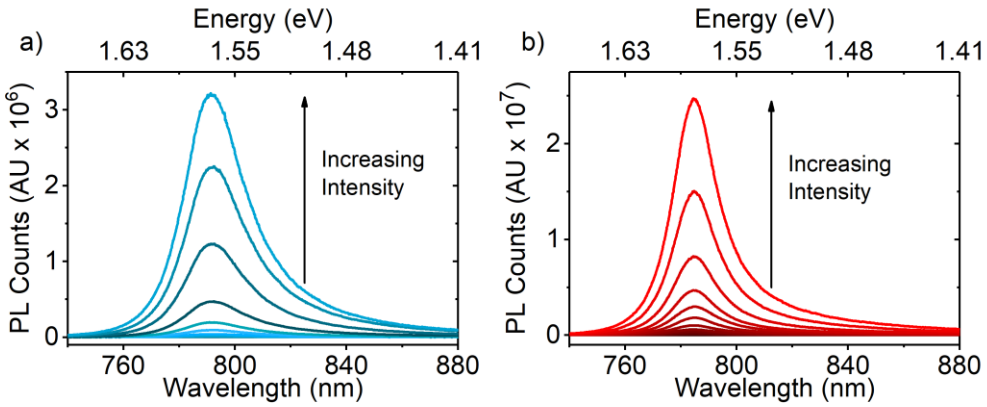

Figure 5.3: $MoSe_2$ PL excitation intensity spectra. a) untreated and**; b)** OA treated MoSe2

Figure 5.4.*a* shows a log-log plot of PL integral as a function of excitation intensity for untreated (blue) and treated (red) samples, derived from the spectra in Figure 5.3. The gradients (*m*) of the series represent the exponent to the power law fit, $I = P^m$.[25] As such the *m* values indicate the exciton recombination regimes observed. Figure 5.4.b. shows the ratio of PL to excitation intensity (γ), which serves as a relative PLQE value.

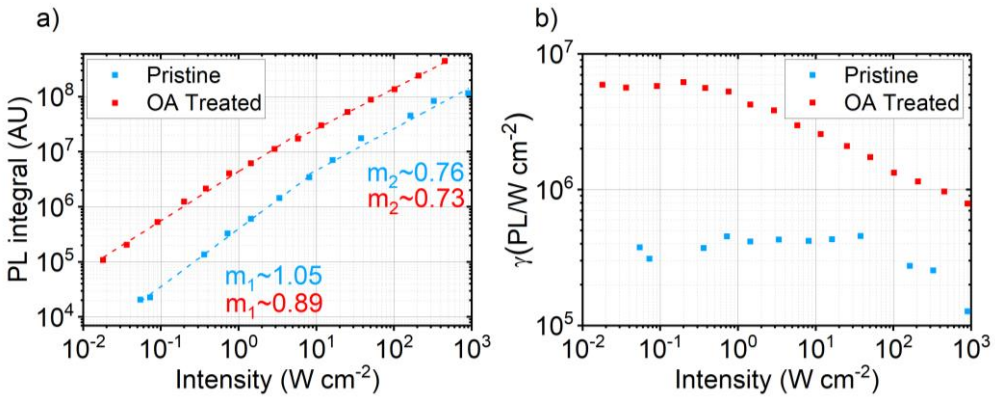

Figure 5.4: $MoSe_2$ PL excitation intensity series. a) PL excitation intensity series for untreated (blue) and OA treated (red) monolayers; **b)** Ratio of PL integral to excitation intensity *i.e.*, relative PLQE (γ) as a function of excitation intensity for untreated (blue) and OA treated (red) monolayers.

At low intensities, the untreated sample shows slight super-linear behaviour (m_1 ~ 1.05), which is indicative of some degree of exciton trapping[27] between 0.06 W cm^{-2} and 0.8 W cm^{-2}. This suggests a lack of non-radiative exciton-exciton annihilation, as given by the little variation γ ratio values between 1 W cm^{-2} and 10 W cm^{-2}, albeit with low PLQE. Beyond 10 W cm^{-2}, the trend becomes sublinear (m_2 ~ 0.76), indicating the onset of non-radiative exciton-exciton annihilation.[20,21,25,75] However, non-radiative trap

assisted recombination processes dominate throughout the series, given the low PLQE of untreated TMD monolayers.[20,21,23–25,27,66,75,84,89]

When treated with OA, the emission follows a sub-linear power law exponent of $m_1 \sim 0.89$ even at lower intensities, signifying the immediate onset of non-radiative exciton-exciton annihilation and becomes more drastic at higher excitation intensities where $m_2 \sim 0.73$. These trends are reflected in the γ ratio which shows a general gradual reduction between 0.02 W cm^{-2} and 0.76 W cm^{-2} before sharply decreasing thereafter due to intensified exciton-exciton annihilation. The immediate onset of exciton-exciton annihilation seen in the OA treated sample is consistent with trap-free exciton diffusion, similar to what has been observed with OA treated WS_2.[27] The increase in relative PLQE, γ, by an average factor of ~17 between 0.02 and 0.1 W cm^{-2} also confirms significant reduction in non-radiative recombination *via* trap states.

We attempt to characterise the exciton species that contribute to PL of OA treated $MoSe_2$. Figure 5.5 *a-c* shows the results obtained from deconvoluting each PL spectrum in the OA treated $MoSe_2$ excitation intensity series (Figure 5.3.*b*). As per previous studies[27,53,59] Gaussian fits were used to identify the emissive excitonic species in the spectra. All fits are shown in Figure 5.5. Figure 5.6.a shows the raw PL spectrum (red) taken in the high intensity regime (455 W cm^{-2}), where trion emission has been observed in OA treated WS_2 monolayers.[27] The dashed maroon and pink Gaussian fits represent the neutral exciton (X) and a low energy species (ζ) respectively. Figure 5.6.*b* shows the excitation intensity series of X and ζ. It is clear that assigned neutral exciton (X) and lower energy species (ζ) obey the same recombination dynamics, with the same power law exponents (m) seen in Figure 5.4.*a*. Figure 5.6.*c* shows the ratio of ζ to X as a function of excitation intensity, which remains fairly constant and < 1 throughout the series.

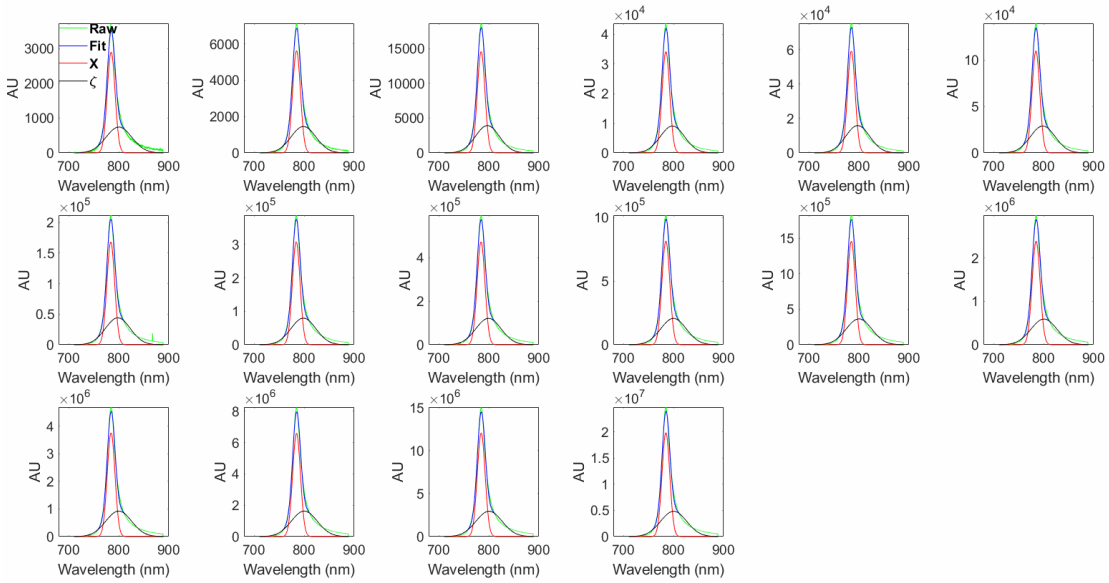

Figure 5.5: Two Gaussian model fits of low energy species (ζ) and neutral exciton (X) PL peaks in OA treated monolayer $MoSe_2$ PL spectra

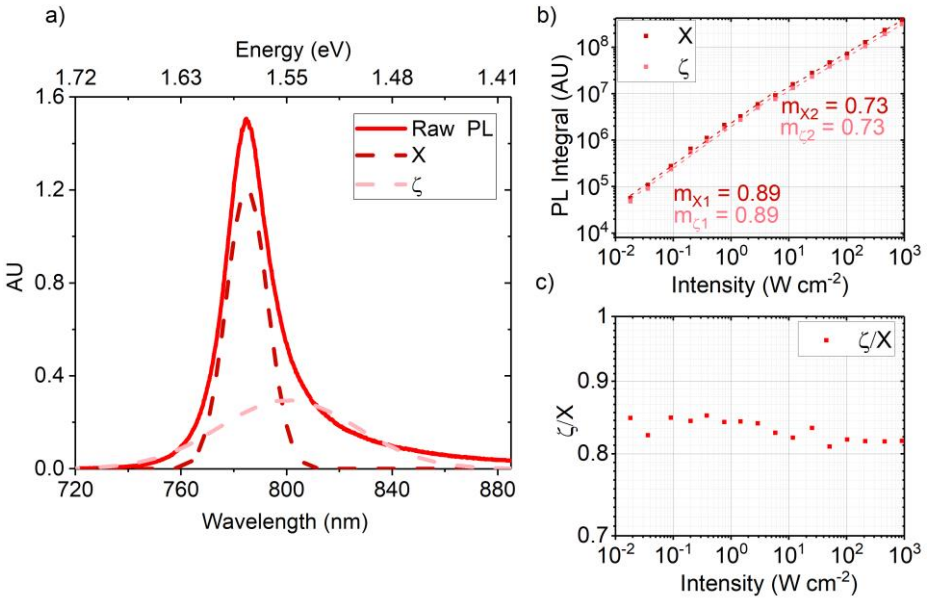

Figure 5.6: Exciton species characterisation in OA treated $MoSe_2$. a) Raw PL spectrum of OA treated $MoSe_2$ (red) taken in the high intensity regime (455 W cm^{-2}). Dashed maroon and pink Gaussian fits represent the neutral exciton (X) and a low energy species (ζ) respectively; **b)** Excitation intensity series of neutral exciton (X) and low energy species (ζ); **c)** Ratio of ζ to X as a function of excitation intensity.

The constant $\zeta/X < 1$ ratio indicates the dominance of neutral excitons compared to low energy species such as trions[58] throughout the series. Trions in particular, evolve from the binding of neutral excitons with free photoionized charges and have been characterised in room temperature WS_2 PL measurements, which show the growth of a broadening and red-shifting low energy feature as a function of increasing excitation intensity.[27,53,58,59] While strong neutral exciton contributions are observed throughout the series, easily discernible trion evolution is not apparent in both pristine and OA treated $MoSe_2$ PL spectra. A recent study on exciton and trion dynamics in $MoSe_2$ concluded that trion formation is suppressed at room temperature due to changes in localisation effects.[178] To this end, OA treatment simply improves neutral exciton PL by reducing the density of non-radiative channels which may take the form of trap states caused by chalcogen vacancies. As per the work cited,[178] identifying the effects of OA treatment on trion emission on $MoSe_2$ would require low temperature PL studies.

5.4 Time Resolved Photoluminescence

To gain further insights into the exciton dynamics present in OA treated $MoSe_2$ we employ time-resolved photoluminescence (TRPL) microscopy. Figure 5.7 shows normalized PL decay signals at room temperature under comparable low intensity 550 nm, 5 MHz pulsed laser excitation. Pulsed excitation intensities used were 0.054 W cm^{-2} and 0.064 W cm^{-2} for pristine (blue) and OA treated (red) cases respectively. Both signals are best described by a bi-exponential decay model (black dashed lines) consisting of a fast τ_1 and slow τ_2 components. The pristine sample (blue) PL decays with $\tau_1 \sim 1.07$ ns and $\tau_2 \sim 3.06$ ns. For the OA treated case (red), PL lifetimes are extended by a factor of 3x and 3.8x versus the pristine sample for fast and slow decays respectively with $\tau_1 \sim 3.3$ ns and $\tau_2 \sim 12.07$ ns. The overall increase in PL lifetimes due to OA treatment versus the pristine case reveals a suppression of non-radiative decay channels.

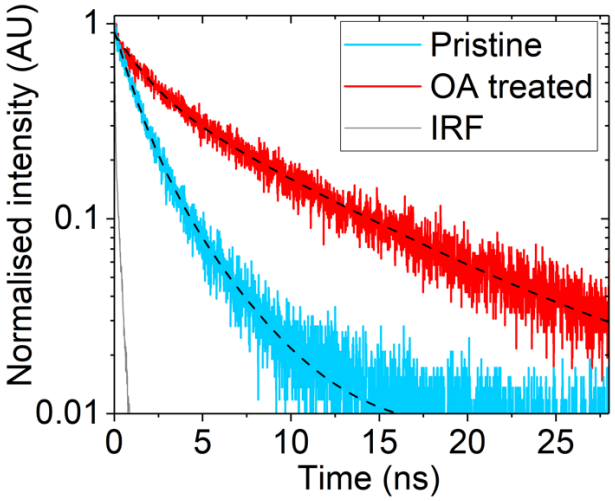

Figure 5.7: Transient PL spectra of pristine and OA treated $MoSe_2$. Pristine (blue) and OA treated (red) $MoSe_2$ monolayers with bi-exponential decay fits (black dashed lines) measured at pump intensities; 0.054 W cm^{-2} (Pristine sample) and 0.064 W cm^{-2} (OA sample) with 550 nm, 5 MHz pulsed excitation.

Figure 5.8.a-b shows time-resolved PL decay spectra at all fluences measured for each untreated (blue) and OA treated (red) samples with bi-exponential decay fits (dashed lines). Decay fits provided time constants (τ) shown in Figure 5.9 as a function of initial carrier concentration (n_o). Initial carrier concentrations were computed using openly available $MoSe_2$ steady state absorption data.[28]

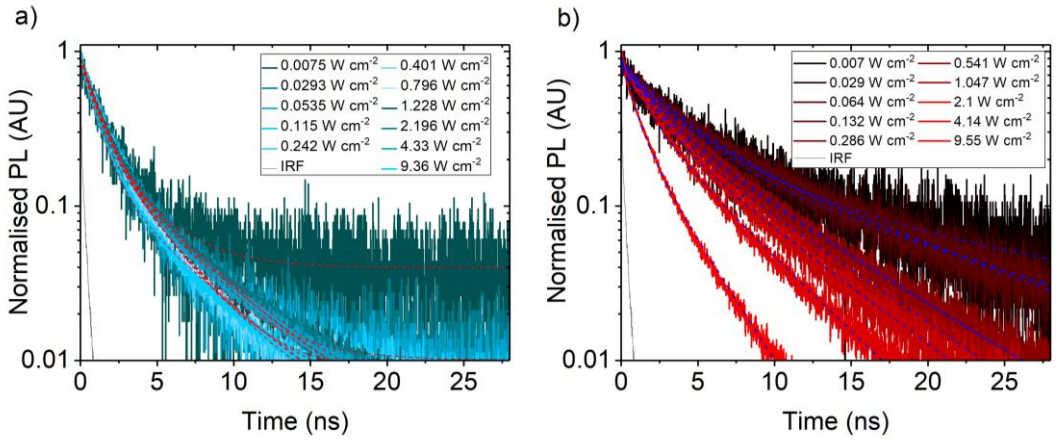

Figure 5.8: Transient PL series spectra of pristine and OA treated $MoSe_2$. a) TRPL signal of pristine $MoSe_2$ with bi-exponential decay fits (red dashed lines); **b)** TRPL signal for OA treated $MoSe_2$ with bi-exponential decay fits (blue dashed lines).

Figure 5.9.a shows the variation in fast decay component τ_1 as a function of initial carrier concentration n_0 over four orders of magnitude. Figure 5.9.b shows the

equivalent data for slow decay component, τ_2. The excitation intensities used fall within the range used for the steady state excitation intensity series shown in Figure 5.4.

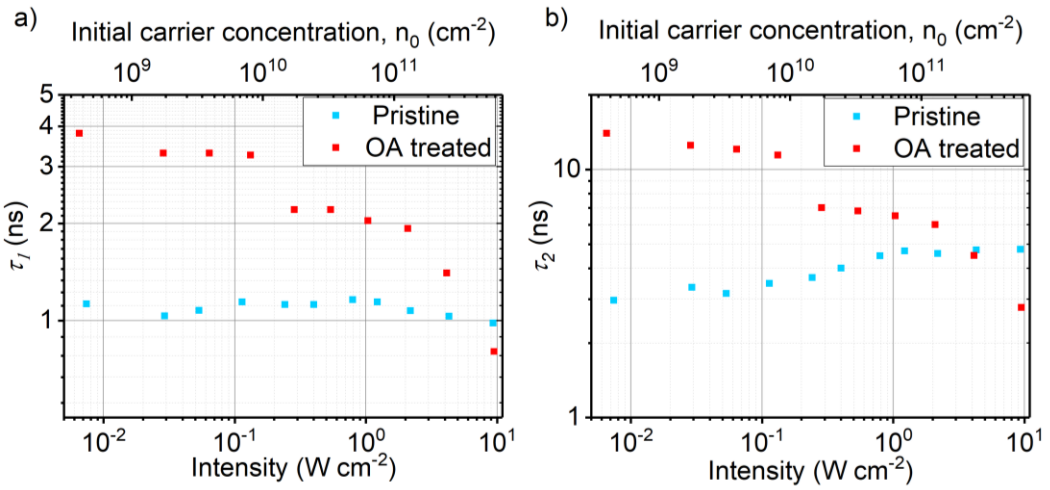

Figure 5.9: Transient PL series of chemically treated WS_2. a) Variation of fast PL decay component, τ_1, with initial carrier concentration and pump intensities (W cm^{-2}); **b)** Variation of slow PL decay component, τ_2, with initial carrier concentration and pump intensities (W cm^{-2}).

The pristine case shows very little variation in τ_1 over the range of n_0, which indicates exciton trapping. In contrast, OA treated $MoSe_2$ shows a general reduction in τ_1 over the n_0 range measured. This lies in agreement with the sub-linear trend measured within the same excitation intensity regime shown in Figure 5.4.*a*, which points to the immediate onset of exciton-exciton annihilation at low excitation fluences. Accordingly, the observed reduction in τ_1 as a function of n_0 in the OA treated sample implies non-trap limited movement of excitons and thus provides further evidence for trap state passivation due to OA treatment. For slow decay component, τ_2, the pristine case shows a general increase in lifetime as a function of n_0 in accordance with trap state filling. Conversely, the OA treated sample shows a reduction τ_2 as a function of n_o, following a similar trend to its fast component, τ_1.

In summary, the steady state PL measurements presented shows that OA treatment greatly enhances the PL of monolayer $MoSe_2$ and its optical quality in terms of emission linewidth and spatial homogeneity in brightness. Steady state excitation intensity dependent PL and TRPL studies reveal trap-free neutral exciton movement in OA treated $MoSe_2$. The observed enhanced PL and trap free exciton annihilation dynamics combined support the hypothesis of true defect passivation by OA.

5.5 Discussion on Surface Chemistry

The exact surface chemistry that gives rise to the observed optical improvement is not fully clear at the moment and future experimental and theoretical studies will be required to understand the underlying mechanism. We however consider that the treatment mechanism would be linked to passivation of chalcogen defects through oleate coordination to Mo dangling bonds as illustrated in Figure 5.10. We however note that Raman spectra of pristine and OA treated $MoSe_2$ in Figure 5.11 show no distinguishable structural changes. Chemical passivation of these vacancy sites suppresses excitonic trap states, resulting in vastly improved PL efficiency due to band-edge recombination. In addition, formation of an OA layer with bulky alkyl chains may provide an insulating encapsulant of the TMD monolayer analogous to hBN encapsulation, resulting in better protection from reactive species formed from atmospheric oxygen and water, and external trap states introduced by adsorbants.

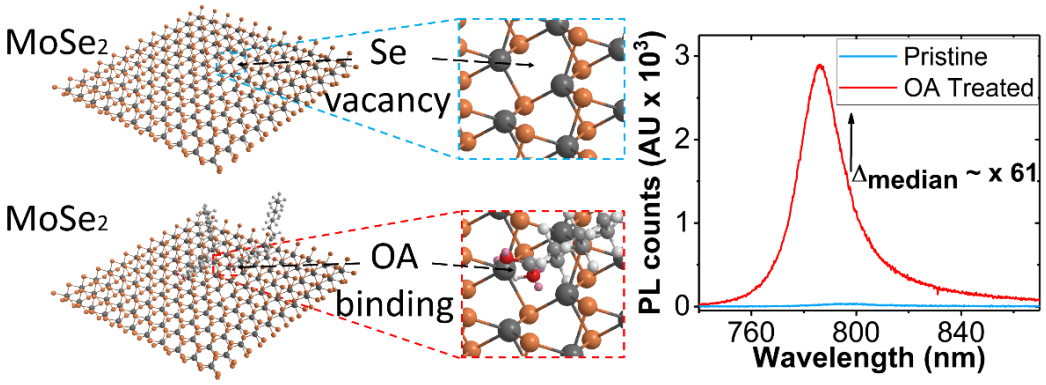

Figure 5.10: Illustration of Se vacancy passivation by OA coordination. OA ligand coordinating to Molybdenum (Mo) atom at chalcogen vacancy in $MoSe_2$ monolayer (LHS) and resulting (median) PL enhancement (RHS).

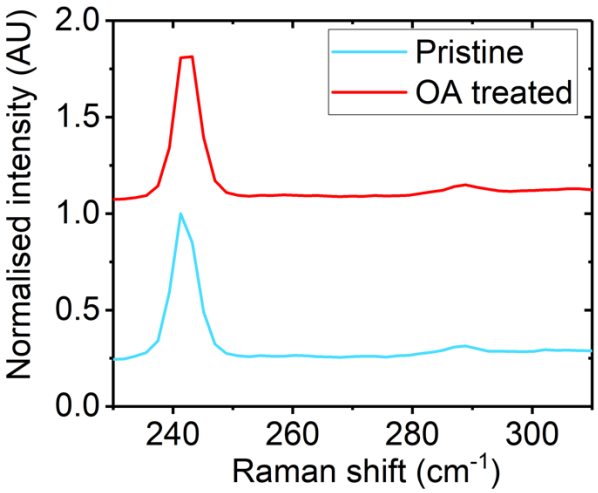

Figure 5.11: Raman characterisation of OA treated $MoSe_2$. Pristine (blue) and OA treated (red) monolayers deposited on glass substrate.

5.6 Electronic Characterisation

Finally, to assess the impact of OA treatment on the electronic properties of monolayer $MoSe_2$, we test back-gated field effect transistors (FETs). Figure 5.12.*a* shows the predominantly *n*-type transfer characteristics of $MoSe_2$ before OA passivation, consistent with previous reports.[179] After OA treatment *n*-type transfer characteristics are preserved. There is a relatively small threshold voltage (V_{th}) shift from $V_{th,Untreated}$ = 4.8 ± 1 V to $V_{th,OA}$ = 1.3 ± 2.3 V (Figure 5.12.*b*) indicating no substantial change in doping induced by the OA treatment. After OA treatment, devices consistently show an improved subthreshold swing (SS) from $SS_{Untreated}$ = 4 ± 0.9 V/dec to SS_{OA} = 1 ± 0.1 V/dec (Figure 5.12.c), which indicates a reduction in interface charge trap density and is consistent with the notion of defect passivation by OA. A higher on-state current, due to reduced charge trapping, and larger off-state resistance after OA treatment leads to an improved on-off current ratio up to ~$5x10^4$ (Figure 5.12.*d*).

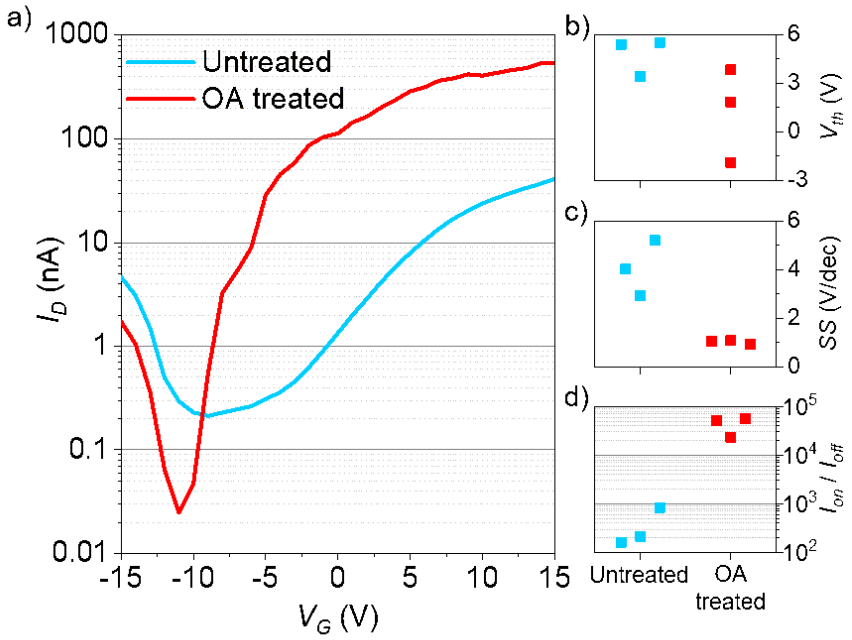

Figure 5.12: Electronic characterisation of OA treated $MoSe_2$ FETs. a) Transfer characteristics of the same back-gated monolayer $MoSe_2$ field effect transistor before (blue) and after (red) OA treatment. **b)** Threshold voltage, **c)** Subthreshold swing, **d)** On-off current ratio for three $MoSe_2$ transistors before (blue) and after (red) OA treatment.

5.7 Conclusions

In conclusion, we have established OA surface treatment of $MoSe_2$ as an effective means of achieving drastically improved PL yield and trap free PL dynamics as compared with untreated monolayers. PL statistics reveal that OA treatment yields monolayers of improved optical quality by way of bright spatially homogenous PL with narrow spectral linewidth. A steady state excitation intensity dependent PL series reveals significantly improved `PLQE' with trap-free exciton dynamics, which is taken as initial evidence of passivation of non-radiative trap states by OA ligands. Analysis of the excitonic species present in the excitation intensity series verifies dominant neutral exciton recombination in OA treated $MoSe_2$ under low to high excitation intensities. Consistent with improved steady state PL, time resolved PL studies reveal significantly improved PL lifetimes. The reduction in PL lifetimes as a function of initial carrier concentration also indicates trap free exciton movement, which further supports the

hypothesis of PL enhancement as a result of ligand passivation. By way of surface chemical interaction between OA and monolayer $MoSe_2$, we hypothesise that the OA ligands coordinate to Mo dangling bonds at Se vacancies, which are known to be exciton trap states, and thus passivating them and yielding increased radiative efficiency. The insulating ligands may also protect the monolayer from atmosphere induced doping and surface induced strain, thus acting as an encapsulant, which may also contribute the PL linewidth narrowing. OA treated $MoSe_2$ based FETs show no significant additional doping. However, we observe a considerable improvement in subthreshold swing with orders of magnitude increase in on-off ratio, which provides further evidence of trap or defect passivation by OA. In essence, the result shows that OA treatment is an effective, simple and versatile `wet' chemistry technique than can improve the PL characteristics of a selenide based TMD. Combined with previous studies on sulphur based TMDs, these results establish the 'ligand' based passivation approach as a universal defect treatment protocol for both sulphide and selenide based TMDs.

5.8 Methods

5.8.1 Steady state Photoluminescence Microscopy

PL spectroscopy was performed on the Renishaw Invia confocal setup described in chapter 3, section 3.3.1, *via* 50× objective (NA = 0.75). Signals were collected in reflection *via* notch filter. The diffraction limited beam spot size was estimated as 0.84 μm. PL signal was dispersed *via* a 600 l/mm grating prior to detection with inbuilt CCD detector. Laser power was measured directly *via* 5× objective with a Thorlabs S130C photodiode and PM100D power meter.

PL maps were generated from multiple $MoSe_2$ monolayers before and after OA treatment. Maps were generated with 1 × 1 μm resolution and 0.5 s integration time with 0.7 μW laser power. A single Gaussian fit from the standard peak fit library in Origin lab was used in Figure 5.2 to estimate changes in FWHM between untreated and OA treated $MoSe_2$ PL signals.

Steady state intensity dependent PL measurements were performed on the $MoSe_2$ monolayers on glass slide. Care was taken to measure PL in the same locations prior to and following treatment. The spatial *x, y* and *z* locations of the measurement site and photodiode were recorded to accurately switch between photodiode and monolayer

location for each PL measurement using the WIRE software piezo stage control interface. PL signals were scaled up to 500 s integration time as used on the lowest excitation intensity. Dark counts were measured for each measurement in the series with the same integration time and subtracted from raw PL data.

Exciton species in Figures 5.5-5.6 were deconvoluted from OA treated $MoSe_2$ PL signals with dark counts subtracted using a procedure written in Matlab, which incorporates the `gauss2' two Gaussian model fit. Further information on the Gaussian model is available on the mathsworks website.

5.8.2 Time resolved Photoluminescence Microscopy

TRPL measurements were performed with a custom-built inverted PL microscope setup equipped with a motorized piezo stage. Excitation was provided by a pulsed super continuum white light source (Fianium Whitelase) filtered *via* a Bentham TMc 300 monochromator. A 550 nm pulsed laser provided sample excitation *via* a 60x oil objective. This produced a 10 μm diameter confocal laser spot on the sample. The laser spot size was measured using the image created on an EMCCD camera (Photometrics QuantEM^{TM} 512SC). The laser repetition rate was set to 5 MHz with 11.4 ps time steps to obtain PL decay data. The $MoSe_2$ PL was collected using a MPD visible single photon avalanche diode (Vis-SPAD) *via* 750 nm long pass and 900 short pass filters, completely filtering out laser excitation and allowing for collection of $MoSe_2$ PL only. Further precaution was taken to remove any long wave component of the excitation line using a 650 nm short pass filter. All signals were scaled up to 3000 s, which was used in the lowest excitation intensity measurement. Laser power was measured in the excitation line using a Thorlabs S130C photodiode and PM100D power meter. Laser excitation power was regulated using a series of neutral density filters. The instrument response function was measured with a blank glass cover slide as used for the sample.

PL decay time constants in Figure 5.9 were fitted using a model developed in Origin, which consists of a Gaussian (as the IRF) convoluted with a bi- exponential decay.

5.8.3 Raman Microscopy

$MoSe_2$ monolayers on thin glass cover slides were characterised *via* Raman spectroscopy using a Renishaw Invia confocal setup similar to what is described in chapter 3, section 3.3.1. Excitation was provided using a 530 nm CW laser *via* 50× objective (NA = 0.75), producing an estimated diffraction limited beam spot size of 0.86 μm. The Raman signal was collected in reflection *via* notch filter and dispersed with a 1800 l/mm grating prior to detection with an inbuilt CCD camera.

5.8.4 Transistor fabrication and characterisation

After exfoliation and transfer onto Si - SiO_2 (90nm) isolated monolayer $MoSe_2$ flakes were identified and electrodes with a typical channel length of 4μm were patterned using e-beam lithography and thermal evaporation of Pd:Au (20nm:80nm) followed by lift-off in acetone. Transfer characteristics were measured using a Keithley 4200 SCS connected to a probe station. The global back-gate was swept from negative to positive voltages and the current was measured under a source-drain bias of 5V.

6 Directed Energy Transfer from Monolayer WS_2 to Near-Infrared Emitting PbS-CdS Quantum Dots

Heterostructures of two-dimensional (2D) transition metal dichalcogenides (TMDs) and inorganic semiconducting zero-dimensional (0D) quantum dots (QDs) offer useful charge and energy transfer pathways which could form the basis of future optoelectronic devices. To date, most has focused on charge transfer and energy transfer from QDs to TMDs, *i.e.*, from 0D to 2D. Here, we present a study of the energy transfer process from a 2D to 0D material, specifically exploring energy transfer from monolayer tungsten disulphide (WS_2) to near infrared (NIR) emitting lead sulphide-cadmium sulphide (PbS-CdS) QDs. The high absorption cross section of WS_2 in the visible region combined with the potentially high photoluminescence (PL) efficiency of PbS QD systems, make this an interesting donor-acceptor system that can effectively use the WS_2 as an antenna and the QD as a tuneable emitter, in this case downshifting the emission energy over hundreds of milli electron volts (meV). We study the energy transfer process using photoluminescence excitation (PLE) and PL microscopy, and show that 58% of the QD PL arises due to energy transfer from the WS_2. Time resolved photoluminescence (TRPL) microscopy studies show that the energy transfer process is faster than the intrinsic PL quenching by trap states in the WS_2, thus allowing for efficient energy transfer. Our results establish that QDs could be used as tuneable and high PL efficiency emitters to modify the emission properties of TMDs. Such TMD/QD heterostructures could have applications in light emitting technologies, artificial light harvesting systems or be used to read out the state of TMD devices optically in various logic and computing applications.

The work detailed in this chapter is adapted from an article published in ACS Nano: Tanoh, A. O. A.; Gauriot, N.; Delport, G.; Xiao, J.; Pandya, R.; Sung, J.; Allardice, J.; Li, Z.; Williams, C. A.; Baldwin, A.; Stranks, S. D.; Rao, A. Directed Energy Transfer from Monolayer WS_2 to Near-Infrared Emitting PbS-CdS Quantum Dots. *ACS Nano*. **2020**, 14 (11), 15374–15384. https://doi.org/10.1021/acsnano.0c05818. **[29]**[29]

All the work in this chapter was performed by the author except where stated. Nicolas Gauriot built photoluminescence excitation (PLE) setup and devised dedicated PLE data logging software/ control interface in Python; Dr. James Xiao synthesised colloidal quantum dots (QDs); Dr. Delport and Alan Baldwin measured TRPL and; Cyan Williams performed confocal absorption microscopy on monolayer WS_2.

6.1 Background and Motivation

Monolayer transition metal dichalcogenides (TMDs), which are derived from their layered bulk crystals *via* dry mechanical cleavage[1] or liquid phase exfoliation[180,143] have attracted a great deal of research interest due to their distinctive optical, electronic and catalytic properties.[6,3,157] Monolayer TMDs can also be obtained *via* epitaxial growth methods, in particular chemical vapour deposition (CVD),[159,77] which is an area of ongoing research. A number of monolayer TMDs such as tungsten disulphide (WS_2) have a direct optical gap.[3] This property compounded with high absorption coefficients, high carrier mobilities[3] and potentially high photoluminescence quantum efficiency[20,21,27] (PLQE) promise great potential for their application in optoelectronic devices namely photodetectors, light emitting diodes (LEDs) and photovoltaics (PV).[181] The reduced dielectric screening in the monolayer limit compared to their bulk counterparts gives rise to tightly bound electron-hole pairs (i.e. excitons) with binding energies of the order of hundreds of meV at room temperature.[56,160] As a consequence, monolayer TMDs provide a convenient medium to study diverse excitonic species that arise *via* exciton-exciton or exciton-charge interaction.[56,2,62,44] Alternatively, these tightly bound excitons can be funnelled to other fluorescent media where they recombine radiatively at lower energy, thus tuning the emission properties of TMD excitons. Nanocrystal quantum dots (QDs),

for example, provide a convenient, colour tuneable high PLQE emission medium[40,182] to which transferred 2D TMD excitons might be funnelled.

The exciton funnelling *i.e.*, nonradiative energy transfer (ET) process can occur *via* two main mechanisms, namely Förster resonance energy transfer[117] (FRET) and Dexter energy transfer (DET).[116] FRET is a long-range process (~1-11 nm)[117] that occurs *via* dipole-dipole coupling, where the electromagnetic near-field of an oscillating transition dipole in the donor induces a transition dipole in the acceptor. Consequently, FRET between donor and acceptor systems is dependent on their physical separation and to a large extent, the overlap of emission and absorption spectra.[116,117,32] On the other hand, DET involves direct simultaneous tunnelling of electron hole pairs from the donor to acceptor due to donor-acceptor charge orbital overlap. As such, DET is strongly distance dependent and requires extremely close proximity between donor and acceptor molecules ($\leq$ 1nm).[116,183]

A considerable amount of research into 2D-QD heterostructures has focused on interfacial charge transfer (CT) between QDs and monolayer TMDs for applications in photodetectors[108–115] and phototransistors.[106,107] To date, studies on energy transfer in 2D-QD heterostructures for light harvesting and light sensing applications have mainly focused on 0D→2D exciton transfer where monolayer TMDs or graphene are used as efficient exciton sinks to which optically or electrically generated excitons from QD emitters are non-radiatively transferred.[30–36,114]

Here, we demonstrate efficient ET from 2D TMDs to 0D QDs. We present a down–shifting heterostructure system, where monolayer tungsten disulphide (WS_2) acts as an antenna from which optically generated excitons are funnelled to lower energy lead sulphide-cadmium sulphide (PbS-CdS) near infrared (NIR) QD emitters. Photoluminescence excitation (PLE) studies confirm 2D→0D ET. Probing the underlying photophysics *via* time resolved optical microscopy reveals a fast, non-radiative ET process that out-competes intrinsic exciton trapping in monolayer WS_2. These results establish ET from 2D TMDs to 0D QDs as an efficient means to control excitonic behaviour, allowing for tuning of emission energies and construction of artificial light-harvesting systems.

6.2 Heterostructure Preparation

Figure 6.1 (1-6) shows the sample fabrication process from the initial exfoliated monolayers to the heterostructure. Monolayer WS_2 on thin (170 μm) 22 mm x 22 mm glass slides were exfoliated *via* the gold assisted technique (see Chapter 3, section 3.1.1).[140] A single QD layer was deposited onto the sample surface using a conventional layer-by-layer method (1-3).[184-185] Sample preparation is detailed as follows:

1) In a nitrogen (N_2) glovebox, the monolayer samples were spin coated at 1000 rpm for 50 seconds with 200 μL of 20 mM 1,3 benzene dithiol dissolved in acetonitrile to forma a linker layer. The choice of ligand ensures strong adhesion of QDs.

2) A dilute 200 μL suspension of 0.5 mg/ml oleic acid (OA)-capped PbS-CdS QDs in toluene was spin coated at 500 rpm for 60 s;

3) Excess nanocrystal and ligand material was rinsed off by spin coating toluene on the sample at 500 rpm for 60 s. A waiting time of 5 minutes was observed between steps.

4) The sample was encapsulated using a top 18 mm x 18 mm thin glass slide with double sided tape at the edges to hold the top slide in place. Gaps between the bottom and top glass slides were sealed with epoxy.

5) The encapsulated sample was left to dry over 24 hours in the N_2 environment.

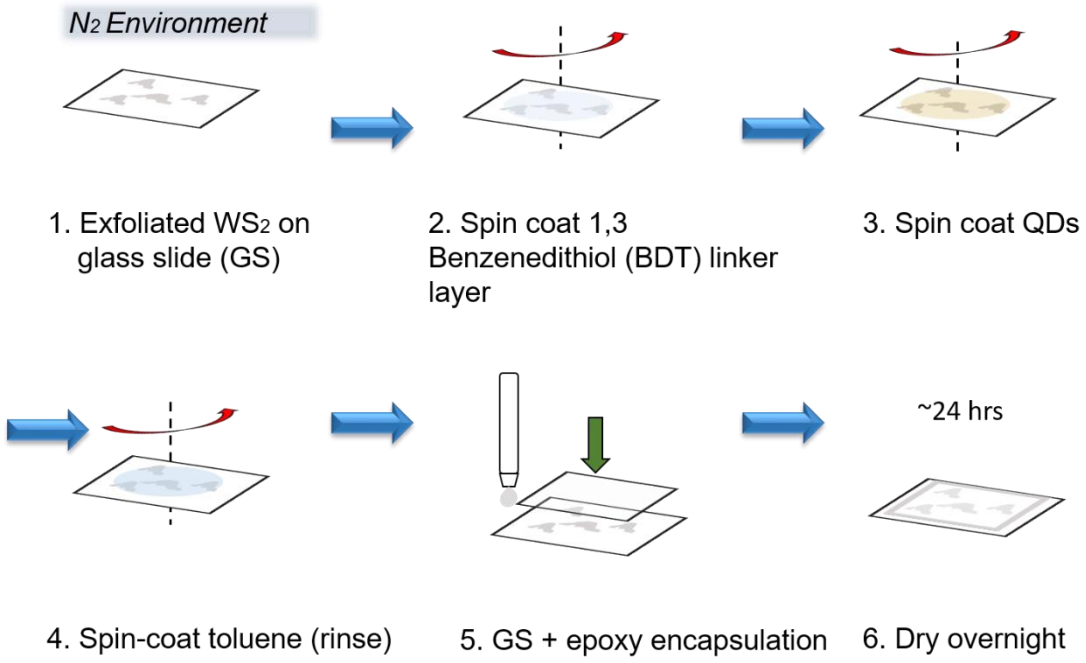

Figure 6.1: Heterostructure preparation. Cartoon Illustration of heterostructure sample fabrication process in a nitrogen environment.

6.3 Steady State Optical Characterisation

We first investigate the steady state optical properties of the heterostructure and its constituent materials. Figure 6.2.*a* shows the absorption and PL spectra of a WS_2 monolayer. The absorption spectrum of the WS_2 monolayer (light blue circles) clearly reveals `A', `B' and `C' excitonic peaks positioned at 2.0 eV (617 nm), 2.4 eV (512 nm) and 2.88 eV (430 nm) respectively. The PL spectrum (dark blue dashed line) is well overlapped with the `A' exciton band. The absorption and PL spectra of the QDs in colloidal suspension are plotted in Figure 6.2.*b*. The colloidal PbS-CdS absorption spectrum (solid black line) reveals an absorption peak at 1.76 eV (704 nm) while the PL spectrum (black dotted line) exhibits the red-shifted peak position at 1.38 eV (900 nm). Interestingly and importantly, the WS_2 PL lies firmly within PbS-CdS absorption spectrum, which is a key requirement for efficient FRET. Consequently, PbS-CdS QDs and WS_2 monolayer were carefully chosen as an efficient energy transfer pair.

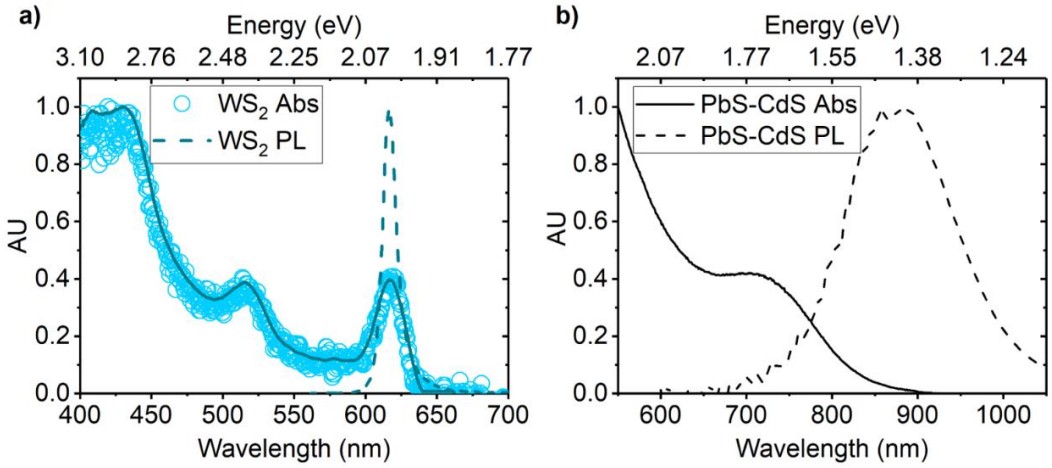

Figure 6.2: Steady state optical characterisation of heterostructure components. a) Monolayer WS_2 normalized absorption (light blue circles with solid dark blue line as guide to eye) and PL (dashed dark blue line); **b)** Colloidal PbS-CdS normalized absorption (black solid line) and PL (black dashed line) spectra.

An additional factor considered was the absorption cross sections of the constituent donor and acceptor materials. The TMD monolayer's role as an optical antenna and exciton generation medium requires that it has a higher absorption cross section compared to the nanocrystal emitter. Whereas the absorption cross sections of monolayer tungsten disulphide (WS_2) and other TMDs in the visible region are not very well documented, the absorption coefficient σ_{gs} of few layer (1-3 monolayers) MoS_2 obtained from a study on non-linear optical performance of MoS_2 films by Zhang *et al*[180] gives a value of σ_{gs} = 4.7 x 10^{-15} cm^2 for 515 nm pulsed excitation. We estimate the absorption cross section for a MoS_2 monolayer by simply dividing σ_{gs} = 4.7 x 10^{-15} cm^2 by the maximum number of layers (n = *3*) in the sample quoted to give $\boldsymbol{\sigma_{gs} \approx 1.6 \times 10^{-15}}$ **cm^2** at 515 nm. We note that the absorption of monolayer WS_2 is similar in magnitude to MoS_2 at 515 nm[25] and hence estimate that their absorption cross sections are comparable at 515 nm. Moreover, considering the transition from indirect to direct optical gap from few layer to monolayer TMD, the actual value of absorption cross section should exceed this estimation. Following Cademartiri *et al.,*[186] we compute the absorption cross section of a single QD *via* Equation *6.1* using the molar extinction coefficient, ε_A [M^{-1} cm^{-1}] estimated later in section 6.3.1. Units are provided in square brackets for clarity.

$$\sigma = \frac{2303\ [cm^3 L^{-1}]}{N_A\ [mol^{-1}]} \varepsilon_A(\lambda)\ [L\ mol^{-1} cm^{-1}] \qquad (6.1)$$

Where N_A is the Avogadro number. This yields a value of $\sigma \approx 8.74 \times 10^{-17}$ cm^2 at 515 nm. Given the estimations made and the shape of the monolayer WS_2 absorption spectrum (Figure 6.2.*a*), we consider that the WS_2 absorption cross-section exceeds that of the QDs by a large factor in the ~ 400 nm – 650 nm range.

Figure 6.3 illustrates confocal PL measurements performed with the sample placed upside down. This was done to excite the monolayer WS_2 directly *via* the thin glass slide and avoid shadowing by the QDs altogether. Optically addressing the monolayer first ensures efficient generation and funnelling of TMD excitons to the QDs as illustrated in the inset image. This results in considerable QD PL enhancement in the heterostructure as subsequently discussed in detail for Figure 6.4. Exciting the QDs directly would otherwise cause sub-optimal exciton generation and funnelling due to absorption of a proportion of incoming photons by the shadowing QDs, amounting to less prominent QD PL enhancement.

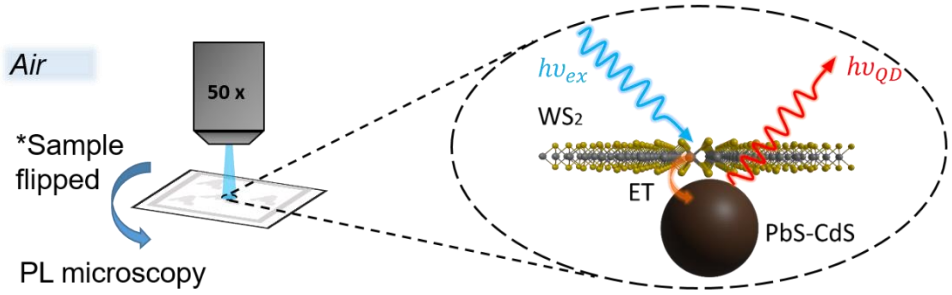

Figure 6.3: Confocal PL characterisation of heterostructure. Cartoon Illustration of initial confocal PL characterisation in air *via* 50x objective. Sample is flipped to avoid shadowing by QDs, and to ensure efficient generation and transfer of 2D excitons to the QD. Inset image depicts excitation energy funnelling from WS_2 monolayer to PbS-CdS QD.

The steady state confocal PL spectra of QD film on the bare substrate (black) and the heterostructure (red) are plotted in Figure 6.4. While the QD film on the bare substrate shows a broad Gaussian PL peak in the NIR region centred at 1.38 eV (900 nm), the heterostructure exhibits two distinctive PL peaks *i.e.*, the narrow WS_2 PL peak in the visible region centred at 2.0 eV (~619 nm) and a broad QD PL peak in the NIR region at 1.42 eV (870 nm). We note that the QD PL spectrum of the heterostructure is blue-shifted by 30 nm and enhanced by a factor of 2.6. The observed blue shift in the heterostructure's QD PL on the WS_2 monolayer compared to the bare substrate may be attributed to the following possibilities: i) a difference in dielectric environment between the surfaces; ii) a difference in QD aggregation concentration of the QD film between the surfaces or; iii)

a combination of both factors. We also note that it is possible that the PL yield of the QDs on the WS_2 monolayer is higher than those on the bare substrate as a result of the aforementioned factors. Whereas ascertaining the nature of the heterostructure's surface morphology and dielectric properties could offer additional explanation towards the observed changes in QD emission properties between the bare substrate and TMD monolayer surface, the scope of this work is confined to investigating the possibility of ET of WS_2 excitons to the QDs as evidenced by the QD PL enhancement on the monolayer surface. [116] Hence, we seek to verify the notion of 2D→ QD ET *via* further optical characterisation studies.

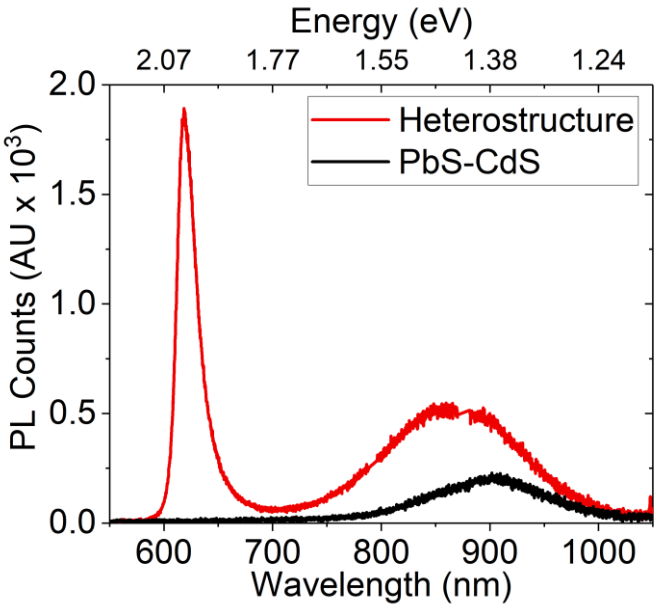

Figure 6.4: Heterostructure steady state PL spectrum. PL spectra of WS_2/PbS-CdS 2D-QD heterostructure (red) and PbS-CdS film (black) measured with 514.5 nm CW laser at 80.2 W cm^{-2}.

Figure 6.5.*a* shows the optical micrograph (left) of a WS_2 flake and confocal NIR (QD) PL map (right) from the same region obtained upon excitation at 514.5 nm. The colour bar represents the PL integral in the 780 - 960 nm spectral range. Enhanced NIR PL from QDs is obtained in the vicinity of the monolayer (dashed line) whereas QD PL in the bulk flakes (solid line) is quenched. The difference in NIR PL intensity between monolayer and bulk flakes suggests that the WS_2 monolayer serves as the ET donor, while the bulk quenches excitons. Figure 6.5.*b*. shows the QD PL spectra from the heterostructure (red) and bare substrate (black) extracted from points marked `*x*' on the QD PL map in Figure 2.*a*., RHS. Lime green dashed lines are single Gaussian peak fits. The QD PL spectrum of the heterostructure is blue-shifted by 47 nm compared with the

QD on bare substrate. We also observe a QD PL enhancement factor of 5.2, which we attribute to energy funnelling from the directly excited WS_2 monolayer.

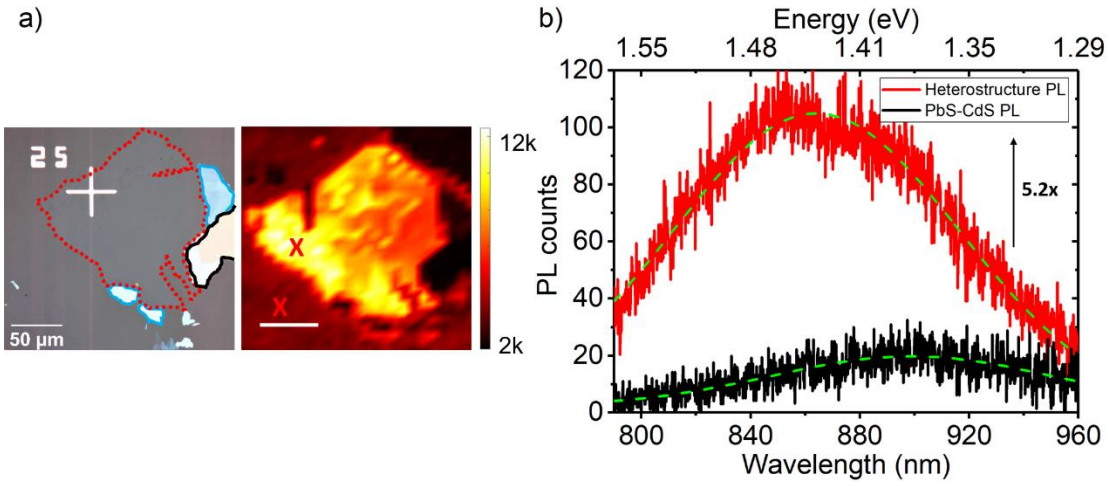

Figure 6.5: QD PL enhancement on WS_2. a) Optical micrograph of a WS_2 flake (left) showing monolayer (red dotted outline), multilayers (blue outline) and bulk crystal (black outline) with corresponding confocal NIR PL map of QD emission from the heterostructure (right) measured with 514.5 nm CW laser at 80.2 W/cm^2. RHS scale bar represents 50 μm; **b)** QD PL spectra from heterostructure (red) and bare substrate (black) taken from points marked `*x'* in Figure 6.5.*a*, RHS. Green dashed lined represent single Gaussian peak fits;

To delve into the possibility ET from the WS_2 monolayer to PbS-CdS QDs, we employ wide-field photoluminescence excitation (PLE) microscopy. We recorded the PL intensity integrated over the NIR region (800-1000 nm), exclusively corresponding to PL from the QDs, and scanned the excitation wavelength across 560-680 nm, mainly resonant to WS_2 at low fluence (c.a., ~0.006 μJ/cm^2 at 620 nm). The PLE spectra shown in Figure 6.6.*a* were taken on the heterostructure (red) and in an area with QDs only (black) away from the heterostructure. We note that the PLE data is normalized with respect to the mean values at wavelengths non-resonant to the WS_2 donor (670-700 nm) to account for the increase in QD emission due to resonant 2D→QD ET only, discounting the effects of other previously discussed factors that may contribute to improved QD emission on the heterostructure. The unscaled PLE data is shown in Appendix 1.

Unlike the PLE spectrum of QD only area (black), the PLE spectrum of the heterostructure (red) clearly reveals the signature `A' excitonic peak centred at 616 nm (~2.0 eV), indicative of a significant contribution of excitation from the underlying WS_2. Furthermore, as shown in Figure 6.6.*b*, the resulting PLE spectrum (red line) obtained by subtracting the normalized QD PLE spectrum (Figure 6.6.*a*, black) from that of

heterostructure (Figure 6.6.*a*, red) is almost perfectly overlapped with a typical WS_2 absorption spectrum (blue circles). This is strong evidence for energy transfer from WS_2 monolayer to the QDs.

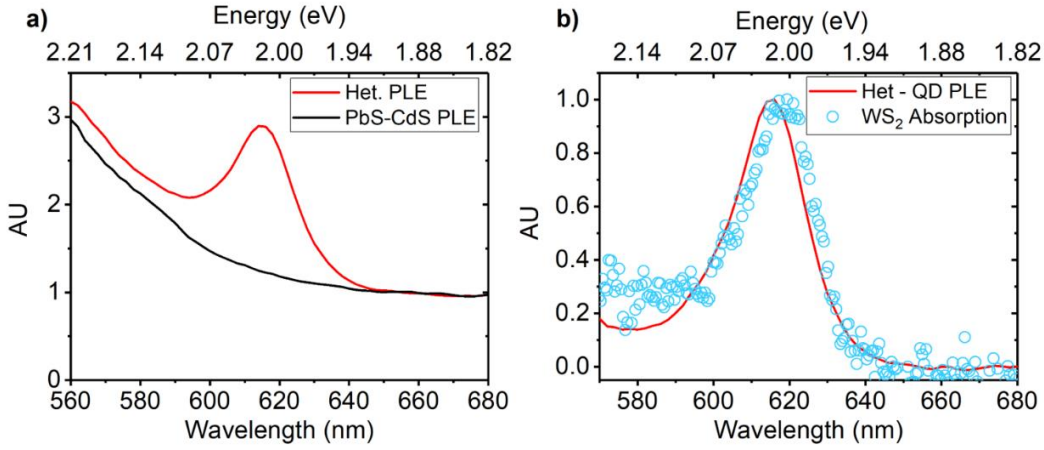

Figure 6.6: Heterostructure confocal PLE spectra. a) Normalized PLE spectra of heterostructure (red) and QD (control) obtained *via* scanning wavelengths about the WS_2 `A' exciton (616 nm) and detecting QD PL (900 nm). PLE spectra normalized by the average signal between 670 nm and 700 nm; **b)** Normalized `subtract' (red) signal derived *via* subtraction of QD PLE signal from heterostructure PLE signal in Fig. 6.6.*a* and overlapped with typical WS_2 absorption spectrum (blue circles).

To quantify ET from WS_2 monolayer to QD, we calculated the photoluminescence contribution, PL_{ctr} as a function of excitation wavelength using PLE data shown in Figure 6.6.*a*. We derive PL_{ctr} using the key underlying assumption of constant QD PLQE as informed by Vavilov's rule,[187] which states that PLQE is independent of excitation wavelength. This is regarded as a reasonable assumption for the wavelength range presented in the PLE data shown in Figure 6.6 (560 – 680 nm). We consider the photoluminescence excitation (PLE) of the QD at resonant and non-resonant excitation wavelengths to the underlying WS_2 monolayer *i.e.*, $PLE_{\lambda*}$ and PLE_{λ} respectively. In each case the PLE from the QD emission detection is given by equations 6.2 and 6.3:

$$PLE_{\lambda*} = \frac{PL_{\lambda*}}{\varphi_{\lambda*}} = Abs_{\lambda*} \times PLQE \tag{6.2}$$

$$PLE_{\lambda} = \frac{PL_{\lambda}}{\varphi_{\lambda}} = Abs_{\lambda} \times PLQE \tag{6.3}$$

Where φ and *Abs* are the number of photons injected per second and absorption of the QDs respectively. By dividing equation 6.2 by equation 6.3 we obtain:

$$\frac{PLE_{\lambda*}}{PLE_{\lambda}} = \left(\frac{\varphi_{\lambda}}{\varphi_{\lambda*}}\right)\frac{PL_{\lambda*}}{PL_{\lambda}} = \left(\frac{Abs_{\lambda*}}{Abs_{\lambda}}\right) \tag{6.4}$$

Hence, we obtain an absorption ratio (R) equivalent to the ratio of (WS_2) resonant PLE to non-resonant PLE:

$$R = \frac{PLE_{\lambda*}}{PLE_{\lambda}} = \left(\frac{\varphi_{\lambda}}{\varphi_{\lambda*}}\right)\frac{PL_{\lambda*}}{PL_{\lambda}} = \left(\frac{Abs_{\lambda*}}{Abs_{\lambda}}\right) \tag{6.5}$$

By comparing the R values on the heterostructure and the QD control, we can identify an additional contribution to the QD absorption *i.e.*, ΔR from the underlying WS_2.

$$\Delta R = R_{Het} - R_{QD} \tag{6.6}$$

Expressing equation 6.6 as a proportion of the heterostructure R value (R_{Het}), we obtain the contribution of PL by the WS_2 to the QDs.

$$PL_{ctr} = \left(\frac{R_{Het} - R_{QD}}{R_{Het}}\right) = \left(\frac{\Delta R}{R_{Het}}\right) \tag{6.7}$$

Figure 6.7. shows that PL_{ctr} is maximized at 616 nm with a value of 58% and reduces considerably thereafter at lower energies least resonant to the donor WS_2.

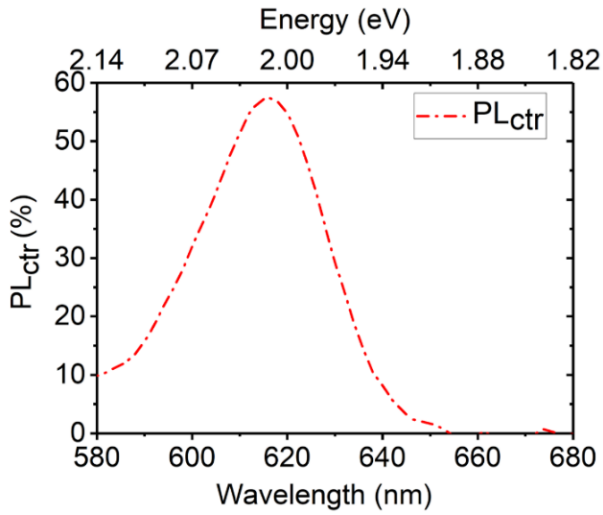

Figure 6.7: QD PL contribution from 2D WS_2. Estimated contribution to QD PL (PL_{ctr}) by the WS_2 monolayer as a function of excitation wavelength with peak value of 58% at 616 nm (~2.0 eV).

As an additional experiment, further PLE measurements were carried out on a series of heterostructures with different QD-2D surface attachment thiol ligands. As well as the heterostructure based on 1,3 benzenedithiol (BDT), 1,4 butanedithiol (BuDT) and 1,6 hexanedithiol (HDT) were also studied. Figure 6.8. shows the normalized wide field PLE spectra of WS_2/PbS-CdS heterostructures based on the different surface attachment ligands. Table 6.1 lists the ligands and their lengths.

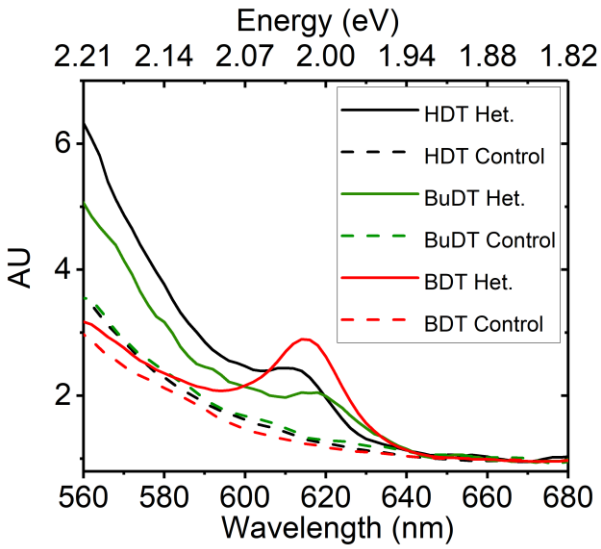

Figure 6.8: PLE of heterostructures with different surface attachment ligands. Normalized PLE spectra of heterostructures with varying QD-2D surface ligands – 1,3 benzenedithiol (BDT) (red), 1,4 butanedithiol (BuDT) (green) and hexanedithiol (HDT) (black). Dashed lines represent control (QD only) PLE signals.

Table 6.1: Dithiol ligands and corresponding lengths. (*) indicates value estimated using calculated dithiol ligand lengths from *ref* 188 (Mispelon *et al.*[188], Table 1, p. 18566) and the known bond angle of the hexagonal planar benzene ring.

Ligand	Length	Reference
1,3 Benzene dithiol (BDT)	0.47 nm	*
1,4 Butane dithiol (BuDT)	0.68 nm	[189]
1,6 Hexane dithiol (HDT)	0.95 nm	[189]

In Figure 6.8. we observe a difference in the of the WS_2 resonant peak, which is due to the variation in size of the WS_2 monolayers used, The BDT sample has the largest

monolayer and hence the most prominent `A' exciton signal with least contribution of the QD emission shoulder blue of the $WS_2$ excitonic peak, unlike the other samples. All signals show the $WS_2$ `A' excitonic peak in the expected spectral region (614 – 620 nm), confirming 2D → QD ET.

From table 6.1, we notice that all surface attachment ligands used are of lengths < 1 nm and thus, in principle, lie within range for ET *via* exciton tunnelling (*i.e.*, DET). Although charge orbital overlap between the monolayer TMD donor and QD acceptor is a possibility at such separation distances, their respective large oscillator strengths highly favours ET *via* FRET[116] over DET. To verify this notion, in section 6.3.1 we quantify the likelihood of FRET as the dominant 2D→QD ET mechanism observed in the heterostructures by estimating the theoretical Förster radius (or FRET radius), R_0, which is defined as the distance between donor and acceptor through which there is a 50% probability of excitation transfer.[116]

6.3.1 Characterising ET Mechanism: Förster Radius Estimation

Considering the 2D TMD as an array of point-like emitters and the QD film as an array of point-like absorbers, the FRET radius, R_0, is defined in equation 7.[117] This system is also well approximated by a 2D quantum well donor and nanoparticle acceptors, which follows a d^{-6} distance dependence for non-radiative energy transfer.[119]

$$R_0^6 = \frac{9ln10}{128\pi^5 N_A}\frac{\kappa^2 PLQE_D}{n^4}J \tag{6.8}$$

N_A is Avogadro's number, n is the refractive index of the medium surrounding the FRET pair, $PLQE_D$ is the donor's intrinsic photoluminescence quantum efficiency and κ^2 is the dipole orientation factor, which is equal to 2/3 for randomly oriented dipoles.[190] J is the overlap integral between the area normalized emission spectrum,[117] F_D and acceptor absorption, as given by the acceptor molar extinction coefficient, ε_A.

$$J = \int_0^\infty F_D(\lambda)\varepsilon_A(\lambda)\lambda^4\, d\lambda \tag{6.9}$$

It must be noted that J is evaluated with the wavelength in [nm] and ε_A in [M^{-1} cm^{-1}]. To compute R_0, we must calculate the overlap integral J from measured $\varepsilon_A(\lambda)$ and $F_D(\lambda)$ data. The molar extinction coefficient is obtained *via* Beer Lambert's law (equation 6.10) for

absorbance, A of a 0.1 mg ml^{-1} suspension of QDs in toluene of molar concentration c, measured with a 1 cm path length, l, cuvette.

$$A(\lambda) = \varepsilon_A(\lambda)cl \tag{6.10}$$

However, to obtain the molar extinction coefficient, the molar concentration, c of QDs in [M] is needed. The first step in calculating c involves estimating the QD size by solving equation 6.10 provided by Moreels *et al.*[191] for PbS QDs of diameter D of band gap energy, E_g. Since the QDs used consist mainly of a PbS core as per the modified preparation method originally developed by Neo *et al.*[192], the use of equation 6.11 is considered reasonable. For the QDs used, where E_g ~ 1.76 eV, we obtain D ~ 2.4 nm.

$$E_g = 0.41 + \frac{1}{0.0252D^2 + 0.283D} \tag{6.11}$$

We then calculate the QD volume assuming a spherical shape. This is followed by multiplying the volume by the density of PbS (7.6 g cm^{-3}) to obtain the mass of a single QD. Multiplying the mass of a single QD by the Avogadro number yields an estimate for the QD molar mass, Mr ~ 33128 g mol^{-1}. Dividing the known QD concentration of 0.1 g L^{-1} (*i.e.*, 0.1 mg mL^{-1}) by the estimated QD molar mass Mr, yields c ~ 3.02 × 10^{-6} M. We rearrange equation 6.9 for the molar extinction coefficient (ε_A) in [M^{-1} cm^{-1}]. Figure 6.9 below shows ε_A along with area normalized donor emission, F_D as functions of wavelength (λ).

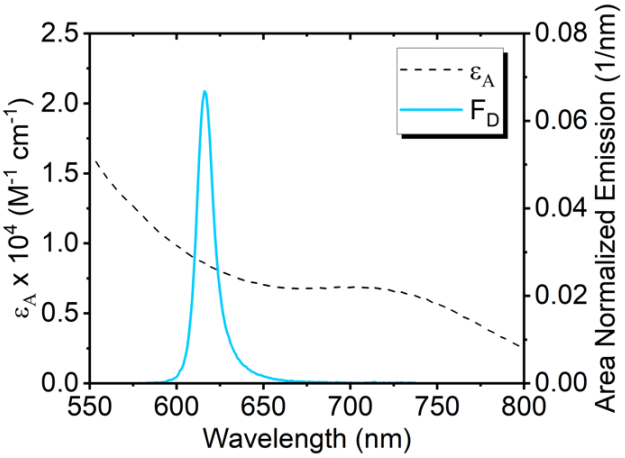

Figure 6.9: QD extinction coefficient and normalized WS_2 PL. (Left axis) Molar extinction coefficient of 3.02 × 10^{-6} M PbS-CdS QDs in toluene measured with 1 cm cuvette. (Right axis) Area normalized WS_2 emission spectrum, F_D used to calculate overlap integral, J.

From the data shown in Figure 6.9, the overlap integral is estimated *via* equation 6.9 as $J \approx 1.23 \times 10^{15}$ M^{-1} cm^{-1} nm^4. Using a simplified version of equation 6.8 below (equation 6.11) we estimate R_0 [nm] by assuming a vacuum between the emitter and absorber, *i.e.*, $n = 1$ and orientation factor $\kappa^2 = 2/3$. For the ideal system, we assume the TMD donor to have unity PLQE. This approximation is considered reasonable as we subsequently discover (in section 6.4) that the energy transfer rate from WS_2 band edge to QD band edge outcompetes the intrinsic exciton quenching in WS_2.

$$R_0 = 0.0211 \left(\frac{\kappa^2 PLQE_D}{n^4} J \right)^{\frac{1}{6}} \tag{6.12}$$

From equation 6.12, we obtain $\boldsymbol{R_0 \approx 6.5}$ **nm**, which exceeds the ligand separation distances between donor TMD and acceptor QD listed in table 6.1. This result emphasizes the significance of the oscillator strength of the constituent heterostructure materials (*i.e.*, TMD donor and QD acceptor) over their physical separation distance, even at low proximity. This strongly suggests FRET as the dominant ET mechanism observed in the heterostructures measured in Figure 6.8. In addition, whereas short ligands such as BDT have previously been shown to improve CT between QDs,[193] the CdS shell encapsulating the PbS core is known to suppress CT.[194]

6.4 Time Resolved Optical Characterisation

To gain further insight into the dynamics of the ET process observed from PLE we turn to time resolved PL (TRPL) microscopy, where we detect changes in emission decay from WS_2 using a 509 nm pulsed laser excitation. Excitation is filtered from the detection line with a 510 nm long pass filter, while QD emission is removed using a 700 nm short-pass filter, allowing for WS_2 monolayer PL detection only. We distinguish bare WS_2 from WS_2 in the heterostructure by referring to the former as `pristine' WS_2.

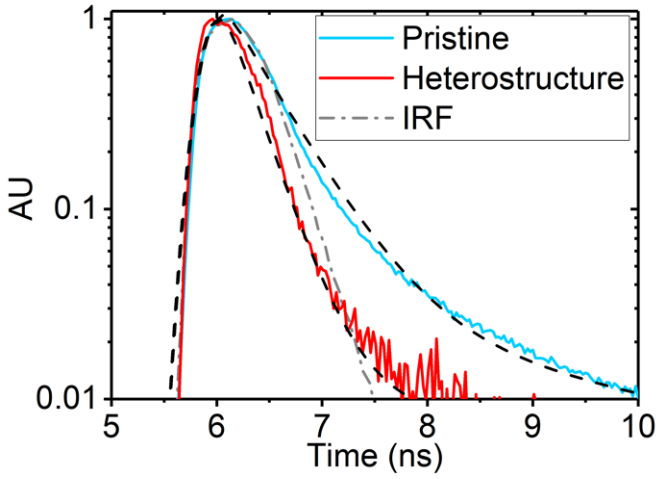

Figure 6.10: Pristine WS_2 and heterostructure low excitation fluence visible TRPL decay spectra. Low fluence time resolved WS_2 PL decay signals from pristine (blue) and heterostructure (red) samples measured with 509 nm pulsed excitation at 0.01 $\mu J/cm^2$. Exponential decay fits are shown as dotted black lines. Grey dashed line represents Instrument response function (IRF). The quenched (red) PL lifetime lies below the sensitivity of the detector (as shown by the signal that appears to decay quicker than the IRF), which is indicative of a fast quenching channel.

Figure 6.10 shows the normalized time resolved PL decay signals of the pristine monolayer and heterostructure under low fluence excitation (0.01 $\mu J\ cm^{-2}$). The transient PL profile of pristine WS_2 shows a bi-exponential decay profile consisting of fast and slow components. On the other hand, we observe that the fast component of the heterostructure's PL profile is quenched below the detector's initial response function (IRF). The two PL decay components observed in the pristine monolayer can be attributed to direct band-edge to ground state excitons transitions and exciton trapping respectively.[27] In contrast, the much faster PL kinetics observed in the heterostructure suggests an additional efficient fast decaying process present in this system. In fact, this quenching observed in the heterostructure is in accordance with what is expected of the PL dynamics of the donor in a nonradiative ET system.[62]

Figure 6.11 shows an excitation fluence series performed on both pristine and heterostructure samples. The pristine case shows a general increase in PL lifetime with fluence, which is indicative of `trap' or `defect' state filling. This trap limited behaviour has also been observed in WS_2 and MoS_2 monolayers treated with bis(trifluoromethane)sulfonimide (TFSI).[91,27]

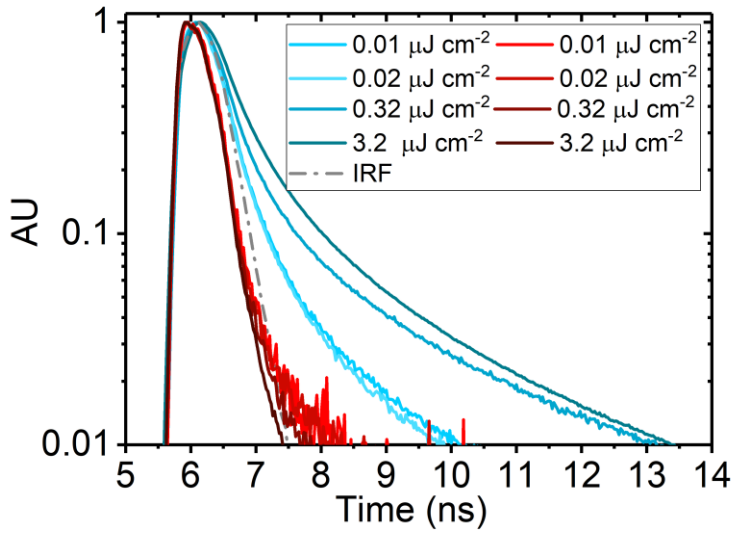

Figure 6.11: Pristine WS_2 and heterostructure visible TRPL excitation fluence series spectra. Time resolved WS_2 PL excitation fluence series from pristine (blue) and heterostructure (red) samples. Pristine WS_2 PL decay signals show general increase in lifetime as a function of pump fluence due to exciton trapping. All WS_2 PL decay signals in heterostructure quenched below the sensitivity of the detector due to fast exciton transfer. Heterostructure PL decay signals therefore appear faster than instrument response function (IRF) (grey dash-dot line).

The apparent increase in the fast component of the PL lifetime with fluence is due to trapping and de-trapping of excitons to the band edge prior to recombination to the ground state. The long-lived component is due to radiative transitions from the trap to ground state.[91] Increasing the excitation fluence would lead to saturation of trap states, forbidding further trapping and promoting dominant band-edge to ground state recombination. The fluence series presented in Figure 6.11 however lies below trap-state saturation. This is given by the increasing fast PL component lifetimes as a function of fluence. Trap-state saturation would otherwise be characterised by a constant fast PL component with increasing excitation fluence.[27] Further increases in fluence would lead to an eventual reduction in fast PL component lifetime, signalling the onset of exciton-exciton annihilation.[27] Interestingly, in the heterostructure case, the fast PL components are quenched below the IRF throughout the series. This outcome suggests that ET rate outcompetes the intrinsic exciton trapping rate in monolayer WS_2, which occurs on a time scale of few picoseconds.[71,91] We therefore predict that the 2D→QD ET occurs at a faster or similar time-scale.

The observation of a concomitant growth in QD PL lifetime with WS_2 PL quenching would provide further confirmation of ET. However, as recently discussed, it is likely that the ET process occurs on a timescale faster than intrinsic trapping in the monolayer TMD (*i.e.*, few ps), too fast to be detected by time-correlated single photon counting (TCSPC) as employed in this study, and perhaps even too fast for Streak Camera measurements. As further confirmation of this hypothesis, Figure 6.12 below shows the normalized time resolved PL (TRPL) decay signals for a heterostructure (red) prepared on spectrosil compared with the QDs on the bare substrate (black). Excitation was provided using the 509 nm pulsed laser at 0.5 MHz repetition rate and 200 ps resolution. The excitation signal was filtered out using a 510 nm long pass filter and QD emission was isolated with an 800 nm long pass filter, removing any signal from the underlying WS_2. The heterostructure decay clearly shows the IRF component convoluted with the long-lived QD PL decay at early time. This indicates the occurrence of a phenomenon much faster than the sensitivity of the setup. Therefore, the expected increase in QD life-time due to ET from the underlying WS_2 occurs at a much earlier time than what is detectable by the TRPL setup available to us.

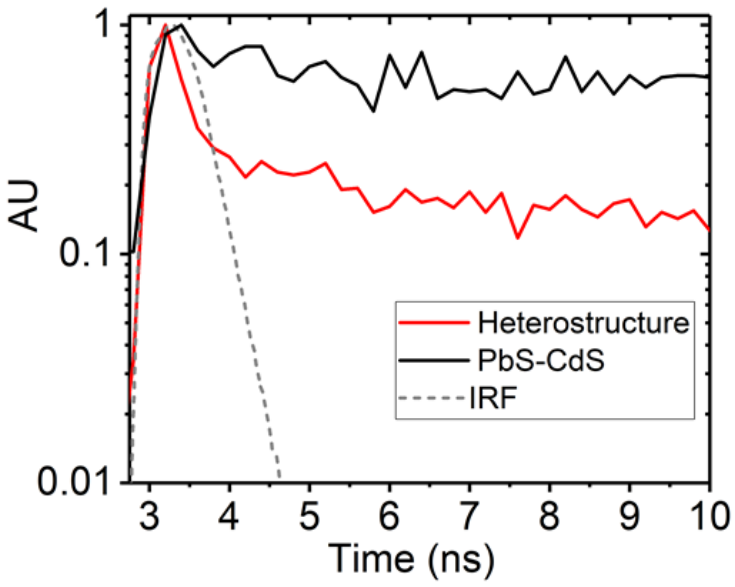

Figure 6.12: QD and heterostructure NIR TRPL decay spectra. QD TRPL decay spectra of heterostructure (red) and bare substrate (black) measured with 509 nm pulsed excitation at 0.5 MHz. The early time signal in heterostructure PL decay convoluted with IRF confirms that ET phenomenon faster than resolution of TCSPC setup available for this study.

6.4.1 Comparing Time Resolved and Steady State PL measurements

Steady state PL measurements provide information on the spectral changes that occur in the WS_2 monolayer PL from the pristine to heterostructure case. Also, comparing steady state PL with TRPL data at similar excitation intensity provides a better understanding of exciton recombination pathways present in the heterostructure.

Figure 6.13.*a* shows a scatter plot of monolayer WS_2 (visible) PL integrals (*y*-axis) with the corresponding PL peak wavelengths (*x*-axis), extracted from spatial PL maps of the sample in pristine (blue) and heterostructure (red) forms. Figure 6.13.*d* shows the 64 μm × 48 μm rectangular region (orange dashed line) within the monolayer (red dashed line) where PL maps were taken before and after QD deposition. A spatial resolution of 2 μm × 2 μm was used. PL maps were measured with a 514 nm continuous wave (CW) laser excitation at 80.2 W cm^{-2} intensity for good signal to noise ratio. It is known that different types of excitons exist in atomically thin nanomaterials (*i.e.*, monolayer WS_2). Accordingly, it is of importance to understand how different types of excitons behave and contribute differently when ET occurs. We begin with analysing steady state PL spectra as it gives an indication of the types of excitons present. Figure 6.13.*b* shows the PL spectra of an exemplary point on the monolayer in pristine (blue) and heterostructure (red) form. The spectra were deconvoluted with Gaussian peaks, which represent the neutral exciton (NE) and lower energy species (X_2) such as trions, which are characterised by broad low energy features in monolayer TMD spectra.[11,27] X_2 may also arise from eventual radiative recombination of neutral excitons trapped in sub-gap states. Upon recombination to the ground state, these excitons can bind with electrons to form trions, which is known to occur in *n*-type TMDs such as WS_2. [27,59]

Figure 6.13.*c* shows the fitted time resolved PL of pristine (blue) and heterostructure (red) cases at high excitation intensity (3.2 μJ cm^{-2} → 63.4 W cm^{-2}). Table 6.2 shows the fitted PL lifetimes (τ) of pristine and heterostructure samples at low and high intensity excitation and ET efficiencies. ET efficiencies were computed *via* equation 6.13. We verify the use of equation 6.12 with a full derivation provided in Appendix 2. Heterostructure lifetimes are denoted by an apostrophe. Given that the fast component of the heterostructure's WS_2 PL lifetime (τ_1') is limited by the IRF, the fitted values presented in table 6.2 represent an upper bound.

$$\eta_{ET} = 1 - \frac{\tau_1'}{\tau_1} \tag{6.13}$$

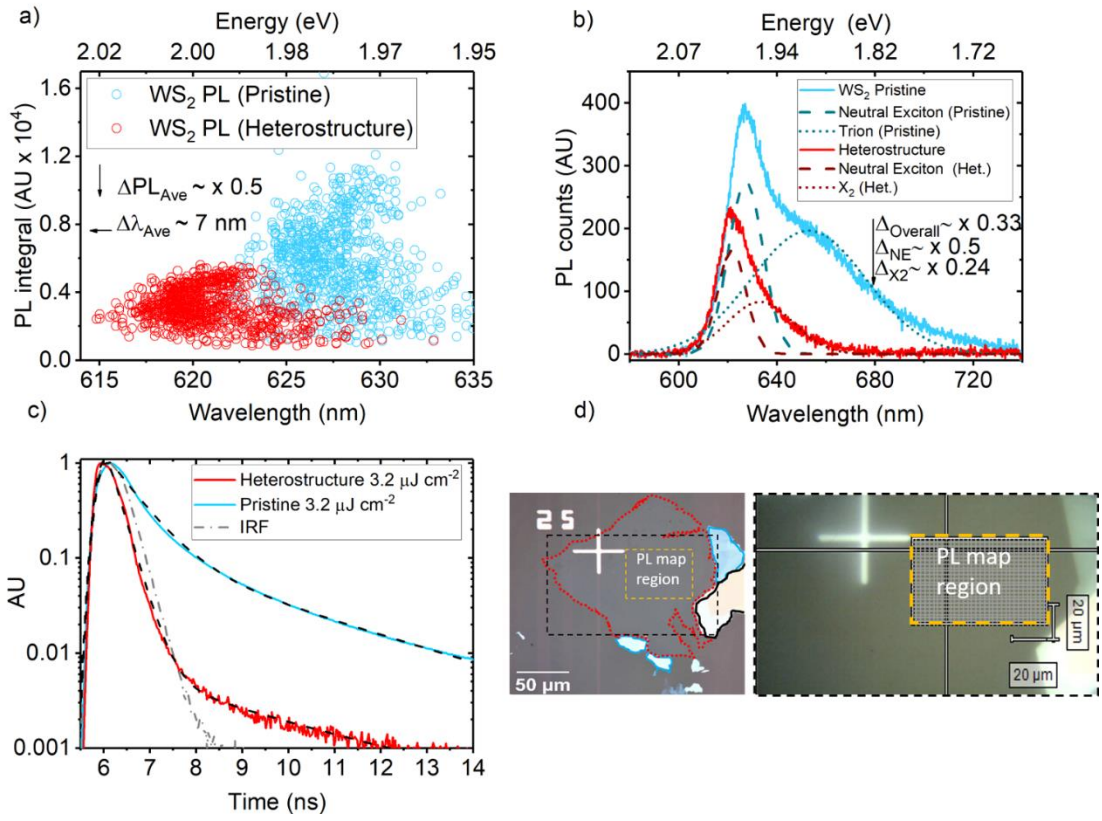

Figure 6.13: Comparing PL and TRPL spectra of pristine and heterostructure samples. **a)** Scatter plots of monolayer WS_2 (visible) PL integrals and the corresponding PL peak wavelengths extracted from spatial PL maps of the sample in pristine (blue) and heterostructure (red) form. PL measured with 514 nm continuous wave (CW) laser excitation at 80.2 W cm^{-2} intensity; **b)** WS_2 PL spectra of an exemplary on the monolayer in pristine (blue) and heterostructure (red) cases. Spectra are deconvoluted with Gaussian peaks which represent the neutral exciton (dashed lines) and a lower energy species X_2 (dotted lines); **c)** TRPL decay spectra of pristine (blue) and heterostructure (red), measured with 509 nm excitation at 63.4 W cm^{-2} intensity. Black dashed lines represent decay fits. IRF given by grey dot-dash line; **d)** Monolayer is outlined with red dashed line on LHS. RHS shows 64 μm x 48 μm rectangular PL map region (orange dashed line).

Table 6.2: Fitted PL lifetimes of pristine and heterostructure samples and resulting estimates for ET efficiencies. Fast components of WS_2 PL decay in heterostructure τ_1' and transfer efficiencies η_{ET} represent upper and lower bound values respectively due to limitations in instrument sensitivity. High intensity excitation values used for comparison with steady state PL are italicised.

Intensity	Pristine $\boldsymbol{\tau_1}$	Heterostructure $\boldsymbol{\tau_1'}$	Pristine $\boldsymbol{\tau_2}$	Heterostructure $\boldsymbol{\tau_2'}$	$\boldsymbol{\eta_{ET}}$
0.21 W cm^{-2}	0.456 ns	0.26 ns	3.63 ns	3.64 ns	42%
63.4 W cm^{-2}	*0.62 ns*	*0.26 ns*	*2.95 ns*	*2.9 ns*	*58%*

Statistical analysis of the scatter data in Figure 6.13.*a* reveals an average PL quenching, ΔPL_{AVE} ~ 50%, and spectral blue shift $\Delta\lambda_{AVE}$ ~ 7 nm from the pristine to the heterostructure case. The spectra in Figure 6.13.b shows that the NE component quenches by 50%, whereas X_2 quenches by 76%. An overall quenching of 67% was computed from the raw PL spectra. The large X_2 quenching helps to explain the spectral narrowing in the red signal and the general blue shift in Figure 6.13.*a*. Interestingly, the difference in quenching between the NE and X_2 species leaves 26% of quenched excitons unaccounted for. This implies an additional exciton recombination pathway. As X_2 may arise from slow exciton recombination from trap states, the excess quenching of X_2 excitons could be explained as non-radiative trap→QD transfer. Table 6.2 however reveals that the slow decay component (τ_2) associated with trap-ground state transition remains practically unchanged between the pristine and heterostructure case for a given excitation intensity, *i.e.*, $\tau_2 \sim \tau_2'$. WS_2 trap state to QD exciton transfer requires that $\tau_2' < \tau_2$ and therefore negates this possibility. This suggests that the excess quenched excitons may dissipate *via* some other non-radiative pathway.

On the other hand, table 6.2 shows that the fast component of the bi-exponential decay, which is associated with neutral exciton recombination,[27] is quenched by 58% from τ_1~0.62 ns in the pristine monolayer to τ_1' ~0.26 ns in the heterostructure case. This lies in close agreement to the 50% NE quenching estimated in steady state PL. The strong fast PL decay lifetime quenching shows that ET occurs *via* neutral excitons transitioning from the WS_2 band edge to the QD acceptor, while intrinsic exciton trapping in the donor and other non-radiative losses compete with this process. This justifies the use of fast decay components (τ_1, τ_1') to compute the lower bound ET efficiencies shown in table 6.2

via equation 6.13. As previously highlighted, exciton trapping and de-trapping in the donor gives rise to increasing τ_1 as a function of fluence, which manifests as an apparent increase in η_{ET} as a function of fluence. While non-radiative pathways are yet to be uncovered, passivating trap states to improve donor PLQE should lead to more efficient ET from the WS_2 donor band edge to the QD acceptor.

Figure 6.14 below provides a clear illustration of radiative exciton pathways in pristine (LHS) and heterostructure (RHS) cases, derived from the PL/TRPL comparison in Figure 6.13.a-c and supported by the TRPL fluence series in Figure 6.11.

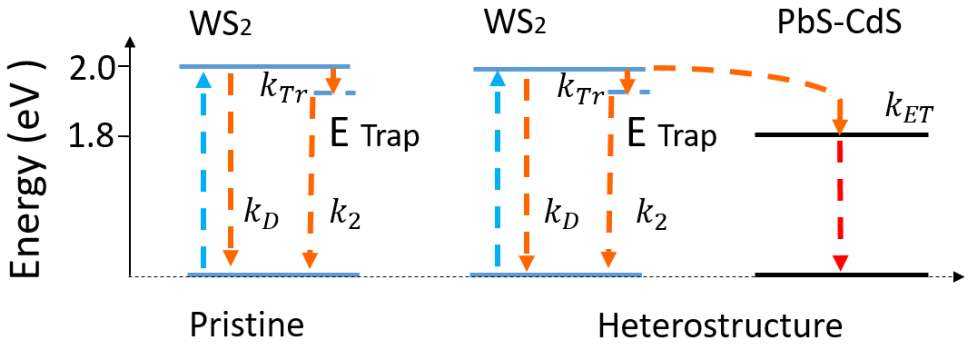

Figure 6.14: Radiative exciton pathways in pristine WS_2 and heterostructure. Energy level diagram illustrating radiative exciton pathways in pristine WS_2 (LHS) and in heterostructure (RHS). Blue arrows represent initial excitation, orange arrows represent WS_2 excitons and red arrows represent down-shifted excitons that recombine at lower energy in the PbS-CdS QD.

In pristine WS_2, upon excitation from the ground state, a proportion of excitons instantaneously transition from the band edge to trap states on the order of few picoseconds[91] at trapping rate k_{TR}, while others recombine radiatively from the band edge to ground state at the rate k_D. Those excitons that are trapped in sub-gap states radiatively recombine to the ground state over long periods on the order of nanoseconds [91] at rate k_2. In the heterostructure, excitons preferentially transfer from the WS_2 band edge to the QD at rate k_{ET}, such that $k_{ET} > k_{TR}$, thus quenching the fast component τ_1 lifetime below the IRF. This also explains the sizeable quenching of X_2 in the steady state PL spectra (Figure 6.13.*b*) as there are fewer excitons being trapped in the presence of an acceptor QD. Band edge excitons that are not trapped, transferred or lost *via* some other non-radiative process, recombine radiatively to the ground state at k_D over tens to hundreds of picoseconds,[71] which is below the instrument response. The remaining emission from direct band edge recombination as shown in Figure 6.13.*b*, strongly suggests that the 2D→QD transfer pathway becomes saturated. As with trap states, the QD band edge can

become saturated, forbidding further incoming excitons, which may return to the WS_2 band-edge and radiatively recombine or dissipate *via* a non-radiative process as suggested by the `lost' quenched excitons identified from Figure 6.13.*b*.

6.5 Summary of Optical Characterisation Measurements

To summarise the results from optical measurements presented, PLE studies confirm ET from monolayer 2D WS_2 to 0D QDs. Further PLE studies on heterostructures with differing surface attachment thiol ligands show ET. Whereas all ligand lengths lie within tunnelling distances favourable for DET (< 1 nm), the large oscillator strengths of the 2D TMD donor and QD acceptor favour FRET, as given by the large theoretical Förster radius computed. The CdS shell surrounding the PbS core in the QDs provides an additional tunnelling barrier, thus supporting FRET as the dominant ET process observed. Time resolved PL provide further confirmation of non-radiative ET by virtue of strong quenching of donor WS_2 PL in the presence of the acceptor QDs. TRPL studies also strongly indicate that this transfer process is faster than intrinsic early time trapping of excitons in the WS_2 monolayer, which would otherwise lead to radiative or non-radiative exciton recombination *via* trap states in the pristine monolayer. Comparing high excitation intensity PL and TRPL measurements provides a clearer understanding of radiative recombination pathways for excitons in the TMD-QD heterostructure. The comparison implies that intrinsic exciton trapping in the TMD monolayer and a non-radiative process compete with ET from 2D to QD. Further analysis also suggests that the exciton transfer channel can become saturated at high excitation intensities.

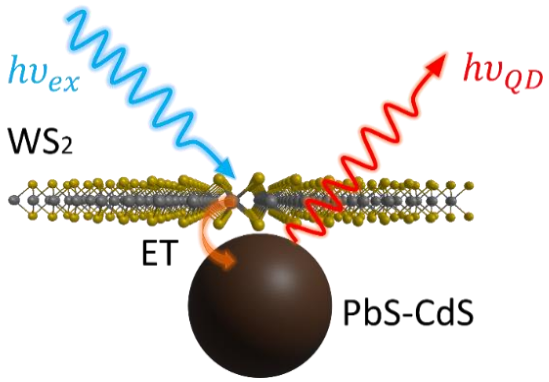

Figure 6.15: Illustration of ET process in 2D-QD heterostructure

6.6 Conclusions

In conclusion, we have demonstrated the ability to transfer excitons from monolayer WS_2 to NIR PbS-CdS QD emitters. PLE studies provide confirmation of ET, with 58% of QD PL donated by monolayer WS_2. The large oscillator strengths of the donor TMD and acceptor QD lead to a large Förster radius, suggesting FRET as the dominant ET mechanism. TRPL studies reveal that the ET process is faster than intrinsic exciton trapping in monolayer WS_2. A comparative study between high excitation steady state PL and TRPL confirms exciton transfer from the WS_2 band edge to the PbS-CdS band edge, while intrinsic exciton trapping in the donor and other non-radiative channels act as competing pathways. Residual emission from the donor in the heterostructure suggests that the ET pathway can be saturated at high excitation intensities. Future studies of such heterostructures could provide a clearer understanding of non-radiative loss mechanisms *via* more sensitive methods such as femtosecond transient absorption (TA) and high resolution TRPL. Trap state passivation *via* monolayer TMD surface treatments can be used to drastically reduce exciton trapping rates, not only enhancing ET, but isolating non-radiative loss pathways so that they can be better understood. The TMD/QD heterostructures demonstrated here combine the high absorption cross-section of monolayer TMDs with the high quality and highly tuneable optical properties of QDs. The ability to tune emission properties of monolayer TMDs using high PLQE QD emitters has potential device applications in areas such as in light emitting technologies namely displays and solid-state lighting and lasers.[32,182] Such structures could also be used to read out the state of TMD devices optically in various logic and computing applications. The heterostructure could also be integrated into artificial light harvesting systems such as luminescent solar concentrators (LSCs) for the purposes of enhancing light capture in conventional PV technologies. This concept is developed further in the next chapter.

6.7 Methods

6.7.1 Quantum Dot Synthesis

Lead-sulphide/cadmium sulphide QDs were synthesised by Dr. James Xiao using previously reported methods with slight modifications. PbS QD synthesis was carried out following Hines & Scholes,[195] and cation exchange for CdS encapsulation was performed using the technique described by Neo *et al.*[192] All chemicals were purchased from Sigma Aldrcih or Romil and used as received. Full details of the synthesis proccess can be found in the published article.[29]

6.7.2 Steady State Optical Characterisation

6.7.2.1 Absorption and PL Spectroscopy

The absorption spectrum of colloidal QDs shown in Figure 6.2.*b* was measured using a Shimadzu UV-VIS spectrometer. 0.1 mg/ml solution of colloidal QDs in toluene in a 1 cm cuvette was placed in an integrating sphere. An identical cuvette filled with toluene was used as a reference. Steady state QD PL in the same figure was obtained using a fluororemter (Edinburgh Instruments), with 0.1 mg/ml solution deposited in a 1 mm cuvette. Excitation wavelength was set to 500 nm and PL was detected with an indium gallium arsenide (InGaAS) array.

6.7.2.2 Steady state Absorption Microscopy

The absorption spectrum of monolayer WS_2 on quartz substrate was measured with a Zeiss axiovert inverted microscope in transmission using a halogen white light source *via* Zeiss EC Epiplan Apochromat 50x objective (numerical aperture (NA) = 0.95) forming a wide-field collection area diameter of 10 μm. Light transmitted *via* the sample was split with a beam splitter, with one component directed to a CCD camera (DCC3240C, Thorlabs) and the other coupled to a UV 600 nm optical fibre (200-800 nm spectral range) connected to a spectrometer (Avaspec-HS2048, Avantes).

6.7.2.3 Steady state Photoluminescence Microscopy

PL microscopy was performed using a Renishaw Invia confocal setup equipped with motorized piezo stage. Laser excitation was from an air-cooled Ar-ion (Argon ion) 514.5 nm continuous wave (CW) laser *via* 50x objective (NA = 0.75). The sample was excited upside down to ensure that the monolayer was excited first *via* the thin substrate to avoid shadowing by the QDs once deposited. Signals were collected in reflection *via* notch filter. The diffraction limited beam spot size was estimated as 0.84 μm. PL signal was dispersed *via* 600 l/mm grating prior to detection with inbuilt CCD detector. Laser power was measured directly *via* 5x objective with a Thorlabs S130C photodiode and PM100D power meter. The detection wavelength range for PL measurements were selected using the setup's inbuilt WIRE software. The Vis-NIR PL spectrum (Figure 6.4) was generated with 10 s integration at a single spot on the heterostructure. The corresponding QD PL spectrum was taken at a location away from the heterostructure. The NIR PL map (Figure 6.5.*a.*) was generated with 8 μm resolution and 2 s integration. The Vis PL maps from which scatter data in figure 6.13.a were derived, was generated with 2 μm resolution and 0.5 s integration. All PL microscopy measurements were performed at 0.44 μW (80.2 W/cm^2).

Excitonic species shown in Figure 6.13.b were deconvoluted from pristine and heterostructure PL spectra using a procedure written in Matlab. The code incorporates the `gauss2' two Gaussian model fit. Further information on the Gaussian model is available *via* the mathsworks website.

6.7.2.4 Photoluminescence Excitation Microscopy

PLE measurements were performed using a custom-built inverted PL microscope setup. The inverted microscope arrangement enabled excitation of WS_2 monolayer first *via* the thin glass slide hence avoiding shadowing by the QDs. Variable wavelength excitation was provided by a pulsed super continuum white light source (Fianium Whitelase) *via* a Bentham TMc 300 monochromator. The optical image of the heterostructure was acquired using 600 nm laser light at low power *via* 60x oil objective, producing a 200 μm circular wide field image on an EMCCD camera (Photometrics QuantEM^{TM} 512SC). A QD PL image of the heterostructure was obtained by filtering out the excitation wavelengths using a combination of 750 nm and 800 nm long pass filters.

Further precaution was taken to remove any long wave component in the excitation line using a 750 nm short pass filter. An example of the QD PL image is shown below in Figure 6.16, which was recorded using 620 nm excitation at 10 MHz pulse rate (~0.006 μJ/cm^2 fluence) and 20 s integration time. The region of interest was isolated by closing an iris in the detection line just before the camera.

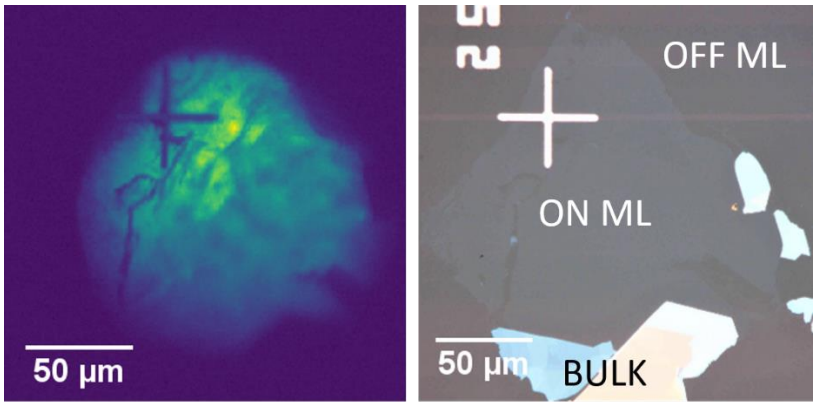

Figure 6.16: Heterostructure FRET image. Heterostructure QD PL image at 620 nm (LHS) excitation and monolayer optical image (RHS). QD PL clearly enhanced on TMD monolayer.

The procedure for obtaining PLE spectra are as follows: i) The laser excitation *via* the monochromator was swept between the visible and NIR range. Given that the optics in the system were optimized for 600 nm and above, excitation was varied between 580 nm and 710 nm with 2 nm resolution. Each excitation was integrated for 20 s using 10 MHz pulses; ii) the wide field PL signal at each excitation was recorded, producing a spectrum of raw PL signal as a function of excitation wavelength; iii) the background signal was obtained by covering the detector and repeating i)-ii). The excitation power was recorded simultaneously using a Thorlabs S130C photodiode placed in the excitation line just before the sample, and a PM100D power meter interfaced with data logging software; iv) finally, the raw data was post-processed in Origin where the background spectrum was subtracted from the raw PL spectrum and normalized by the number of photons injected at each wavelength. Finally, the PLE spectrum was corrected with a system calibration file based on the PLE and absorption spectra of a high PLQE NIR dye. We note that the camera, monochromator, and power meter are controlled externally *via* the data logging software interface written in Python.

6.7.3 Time Resolved Photoluminescence Microscopy

TRPL measurements were performed with an industry standard PicoQuant Microtime 200 confocal time correlated single photon counting (TCSPC) setup using a 509 nm pulsed laser excitation *via* an inverted 20x air objective (NA = 0.4), with estimated diffraction limited spot size of 1.55 μm. The repetition rate was set to 20 MHz with 25 ps resolution to obtain PL decay data. Signals were collected in transmission and detected with a single photon avalanche diode (SPAD). Laser excitation was filtered out with a 510 nm long pass, and the NIR region of both pristine and heterostructure PL were filtered out using a 700 nm short pass filter, allowing for collection of WS_2 PL only. All signals were scaled up to 1500 s, which was used on the lowest fluence measurement in the fluence series. Power was measured using an inbuilt photodetector at each fluence, which was previously calibrated in the same experimental conditions using a standard external power-meter. Care was taken to ensure that measurements were made on the same spot on the monolayer before and after QD deposition. The instrument response function was measured with a blank glass cover slide. PL decay time constants were fitted using a model developed in Origin, which consists of a Gaussian (as the IRF) convoluted with a double exponential decay.

7 Simulating Light harvesting with 2D-QD based LSC

We develop the concept of a luminescent solar concentrator (LSC) based on the previously characterised 2D-QD heterostructure using Monte Carlo (MC) light transport simulations. The heterostructure's perceived potential as LSC luminophore material is inspired by the large Stokes shift between 2D transition metal dichalcogenide (TMD) absorption and quantum dot (QD) emission spectra. Such a large Stokes shift promises minimal losses associated with reabsorption *i.e.*, escape cone and non-radiative losses, potentially boosting LSC efficiencies and concentration factors. Here, we consider a heterostructure luminophore system comprised of monolayer tungsten disulphide (WS_2) and near infrared (NIR) PbS-CdS (1.24 eV) QDs. Using an idealised heterostructure luminophore model, we simulate LSCs under direct solar irradiation. From this we obtain optical performance parameters, and a visual representation of photon transport *via* raytracing. A key model assumption dictates absorption by the TMD and emission by the QD only, with zero absorption or reabsorption by the QD. Comparisons are made to typical luminophore materials, namely Lumogen Red 305 (LR305) dye and a NIR PbS-CdS (1.37 eV) QD, both of which have spectral overlap. LSC performance parameters are computed as a function of luminophore concentration under unity and sub-unity (80%) luminophore quantum yield (QY) conditions. Simulation results reveal superior all-round performance with the heterostructure, which emphasizes the importance of the large Stokes shift. The physical validity of heterostructure model is appraised. From this we identify the model's limitations and offer further suggestions to improve its physical validity for future development of a computational tool for heterostructure LSC design.

7.1 Background & Motivation

Luminescent solar concentrators (LSCs) are examples of light management technologies that are intended to enhance light capture in silicon-based photovoltaics (PV). The basics of LSCs have been introduced in Chapter 2. As discussed there, typically, LSCs are square slabs of transparent waveguide material, such as PMMA, doped with luminophores, which absorb incident light and emit PL. The emission is waveguided by internal reflection and concentrated at the LSC edges, where PV panels of reduced size are located. The concentration of incoming photon flux enables reduced PV panel area. LSCs can concentrate diffuse light and are insensitive to the directionality of incoming photons, potentially providing major cost reductions for standard PV systems that rely on solar tracking for optimized light capture. The key limitations to LSC development are the optical losses associated with the waveguide and luminophore material. Losses attributed to the luminophore include photon reabsorption and sub-unity PL quantum yields (QY). Reabsorption is characterised by an overlap between a luminophore's absorption and emission spectra. Reabsorption aggravates nonradiative (NRD) losses, with sub-unity QY luminophores, and escape cone (EC) losses. EC losses arise due to emission directed below the waveguide's critical angle. Reabsorption can be eliminated by engineering a large Stoke's shift between absorption and emission. We consider the previously studied 2D-QD ET heterostructure to be a potentially viable LSC luminophore. With correct engineering, the system could be fine-tuned for predominant absorption by the 2D monolayer and emission by the QD respectively, forcing a large enough stokes shift. To give credence to our projection, we simulate light transport in LSCs based on WS_2/PbS-CdS (1.24 eV) heterostructures using the Monte Carlo (MC) method described in Chapter 3, section 3.4. We also simulate LSCs based on luminophores with lower Stoke's shift for compassion, namely Lumogen R305 (LR305) and PbS-CdS (1.37 eV) NIR emitting nanocrystal QDs.

7.2 Details of Study

This study is split into two parts. In part I, we perform a parameter study where we investigate the effects of varying luminophore concentrations on LSC optical efficiencies (η_{opt}), assuming unity and sub-unity (80%) QY. We then explore the internal efficiencies and loss mechanisms for each LSC type. Part I uses a non-raytracing code written by Rowan McQueen[153] in Matlab for its ability to process large arrays of input parameters. In part II, we visualise photon transport for each LSC type with fixed luminophore concentrations. Part II employs the ray-tracing algorithm described in chapter 3, section 3.4.1. For the same input data, the two algorithms show close agreement, within 1% error (See Appendix 2). To supplement part II, a more physically accurate visualization of photon transport in a heterostructure LSC is provided using raytracing software developed by Tomi Baikie. The general simulation assumptions are detailed in chapter 3, section 3.4.1.2. An additional set of assumptions are included for modelling the heterostructure luminophore, as detailed below:

- The 2D TMD component of the heterostructure has a characteristic dimension of 50 nm, which lies within the range for large area liquid phase exfoliated monolayers.[196] For simplicity, we assume square monolayers with no defects.
- Heterostructures are assumed to have an extremely low concentration of QDs, such that photons are absorbed exclusively by the 2D and emitted by the QDs, forcing the large Stoke's shift. This is justified by the fact that the absorption cross section of monolayer WS_2 exceeds the PbS-CdS QD in the visible region, as previously established.[29] Also, the sheer difference in projected area between a large WS_2 monolayer (~50 nm) and an individual QD (~ 3.3 nm) tells us that the monolayer will absorb a much larger proportion of an incoming photon flux. Any light absorbed by the QD is considered negligible in comparison.
- 100% FRET efficiency from 2D to QD.
- The LSC optical cavity is a square waveguide with side length, L = 100 cm, and thickness d = 1 cm, giving a geometric ratio (G = L/4d) of 25. An LSC of these dimensions could be used in a building façade.

N.B: LR305 extinction data was measured previously by Dr. Nathaniel Davis. Details of WS_2 Monolayer molar extinction estimations are given in Appendix 4. Extinction data for PbS-CdS (1.37) eV QDs was estimated in Chapter 6, section 6.3.1.

7.3 Part I: Parameter Study

Figure 7.1.*a-c* shows the input molar extinction and emission data for LR305, PbS-CdS (1.37 eV) QDs and the 2D-QD heterostructure. The Stokes shift, that is the difference between the lowest energy excitonic peaks and emission peaks are calculated as 36 nm, 196 nm, and 385 nm for LR305, PbS-CdS (1.37 eV) QDs and the heterostructure, respectively.

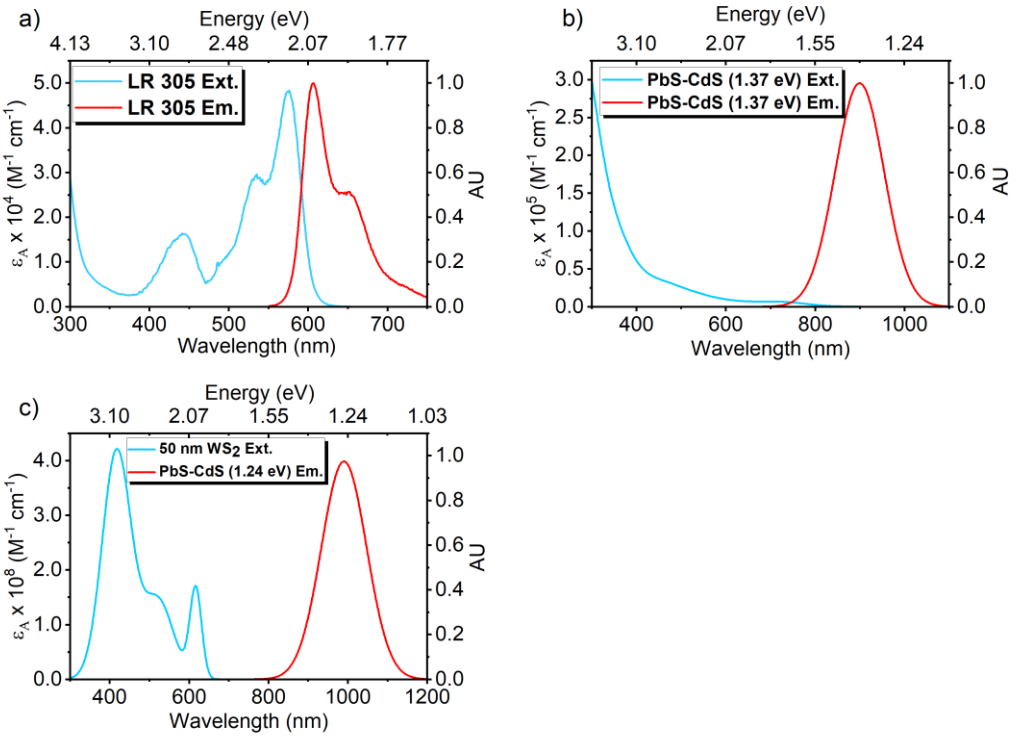

Figure 7.1: LSC simulation input luminophore extinction and emission data. a) LR305; b) PbS-CdS (1.37 eV); c) WS_2/ PbS-CdS (1.24 eV).

LSC Optical efficiency, η_{opt} is the ratio of edge photon flux, Φ_2, to incident photon flux on the LSC planar surface, Φ_1, ($\eta_{opt} = \Phi_2/\Phi_1$). Figure 7.2 shows η_{opt}, as a function of luminophore concentration for LR305 (red), PbS-CdS (black) and the heterostructure (blue). Solid lines and dashed lines represent unity and sub-unity (80%) QY conditions, respectively. A practical Luminophore concentration range between 1 μM – 1 M is defined. We refer to η_{opt} values at 0.18 mM (dotted vertical line) for comparison between unity and sub-unity QY conditions.

LR305 presents the bench-mark case, having the lowest Stokes shift and extinction values. At unity QY, η_{opt} increases to an optimum value of ~20 % at ~0.3 mM and reduces gradually due to a rise in EC losses induced by higher rates of reabsorption

with increasing concentrations. Optical losses are intensified when non-radiative losses are accounted for (QY = 80%). The combination of EC and non-radiative events causes an 8% drop in η_{opt} at 0.18 mM and a steeper decline thereafter. To verify validity of the simulations, we note that the calculated optical efficiency at 0.2 mM (η_{opt} ~ 18.9%) matches closely with LR305 LSC performance measurements and simulations by Vishwanathan *et al.*[197] The authors reported simulated and experimental results of η_{opt}~18% and 19% respectively for QY = 95%.

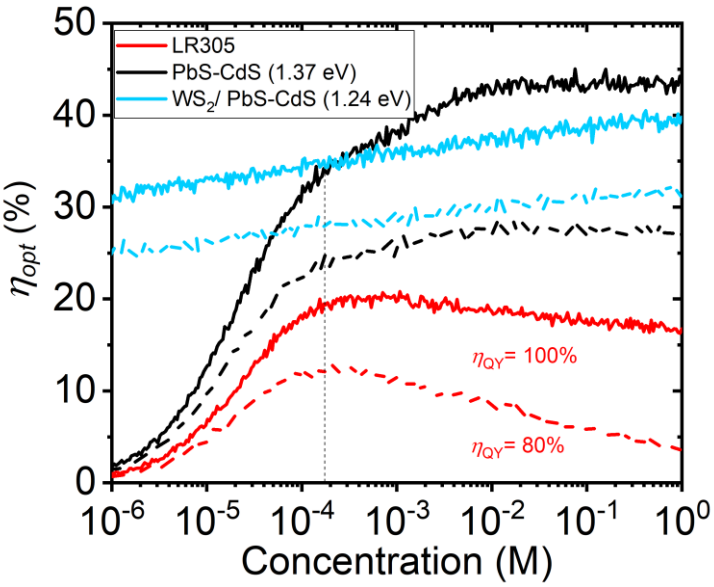

Figure 7.2: Graph of optical efficiency, η_{opt}, as a function of luminophore concentration at unity and sub-unity luminophore QY. Trends for LR305, PbS-CdS (1.37 eV) and WS_2/ PbS-CdS (1.24 eV) given in red, black, and blue, respectively. Solid and dotted lines represent unity and sub-unity (80%) QY conditions. Vertical dotted line denotes 0.18 mM concentration.

The PbS-CdS (1.37 eV) luminophore presents the intermediate case, with sizeable Stokes shift and extinction values. For unity QY, there is a steep increase in η_{opt}. At higher concentrations η_{opt} attains a fairly constant value of ~42% - the maximum for all the cases simulated. This outcome is explained by the broad absorption spectrum of PbS-CdS shown in Figure 7.1.*b*. At high concentrations, PbS-CdS (1.37 eV) absorbs the most solar photons along the LSC cross section. Reabsorption in PbS-CdS however persists due to the small spectral overlap. Once non-radiative losses are factored in (QY = 80%), the effects of reabsorption are severe, reducing η_{opt} by ~12%, from ~36% to 24% at 0.18 mM. This shows that slightest spectral overlap can have significant undesirable impacts on optical performance.

For the heterostructure, unlike the other luminophores, considerably high η_{opt}, and hence concentration factors (C) are attainable at low material concentrations (*e.g.*, η_{opt} ~32.3% at 3.6 μM for QY = 100%), which has positive cost implications. This is owed to the large extinction values of 2D TMD absorber. The increase in η_{opt} is gradual, with no defined peak or constant value in the concentration range. In the unity QY case, absorbed photons experience a single emission event with no further reabsorption. Without reabsorption, EC losses are simply a function of the sub-critical emission angle imposed by the waveguide refractive index. Also, due to the absence of reabsorption, the heterostructure is least impacted by non-radiative losses for all concentrations simulated. Optical efficiency, η_{opt} decreases by ~6% from ~ 34% to 28% at 0.18 mM, and rises steadily, outperforming all other luminophores with QY = 80%.

We now look into the internal loss mechanisms as a function of luminophore concentration. Beforehand, we define Internal performance parameters. The reabsorption ratio, R^* is the ratio of reabsorbed photons to initially absorbed photons, abs_o. Internal quantum efficiency, η^* is the ratio of edge photons to abs_o, *i.e.*, $\eta^* = \Phi_2/abs_o$. Escape cone (EC) and nonradiative (NRD) losses are expressed as proportions of absorbed photons, *i.e.*, $EC^* = EC/abs_o$, and $NRD^* = NRD/abs_o$.

Figure 7.3.*a-d* shows the LSC internal performance parameters for luminophores with QY = 100%. In this instance, losses are attributed to escape cones (EC^*) only. Unsurprisingly, as shown in Figure 7.3.*a.*, LR305 is the most susceptible to reabsorption owing to the large spectral overlap (Figure 7.1.*a.*). From Figure 7.3.*b* we notice that as LR305 concentrations increase, amplified reabsorption causes a growth in EC^* (orange line) at the expense of a declining η^* (red line). We identify a point, $\eta^* = EC^*$, beyond which EC losses exceed edge photons. This further explains the gradual decline in η_{opt} shown in Figure 7.2 (solid red line). Figure 7.3.*a* (black line) shows that reabsorption (R^*) persists with PbS-CdS, which is due to the slight spectral overlap (Figure 7.1.*b*). The sizeable Stoke's shift however limits the extent of reabsorption, keeping η^* and EC^* fairly constant at high concentrations and maintaining EC^* desirably below η^* as shown in in Figure 7.3.*c*. For the heterostructure, Figure 7.3.*d* shows that η^* is constant at ~74.5%, outperforming the other luminophores. Again, due to the absence of reabsorption (Figure 7.3.*a*, blue line), EC losses are limited to the waveguide refractive index.

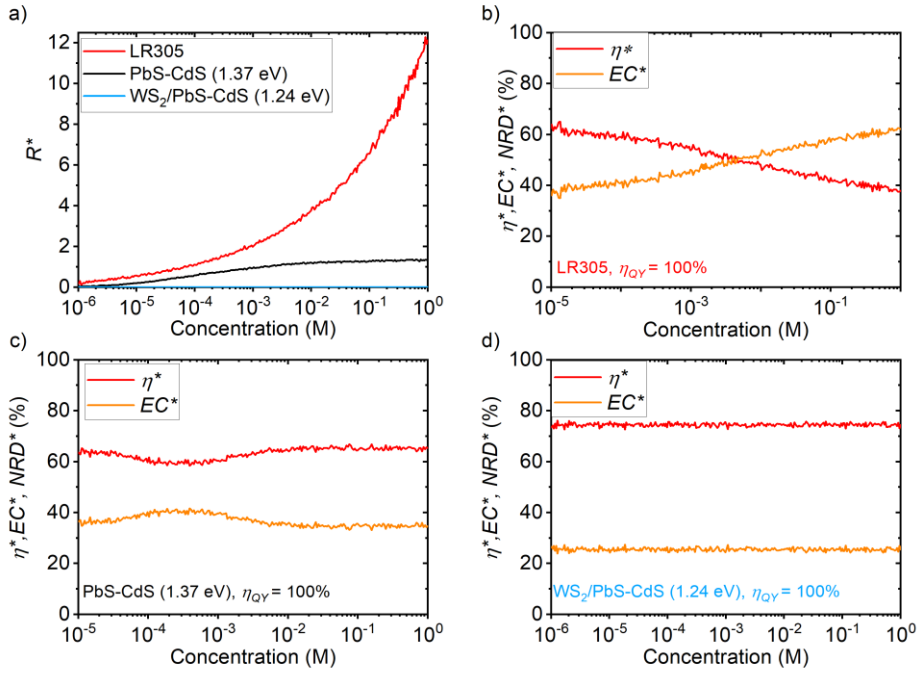

Figure 7.3: LSC internal performance parameters for luminophore QY = 100%. a) Ratio of reabsorbed to initially absorbed photons (R*) for LR305 (red), PbS-CdS (1.37 eV) (black) and WS_2/ PbS-CdS (1.24 eV) (blue) luminophores. (b-d) Internal quantum efficiencies (η*) (red), escape cone losses (EC*) (orange) as function of luminophore concentrations for (b) LR305, (c) PbS-CdS (1.37 eV) and (d) WS_2/ PbS-CdS (1.24 eV).

The internal performance parameters shown in Figure 7.4.*a-d* factor in non-radiative losses (QY = 80%). Comparing Figures 7.3.*a* and 7.4.*a*, there is a large reduction in R* with LR305. This is because further reabsorption is suppressed by non-radiative losses. Figure 7.4.*b* shows that the impact of non-radiative losses on LR305's η* values is profound. The large spectral overlap intensifies NRD*, which grows rapidly with concentration, dramatically exceeding the impact of EC* and quenching η*. With PbS-CdS (1.37 eV) R* is reduced slightly in the presence of non-radiative losses (Figure 7.4.*a*). Due to the slight spectral overlap (Figure 7.1.*b*), Figure 7.4.*c* shows that NRD* quickly becomes the dominant contributor to the decline in η* as QD concentrations increase. Considering the heterostructure, as shown in Figure 7.4.*d*, zero reabsorption ensures that NRD* and EC* losses are constant throughout the concentration range, being limited only to the luminophore QY and waveguide refractive index, respectively, leaving a favourable η* value of ~60% for all concentrations.

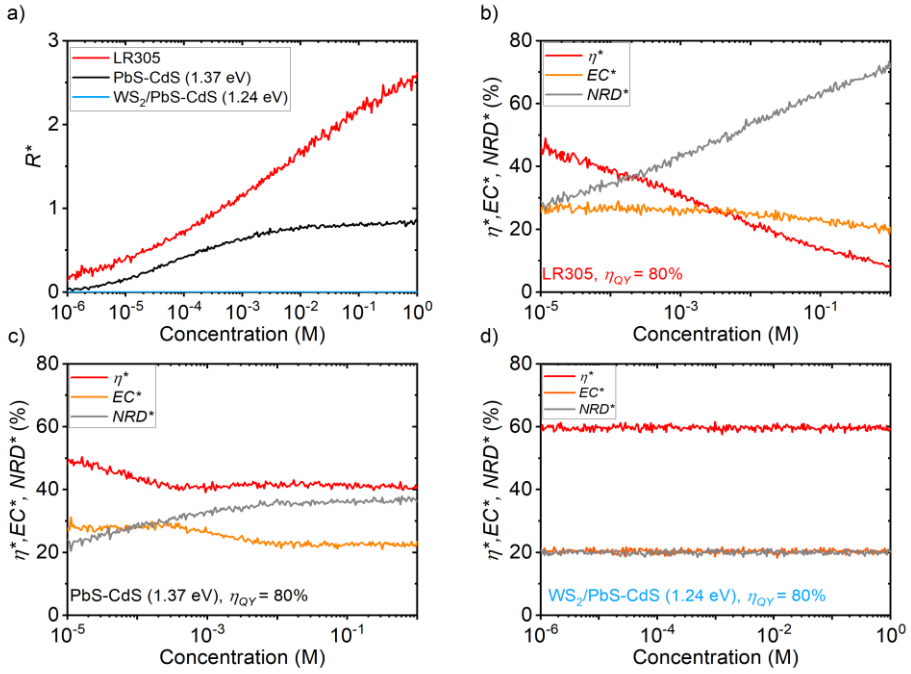

Figure 7.4: LSC internal performance parameters for luminophore QY = 80%. a) Ratio of reabsorbed to initially absorbed photons (*R**) for LR305 (red), PbS-CdS (1.37 eV) (black) and WS_2/ PbS-CdS (1.24 eV) (blue) luminophores. (b-d) Internal quantum efficiencies (η*) (red), escape cone losses (*EC**) (orange), non-radiative losses (*NRD**) (grey) as function of luminophore concentrations for (b) LR305, (c) PbS-CdS (1.37 eV) and (d) WS_2/ PbS-CdS (1.24 eV).

7.4 Part II: Visualising photon transport

Figures 7.5-7.7 overleaf show the paths of waveguided photons for each LSC, as calculated by the raytracing algorithm, initialized with 500 AM1.5G solar photons, unity QY and c = 0.18 mM. The top isometric views clearly show waveguiding to the edges and bottom cross-sectional views show the distribution of edge photons and escape cone losses. A larger density of edge photons is observed in the heterostructure and PbS-CdS (1.37 eV) LSCs compared to the LR305, which is simply due to their larger extinction values.

Table 7.1 summarises the LSC performance parameters corresponding to Figures 7.5-7.7 using 10,000 AM1.5G solar photons. Results for QY = 80% are also

included. Concentration factors are computed simply as $C = \eta_{opt} \times G$. The values presented can be verified in Figures 7.2-7.4.

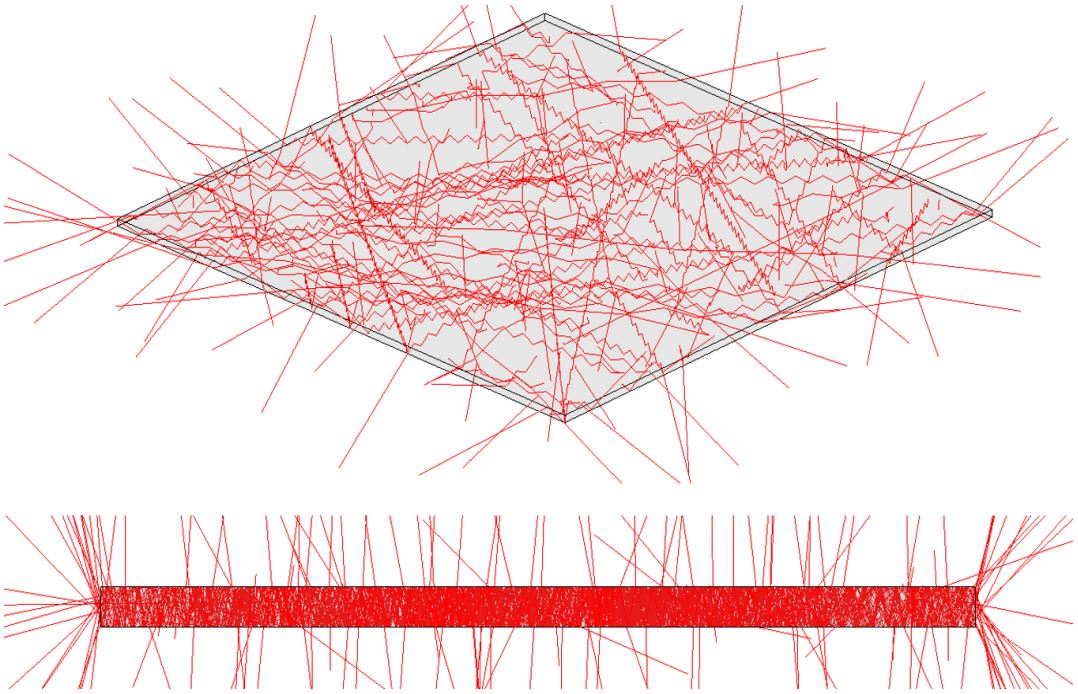

Figure 7.5: LR305 LSC raytracing graphics. (Top) isometric view of photon paths. (Bottom) cross sectional view of edge photons and top and bottom escape cone photons.

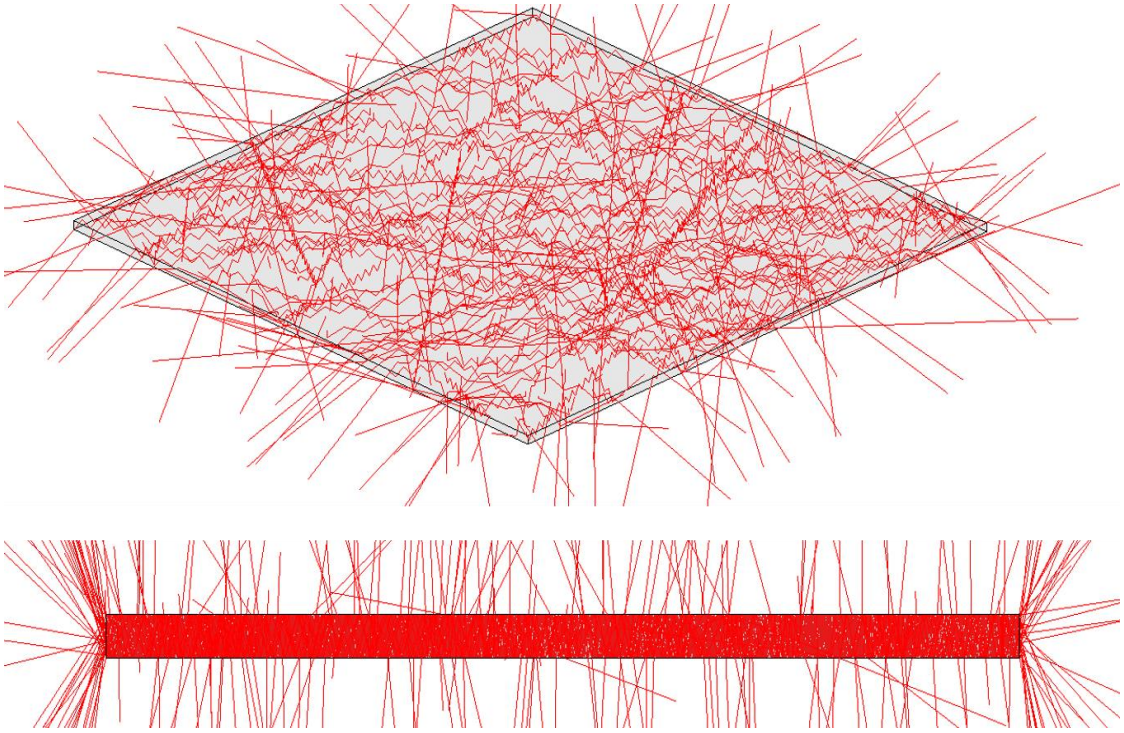

Figure 7.6: PbS-CdS (1.37 eV) LSC raytracing graphics. (Top) isometric view of photon paths. (Bottom) cross sectional view of edge photons and top and bottom escape cone photons.

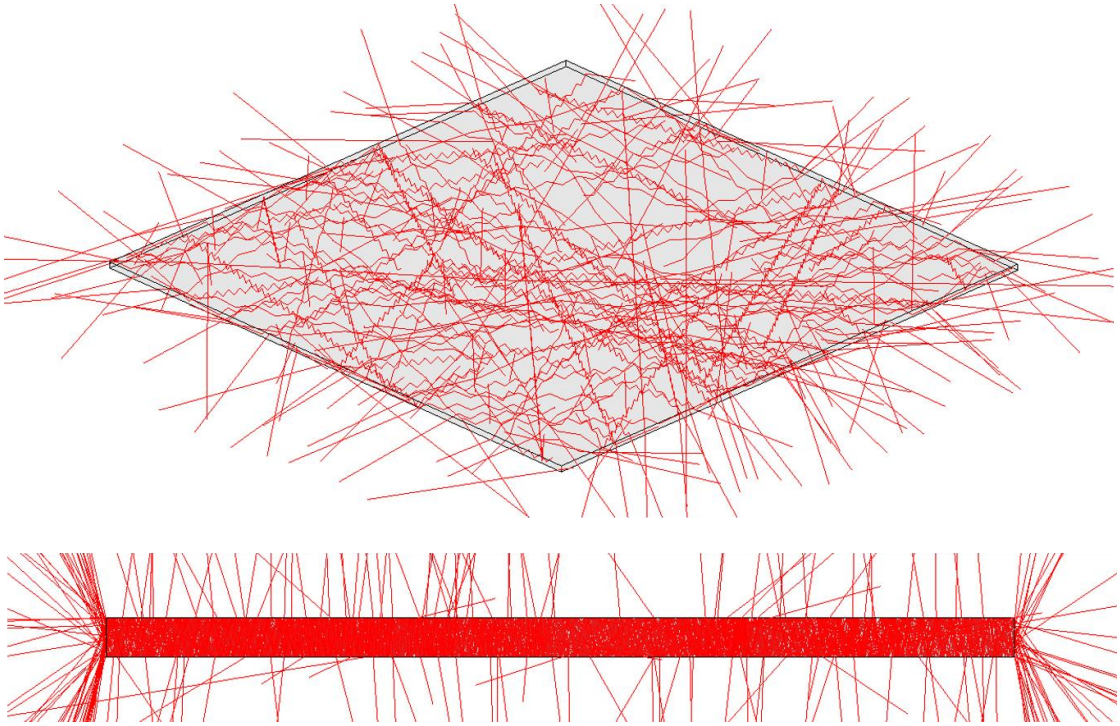

Figure 7.7: Heterostructure LSC raytracing graphics. (Top) isometric view of photon paths. (Bottom) cross sectional view of edge photons and top and bottom escape cone photons.

Table 7.1: Output performance data from raytracing simulations. Input parameters: 10,000 AM1.5G photons, 0.18 mM concentration.

QY = 100%					
Luminophore	η_{opt} *(%)*	*C*	*η* (%)*	*EC* (%)*	*NRD* (%)*
LR305	19.8	4.9	59.8	40.2	0.0
PbS-CdS (1.37 eV)	34.4	8.6	60.0	40.0	0.0
WS_2/ PbS-CdS (1.24 eV)	34.9	8.7	74.7	25.3	0.0
QY = 80%					
Luminophore	η_{opt} *(%)*	*C*	*η* (%)*	*EC* (%)*	*NRD* (%)*
LR305	11.9	3.0	36.2	26.9	36.9
PbS-CdS (1.37 eV)	23.8	6.0	41.6	28.0	30.4
WS_2/ PbS-CdS (1.24 eV)	27.6	6.9	59.6	20.4	20.0

Finally, Figure 7.8 shows photon transport in the WS_2/PbS-CdS (1.24 eV) heterostructure LSC, calculated with a more physically accurate simulator that factors contributions from partially (internally) reflected photons. As explained in section 3.4.1.2, partially reflected photons are those with an incidence angle, α slightly less than the critical angle, that is, $\alpha \sim \theta_{crit}$. These photons have some probability, $P<1$ of being internally reflected before being refracted *via* an escape cone after a number of waveguide reflections, and therefore stand a chance of being collected at an edge if emitted nearby. Efficiency gains from partially reflected photons are however minimal due to the high probability of EC transmission unless they are reabsorbed and emitted at $\alpha > \theta_{crit}$.[155]

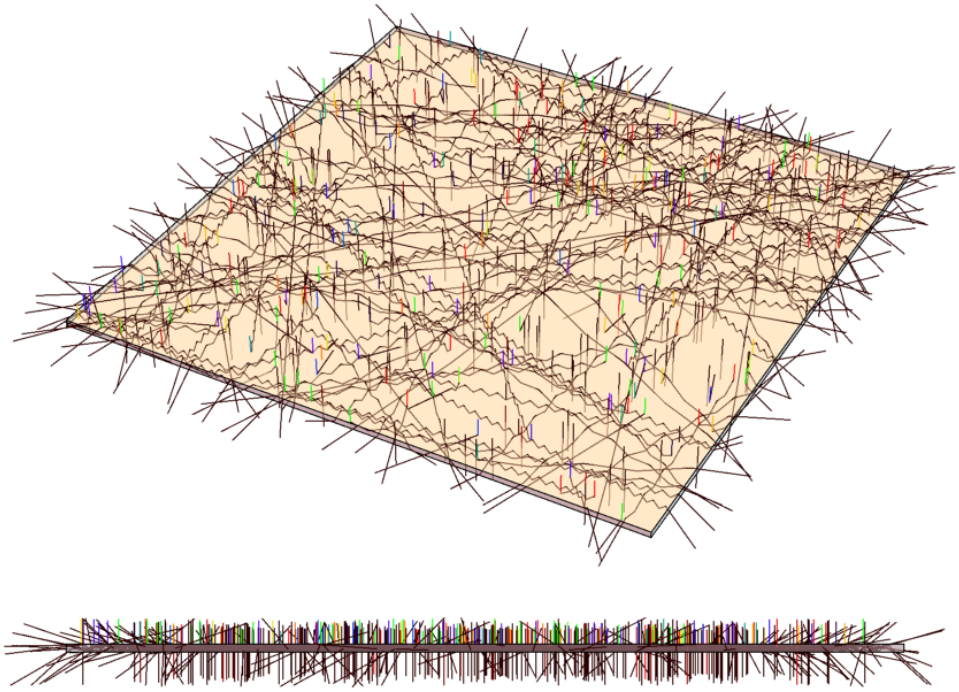

Figure 7.8: Supplementary Heterostructure LSC raytracing graphics. (Top) Isometric view of incoming photons and internally reflected NIR (black) photons. (Bottom) Cross-sectional view showing incident, reflected, transmitted and EC photons.

Input parameters were 10,000 AM1.5G solar photons, 3.6 μM concentration and unity QY. For clarity, 500 photon paths are displayed. Coloured rays represent visible photons. Black rays represent NIR photons. The isometric view shows the internal reflection paths clearly. The cross-sectional view shows incident, reflected, transmitted and, top and bottom EC photons. This simulation yields η_{opt} = 34% and η^*= 74%. This lies in close agreement with an equivalent simulation using the less complex raytracing algorithm developed herein which yields η_{opt} = 32.2% and η^*= 74.9%. The close agreement between simulations shows that the effects of partially reflected photons are

marginal, particularly in the case of the heterostructure model used, where reabsorption is assumed to be absent.

7.5 Summary and critical analysis

Light transport in LSCs based on LR305, PbS-CdS (1.37 eV) and heterostructure WS_2/PbS-CdS (1.24 eV) luminophores were simulated assuming unity and sub-unity (80%) luminophore QY and constant LSC geometric ratio (G = 25). Optical efficiencies η_{opt} and internal performance parameters were assessed as a function of luminophore concentration. Internal parameters include internal quantum efficiency (η*), escape cone losses (*EC**) and non-radiative losses (*NRD**). The simulations predict that the heterostructure LSC yields the best all-round optical performance due to the large absorption cross-section of the 2D WS_2 component, and importantly the large Stokes shift and zero overlap between its absorption and emission spectra. The heterostructure's large molar extinction values enable respectable optical efficiencies at low luminophore concentrations (~ few μM), with η_{opt} ~32.3 % and η_{opt} ~21% for QY = 100% and QY = 80% respectively. The heterostructure's zero spectral overlap eliminates reabsorption, limiting escape cones losses (*EC**) and non-radiative (*NRD**) losses to the wave-guide refractive index and luminophore QY, respectively. This results in favourable LSC internal efficiencies for all concentrations, with η* ~ 74.5% and η*~ 60% for QY = 100% and QY = 80% respectively, outperforming all other luminophores. A more physically accurate simulation of the heterostructure LSC shows that contributions from partially reflected photons are marginal, which is due to the lack of reabsorption. Where reabsorption may be present, efficiency gains from reabsorption of partially reflected photons may be apparent, however such gains are known to be slight.[155] In any case, for a real system with sub-unity QY, these gains will be counteracted.

The performance predictions for the heterostructure LSC's look promising chiefly due to the key assumption of zero absorption/reabsorption by the QD component. Strictly speaking, for a real system, even with low QD concentration per monolayer, there will be some reabsorption by the QDs, and increasingly so at higher luminophore concentrations. We therefore propose that the heterostructure model assumptions made herein are well suited for a heterostructure LSC with low luminophore concentrations, within the μM range, which we found yields favourable performance compared with the other luminophores. Going forward, a more refined heterostructure model that captures

reabsorption by the QD emitters should be developed. In doing so, the ratio of QD to 2D projected area to the incoming photon flux, should be factored in to predict the extent of absorption/ reabsorption by the QDs. For example, the projected area ratio χ could be attached to a probability of absorption by either species. A full understanding of the heterostructure's underlying photophysics is needed to refine the heterostructure model, which calls for further optical studies as concluded is the previous chapter. Ultimately, a heterostructure LSCs must be synthesised and tested to verify the validity of the model and resulting simulations. A realistic heterostructure model could serve as a powerful design tool for 2D-QD heterostructure based LSCs. Due to time constraints, the non-trivial tasks of synthesising heterostructure LSCs and refining the heterostructure model are recommended for future work.

7.6 Conclusions

In conclusion, the Monte Carlo light transport simulations predict that the WS_2/PbS-CdS (1.24 eV) heterostructure luminophores yield superior all-round LSC optical performance compared with LR305 dye and PbS-CdS (1.37 eV) nanocrystal luminophores for all concentrations simulated. This is due to the high molar extinction of the monolayer TMD component, zero spectral overlap between TMD absorption and QD emission and assumed absence of absorption/ reabsorption by the QD emitters as deemed appropriate for a low concentration of QDs per 2D monolayer. Realistically, since reabsorption by QDs is likely to become more significant at higher heterostructure concentrations, we rationalise that the heterostructure model used best approximates a heterostructure LSC with low luminophore concentrations. Towards simulating real behaviour of a heterostructure system, we recommend the development of a refined heterostructure model that factors in the ratio of QD to 2D TMD projected area to the incoming photon flux in order to quantify absorption/reabsorption by the QDs. The photophysics of the heterostructure must be fully uncovered to aid further model refinement. Importantly however, an actual heterostructure LSC must be developed and tested to verify the validity of the model. A physically accurate model could be a useful design tool for 2D-QD heterostructure based LSCs. Refining the heterostructure model and suspending the heterostructures in a polymer matrix to fabricate the LSC present formidable tasks worthy of further study at post-graduate level.

8 Summary and Outlook

8.1 Summary

The chemical stability, potentially high electronic mobilities, direct bandgap and (thus) strong light-coupling of a number of monolayer transition metal dichalcogenides (TMDs) hold great promise for future electronic and optoelectronic device applications. In spite of their promise, significant challenges to realising the full technological potential of 2D TMDs persist. A key challenge lies in the production of defect free, optically perfect material with high photoluminescence quantum efficiencies (PLQEs) (*or* PL quantum yields (PLQYs)). The prevalence of intrinsic defects in newly prepared TMD monolayers, either *via* mechanical cleavage or epitaxial growth, amounts to material of poor optical quality *i.e.*, low PLQE. Chalcogen vacancies, which are the most pervasive of such defects, are known to act as charge traps, where excitons quench non-radiatively due to charge separation, or form low PLQE trions with trapped charges. Vacancies also trap mobile charge carriers, hampering electronic mobilities.

Towards meeting the challenges posed by the detrimental effects of defects, Chapters 4-5 of this thesis detailed a novel chemical surface passivation technique based on oleic acid (OA) ligands. Unlike other treatments reported in the wider literature, OA is shown to enhance PL and transport characteristics in newly exfoliated (*i.e.*, pristine) sulphur and selenium group VI TMDs, tungsten disulphide (WS_2) and molybdenum diselenide ($MoSe_2$).

Chapter 4 compared the effects of OA and bis(trifluoromethane)sulfonimide (TFSI) treatment on WS_2 PL emission at room temperature. PL map statistics revealed higher average PL enhancement and improved spectral uniformity with OA treatment compared with TFSI. PL excitation intensity dependent studies and time resolved pump intensity studies showed trap free exciton dynamics in OA treated WS_2. Trap free exciton movement was characterised by a reduction in PL yields and PL lifetimes as excitation intensities (or initial carrier populations) were increased. This lies in contrast to the trap-limited exciton dynamics observed in TFSI treated samples. Exciton trapping was characterised by an increase or stagnation[91] in PL yields and PL lifetimes in spite of

increased excitation intensity, prior to decline at the onset of exciton-exciton annihilation. Electron withdrawal or *p*-doping by TFSI `frees up' trap states. Excitons occupy and recombine over long periods or become thermally activated to the band edge, and transition radiatively to the ground state.[75,91] Whereas TFSI treatment gives rise to trap-mediated radiative band-edge recombination of thermally activated excitons,[91] OA is perceived to passivate trap states, forbidding trap-assisted exciton decay altogether, promoting radiative direct band-edge recombination. In support of the notion of defect passivation by OA, electronic transport measurements of OA treated WS_2 transistors showed reduced charge trap density, increased field effect mobilities, and no detectable doping. Bright trion emission was also observed at high excitation intensities in OA treated WS_2 only, which is of potential interest for spintronic applications. By way of surface chemistry, we hypothesised that the OA ligand forms a dative covalent bond with the electrophilic metal atom at a chalcogen vacancy, terminating trap states and improving band-edge PL, much like surface defect passivation by OA in colloidal quantum dot (QD) nanocrystals. This prediction however remains to be verified experimentally.

Chapter 5 confirmed OA's ability to enhance PL in selenium TMDs. This is unlike TFSI, which quenches their PL.[25] Here, we investigated large PL enhancement in OA treated $MoSe_2$ using steady state and time resolved PL measurements. As previously done with WS_2, electronic characteristics of OA treated $MoSe_2$ were also measured. Statistical analysis of OA treated $MoSe_2$ PL map data revealed bright spatially homogenous PL, with narrow spectral linewidth. Steady state excitation dependent PL studies showed significantly improved neutral exciton PL yields, which reduces with excitation intensity, as indicative of trap-free exciton dynamics. Time resolved PL (TRPL) spectra showed increased PL lifetimes in treated samples under low pump fluence. Pump intensity studies revealed a reduction in carrier lifetime with increased carrier concentration, consistent with trap-free exciton movement. As in the previous study, trap-free exciton movement is considered an indicator of trap state passivation by OA ligands. The likelihood defect passivation by the ligands was again supported by FET measurements, which showed improved on-off ratios and subthreshold swing, both of which confirmed a reduction in charge trap density. The initial hypothesis for defect passivation is maintained, whereby OA ligands coordinate chalcogen defect sites, terminating traps and improving radiative PL yields. We also speculated that the insulating ligands encapsulate the monolayer, in similar fashion to hexagonal boronitride

h-BN, protecting it from external sources of disorder such as adsorbants and strain, thereby improving spectral linewidths.

The many-body phenomena exhibited by tightly bound TMD excitons are of great fundamental research interest. From a device application perspective however, these excitons could be transferred to other emissive materials with strong light coupling and high PL quantum yields (PLQY) such as quantum dots (QDs). This has applications in *e.g.*, light conversion, and artificial light harvesting with luminescent solar concentrators (LSCs).

Chapter 6 detailed the optical characterisation of a photon energy down-conversion system consisting of a 2D WS_2 absorber combined with a near infrared (NIR) lead sulphide-cadmium sulphide QD emitter. Previous studies on similar heterostructure systems report on QD exciton quenching by a 2D TMD exciton sink for light detection applications. This chapter studied the reverse process, taking advantage of large absorption cross section of monolayer WS_2, from which excitons generated by visible light coupling are nonradiatively transferred to high PLQE nanocrystal NIR QD emitters. Photoluminescence excitation (PLE) studies provided initial confirmation of efficient (~58%) 2D to QD excitation energy transfer (ET). The combined large oscillator strengths of the constituent TMD exciton donor and QD acceptor amounts to a large theoretical ET radius consistent with Förster resonance energy transfer (FRET). Interestingly, TRPL studies showed that 2D to QD ET rates exceed intrinsic exciton trapping rates in monolayer WS_2. A comparison between high excitation intensity steady state PL and TRPL confirmed direct exciton transfer from the WS_2 band edge to the PbS-CdS band edge. Intrinsic exciton trapping in the TMD donor and other non-radiative channels merely act as competing ET pathways.

Chapter 7 developed the concept of an LSC based on the 2D-QD heterostructure using Monte Carlo light transport simulations. The 2D-QD heterostructure is considered as a viable candidate for LSC luminophore material due to the large Stokes shift between 2D absorption and QD emission spectra. This combined with zero spectral overlap can eliminate reabsorption losses seen in typical luminophore materials which have low Stokes shift and large spectral overlap. The luminophore was assumed to have a large area 2D absorber. A key model assumption was no absorption/ reabsorption by the QD emitter. This was deemed appropriate for a low concentration of QDs per 2D monolayer for two reasons. Firstly, for such low concentrations per monolayer, the projected area of the 2D vastly exceeds that of the few QDs. Secondly, the absorption cross section of the

2D is larger than the QD's by orders of magnitude.[29] Therefore, any light absorbed by the QDs was assumed negligible in comparison to the 2D. LSCs based on WS_2/PbS-CdS (1.24 eV) heterostructure, Lumogen Red 305 (LR305) dye and PbS-CdS (1.37 eV) were simulated assuming unity and sub-unity luminophore PLQYs. The resulting performance characteristics were computed as a function of luminophore concentration ranging between 1 μM – 1 M. The simulations essentially predicted that the heterostructure LSC outperforms all other LSC types for the entire concentration range simulated. This was attributed to the large absorption of the 2D component, large Stokes shift with zero spectral overlap, and importantly, the assumption of no reabsorption by the QD emitters. While the latter assumption was deemed appropriate for low luminophore concentrations, in reality, QD absorption/reabsorption is bound to become progressively significant with increasing concentrations. Going forward, further refinements to the luminophore model were recommended to capture real behaviour.

8.2 Outlook

Further experimental work is required to elucidate the surface chemistry of OA treatment. Fourier transform infrared scanning near near-field optical microscopy (FTIR-SNOM) could provide high resolution identification vibrational modes associated carboxylate group coordination at chalcogen vacancies. Alternatively, X-ray photoelectron spectroscopy (XPS) could be used to identify signatures of carboxylate group-TMD surface attachment. Such methods in combination with theoretical calculations ought to be employed to verify or correct the initial hypothesis of vacancy termination by the ligands, thus refining our initial understanding of the mechanism. While questions surrounding this mechanism remain, trion emission in OA treated WS_2 has recently raised some external interest within the spintronics research community. This has garnered an ongoing collaborative effort led by Makoto Kohda (Tohuku University, Japan) to investigate trion spin-polarization lifetimes in OA treated WS_2 at cryogenic temperatures.

Future studies on the 2D-QD ET heterostructure are required to clarify non-radiative loss channels. This should be done using more sensitive spectroscopy techniques such as femtosecond transient absorption (TA) and high resolution TRPL. Passivating trap states in the monolayer TMD absorber *via e.g.*, OA treatment, could be used to drastically reduce exciton trapping losses, and improve ET efficiencies. Importantly, this

is predicted to sufficiently isolate the non-radiative pathways, enabling better understanding of their exciton quenching mechanism, which could offer practical answers towards circumventing these losses to boost ET efficiencies.

To simulate the real behaviour of a heterostructure LSC luminophore, we initially suggest a model that factors in the ratio of QD to 2D TMD projected area (χ) to an incoming photon flux in order to quantify the likelihood of absorption or reabsorption by a QD. For example, this ratio χ could be associated to a probability of absorption by either species. Better understanding of the real heterostructure through additional optical characterisation studies should offer further improvements to the simulation model. Ultimately however, an actual heterostructure LSC ought to be developed and measured, which would serve to refine the model and verify the validity of simulation results. Suspending the heterostructures in a polymer matrix presents formidable practical challenges, which will require long-term research endeavours. A seemingly viable, but non-trivial intermediate step would be to suspend the heterostructure in liquid phase for bulk steady state and time resolved optical characterisation.

9 References

1. Geim, A. K. & Novoselov, K. S. The Rise of Graphene. *Nat. Mater.* **6**, 183–91 (2007).
2. Berkelbach, T. C. & Reichman, D. R. Optical and Excitonic Properties of Atomically Thin Transition-Metal Dichalcogenides. *Annu. Rev. Condens. Matter Phys*. **9**, 379-393 (2018).
3. Mak, K. F. & Shan, J. Photonics and Optoelectronics of 2D Semiconductor Transition metal dichalcogenides. *Nat. Photonics* **10**, 216–226 (2016).
4. Zheng, W. *et al.* Light Emission Properties of 2D Transition Metal Dichalcogenides: Fundamentals and Applications. *Adv. Opt. Mater.* **6**, 1–29 (2018).
5. Wang, Q. H., Kalantar-Zadeh, K., Kis, A., Coleman, J. N. & Strano, M. S. Electronics and Optoelectronics of Two-dimensional Transition Metal Dichalcogenides. *Nat. Nanotechnol.* **7**, 699–712 (2012).
6. Mak, K. F., Lee, C., Hone, J., Shan, J. & Heinz, T. F. Atomically Thin MoS_2: A New Direct-Gap Semiconductor. *Phys. Rev. Lett.* **105**, 136805 (2010).
7. Chhowalla, M., Jena, D. & Zhang, H. Two-dimensional Semiconductors for Transistors. *Nat. Rev. Mater.* **1**, (2016).
8. Withers, F. *et al.* Light-emitting Diodes by Band-structure Engineering in van der Waals Heterostructures. *Nat. Mater.* **14**, 301–306 (2015).
9. Baugher, B. W. H., Churchill, H. O. H., Yang, Y. & Jarillo-Herrero, P. Optoelectronic Devices based on Electrically Tunable *p-n* Diodes in a Monolayer Dichalcogenide. *Nat. Nanotechnol.* **9**, 262–267 (2014).
10. Leng, T. *et al.* Printed Graphene/WS_2 Battery-free Wireless Photosensor on Papers. *2D Mater.* **7**, (2020).
11. Bernardi, M., Palummo, M. & Grossman, J. C. Extraordinary Sunlight Absorption and one nanometer thick Photovoltaics using Two-dimensional Monolayer Materials. *Nano Lett.* **13**, 3664–3670 (2013).
12. Palacios-Berraquero, C. *et al*. Atomically Thin Quantum Light-Emitting Diodes. *Nat. Commun.* **7**, (2016).
13. Rhodes, D., Chae, S. H., Ribeiro-Palau, R. & Hone, J. Disorder in van der Waals Heterostructures of 2D Materials. *Nat. Mater.* **18**, 541–549 (2019).
14. Zhou, W. *et al.* Intrinsic Structural Defects in Monolayer Molybdenum Disulfide. *Nano Lett.* **13**, 2615–2622 (2013).
15. Santosh, K.C., Longo, R. C., Addou, R., Wallace, R. M. & Cho, K. Impact of Intrinsic Atomic Defects on the Electronic Atructure of MoS_2 Monolayers. *Nanotechnology* **25**, (2014).
16. Li, L. & Carter, E. A. Defect-mediated Charge-Carrier Trapping and Nonradiative Recombination in WSe_2 monolayers. *J. Am. Chem. Soc.* **141**, 10451–10461 (2019).

17. Barja, S. *et al.* Identifying Substitutional Oxygen as a Prolific Point Defect in monolayer transition metal dichalcogenides. *Nat. Commun.* **10**, (2019).

18. Pető, J. *et al.* Spontaneous Doping of the Basal Plane of MoS_2 Single Layers through Oxygen Substitution Under Ambient Conditions. *Nat. Chem.* **10**, 1246–1251 (2018).

19. Moody, G., Schaibley, J. & Xu, X. Exciton Dynamics in Monolayer Transition Metal Dichalcogenides. *J. Opt. Soc. Am. B* **33**, C39-C49 (2016).

20. Amani, M. *et al*. Near-unity Photoluminescence Quantum Yield in MoS_2. *Science* **350**, 1065–1068 (2015).

21. Kim, H., Lien, D. H., Amani, M., Ager, J. W. & Javey, A. Highly Stable Near-Unity Photoluminescence Yield in Monolayer MoS_2 by Fluoropolymer Encapsulation and Superacid Treatment. *ACS Nano* **11**, 5179–5185 (2017).

22. Mouri, S., Miyauchi, Y. & Matsuda, K. Tunable Photoluminescence of Monolayer MoS_2 *via* Chemical Doping. *Nano Lett.* **13**, 5944–5948 (2013).

23. Peimyoo, N. *et al.* Chemically Driven Tunable Light Emission of Charged and Neutral Excitons in Monolayer WS_2. *ACS Nano* **8**, 11320–11329 (2014).

24. Su, W. *et al.* Tuning Photoluminescence of Single-Layer MoS_2 using H_2O_2. *RSC Adv.* **5**, 82924–82929 (2015).

25. Amani, M. *et al.* Recombination Kinetics and Effects of Superacid Treatment in Sulfur- and Selenium-Based Transition Metal Dichalcogenides. *Nano Lett.* **16**, 2786–2791 (2016).

26. Li, M., Chen, J. S. & Cotlet, M. Light-Induced Interfacial Phenomena in Atomically Thin 2D van der Waals Material Hybrids and Heterojunctions. *ACS Energy Lett.* **4**, 2323–2335 (2019).

27. Tanoh, A. O. A. *et al.* Enhancing Photoluminescence and Mobilities in WS_2 Monolayers with Oleic Acid Ligands. *Nano Lett.* **19**, 6299–6307 (2019).

28. Tanoh, A. O. A. *et al.* Giant Photoluminescence Enhancement in $MoSe_2$ Monolayers Treated with Oleic Acid Ligands. *Nanoscale Adv.* Advance Article (2021).

29. Tanoh, A. O. A. *et al.* Directed Energy Transfer From Monolayer WS_2 to Near-Infrared Emitting Pbs-Cds Quantum Dots. *ACS Nano* **14**, 15374–15384 (2020).

30. Prins, F., Goodman, A. J. & Tisdale, W. A. Reduced Dielectric Screening and Enhanced Energy Transfer in Single- and Few-Layer MoS_2. *Nano Lett.* **14**, 6087–6091 (2014).

31. Raja, A. *et al.* Energy Transfer from Quantum Dots to Graphene and MoS_2 : The Role of Absorption and Screening in Two-Dimensional Materials. *Nano Lett.* **16**, 2328–2333 (2016).

32. Prasai, D. *et al*. Electrical Control of near-Field Energy Transfer between Quantum Dots and Two-Dimensional Semiconductors. *Nano Lett.* **15**, 4374–4380 (2015).

33. Li, H., Zheng, X., Liu, Y., Zhang, Z. & Jiang, T. Ultrafast Interfacial Energy Transfer and Interlayer Excitons in The Monolayer WS_2/$CsPbBr_3$ Quantum Dot Heterostructure. *Nanoscale* **10**, 1650–1659 (2018).

34. Liu, Y., Li, H., Zheng, X., Cheng, X. & Jiang, T. Giant Photoluminescence Enhancement in Monolayer WS_2 by Energy Transfer from $CsPbBr_3$ Quantum

Dots. *Opt. Mater. Express* **7**, 1327 (2017).

35. Zang, H. *et al.* Nonradiative Energy Transfer from Individual CdSe/ZnS Quantum Dots to Single-Layer and Few-Layer Tin Disulfide. *ACS Nano* **10**, 4790–4796 (2016).
36. Liu, H., Wang, T., Wang, C., Liu, D. & Luo, J. Exciton Radiative Recombination Dynamics and Nonradiative Energy Transfer in Two-Dimensional Transition-Metal Dichalcogenides. *J. Phys. Chem. C* **123**, 10087–10093 (2019).
37. Parker, G. Introductory Semiconductor Device Physics.8-42, (CRC Press , 2004).
38. Wannier, G. H. The Structure of Electronic Excitation Levels in Insulating Crystals. *Phys. Rev*. **52**, 191–197 (1937).
39. Frenkel, J. On The Transformation of Light into Heat in Solids. I. *Phys. Rev.* **37**, 17–44 (1931).
40. Alivisatos, A. P. Semiconductor Clusters, Nanocrystals, and Quantum Dots. *Science*. **271**, 933–937 (1996).
41. Ashoori, R. C. Electrons in Artificial Atoms. *Nature* **379**, 413–419 (1996).
42. Splendiani, A. *et al.* Emerging Photoluminescence in Monolayer MoS_2. *Nano Lett*. **10**, 1271–1275 (2010).
43. Lee, J., Kim, M. & Cheong, H. Raman Spectroscopic Studies on Two-Dimensional Materials. *Appl. Microsc.* **45**, 126–130 (2015).
44. Chernikov, A. *et al.* Exciton Binding Energy and Non-hydrogenic Rydberg Series in Monolayer WS_2. *Phys. Rev. Lett.* **113**, 076802 (2014).
45. Wang, G. *et al.* Colloquium: Excitons in Atomically Thin Transition Metal Dichalcogenides. *Rev. Mod. Phys.* **90**, (2018).
46. Palacios-Berraquero, C. *Introduction: 2d-Based Quantum Technologies*. in Quantum Confined Excitons in 2-Dimensional Materials 7-9 (Springer, 2018).
47. Liu, G. Bin, Xiao, D., Yao, Y., Xu, X. & Yao, W. Electronic Structures and Theoretical Modelling of Two-dimensional Group-VIB Transition Metal Dichalcogenides. *Chem. Soc. Rev.* **44**, 2643–2663 (2015).
48. Özçelik, V. O., Azadani, J. G., Yang, C., Koester, S. J. & Low, T. Band Alignment of Two-Dimensional Semiconductors for Designing Heterostructures with Momentum Space Matching. *Phys. Rev. B* **94**, (2016).
49. Gong, C. *et al.* Band Alignment of Two-Dimensional Transition Metal Dichalcogenides: Application in Tunnel Field Effect Transistors. *Appl. Phys. Lett.* **103**, (2013).
50. Chiu, M. H. *et al.* Determination of Band Alignment in the Single-Layer MoS_2 WSe_2 Heterojunction. *Nat. Commun.* **6**, (2015).
51. Bradley, A. J. *et al.* Probing the Role of Interlayer Coupling and Coulomb Interactions on Electronic Structure in Few-Layer $MoSe_2$ Nanostructures. *Nano Lett.* **15**, 2594–2599 (2015).
52. You, Y. *et al.* Observation of Biexcitons in Monolayer WSe_2. *Nat. Phys.* **11**, 477–481 (2015).
53. Paradisanos, I. *et al.* Room Temperature Observation of Biexcitons in Exfoliated WS_2 monolayers. *Appl. Phys. Lett.* **110**, (2017).

54. Hao, K. *et al.* Neutral and Charged Inter-Valley Biexcitons in Monolayer $MoSe_2$. *Nat. Commun.* **8**, (2017).

55. Mak, K. F. *et al*. Tightly Bound Trions in Monolayer MoS_2. *Nat. Mater.* **12**, 207–211 (2013).

56. Berkelbach, T. C., Hybertsen, M. S. & Reichman, D. R. Theory of Neutral and Charged Excitons in Monolayer Transition Metal Dichalcogenides. *Phys. Rev. B* **88** (2013).

57. Plechinger, G. *et al.* Trion Fine Structure and Coupled Spin-Valley Dynamics in Monolayer Tungsten Disulfide. *Nat. Commun.* (2016).

58. Mitioglu, A. A. *et al.* Optical Manipulation of the Exciton Charge State in Single-Layer Tungsten Disulfide. *Phys. Rev. B* **88** (2013).

59. Wei, K., Liu, Y., Yang, H., Cheng, X. & Jiang, T. Large Range Modification of Exciton Species in Monolayer WS_2. *Appl. Opt.* **55**, 6251 (2016).

60. Kang, Y. & Han, S. An origin of Unintentional Doping in Transition Metal Dichalcogenides: The role of Hydrogen Impurities. *Nanoscale* **9**, 4265–4271 (2017).

61. Li, Z. *et al*. Direct Observation of Gate-Tunable Dark Trions in Monolayer WSe_2. *Nano Lett.* **19**, 6886–6893 (2019).

62. Barbone, M. *et al.* Charge-Tuneable Biexciton Complexes in Monolayer WSe_2. *Nat. Commun.* **9**, 3721 (2018).

63. Ross, J. S. *et al*. Electrical Control of Neutral and Charged Excitons in a Monolayer Semiconductor. *Nat. Commun.* **4**, (2013).

64. Carmiggelt, J. J., Borst, M. & van der Sar, T. Exciton-to-Trion Conversion as a Control Mechanism for Valley Polarization in Room-Temperature Monolayer WS_2. *Sci. Rep.* **10** (2020).

65. Benjamin, C. J., Zhang, S. & Chen, Z. Controlled Doping of Transition Metal Dichalcogenides by Metal Work Function Tuning in Phthalocyanine Compounds. *Nanoscale* **10**, 5148–5153 (2018).

66. Mouri, S., Miyauchi, Y. & Matsuda, K. Tunable Photoluminescence of Monolayer MoS_2 *via* Chemical Doping. *Nano Lett.* **13**, 5944–5948 (2013).

67. Zhao, W. *et al.* Evolution of Electronic Structure in Atomically Thin Sheets of WS_2 and WSe_2. *ACS Nano* **7**, 791–797 (2013).

68. Chow, P. K. *et al.* Defect-Induced Photoluminescence in Monolayer Semiconducting Transition Metal Dichalcogenides. *ACS Nano* **9**, 1520–1527 (2015).

69. Lagarde, D. *et al.* Carrier and Polarization Dynamics in Monolayer MoS_2. *Phys. Rev. Lett.* **112**, (2014).

70. Robert, C. *et al.* Exciton Radiative Lifetime in Transition Metal Dichalcogenide Monolayers. *Phys. Rev. B* **93** (2016).

71. Palummo, M., Bernardi, M. & Grossman, J. C. Exciton Radiative Lifetimes in Two-Dimensional Transition Metal Dichalcogenides. *Nano Lett.* **15**, 2794–2800 (2015).

72. Refaely-Abramson, S., Qiu, D. Y., Louie, S. G. & Neaton, J. B. Defect-Induced Modification of Low-Lying Excitons and Valley Selectivity in Monolayer

Transition Metal Dichalcogenides. *Phys. Rev. Lett.* **121** (2018).

73. Wang, H., Zhang, C. & Rana, F. Ultrafast Dynamics of Defect-Assisted Electron-Hole Recombination in Monolayer MoS_2. *Nano Lett.* **15**, 339–345 (2015).
74. Ross, J. S. *et al.* Electrically Tunable Excitonic Light-Emitting Diodes Based on Monolayer WSe_2 p-n junctions. *Nat. Nanotechnol.* **9**, 268–272 (2014).
75. Lien, D. H. *et al.* Electrical Suppression of all Nonradiative Recombination Pathways in Monolayer Semiconductors. *Science* **364**, 468–471 (2019).
76. Lin, Z. *et al.* Defect Engineering of Two-Dimensional Transition Metal Dichalcogenides. *2D Mater*. **3**, (2016).
77. Briggs, N. *et al.* A Roadmap for Electronic Grade 2D Materials. *2D Mater.* **6**, (2019).
78. Qiu, H. *et al.* Hopping Transport Through Defect-Induced Localized States in Molybdenum Disulphide. *Nat. Commun.* **4**, (2013).
79. Hong, J. *et al.* Exploring Atomic Defects in Molybdenum Disulphide Monolayers. *Nat. Commun.* **6**, (2015).
80. Carozo, V. *et al.* Optical Identification of Sulfur Vacancies: Bound Excitons at the Edges of Monolayer Tungsten Disulfide. *Sci. Adv.* **3**, (2017).
81. Schuler, B. *et al.* Electrically Driven Photon Emission from Individual Atomic Defects in Monolayer WS_2. *Sci. Adv*. **6**, (2020).
82. Schuler, B. *et al.* Large Spin-Orbit Splitting of Deep In-Gap Defect States of Engineered Sulfur Vacancies in Monolayer WS_2. *Phys. Rev. Lett*. **123**, (2019).
83. Yu, X., Guijarro, N., Johnson, M. & Sivula, K. Defect Mitigation of Solution-Processed 2D WSe_2 Nanoflakes for Solar-to-Hydrogen Conversion. *Nano Lett.* **18**, 215–222 (2018).
84. Roy, S. *et al.* Atomic Observation of Filling Vacancies in Monolayer Transition Metal Sulfides by Chemically Sourced Sulfur Atoms. *Nano Lett.* **18**, 4523–4530 (2018).
85. Ajayi, O. A. *et al.* Approaching the Intrinsic Photoluminescence Linewidth in Transition Metal Dichalcogenide Monolayers. *2D Mater*. **4**, (2017).
86. Cadiz, F. *et al.* Excitonic Linewidth Approaching the Homogeneous Limit in MoS_2-based van der Waals Heterostructures. *Phys. Rev. X* **7**, (2017).
87. Courtade, E. *et al.* Spectrally Narrow Exciton Luminescence From Monolayer MoS_2 and $MoSe_2$ Exfoliated onto Epitaxially Grown Hexagonal BN. *Appl. Phys. Lett.* **113**, (2018).
88. Hoshi, Y. *et al.* Suppression of Exciton-Exciton Annihilation in Tungsten Disulfide Monolayers Encapsulated by Hexagonal Boron Nitrides. *Phys. Rev. B* **95**, (2017).
89. Park, J. H. *et al.* Defect Passivation of Transition Metal Dichalcogenides *via* a Charge Transfer van der Waals Interface. *Sci. Adv*. **3**, (2017).
90. Bretscher, H.M. *et al*. The Bright Side of Defects in MoS_2 and WS_2 and a Generalizable Chemical Treatment Protocol for Defect Passivation. *arXiv Prepr*. arXiv2002.03956 (2020).
91. Goodman, A. J., Willard, A. P. & Tisdale, W. A. Exciton Trapping is Responsible

For the Long Apparent Lifetime in Acid-Treated MoS_2. *Phys. Rev. B* **96**, (2017).

92. Han, H. V. *et al.* Photoluminescence Enhancement and Structure Repairing of Monolayer $MoSe_2$ by Hydrohalic Acid Treatment. *ACS Nano* **10**, 1454–1461 (2016).

93. Jing, X. *et al.* Engineering Field Effect Transistors with 2D Semiconducting Channels: Status and Prospects. *Adv. Funct. Mater.* **30**, (2020).

94. Mueller, T. & Malic, E. Exciton Physics and Device Application of Two-Dimensional Transition Metal Dichalcogenide Semiconductors. *npj 2D Mater.* Appl. **2**, (2018).

95. Sundaram, R. S. *et al.* Electroluminescence in Single Layer MoS_2. *Nano Lett.* **13**, 1416–1421 (2013).

96. Pospischil, A., Furchi, M. M. & Mueller, T. Solar-Energy Conversion and Light Emission in an Atomic Monolayer *p-n* diode. *Nat. Nanotechnol.* **9**, 257–261 (2014).

97. Ross, J. S. *et al.* Electrically Tunable Excitonic Light-Emitting Diodes Based on Monolayer WSe_2 *p-n* Junctions. *Nat. Nanotechnol.* **9**, 268–272 (2014).

98. Jariwala, D., Davoyan, A. R., Wong, J. & Atwater, H. A. Van der Waals Materials for Atomically-Thin Photovoltaics: Promise and Outlook. *ACS Photonics* **4**, 2962–2970 (2017).

99. Furchi, M. M., Pospischil, A., Libisch, F., Burgdörfer, J. & Mueller, T. Photovoltaic Effect in an Electrically Tunable Van der Waals Heterojunction. *Nano Lett.* **14**, 4785–4791 (2014).

100. Lee, C. H. *et al.* Atomically Thin *p-n* Junctions with van der Waals Heterointerfaces. *Nat. Nanotechnol.* **9**, 676–681 (2014).

101. Cheng, R. et al. Electroluminescence and Photocurrent Generation from Atomically Sharp WSe_2/MoS_2 Heterojunction *p-n* Diodes. *Nano Lett.* **14**, 5590–5597 (2014).

102. Wong, J. *et al.* High Photovoltaic Quantum Efficiency in Ultrathin van der Waals Heterostructures. *ACS Nano* **11**, 7230–7240 (2017).

103. Pospischil, A. & Mueller, T. Optoelectronic Devices Based on Atomically Thin Transition Metal Dichalcogenides. *Appl. Sci.* **6**, (2016).

104. Lopez-Sanchez, O., Lembke, D., Kayci, M., Radenovic, A. & Kis, A. Ultrasensitive Photodetectors Based on Monolayer MoS_2. *Nat. Nanotechnol.* **8**, 497–501 (2013).

105. Zhou, X. *et al.* Vertical Heterostructures Based on SnSe2/MoS2 for High Performance Photodetectors. *2D Mater.* **4**, (2017).

106. Yu, Y. *et al.* PbS-Decorated WS2 Phototransistors with Fast Response. *ACS Photonics* **4**, 950–956 (2017).

107. Hu, C. *et al*. Synergistic Effect of Hybrid PbS Quantum Dots/2D-WSe_2 Toward High Performance and Broadband Phototransistors. *Adv. Funct. Mater*. **27**, (2017).

108. Boulesbaa, A. *et al.* Ultrafast Charge Transfer and Hybrid Exciton Formation in 2D/0D Heterostructures. *J. Am. Chem. Soc.* **138**, 14713–14719 (2016).

109. Kufer, D. *et al.* Hybrid 2D-0D MoS_2-PbS Quantum Dot photodetectors. *Adv. Mater.* **27**, 176–180 (2015).

110. Huang, Y. *et al.* Van der Waals Coupled Organic Molecules with Monolayer MoS_2 for Fast Response Photodetectors with Gate-Tunable Responsivity. *ACS Nano* **12**, 4062–4073 (2018).

111. Huo, N., Gupta, S. & Konstantatos, G. MoS_2–HgTe Quantum Dot Hybrid Photodetectors beyond 2 μm. *Adv. Mater.* **29**, 1606576 (2017).

112. Nazir, G. *et al.* Enhanced Photoresponse of ZnO Quantum Dot-Decorated MoS_2 Thin Films. *RSC Adv.* **7**, 16890–16900 (2017).

113. Wu, H. *et al.* All-Inorganic Perovskite Quantum Dot-Monolayer MoS_2 Mixed-Dimensional van der Waals Heterostructure for Ultrasensitive Photodetector. *Adv. Sci.* **5**, (2018).

114. Li, M. *et al.* Distinct Optoelectronic Signatures for Charge Transfer and Energy Transfer in Quantum Dot–MoS_2 Hybrid Photodetectors Revealed by Photocurrent Imaging Microscopy. *Adv. Funct. Mater.* **28**, (2018).

115. Kang, D. H. *et al.* An Ultrahigh-Performance Photodetector Based on a Perovskite–Transition-Metal-Dichalcogenide Hybrid Structure. *Adv. Mater.* **28**, 7799–7806 (2016).

116. Guzelturk, B. & Demir, H. V. Near-Field Energy Transfer Using Nanoemitters For Optoelectronics. *Adv. Funct. Mater.* **26**, 8158–8177 (2016).

117. Förster, T. Transfer Mechanisms of Electronic Excitation. *Discuss. Faraday Soc.* **27**, 7–17 (1959).

118. Scholes, G. D. Long-Range Resonance Energy Transfer in Molecular Systems. *Annu. Rev. Phys. Chem.* **54**, 57–87 (2003).

119. Hernández-Martínez, P. L., Govorov, A. O. & Demir, H. V. Generalized Theory of Förster-type Nonradiative Energy Transfer in Nanostructures with Mixed Dimensionality. *J. Phys. Chem. C* **117**, 10203–10212 (2013).

120. Dexter, D. L. A theory of Sensitized Luminescence in Solids. *J. Chem. Phys.* **21**, (1953).

121. Rao, A. & Friend, R. H. Harnessing Singlet Exciton Fission to Break the Shockley–Queisser limit. *Nat. Rev. Mater.* **2**, (2017).

122. Meinardi, F., Bruni, F. & Brovelli, S. Luminescent Solar Concentrators for Building-Integrated photovoltaics. *Nat. Rev. Mater.* **2**, (2017).

123. Klimov, V. I., Baker, T. A., Lim, J., Velizhanin, K. A. & McDaniel, H. Quality Factor of Luminescent Solar Concentrators and Practical Concentration Limits Attainable with Semiconductor Quantum Dots. *ACS Photonics* **3**, 1138–1148 (2016).

124. Yablonovitch, E. Thermodynamics of the Fluorescent Planar Concentrator. *J. Opt. Soc. Am.* **70**, 1362-1363 (1980).

125. Debije, M. G. & Verbunt, P. P. C. Thirty Years of Luminescent Solar Concentrator Research: Solar Energy for the Built Environment. *Adv. Energy Mater.* **2**, 12–35 (2012).

126. Meinardi, F. *et al.* Highly Efficient Large-Area Colourless Luminescent Solar Concentrators using Heavy-Metal-Free Colloidal Quantum Dots. *Nat. Nanotechnol.* **10**, 878–885 (2015).

127. Bronstein, N. D. *et al.* Luminescent Solar Concentration with Semiconductor

Nanorods and Transfer-Printed Micro-Silicon Solar cells. *ACS Nano* **8**, 44–53 (2014).

128. Zhou, Y. *et al.* Luminescent Solar Concentrators: Near Infrared, Highly Efficient Luminescent Solar Concentrators. *Adv. Energy Mater*. **6**, (2016).

129. Coropceanu, I. & Bawendi, M. G. Core/Shell Quantum Dot Based Luminescent Solar Concentrators with Reduced Reabsorption and Enhanced efficiency. *Nano Lett*. **14**, 4097–4101 (2014).

130. Bronstein, N. D. *et al*. Quantum Dot Luminescent Concentrator Cavity Exhibiting 30-fold Concentration. *ACS Photonics* **2**, 1576–1583 (2015).

131. Cambié, D., Zhao, F., Hessel, V., Debije, M. G. & Noël, T. Every Photon Counts: Understanding and Optimizing Photon Paths in Luminescent Solar Concentrator-Based Photomicroreactors (LSC-PMs). *React. Chem. Eng*. **2**, 561–566 (2017).

132. Benameur, M. M. *et al.* Visibility of Dichalcogenide Nanolayers. *Nanotechnology* **22**, (2011).

133. Li, H. *et al.* Rapid and Reliable Thickness Identification of Two-Dimensional Nanosheets using Optical Microscopy. *ACS Nano* **7**, 10344–10353 (2013).

134. Xu, X., Yao, W., Xiao, D. & Heinz, T. F. Spin and Pseudospins in Layered Transition Metal Dichalcogenides. *Nat. Phys.* **10**, 343–350 (2014).

135. Li, H., Wu, J., Yin, Z. & Zhang, H. Preparation and Applications of Mechanically Exfoliated Single-Layer and Multilayer MoS_2 and WSe_2 nanosheets. *Acc. Chem. Res.* **47**, 1067–1075 (2014).

136. Budania, P. *et al*. Comparison Between Scotch Tape and Gel-Assisted Mechanical Exfoliation Techniques for Preparation of 2D Transition Metal Dichalcogenide Flakes. *Micro Nano Lett.* **12**, 970-973 (2017).

137. Magda, G. Z. *et al.* Exfoliation of Large-Area Transition Metal Chalcogenide Single Layers. *Sci. Rep*. **5**, (2015).

138. Huang, Y. *et al*. Universal Mechanical Exfoliation of Large-Area 2D crystals. *Nat. Commun.* **11**, (2020).

139. Liu, F. *et al.* Disassembling 2D van der Waals Crystals into Macroscopic Monolayers and Reassembling into Artificial Lattices. *Science* **367**, 903–906 (2020).

140. Desai, S. B. *et al*. Gold-Mediated Exfoliation of Ultralarge Optoelectronically-Perfect Monolayers. *Adv. Mater.* **28**, 4053–4058 (2016).

141. Velický, M. *et al.* Mechanism of Gold-Assisted Exfoliation of Centimeter-Sized Transition-Metal Dichalcogenide Monolayers. *ACS Nano* **12**, 10463–10472 (2018).

142. Seo, J. W. T. *et al.* Fully Inkjet-Printed, Mechanically Flexible MoS_2 Nanosheet Photodetectors. *ACS Appl. Mater. Interfaces* **11**, 5675–5681 (2019).

143. Nicolosi, V., Chhowalla, M., Kanatzidis, M. G., Strano, M. S. & Coleman, J. N. Liquid Exfoliation of Layered Materials. *Science* **340**, 1226419 (2013).

144. Bonaccorso, F. *et al.* Production and Processing of Graphene and 2d Crystals. *Mater. Today* **15**, 564–589 (2012).

145. Huo, C., Yan, Z., Song, X. & Zeng, H. 2D materials *via* Liquid Exfoliation: A Review on Fabrication and Applications. *Sci. Bull.* **60**, 1994–2008 (2015).

146. Zhang, Y. *et al.* Recent Progress in CVD Growth of 2D Transition Metal Dichalcogenides and Related Heterostructures. *Adv. Mater.* **31**, (2019).

147. Das, R. S. & Agrawal, Y. K. Raman Spectroscopy: Recent Advancements, Techniques and Applications. *Vib. Spectrosc.* **57**, 163–176 (2011).

148. Swinehart, D. F. The Beer-Lambert law. J. Chem. Educ. **39**, 333–335 (1962).

149. Wahl, M. *Technical Notes: Time-correlated single photon counting*. (PicoQuant GmbH, 2014).

150. Rubinstein, R. Y. & Kroese, D. P. *Simulation and the Monte Carlo method*. (John Wiley & Sons, Incorporated, 2017).

151. Gajic, M. *Non-imaging technologies for designing a hybrid photovoltaic and solar thermal collector*. (Research Gate, 2017). Available at: https://www.researchgate.net/publication/326579362_Non-imaging_technologies_for_designing_a_hybrid_photovoltaic_and_solar_thermal_collector. (Accessed: 1st March 2021)

152. Şahin, D., Ilan, B. & Kelley, D. F. Monte-Carlo Simulations of Light Propagation in Luminescent Solar Concentrators Based on Semiconductor nanoparticles. *J. Appl. Phys.* **110**, (2011).

153. Davis, N. J. L. K. *et al.* Star-Shaped Fluorene–BODIPY Oligomers: Versatile Donor–Acceptor Systems for Luminescent Solar Concentrators. *J. Mater. Chem. C* **5**, 1952–1962 (2017).

154. Gajic, M. *Monte Carlo Raytracing of a Luminescent Solar Concentrator*. MathsWorks (2021). Available at: https://www.mathworks.com/matlabcentral/fileexchange/61104-monte-carlo-raytracing-of-a-luminescent-solar-concentrator. (Accessed: 10th November 2017)

155. Wilton, S.R. *Monte Carlo Ray-Tracing Simulation For Optimizing Luminescent Solar Concentrators*. (Pennsylvania State University, 2012). Available at: https://etda.libraries.psu.edu/catalog/13856. (Accessed 1st March 2021)

156. National Renewable Energy Laboratory. *Reference Air Mass 1.5 Spectra*. NREL (2021). Available at: https://www.nrel.gov/grid/solar-resource/spectra-am1.5.html. (Accessed: 15th March 2021)

157. Liu, H. L. *et al.* Optical Properties of Monolayer Transition Metal Dichalcogenides Probed by Spectroscopic Ellipsometry. *Appl. Phys. Lett.* **105**, 201905 (2014).

158. Shen, J. *et al.* Liquid Phase Exfoliation of Two-Dimensional Materials by Directly Probing and Matching Surface Tension Components. *Nano Lett.* **15**, 5449–5454 (2015).

159. Kang, K. *et al.* High-mobility Three-Atom-Thick Semiconducting Films with Wafer-scale Homogeneity. *Nature* **520**, 656–660 (2015).

160. Ye, Z. *et al.* Probing Excitonic Dark States in Single-Layer Tungsten Disulphide. *Nature* **513**, 214–218 (2014).

161. Qiu, D. Y., Da Jornada, F. H. & Louie, S. G. Optical spectrum of MoS_2: Many-Body Effects and Diversity of Exciton States. *Phys. Rev. Lett.* **111**, (2013).

162. Palacios-Berraquero, C. *et al.* Large-Scale Quantum-Emitter Arrays in Atomically Thin Semiconductors. *Nat. Commun.* **8**, (2017).

163. Lagoudakis, K. G. *et al.* Ultrafast Coherent Manipulation of Trions in Site-

Controlled Nanowire Quantum dots. *Optica* **3**, 1430-1435 (2016).

164. Wang, K. *et al.* Electrical Control of Charged Carriers and Excitons in Atomically Thin Materials. *Nat. Nanotechnol.* **13**, 128–132 (2018).

165. Lu, H., Kummel, A. & Robertson, J. Passivating the Sulfur Vacancy in Monolayer MoS_2. *APL Mater.* **6**, 066104 (2018).

166. Alharbi, A., Zahl, P. & Shahrjerdi, D. Material and Device Properties of Superacid-Treated Monolayer Molybdenum Disulfide. *Appl. Phys. Lett.* **110**, (2017).

167. Schaibley, J. R. *et al.* Valleytronics in 2D materials. *Nat. Rev. Mater.* **1**, (2016).

168. Liu, Z. *et al.* Strain and Structure Heterogeneity in MoS_2 Atomic Layers Grown by Chemical Vapour Deposition. *Nat. Commun.* **5**, 5246 (2014).

169. Addou, R. *et al.* Impurities and Electronic Property Variations of Natural MoS_2 Crystal Surfaces. *ACS Nano* **9**, 9124–9133 (2015).

170. Atallah, T. L. *et al.* Electrostatic Screening of Charged Defects in Monolayer MoS_2. *J. Phys. Chem. Lett.* **8**, 2148–2152 (2017).

171. Cao, Y., Stavrinadis, A., Lasanta, T., So, D. & Konstantatos, G. The Role of Surface Passivation for Efficient and Photostable PbS Quantum Dot Solar Cells. *Nat. Energy* **1**, (2016).

172. Zherebetskyy, D. *et al*. Hydroxylation of the Surface of PbS Nanocrystals Passivated with Oleic Acid. *Science*. **344**, 1380–1384 (2014).

173. Grandhi, G. K., Arunkumar, M. & Viswanatha, R. Understanding the Role of Surface Capping Ligands in Passivating the Quantum Dots Using Copper Dopants as Internal Sensor. *J. Phys. Chem. C* **120**, 19785–19795 (2016).

174. Wang, Y. *et al.* Van der Waals Contacts Between Three-Dimensional Metals and Two-Dimensional Semiconductors. *Nature* **568**, 70–74 (2019).

175. Enderlein, J. & Erdmann, R. Fast Fitting of Multi-Exponential Decay Curves. *Opt. Commun.* **134**, 371–378 (1997).

176. Kim, H. *et al*. Synthetic WSe_2 Monolayers with High Photoluminescence Quantum Yield. *Sci. Adv.* **5**, (2019).

177. Johari, P. & Shenoy, V. B. Tuning the Electronic Properties of Semiconducting Transition Metal Dichalcogenides by Applying Mechanical Strains. *ACS Nano* **6**, 5449–5456 (2012).

178. Godde, T. *et al.* Exciton and Trion Dynamics in Atomically Thin $MoSe_2$ and WSe_2: Effect of localization. *Phys. Rev. B* **94**, (2016).

179. Larentis, S., Fallahazad, B. & Tutuc, E. Field-effect Transistors and Intrinsic Mobility in Ultra-Thin $MoSe_2$ Layers. *Appl. Phys. Lett*. **101**, (2012).

180. Zhang, X. *et al.* Facile Fabrication of Wafer-Scale MoS_2 Neat Films with Enhanced Third-order Nonlinear Optical performance. *Nanoscale* **7**, 2978–2986 (2015).

181. Wang, Q., Kalantar-Zadeh, K., Kis, A., Coleman, J. N. & Strano, M. S. Electronics and Optoelectronics of Two-Dimensional Transition Metal Dichalcogenides. *Nat. Nanotechnol.* **7**, 699–712 (2012).

182. Achermann, M. *et al.* Energy-Transfer Pumping of Semiconductor Nanocrystals using an Epitaxial Quantum Well. *Nature* **429**, 642–646 (2004).

183. Wu, L., Chen, Y., Zhou, H. & Zhu, H. Ultrafast Energy Transfer of both Bright and Dark Excitons in 2D van der Waals Heterostructures Beyond Dipolar Coupling. *ACS Nano* **13**, 2341–2348 (2019).

184. Ehrler, B. *et al. In situ* Measurement of Exciton Energy in Hybrid Singlet-Fission Solar Cells. *Nat. Commun*. **3**, (2012).

185. Tabachnyk, M. *et al*. Resonant Energy Transfer of Triplet Excitons from Pentacene to PbSe Nanocrystals. *Nat. Mater*. **13**, 1033–1038 (2014).

186. Cademartiri, L. *et al.* Size-Dependent extinction Coefficients of PbS Quantum Dots. *J. Am. Chem. Soc.* **128**, 10337–10346 (2006).

187. Del Valle, J. C. & Catalán, J. Kasha's rule: A Reappraisal. *Phys. Chem.* **21**, 10061–10069 (2019).

188. Mispelon, A. *et al.* Effects of Added Thiol Ligand Structure on Aggregation of Non-Aqueous ZnO Dispersions and Morphology of Spin-Coated Films. *RSC Adv.* **5**, 18565–18577 (2015).

189. Liu, Y. *et al.* Dependence of Carrier Mobility on Nanocrystal Size and Ligand Length in PbSe Nanocrystal Solids. *Nano Lett.* **10**, 1960–1969 (2010).

190. Melle, S. *et al*. Förster Resonance Energy Transfer Distance Dependence from Upconverting Nanoparticles to Quantum Dots. *J. Phys. Chem. C* **122**, 18751–18758 (2018).

191. Moreels, I. *et al.* Size-Dependent Optical Properties of Colloidal PbS Quantum Dots. *ACS Nano* **3**, 3023–3030 (2009).

192. Neo, M. S., Venkatram, N., Li, G. S., Chin, W. S. & Ji, W. Synthesis of PbS/CdS Core-Shell QDs and their Nonlinear Optical Properties. *J. Phys. Chem. C* **114**, 18037–18044 (2010).

193. Xu, F. *et al*. Impact of Different Surface Ligands on the Optical Properties of PbS Quantum Dot solids. *Materials (Basel)*. **8**, 1858–1870 (2015).

194. Huang, Z. *et al.* PbS/CdS Core–Shell Quantum Dots Suppress Charge Transfer and Enhance Triplet Transfer. *Angew. Chem Int. Ed.* **56**, 16583–16587 (2017).

195. Hines, M. A. & Scholes, G. D. Colloidal PbS Nanocrystals with Size-Tunable Near-Infrared Emission: Observation of Post-Synthesis Self-Narrowing of the Particle Size Distribution. *Adv. Mater.* **15**, 1844–1849 (2003).

196. Backes, C. *et al.* Production of Highly Monolayer Enriched Dispersions of Liquid-Exfoliated Nanosheets by Liquid Cascade Centrifugation. *ACS Nano* **10**, 1589-1601 (2016)

197. Vishwanathan, B. *et al.* A Comparison of Performance of Flat and Bent Photovoltaic Luminescent Solar Concentrators. *Sol. Energy* **112**, 120–127 (2015).

198. Paton, K. R. & Coleman, J. N. Relating the Optical Absorption Coefficient of Nanosheet Dispersions to the Intrinsic Monolayer Absorption. *Carbon*. **107**, 733–738 (2016).

10 Appendices

APPENDIX 1: PHOTOLUMINESCENCE EXCITATION (PLE) SPECTRA NORMALIZATION

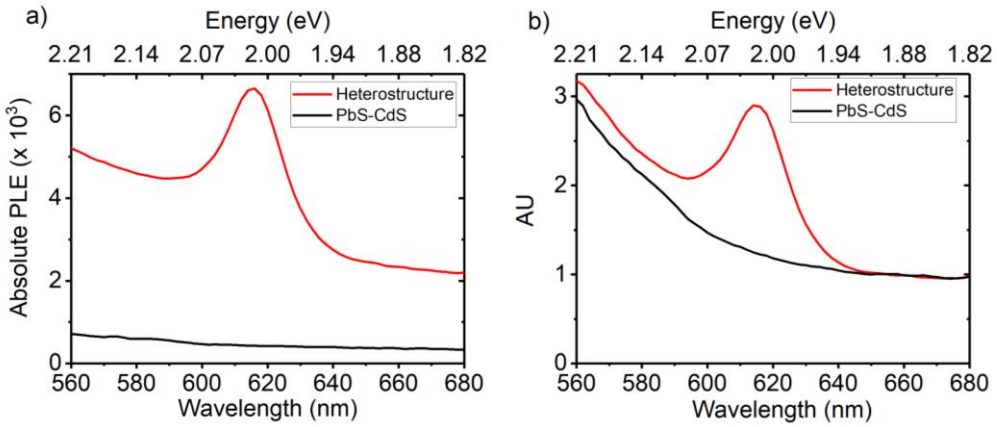

Figure 10.1: Heterostructure PLE spectrum normalization. **a)** Unscaled heterostructure (red) and PbS-CdS (black) PLE data. **b)** Heterostructure and PbS-CdS PLE normalized to mean PLE values off-resonant to underlying WS_2 donor (670-700 nm).

APPENDIX 2: 2D-QD ENERGY TRANSFER EFFICIENCY DERIVATION

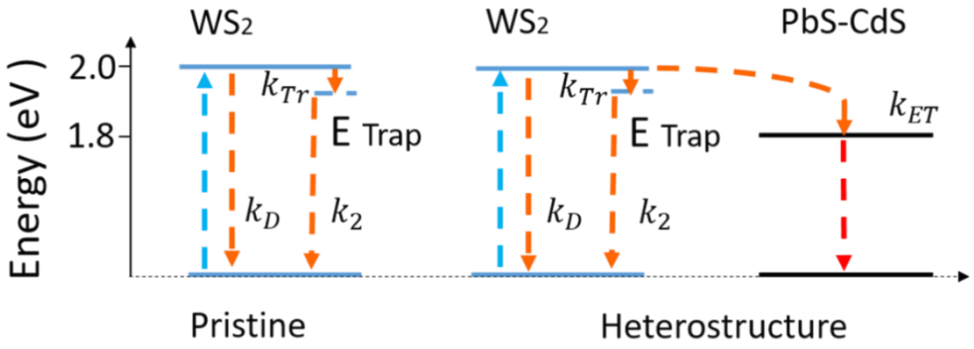

Figure 10.2: Radiative exciton pathways in pristine WS2 and heterostructure

Following the RHS of Figure 10.2, WS_2 donor PL kinetics in the heterostructure can be described *via* the following set of related ordinary differential equations (ODEs):

$$\frac{dD^*}{dt} = -(k_D + k_{TR} + k_{ET})D^* \tag{10.1}$$

$$\frac{dTr}{dt} = k_{TR}D^* - k_2 Tr \tag{10.2}$$

Where D^* and Tr represent the WS_2 donor and trap state exciton populations respectively. The constants k_D, k_{TR}, k_{ET} and k_2 represent the donor's intrinsic recombination rate; intrinsic trapping rate; donor-acceptor energy transfer (ET) rate; and trap-ground state recombination rate respectively. By integration we arrive at the solutions to equations 10.1 and 10.2.

$$D^*(t) = D_0^* e^{-(k_D + k_{TR} + k_{ET})t} \tag{10.3}$$

$$Tr(t) = \frac{k_{TR}D_0^*}{[k_2 - (k_D + k_{TR} + k_{ET})]}\left(e^{-(k_D + k_{TR} + k_{ET})t} - e^{-k_2 t}\right) \tag{10.4}$$

Where D^*_0 represents the initial donor population. As such, the PL dynamics in the heterostructure can be defined as the sum of donor and trap population decay terms given by equations 10.3 and 10.4:

$$PL(t) = D^*(t) + Tr(t) \tag{10.5}$$

i.e.,

$$PL(t) = D_0^* e^{-(k_D + k_{TR} + k_{ET})t} + \left(\frac{k_{TR} D_0^*}{[k_2 - (k_D + k_{TR} + k_{ET})]} \left(e^{-(k_D + k_{TR} + k_{ET})t} - e^{-k_2 t} \right) \right) \tag{10.6}$$

In the absence of the QD acceptor the pristine WS_2 kinetics can be modelled by setting the transfer term $k_{ET} = 0$ so that:

$$PL(t) = D_0^* e^{-(k_D + k_{TR})t} + \left(\frac{k_{TR} D_0^*}{[k_2 - (k_D + k_{TR})]} \left(e^{-(k_D + k_{TR})t} - e^{-k_2 t} \right) \right) \tag{10.7}$$

The PL dynamics described by equations 10.6 and 10.7 consist of fast and slow decay components. In the pristine case (equation 10.7), at short time, *i.e.*, $t \rightarrow 0$, the fast decay time constant is given by:

$$\tau_1 \sim {}^{1}/_{(k_D + k_{TR})} \tag{10.8}$$

Similarly, in the heterostructure case (equation 10.6):

$$\tau_1' \sim {}^{1}/_{(k_D + k_{TR} + k_{ET})} \tag{10.9}$$

At long time *i.e.*, $t \rightarrow \infty$, given that the slow decay component (τ_2) remains unchanged for a given fluence (Table 6.2), the slow decay time in both pristine and heterostructure cases is given as:

$$\tau_2 \sim \tau_2' \sim {}^{1}/_{(k_2)} \tag{10.10}$$

From equations 10.8 and 10.9, we can deduce the ET rate, k_{ET}, as:

$$k_{ET} = (k_D + k_{TR} + k_{ET}) - (k_D + k_{TR}) \tag{10.11}$$

The ET efficiency can then be determined in terms of rate constants. Using equations 10.8, 10.9 and 10.11, the ET efficiency can then be simplified in terms of fast decay time constants to obtain equation 6.12, chapter 6:

$$\eta_{ET} = \frac{k_{ET}}{(k_D + k_{TR} + k_{ET})} = 1 - \frac{\tau_1'}{\tau_1} \tag{10.12}$$

APPENDIX 3: LSC SIMULATION VALIDATION TESTS

Table 10.1: LSC simulation validation tests. Input parameters: Quantum Yield, QY = 80%; concentration, c = 0.18 mM. A.T (Arelo Tanoh); R.M. (Rowan Mac Queen)

Luminophore	η_{opt} (A.T F90)	η_{opt} (RM, Matlab)	Error (%)
LR305	11.92	11.5	0.42
PbS-CdS (1.37 eV)	23.84	23.34	0.5
WS2/PbS-CdS (1.24 eV)	27.6	27.27	0.33

APPENDIX 4: PREPARING MONOLAYER WS_2 MOLAR EXTINCTION DATA

We refer to the work of Paton *et al.*[198] to estimate molar extinction coefficients $\varepsilon(\lambda)$ for a monolayer WS_2 suspension from a single monolayer absorption measurement. The authors derive the expression below, which relates the optical absorption coefficients of TMD nanosheet dispersions $\alpha(\lambda)$ to intrinsic monolayer absorption, $A_{ML}(\lambda)$. The full derivation is provided in the work cited.

$$\boldsymbol{\alpha(\lambda) = \frac{3log_{10}e}{8\rho_{NS}d_o}A_{ML}(\lambda)} \tag{10.13}$$

Where ρ_{NS} is the nanosheet (or monolayer) density is quoted in [g L^{-1}] and d_o is the monolayer thickness in [cm]. The units of $\alpha(\lambda)$ are therefore in [Lg^{-1} cm^{-1}]. Converting $\alpha(\lambda)$ in [Lg^{-1} cm^{-1}] to $\varepsilon(\lambda)$ in [M^{-1} cm^{-1}] is simply a matter of multiplying by the molar mass, Mr_{ML} [g mol^{-1}] of a monolayer as shown in Equation 10.14 below.

$$\boldsymbol{\varepsilon(\lambda) = \frac{3log_{10}e}{8\rho_{NS}d_o}A_{ML}(\lambda)Mr_{ML}} \tag{10.14}$$

The monolayer molar mass, Mr_{ML}, needs to be estimated. This is done *via* the equation:

$$\boldsymbol{Mr_{ML} = N_A\Omega_{ML}\rho_{ML}d_o} \tag{10.15}$$

, where N_A is the Avogadro number in [mol^{-1}], Ω_{ML} is the monolayer area [cm^2] and ρ_{ML} is the monolayer density in [g cm^{-3}].

As an example, estimate the extinction coefficients for a square 50 nm × 50 nm WS_2 monolayer of thickness ~ 0.7 nm. First, the monolayer molecular mass is estimated *via* Equation 10.15. Table 10.2. shows the input values and the result.

Table 10.2: Estimating WS2 monolayer molar mass

N_A	6.022×10^{23} [mol^{-1}]
Ω_{ML}	$(50\times10^{-7})^2$ [cm^2]
ρ_{ML}	7.5 [g cm^{-3}]
d_o	0.7×10^{-7} [cm]
$\boldsymbol{Mr_{ML}}$	$\mathbf{7.9\times10^6}$ **[g $\mathbf{mol^{-1}}$]**

Now, using equation 10.14, the extinction coefficient is estimated using fitted monolayer extinction data. First however, it is important to note that ρ_{NS} is 7500 [g L^{-1}] *or* 1000×ρ_{ML}. Absorption data was fitted using the three Gaussian model, Gauss 3 in Matlab. Figure 10.4.1 *a-c* shows the fitting process. Figure 10.3.*d* shows the resulting estimated extinction spectrum used for LSC simulations in chapter 7.

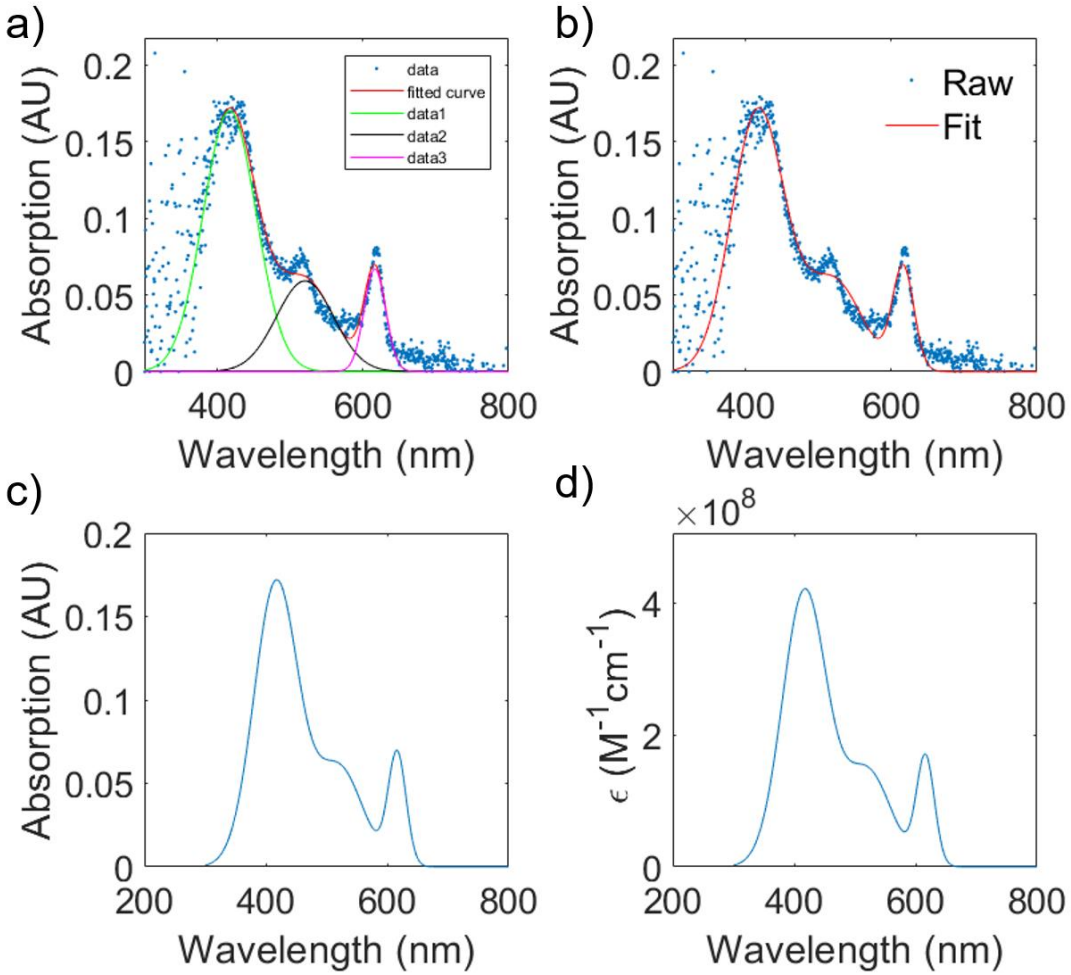

Figure 10.3: Preparing Monolayer WS_2 molar extinction data. a) Three Gaussian fitting; b) Fitted absorption overlapping raw data; c) Fitted absorption data; d) Estimated molar extinction spectrum.